UNIVERSITY OF
BIRMINGHAM

Bistatic Synthetic Aperture Radar using GNSS as Transmitters of Opportunity

by

RUI ZUO

A thesis submitted to
The University of Birmingham
for the Degree of
DOCTOR OF PHILOSOPHY

School of Electronic, Electrical
and Computer Engineering
The University of Birmingham
September 2011

UNIVERSITY OF
BIRMINGHAM

University of Birmingham Research Archive

e-theses repository

This unpublished thesis/dissertation is copyright of the author and/or third parties. The intellectual property rights of the author or third parties in respect of this work are as defined by The Copyright Designs and Patents Act 1988 or as modified by any successor legislation.

Any use made of information contained in this thesis/dissertation must be in accordance with that legislation and must be properly acknowledged. Further distribution or reproduction in any format is prohibited without the permission of the copyright holder.

Abstract

The thesis summarizes the research on the feasibility investigation of Space-Surface (i.e. a spaceborne transmitter and an airborne receiver) Bistatic Synthetic Aperture Radar (SS-BSAR) with a Global Navigation Satellite System (GNSS) which is used as a transmitter of opportunity. The most promising non-cooperative transmitter, among the existing GNSS, for the practical radar applications is the newly introduced European Galileo system. Three main areas are included in the thesis: the system overview, hardware and experimentation, and the experiential results analysis. The system overview discusses the key operation principles (topology, synchronization, etc.) of the proposed radar system and an analysis of the system parameters (power budget, spatial resolution etc.). A hardware was specially developed and the experiments have been conducted to investigate the system feasibility and performance. Synchronisation and image formation algorithms are discussed with the dedication to the proposed radar system. The experimental results, obtained from the synchronisation, stationary receiver and ground moving receiver experiments are presented and analysed in the thesis.

Acknowledgement

First and foremost I offer my sincerest gratitude to my supervisor, Prof Mike Cherniakov, who has supported me throughout my thesis writing with his patience and knowledge. His encouragement, guidance and support from the first day of my PhD to today enabled me to develop a thorough understanding of the subject.

Secondly, I offer my regards and blessings to all of those who supported me in any respect during the completion of my PhD project.

Last not the least, I would like to thank my wife and parents for supporting me spiritually and materially throughout all the years in my life.

CONTENTS

List of Figures

List of Tables

Abbreviations

ACF	**Auto-Correlation Function**
ADC	**Analog-to-Digital Converter**
AF	**Ambiguity Function**
AltBOC	**Alternative Binary Offset Carrier**
ASR	**Azimuth Sampling Rate**
BASS	**Block Adjustment of Synchronising Signal**
BBPA	**Bistatic Back-Projection Algorithm**
BOC	**Binary Offset Carrier**
BPA	**Back-Projection Algorithm**
BPF	**Band Pass Filter**
BPSK	**Binary Phase Shift Keying**
BRCS	**Bistatic Radar Cross Section**
BSAR	**Bistatic Synthetic Aperture Radar**
CCF	**Cross-correlation Function**
CDMA	**Code Division Multiple Access**
CNR	**Carrier Noise Ratio**
CR	**Corner Reflector**
CW	**Continuous Wave**
DFT	**Discrete Fourier Transform**
DLL	**Delay Lock Loop**
DTB-S	**Digital Television Broadcasting Satellite**
ECEF	**Earth Centered, Earth Fixed**
EIRP	**Effective Isotropic Radiated Power**
FDMA	**Frequency Division Multiple Access**
FFT	**Fast Fourier Transform**
FIFO	**First In First Out**
FM	**Frequency Modulation**
FPGA	**Field Programmable Gate Array**
FT	**Fourier Transform**
GEO	**Geostationary Earth Orbit**
GIOVE A/B	**Galileo In-Orbit Validation Element A/B**
GLONASS	**Global Orbiting Navigation Satellite System**
GNSS	**Global Navigation Satellite System**
GPS	**Global Positioning System**
HC	**Heterodyne Channel**

HEO	**High Earth Orbit**
HPBW	**Half-Power Beam Width**
ICO	**Intermediate Circular Orbit**
IF	**Intermediate Frequency**
IFFT	**Inverse Fast Fourier Transform**
IFT	**Inverse Fourier Transform**
INS	**Inertial Navigation System**
I/Q	**In-phase/Quadrature**
LEO	**Low Earth Orbit**
LFM	**Linear Frequency Modulation**
LHCP	**Left Hand Circular Polarisation**
LMS	**Least Mean Square**
LNA	**Low Noise Amplifier**
LO	**Local Oscillator**
LOS	**Line Of Sight**
LPF	**Low Pass Filter**
LS	**Least Square**
MEO	**Medium Earth Orbit**
MISL	**Microwave Integrated Systems Laboratory**
NCT	**Non-Cooperative Transmitter**
NRZ	**Not Return Zero**
PCI	**Peripheral Component Interconnect**
PCS	**Personal Communication Satellite**
PLL	**Phase Lock Loop**
PPP	**Precision Position Processing**
PRF	**Pulse Repetition Frequency**
PRN	**Pseudo-Random Noise**
PSF	**Point Spread Function**
PSD	**Power Spectrum Density**
QPSK	**Quadrature Phase Shift Keying**
RCM	**Range Cell Migration**
RC	**Radar Channel**
RCS	**Radar Cross Section**
RDA	**Range-Doppler Algorithm**
RF	**Radio Frequency**
RHCP	**Right Hand Circular Polarisation**
RINEX	**Receiver Independent Exchange Format**
RMS	**Root Mean Square**
RS	**Reflected Signal**

SAR	**Synthetic Aperture Radar**
SAW	**Surface Acoustic Wave**
SC	**Spare Channel**
SIR	**Signal-to-Interference Ratio**
SL	**Synchronization Link**
SNIR	**Signal to Noise and Interference Ratio**
SNR	**Signal-to-Noise Ratio**
SS	**Space-borne Segment**
SS-BSAR	**Space Surface Bistatic Synthetic Aperture Radar**
SV	**Space Vehicle**
TLE	**Two Line Element**
UAV	**Unmanned Aerial Vehicles**
VCO	**Voltage Control Oscillator**
VSWR	**Voltage Standing Wave Ratio**
WGS 84	**World Geodetic System 1984**

Chapter 1 Introduction and Background

1.1 Radar and Synthetic Aperture Radar

The basic concept of radar, which is the detection and location of reflecting objects, was first demonstrated through the experiments conducted by the German physicist between 1885 and 1888. Following this other evidence on the radar method appeared and was examined by scientists from many other countries, for example Britain and the USA. This method did not become truly useful until the transmitter and receiver were collocated at a single site and pulse waveforms were used. From the 1930s to World War II, radar was rediscovered and many radar systems were developed almost simultaneously and independently in many countries [1]. The original systems measured the range to a target via time delay, and the direction of a target via antenna directivity. It was not long before Doppler shifts were used to measure target speed. Then, in 1951, it was discovered that the Doppler shifts could be processed to obtain fine resolution in a direction that was perpendicular to the range or beam direction. This method was termed Synthetic Aperture Radar (SAR), which referred to the concept of achieving high resolution in the cross-range dimension by taking advantage of the motion of the platform carrying the radar to synthesize the effect of a large antenna aperture through signal processing [2].

In the remote sensing context, a SAR system makes an image of the Earth's surface from a spaceborne or airborne platform. It (Figure 1.1) does this by pointing a radar beam approximately perpendicular to the sensor's motion vector, transmitting phase-encoded

pulses, and recording the radar echoes as they reflect off the Earth's surface. To form an image, intensity measurements must be taken in two orthogonal directions. One dimension is parallel to the radar beam, as the time delay of the received echo is proportional to the distance or range along the beam to the target. The second dimension of the image is given by the travel of the sensor itself. By integrating the received echo along the moving platform, the targets along the azimuth direction can be separated by a fine resolution.

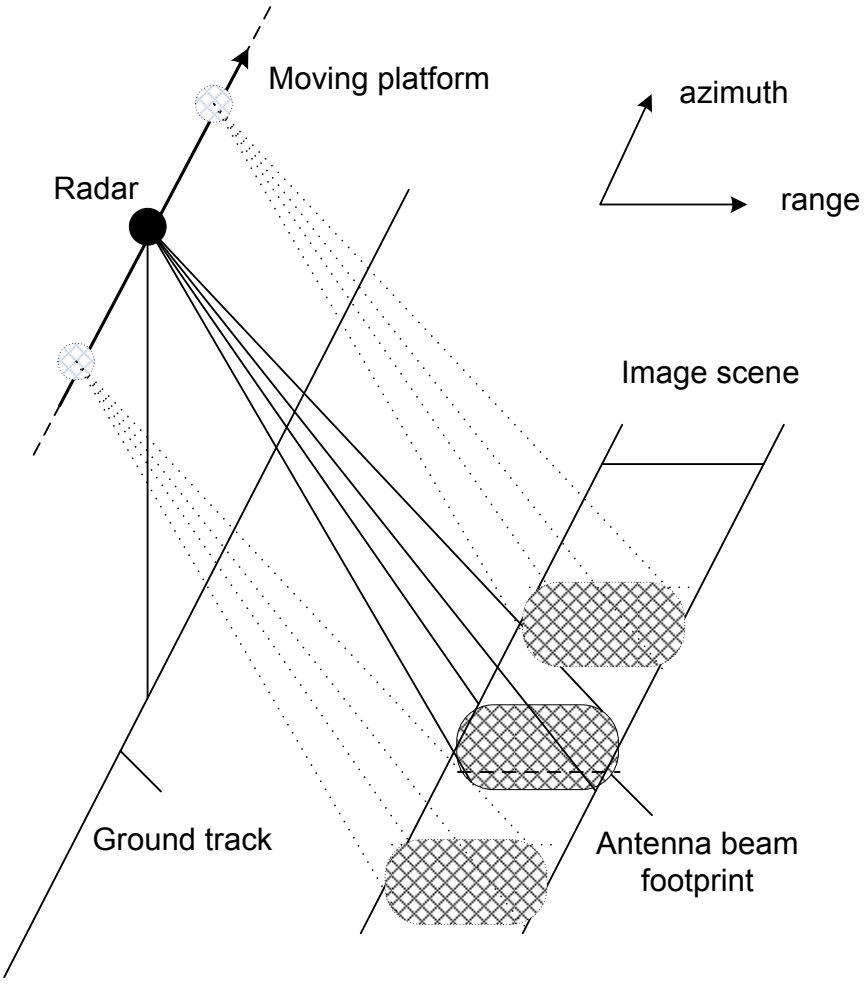

Figure 1.1: *Monostatic SAR Topology (strip-map mode)*

An account of the early development of SAR is given in the first few chapters of [3]. The imaging of the Earth's surface by SAR to provide a map-like display can be applied to military reconnaissance, surveillance and targeting, environmental monitoring, and other remote sensing applications [1]. The application fields of SAR data are very wide. A current review of the application of SAR in remote sensing is given in the Manual of Remote Sensing [4], as well as many websites. The applications include oceanography (wave spectra, wind speed, velocity of ocean currents), glaciology (snow wetness, snow water equivalent, glacier monitoring), agriculture (crop classification and monitoring, soil moisture), geology (terrain discrimination, subsurface imaging), forestry (forest height, biomass, deforestation), deformation monitoring (volcano, Earthquake and subsidence monitoring with differential interferometry), environment monitoring (oil spills, flooding, urban growth, global change), cartography and infrastructure planning as well as military surveillance and reconnaissance [5]. These applications increase almost daily as new technologies and innovative ideas are developed.

1.2 Bistatic Radar

Bistatic radar is defined as radar that uses antennas at different locations for transmission and reception. A transmitting antenna is placed at one site and a receiving antenna is placed at a second site. They are separated by a distance L called the baseline (see Figure 1.2). The target is located at a third site. Any of the sites can be on the Earth, airborne, or in space, and may be stationary or moving with respect to the Earth [6]. Surprisingly, in contrast to most of the currently deployed systems which are working in the monostatic mode, all early radar experiments were of the bistatic type. Before and during

World War II, Germany, Japan, France and the Soviet Union all deployed bistatic radars for aircraft detection. Even the famous British Chain Home monostatic radars had a reversionary bistatic mode. After this bistatic radars went through a few periodic resurgences in interest when specific bistatic applications were found to be attractive [7].

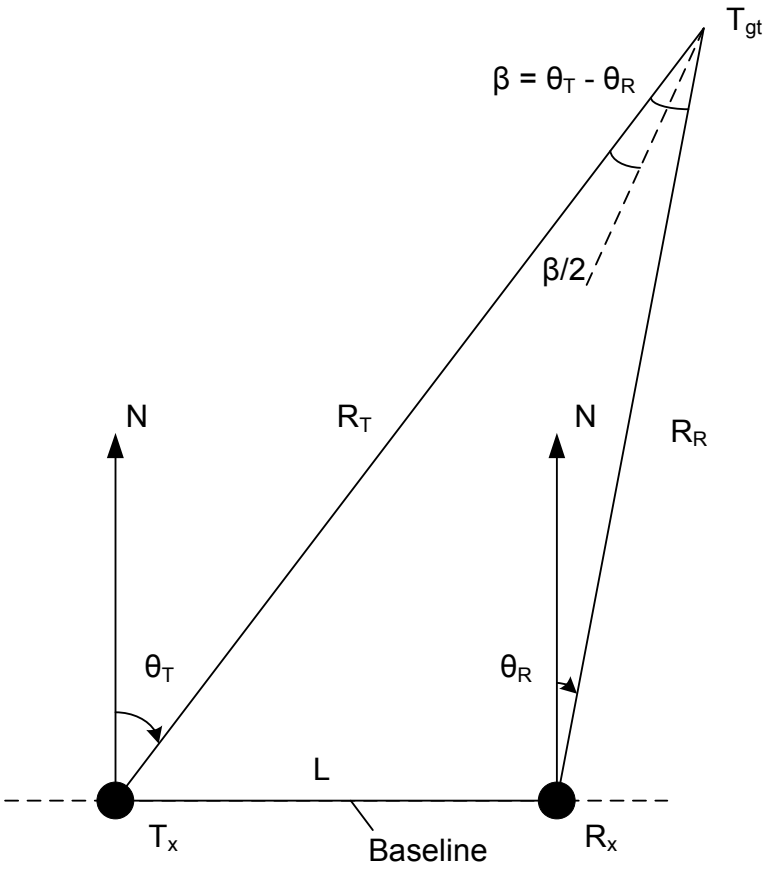

Figure 1.2: *Bistatic Radar in Two Dimensions (courtesy of [6])*

One of the peculiarities of bistatic radar is that the location of the receiver is not revealed by radar emissions; therefore it has been extensively adopted for defence applications. In addition, current stealth technology is effective against a monostatic illuminator, whereas the echoes reflected in other directions cannot be easily reduced. Referring to remote sensing applications, bistatic data provides additional qualitative and quantitative measurements of microwave scattering from a surface and the objects on it. In a number

of situations it is possible to combine monostatic and bistatic data reflected from an observation area and to improve the remote sensing performance.

Passive Bistatic Radar

In recent years there has been growing interest in bistatic radar using transmitters of opportunity, which is termed passive bistatic radar (PBR) [8]. As there is no need for a dedicated transmitter, this makes PBR inherently low cost and hence attractive for a broad range of applications. This technology can utilise existing terrestrial and spaceborne illuminators, such as narrowband digital audio/TV signals [9, 10], wideband FM signal [11], spaceborne/mobile communication signals [12-14] and global navigation signals, etc. There is a relatively wide diffusion of such non-cooperative signal sources. These sources are stable and their characteristics are well known. This makes their use reliable and inexpensive. However, it is worth noting that in this case the geometric and radiometric characteristics of bistatic observation are strictly dictated by illuminator configuration and operation.

Global navigation satellite systems (GNSS) have a number of advantages over these restrictions as non-cooperative transmitters (NCT), compared to other signal sources. Bistatic GNSS radar data can be analysed either by examining the correlation of a reflected waveform or by using the bistatic synthetic aperture radar (BSAR) theory. The shape and strength of the reflected correlation waveform is determined by the roughness and dielectric properties of the surface, while the delay of the reflection with respect to the direct signal gives information about the distance to the receiver. The possibility of

using these properties for remote sensing with GNSS bistatic radar was first presented in [15] as a possible means of measuring differences in ocean heights from a satellite. Other applications include the remote sensing of ocean wave height and wind speeds close to the ocean surface [16-18] and measurements of soil moisture content [19]. The concept of bistatic SAR using a non-cooperative transmitter (NCT) can be used to get a more comprehensive picture of the observed surface. This will be discussed in more detail in the next section.

1.3 Bistatic Synthetic Aperture Radar

As in bistatic radar generally, a bistatic SAR employs a receiving antenna which is located separately from the transmitting antenna, and a synthetic aperture is formed by the motion of one or both antennas (see Figure 1.3). Transmitter and receiver movement may be independent, the trajectories and velocities may be different and even possibly uncoordinated. So the signal synchronisation and trajectory control aspects are even more demanding for bistatic synthetic aperture radar (BSAR), due to the need to form the synthetic aperture. The first documented experiment of synthetic aperture radar in bistatic geometry was conducted using ship-borne radar to observe wave conditions [20]; the motion of the ship was used to synthesize apertures approximately 350m long. The first successful experiment that adopted two airborne SARs flying with programmed separations showed particular aspects of bistatic scattering from rural and urban areas [21].

Advantages connected to the use of synthetic apertures (for example in terms of resolution and image quality parameters) are well known and, consequently, a worldwide interest in the development and exploitation of BSAR is increasing in the scientific community and among remote sensing users [22-24]. More recently, a number of bistatic SAR campaigns have been undertaken by research institutes in Europe. For example, in 2002, QinetiQ performed trials with the two UK systems ESR (transmitter) and ADAS (receiver) that were installed onboard an aircraft and a helicopter, respectively [25]. In 2003, a joint French-German campaign was carried out with RAMSES from ONERA in France and E-SAR from DLR in Germany, both of which were installed onboard aircraft platforms [26]. Also, in 2003 FGAN in Germany collected bistatic SAR data with their two SAR systems AER-II (transmitter) and PAMIR (receiver) in separate aircrafts [27]. With the launch of the satellite TerraSAR-X, both DLR and FGAN have performed bistatic SAR experiments using the Spaceborne sensor as a transmitter of opportunity with FSAR and PAMIR in receive mode, respectively [28, 29].

Although the basic operation of all BSAR systems is much the same, the differences are mainly a consequence of the geometry employed. As a result, both the general and specific analytical BSAR research could be directly, or with some modification, applied to other BSAR systems. Hence, an extensive literature review of past BSAR systems and current development should highlight the direction of the research carried out by this thesis. The review would mainly concentrate on the references which report BSAR system analysis, experimentation descriptions, results and applications, rather than the

references discussing BSAR image formation algorithms, as its derivation and development is beyond the scope of this study.

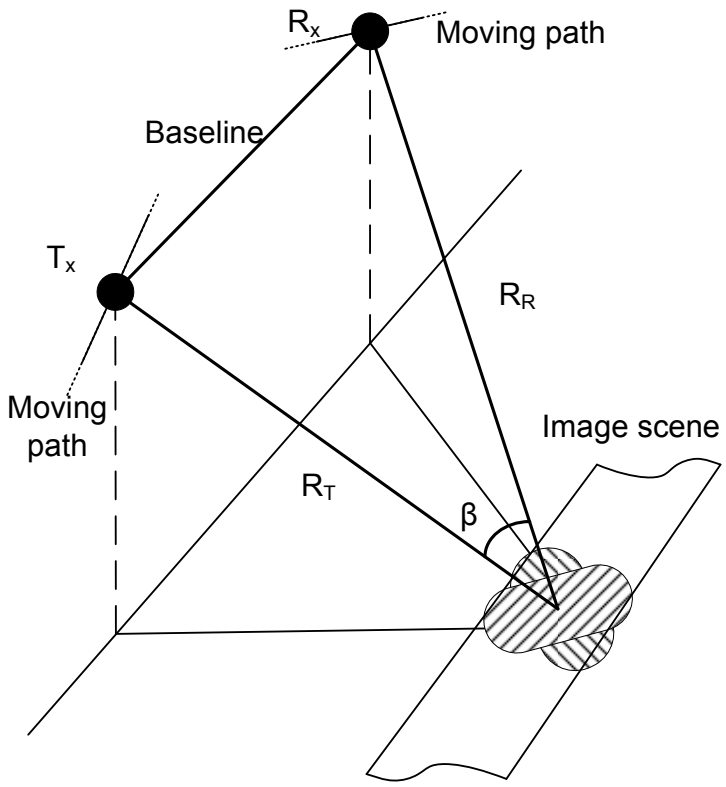

Figure 1.3: *Bistatic SAR General Topology (spaceborne or airborne platform)*

In the section below, three BSAR classes are considered according to their topologies: spaceborne, airborne and space-surface systems. From their names one can easily recognise that in the first case transmitters and receivers are based on two or more satellites, whereas for airborne systems transmitters and receivers are situated on separate airborne platforms. The space-surface BSAR (SS-BSAR) consists of a spaceborne transmitter and a receiver mounted near or on the Earth's surface. The receivers could be airborne, mounted on a ground vehicle or onboard a ship, or even at a stationary position on the ground. For the latter case satellite motion should be used to provide aperture synthesis.

1.3.1 Spaceborne BSAR

As indicated above, spaceborne BSAR consists of two or more satellites, which could be located on different orbits; one conventional monostatic SAR transmitter with one or multiple passive receivers, or vice versa. The reference [30] gives an overview of innovative technologies and applications for future spaceborne bi- and multi-static SAR systems. Several operational advantages which will increase the capability, reliability and flexibility of future SAR missions have been summarized as follows: single-pass interferometry and sparse aperture sensing; frequent monitoring and increased coverage; multi-angle observation and flexible geometry; and cost reduction. Challenges have also been identified, such as precise phase synchronisation, accurate knowledge of orbit trajectory and multi-static image formation algorithms.

For example, a BSAR system, which combines a geostationary transmitter with multiple passive receivers in low Earth orbit (LEO) has been proposed and studied by the authors of [31-33]. A closer look at the resolution cell of such bistatic SAR is included and the system sensitivity is presented by the calculation of the noise equivalent sigma zero (NESZ). It concluded that bistatic SAR focusing will be possible on the basis of appropriately selected ultra-stable quartz oscillators and phase synchronisation will be required. It also indicated achievable baseline estimation accuracy in the millimetre range on the basis of a differential evaluation of the GPS carrier phase.

The authors of [34] present a scientific space mission, BISSAT, Bistatic SAR Satellite, consisting of a satellite carrying a receiving only SAR which receives the signal

transmitted by the existing SAR satellite. According to [35, 36], the BISSAT experiment would be the first bistatic SAR implementation in space with two separate platforms. COSMO/SkyMed SAR has been selected as the primary radar. Its constellation consists of four satellites in one orbital plane. The technical feasibility of the mission has been demonstrated through the orbit and antenna pointing design for bistatic acquisition. An analysis of the attainable performance of a bistatic SAR for oceanographic applications, such as the determination of sea state parameters and the reconstruction of the sea wave spectrum is reported in [37].

There is another BSAR constellation, TanDEM-X, proposed by German scientists [38], which is built by adding a second spacecraft to TerraSAR-X and flying two satellites in a closely controlled formation. Using two spacecraft provides the highly flexible and reconfigurable imaging geometry required for the different mission objectives. It is the first demonstration of a bistatic interferometric satellite formation in space, as well as the first close formation flight in operational mode according to [39, 40]. Several new SAR techniques will also be demonstrated for the first time such as digital beam forming with two satellites, single-pass polarimetric SAR interferometry, as well as single-pass along-track interferometry with varying baselines.

Besides the above-mentioned spaceborne constellation dedicatedly developed for BSAR applications, a synthetic aperture radar is considered in [41], located on a geosynchronous receiver, and illuminated by the backscattered energy of satellite broadcast digital audio or television signals. Spatial resolution, link budget, and possible focusing techniques are

evaluated for the proposed geometry. The main restriction is that only objects that remain stationary half a day could be imaged by the proposed system. Sea, foliage screens, and, in general, whatever moves in a few milliseconds would almost certainly not be imaged. Limited areas could be observed from grounded platforms as well, if it is the transmitter that wanders in the sky. In this case, the more favourable link budget allows shorter integration times and therefore the use of LEO communication satellites.

1.3.2 Airborne BSAR

The first results of an airborne bistatic SAR demonstration were published in 1984 by Auterman [21]. In his experiments both aircraft were constrained to flying parallel flight paths. But technical problems – like the synchronisation of the oscillators, the involved adjustment of transmit pulse versus receive gate timing, antenna pointing, flight coordination, double trajectory measurement and motion compensation and the focusing of bistatic radar data are still not sufficiently solved. In recent decades, more practical work on this topic has been reported with successful results [25, 27, 42-51].

Horne and Yates [25] has provided an overview of a programme of research addressing the problems of airborne bistatic SAR imaging. It has shown that imaging is possible over a surprising range of bistatic geometries with reasonable efficiency. The theory of bistatic synchronisation has been set out and the effect of oscillator phase noise considered in detail, showing that cesium atomic clocks provide a viable solution. The following work presented in [42] focuses on a fully airborne, synchronised bistatic SAR demonstration using QinetiQ's enhanced surveillance radar and the Thales/QinetiQ

airborne data acquisition system, which took place in September 2002. Some of the bistatic imagery from the trial is presented here and compared and contrasted with the monostatic imagery collected at the same time. This initial work has shown that, at a high level, the images appear to be similar to the monostatic ones.

The references [27, 43, 44] deal with an airborne bistatic experiment performed in November 2003: Two SAR systems of FGAN were flown on two different airplanes, the AER-II system was used as a transmitter and the PAMIR system as a receiver. Different spatially invariant flight geometries were tested. High resolution bistatic SAR images were generated successfully. The bistatic range-Doppler processor and the bistatic back projection processor were applied to real data. The experiments consisted of several flight configurations with bistatic angles from 13^{o} up to 76^{o}.

Similar airborne campaigns are described [45, 46] for the first successes in obtaining bistatic cross-platform interferograms from a two aircraft *SAR* acquisition campaign performed between October 2002 and February 2003 by the DLR and ONERA using their E-SAR and RAMSES facilities. The main challenging issues in the signal processing involved are the estimation and compensation of phase drift between the two radars' master oscillators (the bistatic receive signal is demodulated with a local oscillator which is not coherent with the transmitter one) and the determination of the relative aircraft trajectories - *i.e.* interferometric baseline – accurate to the millimetre. The two main geometrical configurations were flown, the quasi-monostatic mode, and a mode with a large bistatic angle. The authors describe this research programme, including the

preparation phase, the analysis of the technological challenges that had to be solved before the acquisition, the strategy adopted for bistatic image processing, the first results and a preliminary analysis of the acquired images.

In the paper [47], authors investigate the potential of bistatic SAR for detecting targets concealed in foliage by numerical electromagnetic simulations. Bistatic SAR imaging in the low VHF-band (28- 73 MHz) was demonstrated by FOI in 2006 [48] and 2007 [49] with CARABAS-II (transmitter) airborne and LORA (receiver) located on the ground. The experiment in 2007 was conducted in Switzerland with Arm Suisse. LORA was deployed on Mount Niesen to achieve steeper incidence angles within the ground scene in order to demonstrate bistatic clutter suppression in forested and urban environments. In December 2009, bistatic SAR data in the VHF/UHF-band (222-460 MHz) were also acquired using two airborne platforms with LORA accompanied by the SETHI sensor which was operated by ONERA [50, 51]. From the results, images with a bistatic elevation angle of 4^{o} (quasi-monostatic case) show similar characteristics to the monostatic images. The images with bistatic elevation angles of 10^{o} and 20^{o}, however, indicate that the clutter level decreases over both forested and urban areas. Measurements show that the signal-to-clutter ratio for a truck vehicle in a forest background increases by up to 10 dB in comparison to the quasi-monostatic case. It is also mentioned that the implemented synchronization method is based on a GPS disciplined 10 MHz reference signal that is generated in both systems. The results showed that two independent GPS systems have, after about a 5 minute warm up period, a maximum drift of 150ns between the 1-PPS signals during 3 hours of measurements.

1.3.3 SS-BSAR

From the SS-BSAR definition, it could have two different configurations, an airborne/ground moving receiver (Figure 1.5) or a stationary receiver (Figure 1.4). The distinguishing feature of such systems is their essentially asymmetric topology, the illumination path being much longer than the echo propagation path. An early SS-BSAR experiment was conducted in 1994 with the NASA/JPL AIRSAR system acting as the passive receiver and a spaceborne C-band SAR acting as the illuminator. A range-Doppler algorithm was used to generate bistatic SAR images [52].

Spaceborne TX – Stationary RX

Most of the BSAR systems proposed in this category are utilising a transmitter of opportunity, such as broadcasting, communications and navigation satellites, or even a non-cooperative radar satellite. For example, Griffiths [13] presented a system concept of a bistatic radar using a satellite-based illuminator of opportunity and a static ground-based receiver. The properties of the satellite illuminator sources have been reviewed in terms of coverage, power density and form of signal, leading to the selection of an Envisat transmitter in low Earth orbit, though it has the significant disadvantage that it is only available for about one second per orbit repeat.The authors of [53, 54] present the results of an experimental test which aimed to evaluate the performance of a SAR system based on the use of an almost geostationary TV satellite as a transmitter and a ground based receiver. The synthetic aperture can be obtained directly by exploiting the satellite daily motion. The receiver implemented for the experiment is described. The resolution capabilities and the link budget of the system have been analysed. It was experimentally

shown that the daily orbit of geostationary TV satellites offers a sufficient synthetic aperture for realizing a parasitic SAR system with a resolution in azimuth direction of about 10 m. Authors were able to measure the satellite location and to image an area of about 40000 m^2 (200 m x 200 m), with a ground resolution cell of about 10 x 10 m^2.

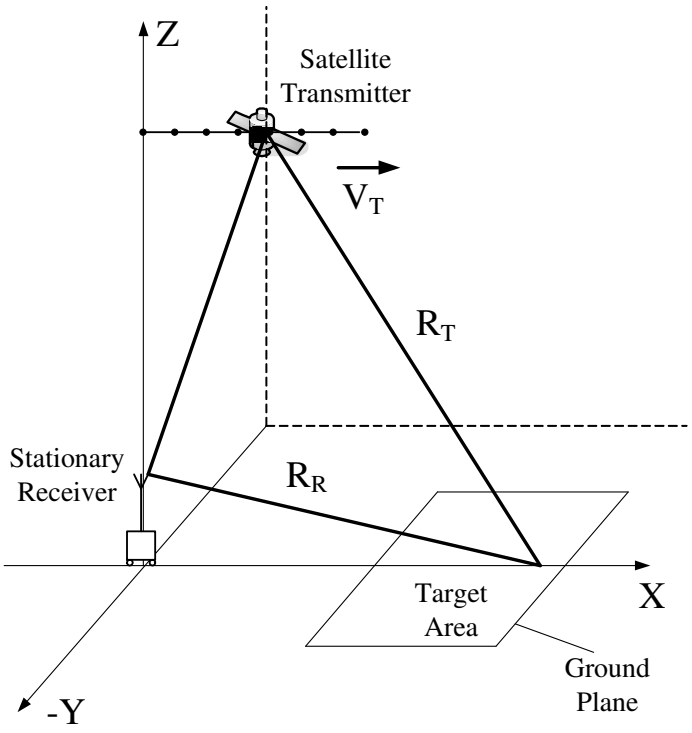

Figure 1.4: *SS-BSAR, Spaceborne Transmitter and Stationary Receiver*

According to [55], communication LEOS, such as Globalstar, ICO and Iridium, could also be effectively used for bistatic synthetic aperture radar design. These satellites transmit signals in the L or S frequency bands and provide sufficient power spectral density near the Earth's surface for effective communication, Moreover, the targets will be characterised by their bistatic radar cross-section (RCS) that could be 20 to 40 dB larger than the monostatic RCS [56]. Furthermore, greater improvements in spatial

resolution and/or reduction in spatial ambiguities are achievable by employing a multi-beam receiver and by simultaneous sensing by multiple LEOS satellites. The direct communication line could be used for the heterodyne synchronization. The 2-D resolving capability of such systems is characterized quantitatively within the ground plane and demonstrated via a meaningful simulation.

Spaceborne TX –Airborne RX

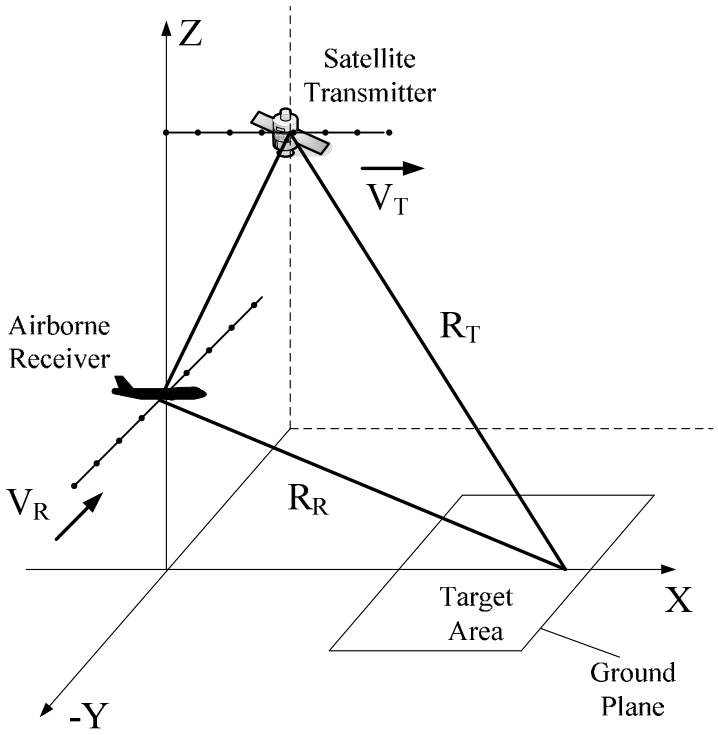

Figure 1.5: *SS-BSAR, Spaceborne Transmitter and Airborne Receiver*

These papers [29, 57, 58] present the first considerations with respect to the optimization of possible geometries between the spaceborne and the airborne SAR sensor. It is concluded that the bistatic geometry has to be adapted to the scene to be imaged. One has to find a compromise between shading effects, a high resolution, possible restriction

in airspace and the demand to receive the direct satellite signal with the airborne platform. Due to the extreme platform velocity differences, SAR modes with flexible steering of the antenna beams are necessary [59]. Several aspects like the ground resolution, Doppler frequency and Doppler-bandwidth have been analysed. Synchronization problems, which arise in bistatic SAR missions have been discussed and solutions for the hybrid bistatic experiment have been presented [60]. Bistatic data acquisition using TerraSAR-X as a transmitter and PAMIR as a receiver and the image results of two experiments have been presented and analysed [61]. The data could be focused using a time-domain and a frequency-domain processor. Finally, the bistatic images have been compared with the monostatic SAR images of TerraSAR-X and PAMIR.

A special configuration is given [62, 63] when the receive antenna looks in a forward direction, which is called bistatic forward-looking SAR. These papers analyse a bistatic forward-looking configuration and demonstrate the capability and feasibility of imaging in the forward or backward directions using the radar satellite TerraSAR-X as the transmitter and the airborne SAR system PAMIR as the receiver. The corresponding iso-range and iso-Doppler contours have been explained. The processed SAR image shows the feasibility of imaging in the forward direction for the first time using a spatially separated transmitter and receiver.

Another spaceborne/airborne bistatic experiment was successfully performed early in November 2007 [64, 65]. TerraSAR-X was used as the transmitter and DLR's new airborne radar system, F-SAR, as the receiver. Monostatic data were also recorded during

the acquisition. Since neither absolute range nor Doppler references are available in the bistatic data set, synchronisation is done with the help of calibration targets on the ground and based on the analysis of the acquired data compared to expected data.

After the first experiment, DLR performed a second bistatic experiment in July 2008 [66] with new challenging acquisitions. The new SAR imaging algorithm, based on the fast factorized back projection algorithm, has demonstrated very good focusing qualities while dramatically reducing (up to a factor of 100 with respect to direct back projection) the overall computational load. These papers [67-69] have given a comprehensive report of the TerraSAR-X/F-SAR bistatic SAR experiment including a description, performance estimation, data processing and results. The experiment was the first X-band bistatic spaceborne/airborne acquisition and the first including full synchronization (performed in processing steps) and high-resolution imaging. The performance analysis presented for this azimuth-variant acquisition has been validated, including the quantitative analysis of the effects of antenna patterns on the along-track resolution and SNR. Finally, a comparison of the monostatic TerraSAR-X and bistatic TerraSAR-X/F-SAR images has shown some interesting properties. The bistatic image has an advantage in terms of resolution and SNR and in the complete absence of range ambiguities (highly dependent on configuration and acquisition).

Besides conventional radar satellites, global navigation satellites are also considered to be suitable for SS-BSAR applications. For example, in paper [70], the traditional bistatic GNSS radar and bistatic synthetic aperture radar (SAR) concepts are fused into a more

generic multistatic GNSS SAR system for surface characterization. This is done by using the range and Doppler processing techniques on signals transmitted by multiple satellites to determine the angular dependence of the surface reflectivity.

This thesis is dedicated to the case of SS-BSAR with a GNSS transmitter of opportunity i.e. GPS (US), GLONASS (RU) and Galileo (EU). As the non-cooperative transmitter, GNSS satellites have advantages and drawbacks in comparison with other signal sources. The unique feature is that GNSS operates with a large constellation of satellites. Typically, at any point on the Earth's surface, 4 to 8 satellites are above the horizon (Figure 1.6). As a result, a particular satellite in the best (or at least a suitable) position can be selected and there is no need for a very specific receiver trajectory to allow the observation of an area. Moreover, signals from more than one satellite could potentially be used to provide radiogrammetric 3-D surface mapping. Another advantage is a relatively simple synchronisation of GNSS signals. This follows on from the fact that navigation signals were designed to be optimal for remote synchronisation.

The main drawback is a relatively low power budget, e.g. Direct Satellite TV (DTB-S) broadcasting transmitters introduce about a 20 dB stronger power flux density near the Earth's surface in comparison to GNSS. The power budget analysis of GNSS based BSAR is analysed against thermal noise, as well as interference from other satellites [71, 72]. GNSS radiating power is about a 10-15 dB signal-to-noise ratio (SNR) over one millisecond of integration time at the matched receiver output. The second problem, the signal-to-interference ratio (SIR), should be evaluated. The direct path interference and

adjacent path interference power density in the targets-receiver areas are near equal (GNSS transmitting antenna introduce a flat power density near the surface irrelevant to the satellites elevation up to 10 degrees). Increasing the integration time will result in the adjacent path interference level decreasing proportionally.

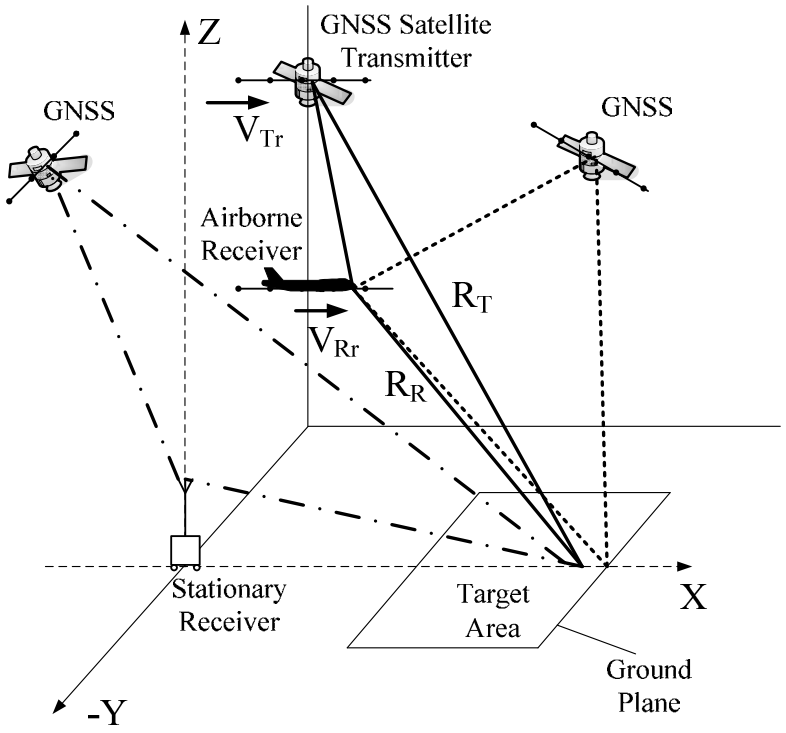

Figure 1.6: *GNSS based SS-BSAR*

1.4 Summary of Research

1.4.1 Research Contributions

This research focuses on SS-BSAR using GNSS as the transmitter of opportunity. The main goal of this research is to investigate the feasibility of BSAR systems using spaceborne navigation satellites and to verify its performance, such as spatial resolution

and signal-to-noise ratio. Figure 1.7 below presents the block diagram of the proposed SS-BSAR system. It consists of a non-cooperative spaceborne transmitter and a passive receiver with two receiving channels. The synchronisation and motion compensation will be applied to the heterodyne channel signal, and the radar image will be obtained by the image formation algorithm.

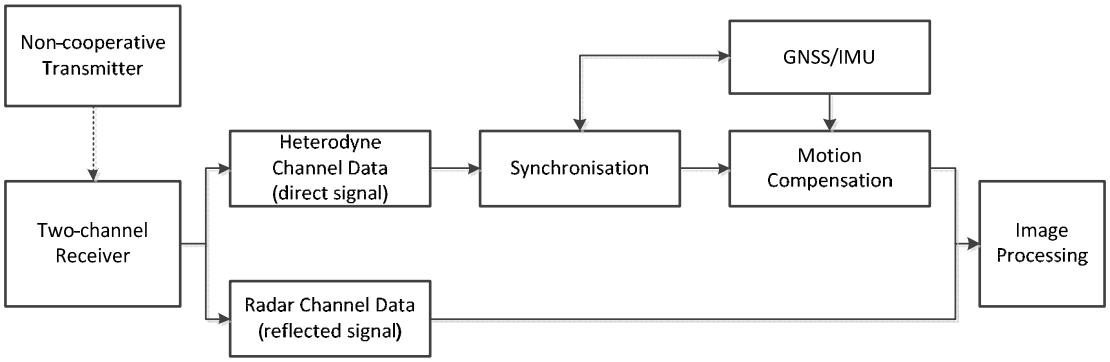

Figure 1.7: *The Block Diagram of the proposed SS-BSAR System*

For the system analysis, the stationary and airborne receivers have been considered, and both GLONASS and Galileo satellites have been used as the non-cooperative transmitter for the experimentation. The main goal of this research is to investigate the feasibility of BSAR systems using spaceborne navigation satellites and to verify its performance, such as spatial resolution and signal-to-noise ratio.

First of all, system analysis has been determined in theory by analysing the system parameters such as the transmitter parameters, spatial resolution, power budget and the property of ranging signals. It was highlighted that the GNSS satellite transmits more

than 10 dB less power compared to other satellites. However, it has the advantage of satellite diversity and thus one can choose the desired bistatic topology for low resolution loss. It is concluded that overall GNSS satellites are the most suitable non-cooperative transmitter candidates for SS-BSAR applications. It provides a reasonable range resolution of ~ 3-8 m and a target detection range of ~ 3-12 km for 50 m^2 targets.

As GNSS signals are designed for navigation purposes, one navigation signal (Galileo E5) has been studied analytically in terms of radar application. Its correlation property has been investigated by simulation and a technique has been invented to combine full E5 bandwidth and to improve potential range resolution for GNSS based SS-BSAR systems. Synchronisation, as an inevitable issue for non-cooperative bistatic system, has also been investigated. In our case, phase synchronisation is the most important, as the largely separated transmitter and receiver must be coherent over extremely long intervals of time. Synchronisation using a direct link signal has been proposed and the algorithm to extract the required information has been applied to the simulated and experimental data.

To obtain the experimental data for image formation and to confirm the system analysis results, an experimental test bed for the proposed SS-BSAR system has been developed and tested with full functionality. Experimentation methodology has been planned and a number of experiments have been conducted. It includes a synchronisation experiment, a stationary receiver experiment, and a ground moving receiver experiment, and for the final stage, an airborne receiver experiment. The synchronisation experiment will be used to prove the functioning of the hardware and the synchronisation algorithm. With

the complexity of the bistatic SAR image formation, a stationary receiver experiment will be used to test the basic functioning and procedure of the image formation algorithm. Only after this, the moving receiver experiment can be conducted and a set of data has been collected according to the above mentioned requirements.

Image formation algorithms for SS-BSAR, such as range-Doppler and back-projection algorithms have been studied and briefly discussed. As the development of focusing techniques for general bistatic topology is beyond the scope of this thesis, the detailed discussion of the image formation algorithm for SS-BSAR using GNSS can be found at [73, 74]. To generate a bistatic image, certain issues such as parameter estimation (transmitter and receiver trajectory history) and motion compensation have also been considered. The solutions have been proposed and applied to experimental data. Using the data from moving ground-based receiver and airborne receiver trials, radar images for two target scenes have been obtained successfully and analysed to some extent.

In term of publications, three journal papers have been published (author and co-author) and three papers have been presented at conferences with a number of co-authored conference papers during the Ph.D. study period. The list of papers is included in the Appendix H.

1.4.2 Organization of Thesis

Chapter 2 discussed the selection of non-cooperative transmitters for SS-BSAR with an airborne receiver. Four different types of spaceborne transmitters, including communications, broadcasting and navigation satellites, are analysed and compared in terms of availability, coverage and visibility time in section 2.2. Section 2.3 focuses on potential range resolution (with respect to available signal bandwidth) and achievable azimuth resolution. It also highlights the effect of resolution degradation due to bistatic topology. The iso-range and iso-Doppler contours are plotted and compared for different geometries, including monostatic, quasi-monostatic and bistatic topology. The system power budget obtained using GNSS is specifically formulated in section 2.4. Transmitter parameters are presented and the signal-to-noise ratio is analysed for the heterodyne and radar channels.

Chapter 3 contains an analysis of GNSS signals from the radar application point of view. As Galileo E5 was mainly used for real data collection, its characteristics are discussed in section 3.2, including its equation, modulation, spectrum and block diagrams for generation and reception. More details are included in Appendix A for the generation of spreading codes for Galileo E5 signals. Section 3.3 examines the correlation property of GNSS signals, including GLONASS L1 signal, E5a, E5b and full E5 signals. In section 3.4 the range resolution enhancement is proposed by combining the full E5 bandwidth and achieving an improved range resolution of a factor of two. The preliminary simulation results are given using the proposed method at the end of Chapter 3.

One of the most sensitive problems of SS-BSAR system functionality, i.e. synchronisation, is addressed in Chapter 4. The problem of synchronisation is introduced in section 4.1. The equations of the received signal are presented and its dynamics are analysed. An algorithm is specially proposed for the synchronisation of SS-BSAR using GNSS. Section 4.2 provides the description of the signal acquisition method, as a coarse estimation. Fine tracking of information, such as code delay, Doppler shift and carrier phase, has been discussed in section 4.3. In section 4.4, the proposed synchronisation methods and algorithms are confirmed by the experimentation. The results from the synchronisation channel focusing are also given at the end of Chapter 4.

In Chapter 5 the hardware design and development of the SS-BSAR test-bed is described in detail. The functionality of each hardware block is discussed and justified, including antennas, RF front-end, receiving chain, ADC and sampling clock, etc. A set of testing set-ups is also included in section 5.3. More details, descriptions and testing results can be found for all the hardware in Appendices C-G.

Chapter 6 consists of two main parts. The first part introduces the programme of experimentation leading to airborne SS-BSAR imaging. Experiment strategies and trial plans are designed to confirm the system performance. It has been divided into three stages: stationary receiver, ground moving receiver and airborne receiver. The actual experimental parameters and set-up block diagrams are also given. The second part discusses the parameter estimation procedures for the experimental data. Before applying

the image formation algorithm to the experimental data, the parameters such as the transmitter/receiver trajectories, Doppler shift and phase histories need to be estimated with defined accuracy. Two problems, residual Doppler shift and motion compensation are briefly discussed in section 6.5. The practical methods are proposed for transmitter/receiver parameter extraction and compensation. Also, the estimation results from the real experimental data are discussed at the end of Chapter 6.

The final part of the thesis is dedicated to the BSAR image formation and results analysis. Original SS-BSAR focusing algorithms are briefly described. Images obtained from stationary receiver experiments have been analysed in section 7.2. A reference target (corner reflector) has been used to confirm the expected system performance. In section 7.3, the image results from a ground moving receiver are shown and analysed in terms of resolution, around natural targets, such as houses. The peculiarity is that the images are obtained from two simultaneously received Galileo satellites for the same target area.

The main conclusions regarding the research during the Ph.D. period can be found in Chapter 8. The feasibility of the proposed SS-BSAR using GNSS as a non-cooperative transmitter system has been verified with the support of the experimental imaging results; and the system performance has been investigated to some extent. The direction for future SS-BSAR research is discussed. A number of problems, which have not been fully addressed within the thesis, are identified and some suggestions are included at the end of Chapter 8.

References

1. Skolnik, M.I., *Introduction to Radar Systems*. third edition ed. 2002: McGraw Hill.
2. Skolnik, M.I., *Radar Handbook*. 1990: McGraw Hill.
3. Patrick, F.J., *Synthetic Aperture Radar*. 1988, Springer-Verlag.
4. *Manual of Remote Sensing - Theory, Instruments and Techniques*. 1975, The American Society of Photogrammetry.
5. Cumming, I.G. and F.H. Wong, *Digital processing of Synthetic Aperture Radar data*. 2005: Artech House.
6. Willis, N.J., *Bistatic Radar*. 1991: Artech House.
7. Willis, N.J. and H.D. Griffiths, *Advances in Bistatic Radar*. 2007: SciTech Publishing.
8. *Bistatic Radar: Emerging Technology*, ed. M. Cherniakov. 2008: John Wiley & Sons.
9. Saini, R. and M. Cherniakov, *DTV signal ambiguity function analysis for radar application.* IEE Proceeding Radar, Sonar and Navigation, 2005. **152**(3): p. 133-142.
10. Poullin, D., M. Flecheus, and M. Klein, *New capabilities for PCL system: 3D measurement for receiver in multidonors configuration*, in *2010 European Radar Conference*. 2010. p. 344-347.
11. Cardinali, R., et al., *Multipath cancellation on reference antenna for passive radar which exploits FM transmission*, in *IET International Conference on Radar Systems*. 2007. p. 1-5.
12. Cherniakov, M., D. Nezlin, and K. Kubik, *Air target detection via bistatic radar based on LEOS communication signals* IEE Proceeding Radar, Sonar and Navigation, 2002. **149**(1): p. 33-38.
13. Griffiths, H.D., et al., *Bistatic radar using satellite-borne illuminators*, in *RADAR-92 Conference*. 1992. p. 276-279.
14. Tan, D.K.P., et al., *Passive radar using global system for mobile communication signal: theory, implementation and measurements.* IEE Proceedings Radar, Sonar and Navigation, 2005. **152**(3): p. 116 - 123.
15. Clifford, S.F., et al., *GPS sounding of ocean surface waves: theoretical assessment*, in *In Proc. Int. Geosci. and Remote Sens. Symp.* 1988: Seattle, USA. p. 2005-2007.
16. Garrison, J.L. and S.J. Katzberg, *The application of reflected GPS signals to ocean remote sensing*. Remote Sens. Environ., 2000. **73**: p. 175-187.
17. Elfouhaily, T., D.R. Thompson, and L. Linstrom, *Delay-Doppler Analysis of Bistatically Reflected Signals From the Ocean Surface: Theory and Application, , vol. , No, pp. .* IEEE Trans. Geosci. Remote Sens., 2002. **40**(3): p. 560-573.
18. Armatys, M., et al., *A Comparison of GPS and Scatterometer Sensing of Ocean Wind Speed and Direction*, in *IGARSS 2000*. 2000: Honolulu, HI.

19. Zavorotny, V.U. and A.G. Voronovich, *Bistatic GPS signal reflections at various polarizations from rough land surface with moisture content*, in *In the Proceedings of the IEEE International Geoscience and Remote Sensing Symposium (IGARSS)*. 2000: Piscataway, NJ. p. 2852-2854.
20. Teague, C.C., G.L. Tyler, and R.H. Stewart, *Studies of the sea using HF radio scatter.* IEEE Journal of Oceanic Engineering, 1977. **2**(1): p. 12 - 19.
21. Autermann, J.L., *Phase stability requirements for a bistatic SAR*, in *IEEE National Radar Conference*. 1984. p. 48 - 52.
22. D'Addio, E. and A. Farina, *Overview of detection theory in multistatic radar.* IEE Proceedings-F, 1986. **133**(7): p. 613-623.
23. Hanle, E., *Survey of bistatic and multistatic radar.* IEE Proceedings-F, 1986. **133**(7): p. 587-595.
24. Hsu, Y.S. and D.C. Lorti, *Spaceborne bistatic radar - an overview.* IEE Proceedings-F, 1986. **133**(7): p. 642-648.
25. Horne, A.M. and G. Yates, *Bistatic synthetic aperture radar*, in *IEE Radar Conference*. 2002. p. 6-10.
26. Cantalloube, H., et al., *A first bistatic airborne SAR interferometry experiment - preliminary results*, in *Sensor Array and Multichannel Signal Processing Workshop Proceedings, 2004* 2004. p. 667 - 671.
27. Ender, J.H.G., I. Walterscheid, and A.R. Brenner, *New aspects of bistatic SAR: processing and experiments*, in *Geoscience and Remote Sensing Symposium, 2004. IGARSS '04. Proceedings. 2004 IEEE International* 2004. p. 1758 - 1762.
28. Younis, M., R. Metzig, and G. Krieger, *Performance prediction of a phase synchronization link for bistatic SAR.* Geoscience and Remote Sensing Letters, IEEE 2006. **3**(3): p. 429 - 433.
29. Ender, J.H.G., et al., *Bistatic Exploration using Spaceborne and Airborne SAR Sensors: A Close Collaboration Between FGAN, ZESS, and FOMAAS*, in *Geoscience and Remote Sensing Symposium, 2006. IGARSS 2006. IEEE International Conference on* 2006 p. 1828 - 1831.
30. Moccia, A. and G. Krieger, *Spaceborne Synthetic Aperture Radar (SAR) Systems: State of the Art and Future Developments*, in *33rd European Microwave Conference*. 2003: Munich, Germany. p. 101 - 104.
31. Krieger, G., et al., *Analysis of system concepts for Bi- and Multi-static SAR missions*, in *IEEE IGARSS*. 2003. p. 770-772.
32. Krieger, G., H. Fiedler, and A. Moreira, *Bi- and multistatic SAR: potentials and challengers*, in *EUSAR*. 2004. p. 265-270.
33. Krieger, G. and A. Moreira, *Spaceborne bi- and multistatic SAR: potentials and challengers.* IEE Proc.-Radar Sonar Navig., 2006. **153**(3).
34. D'Errico, M., M. Grassi, and S. Vetrella, *A Bistatic SAR Mission for Earth Observation based on a small satellite.* Acta Astronautica, 1996. **39**(9-12): p. 837-846.

35. D'Errico, M. and A. Moccia, *The BISSAT mission: A bistatic SAR operating in formation with COSMO/SkyMed X-band radar*, in *IEEE Conference in Aerospace*. 2002. p. 2-809 to 2-818.
36. Moccia, A., et al., *BISSAT: a bistatic SAR for earth observation*. 2002.
37. Moccia, A., et al., *Oceanographic applications of Spaceborne bistatic SAR*, in *IEEE IGARSS*. 2003. p. 1452-1454.
38. Keieger, G., et al., *TanDEM-X: mission concept and performance analysis*, in *Geoscience and Remote Sensing Symposium IEEE International*. 2005. p. 4890 - 4893.
39. Nies, H., O. Loffeld, and K. Natroshvili, *The bistatic aspect of the TanDEM-X mission*, in *Geoscience and Remote Sensing Symposium IEEE International*. 2007. p. 631 - 634.
40. Zink, M., et al., *The TanDEM-X mission: overview and status*, in *Geoscience and Remote Sensing Symposium IEEE International*. 2007. p. 3944 - 3947.
41. Prati, C., et al., *Passive Geosynchronous SAR system reusing backscattered digital audio broadcasting signals.* IEEE Transactions on Geoscience and Remote Sensing, 1998. **36**(8): p. 1973-1976.
42. Yates, G., et al., *Bistatic SAR image formation.* Radar, Sonar and Navigation, IEE Proceedings - 2006. **153**(3): p. 208 - 213.
43. Walterscheid, I., A.R. Brenner, and J.H.G. Ender, *Results on bistatic synthetic aperture radar.* Electronics Letters 2004. **40**(19): p. 1224 - 1225.
44. Walterscheid, I., et al., *Bistatic SAR Processing and Experiments.* Geoscience and Remote Sensing, IEEE Transactions on 2006. **44**(10): p. 2710 - 2717.
45. Dreuillet, P., et al., *The ONERA RAMSES SAR: latest significant results and future developments*, in *Radar, 2006 IEEE Conference on* 2006. p. 518 - 524.
46. Dubois-Fernandez, P., et al., *ONERA-DLR bistatic SAR campaign: planning, data acquistiton, and first analysis of bistatic scattering behaviour of natural and urban targets.* Radar, Sonar and Navigation, IEE Proceedings - 2006. **153**(3): p. 214 - 223.
47. Ulander, L.M.H. and T. Martin, *Bistatic ultra-wideband SAR for imaging of ground targets under foliage*, in *Radar Conference, 2005 IEEE International* 2005. p. 419 - 423.
48. Ulander, L.M.H., et al., *Bistatic Experiment with Ultra-Wideband VHF-band Synthetic- Aperture Radar*, in *Synthetic Aperture Radar (EUSAR), 2008 7th European Conference on* 2008. p. 1 - 4.
49. Barmettler, A., et al., *Swiss Airborne Monostatic and Bistatic Dual-Pol SAR Experiment at the VHF-Band*, in *Synthetic Aperture Radar (EUSAR), 2008 7th European Conference on* 2008. p. 1 - 4.
50. Baqué, R., et al., *LORAMbis A bistatic VHF/UHF SAR experiment for FOPEN*, in *Radar Conference, 2010 IEEE* 2010. p. 832 - 837.
51. Ulander, L.M.H., et al., *Signal-to-clutter ratio enhancement in bistatic very high frequency (VHF)-band SAR images of truck vehicles in forested and urban terrain.* Radar, Sonar & Navigation, IET 2010. **4**(3): p. 438 - 448.

52. Martinsek, D. and R. Goldstein, *Bistatic radar experiment*, in *Proc. EUSAR'98*. 1994: Friedrichshafen, Germany. p. 31-34.

53. Cazzani, L., et al., *A ground based parasitic SAR experiment*, in *Geoscience and Remote Sensing Symposium, 1999. IGARSS '99 Proceedings. IEEE 1999 International* 1999. p. 1525 - 1527.

54. Cazzani, L., et al., *A ground-based parasitic SAR experiment.* Geoscience and Remote Sensing, IEEE Transactions on 2000. **38**(5): p. 2132 - 2141.

55. Cherniakov, M., K. Kubik, and D. Nezlin, *Bistatic synthetic aperture radar with non-cooperative LEOS based transmitter*, in *Geoscience and Remote Sensing Symposium, 2000. Proceedings. IGARSS 2000. IEEE 2000 International* 2000. p. 861 - 862.

56. Homer, J., et al., *Passive bistatic radar sensing with LEOS based transmitters*. 2002. p. 438 - 440.

57. Klare, J., et al., *Evaluation and Optimisation of Configurations of a Hybrid Bistatic SAR Experiment Between TerraSAR-X and PAMIR*, in *Geoscience and Remote Sensing Symposium, 2006. IGARSS 2006. IEEE International Conference on* 2006. p. 1208 - 1211.

58. Walterscheid, I., J.H.G. Ender, and O. Loffeld, *Bistatic Image Processing for a Hybrid SAR Experiment Between TerraSAR-X and PAMIR*, in *Geoscience and Remote Sensing Symposium, 2006. IGARSS 2006. IEEE International Conference on* 2006. p. 1934 - 1937.

59. Walterscheid, I., T. Espeter, and J.H.G. Ender, *Performance analysis of a hybrid bistatic SAR system operating in the double sliding spotlight mode*, in *Geoscience and Remote Sensing Symposium, 2007. IGARSS 2007. IEEE International* 2007. p. 2144 - 2147.

60. Espeter, T., et al., *Synchronization techniques for the bistatic spaceborne/airborne SAR experiment with TerraSAR-X and PAMIR*, in *Geoscience and Remote Sensing Symposium, 2007. IGARSS 2007. IEEE International* 2007. p. 2160 - 2163.

61. Walterscheid, I., et al., *Bistatic SAR Experiments With PAMIR and TerraSAR-X—Setup, Processing, and Image Results.* Geoscience and Remote Sensing, IEEE Transactions on 2010. **48**(8): p. 3268 - 3279.

62. Espeter, T., et al., *Bistatic Forward-Looking SAR: Results of a Spaceborne–Airborne Experiment.* Geoscience and Remote Sensing Letters, IEEE, 2011. **8**(4): p. 765 - 768.

63. Walterscheid, I., et al., *Potential and limitations of forward-looking bistatic SAR*, in *Geoscience and Remote Sensing Symposium (IGARSS), 2010 IEEE International* 2010. p. 216 - 219.

64. Baumgartner, S.V., et al., *Bistatic Experiment Using TerraSAR-X and DLR's new F-SAR System*, in *Synthetic Aperture Radar (EUSAR), 2008 7th European Conference on* 2008. p. 1 - 4.

65. Rodriguez-Cassola, M., et al., *Bistatic spaceborne-airborne experiment TerraSAR-X/F-SAR: data processing and results*, in *Geoscience and Remote*

Sensing Symposium, 2008. IGARSS 2008. IEEE International 2008. p. 451 - 454.

66. Rodriguez-Cassola, M., et al., *New processing approach and results for bistatic TerraSAR-X/F-SAR spaceborne-airborne experiments*, in *Geoscience and Remote Sensing Symposium,2009 IEEE International,IGARSS 2009* 2009. p. 242 - 245.
67. Rodriguez-Cassola, M., et al., *Bistatic TerraSAR-X/F-SAR Spaceborne–Airborne SAR Experiment: Description, Data Processing, and Results.* Geoscience and Remote Sensing, IEEE Transactions on 2010. **48**(2): p. 781 - 794
68. Rodriguez-Cassola, M., et al., *Efficient Time-Domain Focussing for General Bistatic SAR Configurations: Bistatic Fast Factorised Backprojection*, in *Synthetic Aperture Radar (EUSAR), 2010 8th European Conference on* 2010. p. 1 - 4.
69. Rodriguez-Cassola, M., et al., *General Processing Approach for Bistatic SAR Systems: Description and Performance Analysis*, in *Synthetic Aperture Radar (EUSAR), 2010 8th European Conference on* 2010. p. 1 - 4
70. Lindgren, T. and D.M. Akos, *A Multistatic GNSS Synthetic Aperture Radar for Surface Characterization.* Geoscience and Remote Sensing, IEEE Transactions on 2008. **46**(8): p. 2249 - 2253.
71. He, X., Z. T., and M. Cherniakov, *Interference Level Evaluation In SS-BSAR With GNSS Non- Cooperative Transmitter.* IEE Electronic Letters, 2004. **40**(19): p. 1222-1224.
72. He, X., T. Zeng, and M. Cherniakov, *Signal detectability in SS-BSAR with GNSS non-cooperative transmitter.* Radar, Sonar and Navigation, IEE Proceedings - 2005. **152**(3): p. 124 - 132
73. Antoniou, M., M. Cherniakov, and C. Hu, *Space-Surface Bistatic SAR Image Formation Algorithms.* Geoscience and Remote Sensing, IEEE Transactions on 2009. **47**(6): p. 1827 - 1843.
74. Antoniou, M., R. Saini, and M. Cherniakov, *Results of a Space-Surface Bistatic SAR Image Formation Algorithm.* Geoscience and Remote Sensing, IEEE Transactions on 2007. **45**(11): p. 3359 - 3371

Chapter 2 Non-cooperative Transmitter for SS-BSAR

2.1 Introduction

Bistatic radar is radar operating with separated transmitting and receiving antennas. The co-operative bistatic radar means that the transmitter and the receiver are specially designed to operate together and have built-in methods of synchronisation. The system specifications, such as power, waveform, antenna beam coverage, signal processing etc, are also chosen to suit a particular application. The non-cooperative bistatic radar, on the other hand, employs a radar receiver to 'hitchhike' off other sources of illumination. The sources can be other radar transmitters, transmissions from audio-video broadcasting, navigation or communications satellites. This mode of operation is termed as non-cooperative since the illuminator is not specifically built to support the planned operation.

In general, SS-BSAR does not only assume the use of cooperative spaceborne transmitters, but also the use of existing non-cooperative transmitters in space, such as broadcasting, navigation, communications and other radar satellites. The fundamental requirement for such a transmitter is the availability and reliability. It should not be deliberately switched off without appropriate notification and/or authorization. In addition, the optimal transmitter should have system diversity and unlimited coverage. It increases the system flexibility and the bi (multi) static system architecture can be properly structured. Moreover, the most vitally important parameters for optimal NCT are the transmitter's radiating power and the property of the transmitting signal. The

reflected signal should have enough energy for radar applications considering most of satellite signals are designed for direct reception; the bandwidth and modulation of this signal should provide reasonable resolution and simplicity for radar processing. For remote sensing applications, they must provide reasonable target detection with appropriate range resolution at the operating distance.

Potentially most of the existing satellites in space can be used as the non-cooperative transmitter for SS-BSAR. Classified by orbit altitude, which has the most effect on the formation of SS-BSAR geometry, they are divided into three categories: low earth orbit (LEO), medium earth orbit (MEO) and high earth orbit (HEO, include geostationary orbit). Classified by spaceborne application, which decides the characteristics of the transmitting signal, there are broadcasting, navigation, communications and other radar satellites.

In this chapter, different satellite systems are considered and justified as the NCT candidates for SS-BSAR. They are:

1) GNSS (MEO), including GPS (USA), GLONASS (Russia) and Galileo, the forthcoming European system.
2) Geostationary broadcasting/communications satellites (HEO), which are for the purpose of international telephony, TV and radio transmission etc. ASTRA, a group of thirteen satellites provides direct-to-home transmission of TV, radio and multimedia services in Europe; and Inmarsat-3, five satellites provide telephony and data services to users world-wide, are used for calculation.

3) LEO satellite systems, providing a wide variety of mobile services, such as voice, data, and facsimile transmission. Iridium, a system of 66 active communication satellites allowing worldwide voice and data communications, is considered as the example.

2.2 Availability and Reliability

The fundamental problem of bistatic radar with the utilization of non-cooperative transmitter is the transmitter's availability and reliability. Firstly these transmitters should not be deliberately switched off without appropriate authorization, and secondly they should not be easily destroyed by a hostile activity. From these points of view the best candidates are transmitters on broadcasting, navigation and communications satellites. From the previous chapter, it is noted that a number of SS-BSAR systems have been proposed and studied using the conventional spaceborne monostatic SAR as the transmitter [1, 2]. In this case they are regarded as cooperative transmitters from the operation point of view and will not be included in the discussion below.

2.2.1 GNSS

GNSS is the common name of satellite-based systems for global navigation, positioning and time transfer. The most well-known of these is the Global Positioning System (GPS), provided by the United States, which became fully operational in 1995. Russia also has a similar system, called the GLObal NAvigation Satellite System (GLONASS), which has had operational status since the beginning of the 1990's. Galileo is a future

European system: the first two testing satellite have been launched and the system should be in operation by 2013.

The nominal GPS operational constellation consists of 24 satellites that orbit the earth in about 12 hours. The orbit altitude is 20,180 km and the satellite constellation repeats its position, with respect to any point on the earth's surface, every 24 hours approximately (4 minutes earlier each day). There are six orbital planes (with nominally four space vehicles in each), and inclined at about fifty-five degrees with respect to the equatorial plane. The four satellites in the same orbit plane are not equally spaced, the spacing being chosen to minimize the effects of a single satellite failure on system performance. At any time and at any location on the earth (neglecting obstacles such as mountains and tall buildings) a GPS receiver should have a direct line of sight to between four and eleven operational satellites.

The operational space segment of GLONASS consists of 24 satellites in 3 orbital planes, with 3 on-orbit spares. The three orbital planes are separated by 120°, with the satellites equally spaced within the same orbital plane, being 45° apart. Each satellite operates in a circular orbit at an altitude of 19,130 km (slightly lower than that of the GPS satellites) with an inclination angle of 64.8 degrees; each satellite completes an orbit in approximately 11 hours 15 minutes. A characteristic of the GLONASS constellation is that the satellite orbits repeat the same ground track after 8 days. As each orbit plane contains 8 satellites, there is a non-identical repeat (i.e., another satellite will occupy the same place in the sky) after one sidereal day. This differs from the GPS identical repeat

period of one sidereal day. The spacing of the satellites in orbit is arranged so that at least 5 satellites are in view at any given time, allowing the provision of continuous and global coverage of the terrestrial surface and the near-earth space. The GLONASS constellation is currently operating in a degraded mode with only 18 satellites fully operational.

When Galileo, Europe's own global satellite navigation system, is fully operational in 2013, there will be 30 new satellites in Medium Earth Orbit (MEO) around the earth at an altitude of 23,222 km. Ten satellites will occupy each of three orbital planes inclined at an angle of 56° to the equator. The satellites will be spread evenly around each plane and will take about 14 hours to orbit the Earth. One satellite in each plane will be a spare; on stand-by to replace any operational satellite fail. The inclination of the orbits was chosen to ensure good coverage of polar latitudes, which are poorly served by GPS. With 30 satellites at such an altitude, there is a very high probability (more than 90%) that anyone anywhere in the world will always be in sight of at least four satellites. From most locations, six to eight satellites will always be visible.

Within three different GNSS systems, GPS is mainly for military purpose although it provides civil signals. GLONASS is currently in degradation status with partial constellation in space. European Galileo will be a complete civil system with 30 satellites in space and probably the most suitable non-cooperative transmitter for the experiments carried out by the research described in this thesis.

2.2.2 Geostationary Communications Satellites

A satellite in a geostationary orbit appears to be in a fixed position to an earth-based observer, which revolves around the earth at a constant speed once per day. Geostationary orbits can only be achieved very close to the ring 35,786 km directly above the equator. This section will consider two geostationary satellite systems: the Astra series and Inmarsat-3. SES Astra operates thirteen satellites from four orbital locations, seven at 19.2°E, three at 28.2°E, two at 23.5°E and one at 37.5°W. The principle of "co-location" (several satellites in the same orbital location) increases flexibility and redundancy. There are five Inmarsat-3 satellites in space providing global coverage except poles. Each satellite is equipped with a single global beam that covers up to one-third of the Earth's surface, apart from the poles. In general, global beam coverage extends from latitudes of −78 to +78 degrees regardless of longitude. It also has a maximum of seven wide spot beams, which are optimized for covering most areas of interest and is thus somewhat limited in comparison to global beam coverage. Geostationary communications satellites have an extremely wide footprint on the ground and time-invariant elevation angles to the satellites. However, they have power-limited links and extremely low elevation angles in high-latitude countries and Polar Regions.

2.2.3 LEO Satellite Systems

A LEO is generally defined as an orbit within the locus extending from the Earth's surface up to an altitude of 2,000 km. Given the rapid orbital decay of objects below approximately 200 km, the commonly accepted definition for LEO is from 200 to 2000 km above the Earth's surface. LEO systems have low propagation loss and feature global

service capability. However, they have a shorter satellite visibility period and a much larger Doppler shift. There are a few LEO systems in operation now. In this section, we will consider Iridium as the example. The Iridium network consists of a constellation of 66 satellites, 785 km in altitude, with 6 polar orbital planes inclined 86.4 degrees, each containing 11 satellites. The resulting orbital period is roughly 100 minutes from pole to pole. This design means that there is excellent satellite visibility and service coverage at the North and South poles.

2.2.4 Comparisons

In this chapter, satellite systems from three different orbits are chosen for comparison as the non-cooperative transmitter for SS-BSAR. As transmitters of opportunity, they all are reliable sources of illumination. In term of availability, GNSS and Iridium provide global coverage, Inmarsat-3 covers most of earth surface except poles and ASTRA mainly covers Europe (but there are always other DTV satellite providing services in other continents). Table 2.1 below shows the availability for each system and Figures A.1-4 (in appendix A) show the satellite footprints, which is generated by software GPS simulation [3] for the considered satellite and constellation.

Table 2-1: *Satellite Availability*

	GPS	GLONASS	Galileo	ASTRA	Inmarsat 3	Iridium
Number of Satellites	24	24	30	13	5	66
Coverage	Global	Global	Global	Europe	Global except poles	Global
Multi-satellite Visibility	4-8	4-8	4-10	1	1	1 or 2
Visible Time (minutes)	60-360	60-360	60-360	All the time	All the time	11

It can be seen from the table above that GNSS systems have more flexibility and redundancy than other systems to form an optimal bistatic geometry because of its multiple satellite visibility and long satellite visibility time. The unique feature of GNSS is that it operates with a large constellation of satellites. Typically, at any point on the earth's surface, 4 to 8 satellites are simultaneously visible above the horizon from a single GNSS constellation. As a result, a particular satellite in the best (or at least suitable) position can be selected and there is no need for a specific receiver trajectory to allow the observation of a selected area. Moreover, signals from more than one GNSS satellite could be potentially used to provide radiogrammetric 3-D surface mapping. The Iridium system also has a large constellation of satellites; however, only 1 or 2 Iridium satellites are available at the same time due to its low earth orbit. Another advantage of GNSS is its relatively long satellite visible period comparing with LEO satellite systems. It varies from 60 to 360 minutes depending on satellite orbit trajectory and the observation position on the earth's surface.

The main drawback of using GNSS as a non-cooperative transmitter focuses on the limited bandwidth of the navigation signals and relatively low power budget, which is not specially designed for radar applications. These will be discussed in the following sections.

2.3 Target Resolution

The definition of bistatic target resolution is identical to that of monostatic target resolution: the degree to which two or more targets may be separated in one or more dimensions, such as angle, range, velocity (or Doppler) etc [4]. For monostatic range resolution, a separation between two target echoes at the radar is conventionally taken to be $C/2B$, where B is the signal bandwidth; the achievable azimuth resolution for focused monostatic SAR is independent both of the range and of the wavelength used, but equals to half of antenna physical aperture, $D/2$. In bistatic SAR, the spatial resolution is determined by not only the signal bandwidth and the length of the antenna aperture, but also the trajectories of the transmitter and receiver, which eventually specifies the bistatic geometry. For SS-BSAR case, the slant range resolution along the bistatic bisector is calculated by the equation

$$\Delta_R = \frac{C}{2B} \cdot \frac{1}{\cos(\beta/2)} \tag{2.1}$$

An important observation to make is that range resolution depends only on the direction from the target to the transmitter and receiver but not the slant range distance. Figure 2.1 below shows the bistatic geometry for SS-BSAR with a spaceborne transmitter and an airborne receiver, where

L is the bistatic baseline;

$\overrightarrow{V_T}, \vec{\omega}_T, A_T$ are the transmitter's velocity, angular speed and total angular movement respected to the target;

$\overrightarrow{V_R}, \vec{\omega}_R, A_R$ are the receiver's velocity, angular speed and total angular movement respected to the target;

$\overrightarrow{U_T}, \overrightarrow{U_R}$ are the unit vector from the transmitter and receiver to the target.

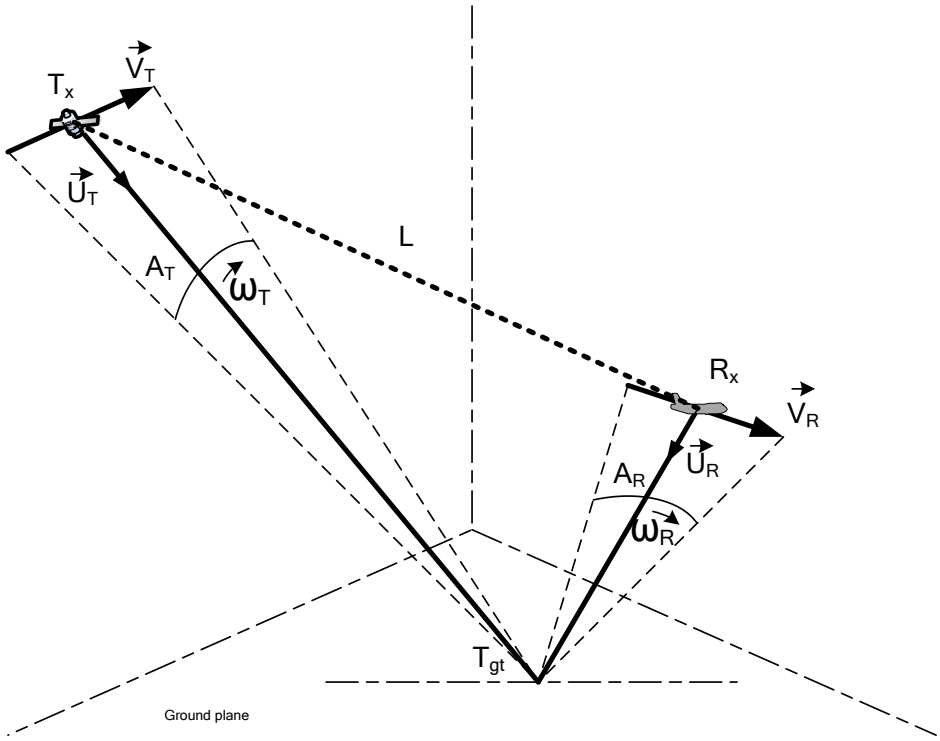

Figure 2.1: *Bistatic Geometry for SS-BSAR*

Most of time, the range resolution projected on the ground has more practical meanings, and it can be calculated by

$$\Delta_{Rg} = \frac{\Delta_R}{\cos(\varphi)} = \frac{C}{2B} \cdot \frac{1}{\cos(\beta/2)\cos(\varphi)} \tag{2.2}$$

where φ is the angle between the bistatic bisector and the ground plane, see Figure 2.2. It shows the projection of bistatic resolution on the ground plane, its direction is along the ground projection of the vector, $\overrightarrow{U} = \overrightarrow{U_T} + \overrightarrow{U_R}$.

In SS-BSAR, if both the transmitter and the receiver move significantly during the integration time, the Doppler shift of the signal received from a target may be written as

$$f_{Dop} = \frac{|\overrightarrow{V_T} \cdot \overrightarrow{U_T} + \overrightarrow{V_R} \cdot \overrightarrow{U_R}|}{\lambda} \tag{2.3}$$

where $\overrightarrow{V_T} \cdot \overrightarrow{U_T}$ is the projection of transmitter's instantaneous velocity to the line-of-sight of transmitter to target. The Doppler resolving capability depends on the coherent integration time T_c, how long the combined antenna beam illuminates the target. The radar can resolve two point targets separated in Doppler shift by $\Delta f_{Dop} = \frac{1}{T_c}$. And the Doppler resolution is finest along the direction of equivalent angular speed, which is the vector summation of transmitter and receiver angular speed, $\overrightarrow{\omega} = \overrightarrow{\omega_T} + \overrightarrow{\omega_R}$. The azimuth resolution is determined by this equivalent angular speed of bistatic system. We have

$$\Delta_{az} = \frac{\lambda}{T_c \cdot |\overrightarrow{\omega_T} + \overrightarrow{\omega_R}|} \tag{2.4}$$

where λ is the wavelength.

It can be concluded that for a high altitude transmitter and low altitude receiver (most cases in SS-BSAR), the receiver dominates the azimuth resolution since the angular speed of the receiver to the target is much bigger due to closer range to the target. If geostationary satellites are used, the transmitter's angular speed is negligible with respect

to the ground target so that only the receiver motion is taken into account to generate aperture synthesis. The potential azimuth resolution for bistatic SAR can be written as

$$\Delta_{az} = \frac{\lambda R_R}{L_c} = \frac{\lambda R_R}{V_R T_c} \tag{2.5}$$

where L_c is the length of the synthetic aperture. For a given real antenna, the maximum length of the aperture is given by $L_{\max} \approx \theta_R R = \frac{\lambda}{D} R$, where θ_R is a beamwidth of the aircraft's antenna pattern and D is the effective along-track dimension of the antenna. Substituting $L_{\max}$ for L_c in equation 2.5, we find the finest azimuth resolution in the focused bistatic SAR case is:

$$\Delta_{az} = D \tag{2.6}$$

This means that the inherent azimuth resolution for bistatic SAR is the physical antenna's along track dimension and is independent of range, velocity, or wavelength.

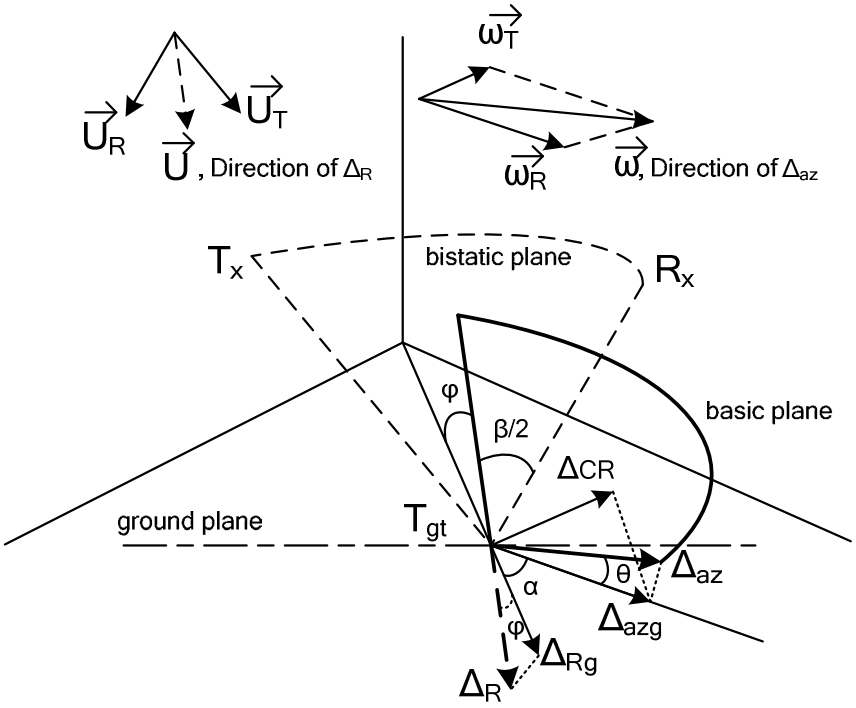

Figure 2.2: *Resolution Projection on the Ground Plane*

Figure 2.2 presents the general case of bistatic resolution projection on the ground. It can be found that the ground azimuth resolution can be written as

$$\Delta_{azg} = \frac{\Delta_{az}}{\cos(\theta)} = \frac{\lambda}{T_c \cdot |\vec{\omega}_{Tr} + \vec{\omega}_{Rx}| \cdot \cos(\theta)} \tag{2.7}$$

where θ is the angle between the equivalent angular speed and the ground plane.

In SAR mapping, the size of the image pixels is an important parameter of the system performance. As shown in Figure 2.3, the ground range and azimuth resolutions derived in bistatic SAR do not by themselves specify the pixel size in a meaningful way since they are not necessarily orthogonal. Defining α to be the angle between the directions of the ground range and azimuth resolution, a representation of the resolution cell size is its area given by

$$S_g = \frac{\Delta_{Rg} \cdot \Delta_{azg}}{\sin(\alpha)} \tag{2.8}$$

The cross range resolution can be defined to produce an equivalent rectangle with the same pixel area

$$\Delta_{CR} = \frac{\Delta_{azg}}{\sin(\alpha)} = \frac{\lambda}{T_c \cdot |\vec{\omega}_{Tr} + \vec{\omega}_{Rx}| \cdot \cos(\theta)\sin(\alpha)} \tag{2.9}$$

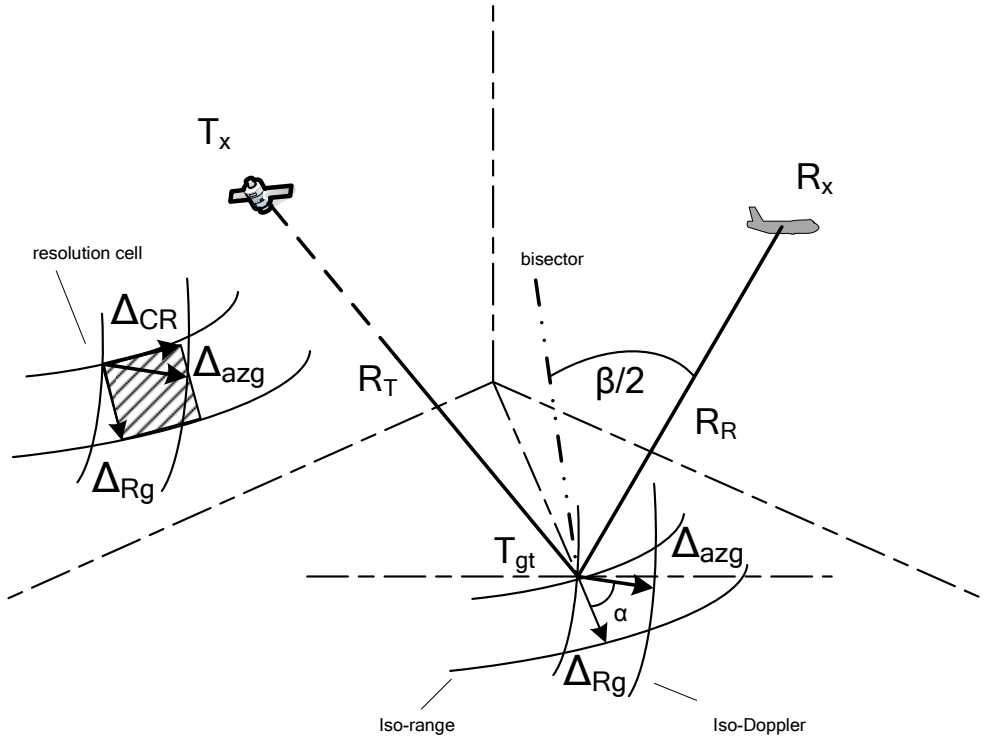

Figure 2.3: *SS-BSAR Resolution Cell*

Table 2-2 shows the potential range resolution of different satellite systems. We can see that Galileo transmits an E5a/b signal with the same bandwidth of GPS L5 & P codes and twice of GLONASS P-code; and the full bandwidth of the E5 signal may be combined by signal processing techniques utilizing 20-50 MHz bandwidth to gain better range resolution (3 to 8 meters). The range resolutions shown in the table are only achievable by the quasi-monostatic SAR geometry, which means the space transmitter is always positioned on, or near, the continuous line of target-to-receiver line-of-sight and the parallel transmitter and receiver's trajectories required during the whole period of the synthetic aperture.

Figure 2.4 shows that the range resolution degrades with the increasing bistatic angle. For this reason satellite diversity,(multiple satellites visible simultaneously above the horizon) will enable the receiver to pick up the signal from the optimal transmitter position minimizing the bistatic angle. The favourable constellation of GNSS satellites enables a random receiver trajectory to find a suitable satellite to format the desired quasi-monostatic geometry. But for the other three satellite systems, the effects of geostationary or poor multiple satellite visibility, implies that a specific receiver trajectory will be required to achieve the potential quasi-monostatic SAR range resolution, which is not practical in some cases.

Table 2-2: *Potential Range Resolution*

Transmitter	Signal Bandwidth (MHz)	Aggregated Bandwidth* (MHz)	Quasi- Monostatic SAR Range Resolution (m)
ASTRA	2	20	7.5*
Galileo E5a/b	10.23	-	15
Galileo E5	-	20-50	3-8
GPS L5/P	10.23	-	15
GLONASS P	5.11	-	30
Inmarsat 3	2	20	7.5*
Iridium	0.04	10	15*

* Bandwidth and resolution achieved by combining multiple channels

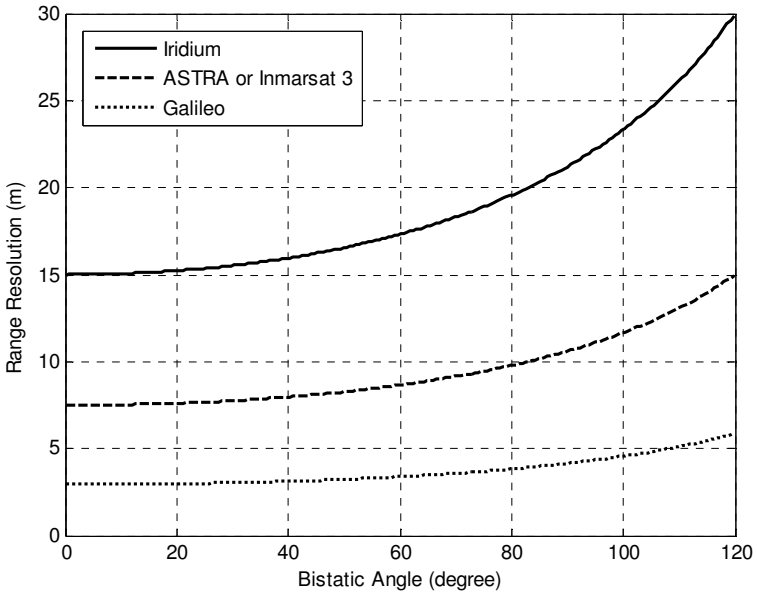

Figure 2.4: *Range Resolution vs Bistatic Angle*

Table 2-3: *Calculation Parameters*

Transmitter to target centre range	20000 km
Transmitter incident angle	45 degree
Transmitter speed	3000 m/s
Receiver altitude	500 m
Receiver speed	10 m/s
Integration time	100 s
Signal bandwidth	10.23 MHz
Monostatic range resolution	15 m
Carrier frequency	1191.795 MHz (Galileo E5)

Earlier works by Willis [5], Jones [6] derived the traditional bistatic radar resolution using a geometrical method, similar to equation 2.9 derived above. There is another method, vector gradient, used by Cardillo [7] to define bistatic SAR range and Doppler

resolution. This approach provides a more consistent way to derive the resolution without the need for the approximations used in earlier works. This method will be applied to a typical SS-BSAR geometry example, given in Figure 2.5. Table 2.3 gives the parameters necessary for the resolution calculation. Iso-contours and bistatic resolution are derived and plotted in Figure 2.6.

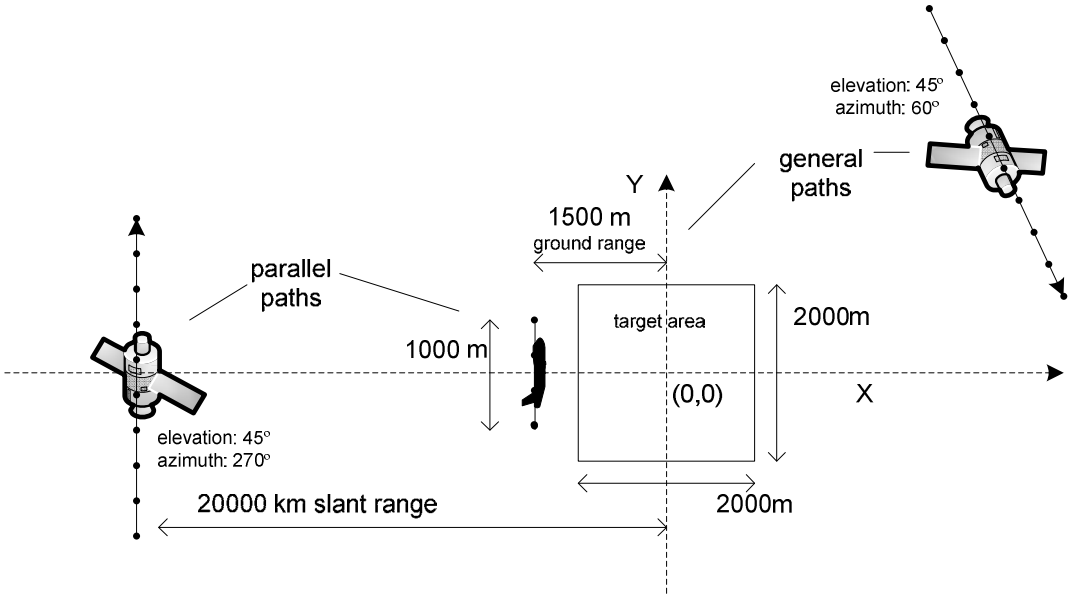

Figure 2.5: *2D Bistatic Geometry*

Figure 2.6 shows the contours with constant range (thick line in blue) and Doppler (thin line) on the ground plane, parallel to the earth's surface. Figures 2.6(a) and 2.6(b) are for the conventional monostatic SAR and quasi-monostatic SAR with stationary receiver, to provide the comparison with the bistatic SAR case. The coordinate origin in the centre denotes the receiver position and the arrow indicates the receiver velocity. Figures 2.6(c) and 2.6(d) are for bistatic SAR with parallel transmitter and receiver paths and general (non-parallel) paths, as shown in Figure 2.5. It is clearly shown in Figure 2.6(d) that range contours become asymmetric for the non-parallel case due to large bistatic angle

but Doppler contours remain similar in both parallel and non-parallel cases. This is because of the large difference in transmitter-to-target and receiver-to-target slant range, giving a ratio of 20000 km to 1500 m. Hence the bistatic range is dominated by the transmitter-to-target slant range; and the Doppler shift (equivalent angular speed) would be dominated by the receiver motion.

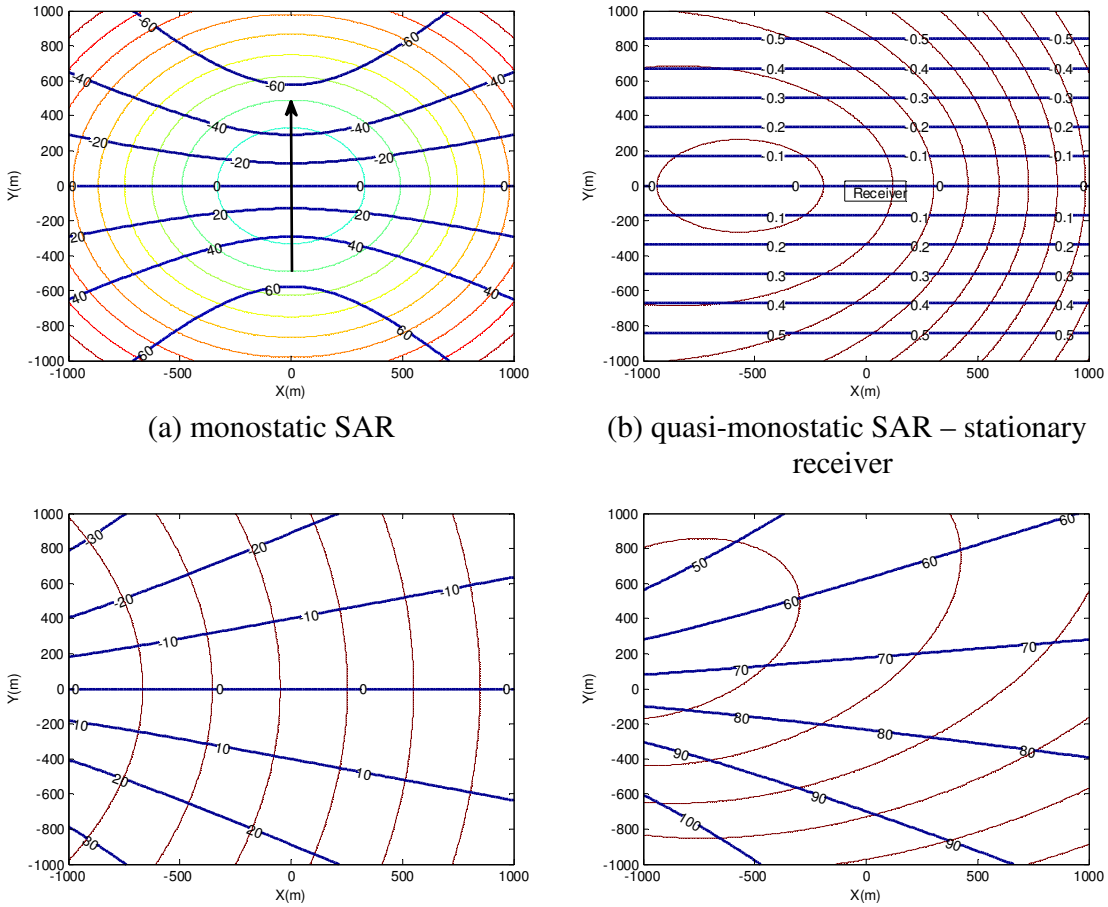

(a) monostatic SAR

(b) quasi-monostatic SAR – stationary receiver

(c) SS-BSAR – parallel paths

(d) SS-BSAR – non parallel paths

Figure 2.6: *Bistatic Image Grid: Iso-range Contours and Iso-Doppler Contours*

Figure 2.7 shows bistatic resolution and ground resolution for the SS-BSAR parallel paths case. The ground projection for both range and azimuth resolutions degrade slightly because of the relatively small bistatic angle in this case. Similar to the Doppler

contours plotted above, azimuth resolution is mainly decided by receiver speed and the direction of motion. Considering the short integration time, SS-BSAR with parallel paths may be considered similar to the quasi-monostatic SAR case and Equation 2.5 could be used to approximately define azimuth resolution.

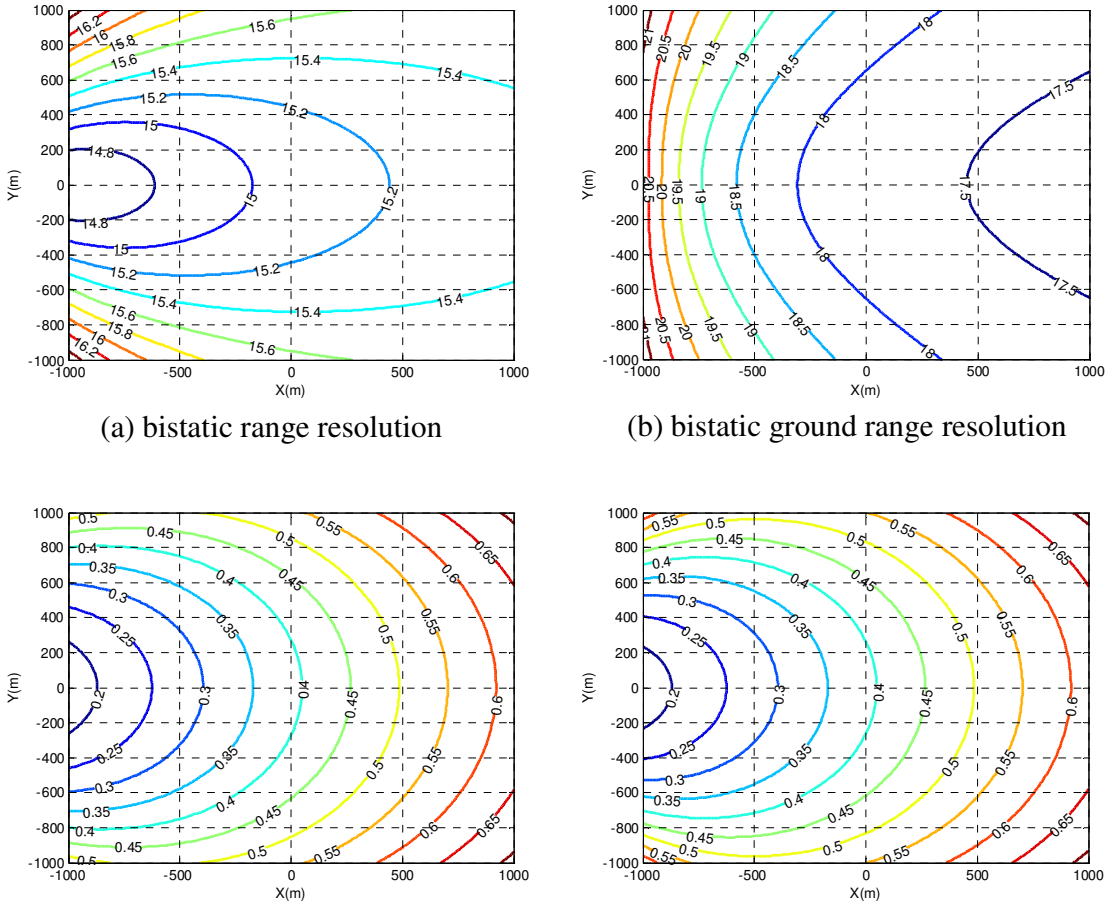

(a) bistatic range resolution

(b) bistatic ground range resolution

(c) bistatic azimuth resolution

(d) bistatic ground azimuth resolution

Figure 2.7: *Bistatic Resolution – Parallel Paths Case*

Figure 2.8 below shows the bistatic resolution and the ground resolution for the SS-BSAR non-parallel paths case. The ground projection for range resolutions degrades

substantially due to the large bistatic angle in this case. But azimuth resolution and its ground projection are still mainly dominated by the receiver speed and direction of motion.

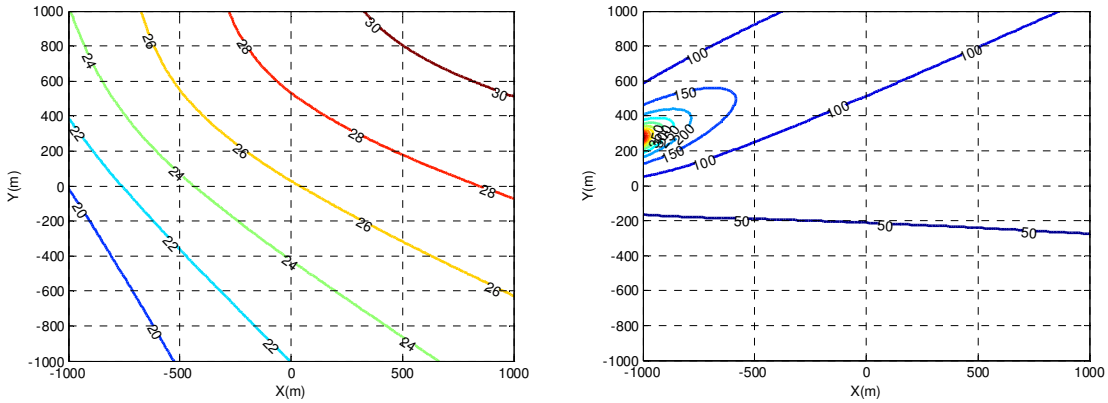

(a) bistatic range resolution

(b) bistatic ground range resolution

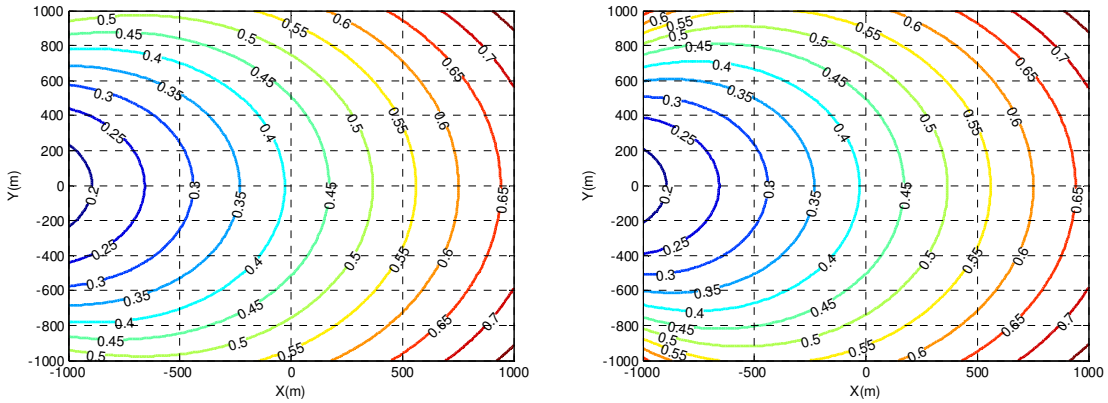

(c) bistatic azimuth resolution

(d) bistatic ground azimuth resolution

Figure 2.8: *Bistatic Resolution – Non Parallel Paths Case*

2.4 Power Budget

This section presents the power budget analysis for the proposed SS-SAR system when utilising a transmitter of opportunity. To identify the optimal non-cooperative

transmitter, the parameters, such as transmitter power output, equivalent isotropical radiated power (EIRP), will be discussed and compared using the information from the different satellite systems. The proposed SS-BSAR system consists of two receiving channels: the channel to receive direct signal and the channel to receive the reflected signal. Hence the power budget of both channels will be discussed separately.

2.4.1 EIRP and Minimum Received Power

The first two parameters required in a power budget calculation are the power transmitted by the transmitter and the power available on, or near, the receiver or target area. In radio communication systems, EIRP is the amount of power that would have to be emitted by an isotropic antenna (that evenly distributes power in all directions and is a theoretical construct) to produce the peak power density observed in the direction of maximum antenna gain. EIRP can take into account the losses in the transmission line and connectors and includes the gain of the antenna. The EIRP allows comparisons to be made between different transmitters regardless of type, size or form. From the EIRP, and with knowledge of an antenna's gain, it is possible to calculate the actual power and field strength values.

$$EIRP = P_T - L_f + G_a \tag{2.10}$$

where EIRP and P_T (power output of transmitter) are in dBm, cable losses (L_f) is in dB, and antenna gain (G_a) is expressed in dBi, relative to a (theoretical) isotropic reference antenna.

In general, the EIRP coverage of a GNSS signal produces a uniform power flux density on the earth's surface; however, this is not the case for most of the broadcasting and communications satellites. One can expect about 5-6 dB signal power difference between the communications satellite's antenna beam centre and the edge of the beam. Some communications satellites, like Inmarsat 3, are equipped with both a global beam and a spot beam. The spot beam normally provides about 8-9 dB higher signal power than using the global beam.

Table 2-4: *Transmitter's Parameters*

Transmitter	Power output (W)	EIRP (dBW)	Orbit Altitude (km)	Power Density (dBW/m^2)
Galileo	50	32	23222	-126
GPS	50	30	20180	-127
GLONASS	50	28	19130	-128
ASTRA	-	51	35786	-111
Inmarsat 3	-	39	35786	-123
Iridium	-	21	785	-108

Table 2.4 shows the main parameters relating to signals radiated by GNSS and other satellite systems. The values are based on free space propagation and the global beam is considered. All three GNSS systems generate more, or less, the same EIRP with the latest Galileo having 4 dB higher EIRP than GLONASS. Furthermore, ASTRA and Iridium generate a much stronger power flux density than the other candidates. This is due to its higher EIRP and lower orbit altitude.

From this information, the power density (ρ) of the satellite signals on the earth's surface can be derived. The calculation assumes that a receiver is located in the main lobe of the satellite antenna beam. The flux through a 1 m^2 area on the earth's surface, over the entire signal bandwidth, will be

$$\rho = \frac{EIRP}{4\pi R_T{}^2} \tag{2.11}$$

where R_T is the distance from the satellite to the receiver or target, which varies with satellite elevation. However, the GNSS transmitting antenna produces a beam that is slightly weaker at the centre (causing EIRP to vary with elevation), which is designed to compensate for variations in the power received by a standard antenna. For example, the Galileo EIRP mask boundaries within the visible Earth coverage [8] shows 2 dBW isoflux height differences from end-of-coverage (EOC) EIRP to centre EIRP.

For GNSS systems, power flux density also can be derived from the satellite system specification, which quotes a minimum power received using an antenna with a nominated effective area. The power density of the satellite signals on the surface of the earth is $\rho = \frac{P_r}{A_e}$, where P_r is the guaranteed minimum signal power levels for directly received signals and A_e is the effective area of receiving antenna. The guaranteed minimum signal power levels for three GNSS systems are specified in Table 2-5 below. It is assumed that the signal power level is measured at the output of a linearly polarized receiving antenna with a gain of 0 dBi, the angle of elevation is at least 10°, and

atmospheric attenuation is 2 dB. From Table 2-5, we can see that the three GNSS systems have exactly same power output but slight different EIRP and power density; this is mainly due to the difference in the transmitting antenna specification and the orbit altitude. In terms of minimum received power and signal bandwidth, Galileo and the new GPS L5 will provide more flexibility for target detection compared to other GNSS signals.

It is also worth noting that the received signal power is changing with the different satellite elevations. The received GLONASS L1/L2 signal power level for a user located on the ground, as a function of satellite elevation angle is shown in Figure 2.9 [9]. The highest received power level can be expected from the satellites at about 50° elevation angle. This is due to many reasons, such as deviation (within admissible range) from nominal orbit altitude; different values of gain of satellite transmitting antenna in different azimuths and frequency band; accuracy of angular orientation of the satellite; variations in output signal power due to technological reasons, temperature, voltage and gain variations, and variations in atmospheric attenuation [10].

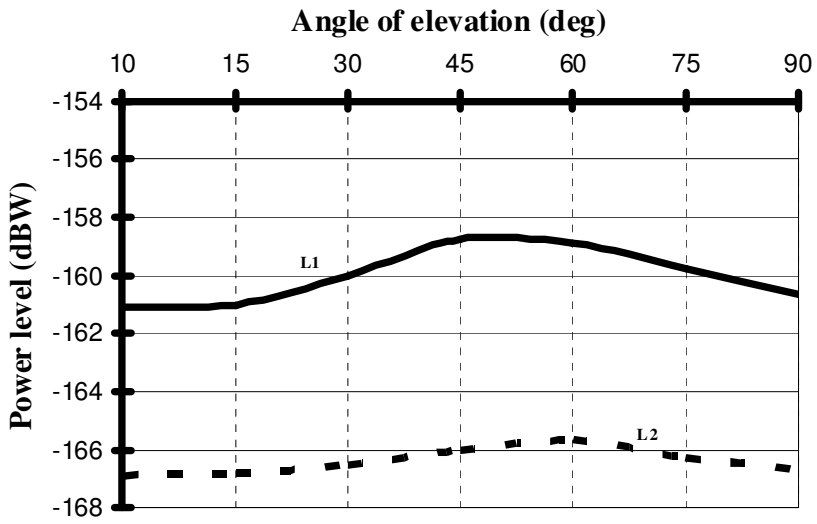

Figure 2.9: *Relationship between Minimum Received Power Level and Elevation Angle for GLONASS*

GNSS	Galileo			GPS			GLONASS	
Channel	E5a/b	E6	E1	L1	L2	L5	L1	L2
Central Frequency (MHz)	1191.795	1278.75	1575.42	1575.42	1227.60	1176.45	1602.5625-1615.5	1246-1257
Chip Rate (M/s)	10.23	5.11	2.04	C/A: 1.023 P-code: 10.23	P-code: 10.23	10.23	C/A: 0.511 P-code: 5.11	P-code: 5.11
Antenna gain (dBi)	15	15	15	13.5	13.5	-	11	11
Beam width	38°-40°	38°-40°	38°-40°	38°	38°	38°	36°	36°
Power output (W)	50	50	50	50	50	-	50	50
EIRP (dBW)	29.7	29.7	29.5	26.5	26.5	-	25-27	25-27
Min power received (dBW)	-155	-155	-157	-158	-158	-154.9	-161	-167

Table 2-5: *Parameters of GNSS Satellite Transmitters*

2.4.2 The Heterodyne Channel

Usually in a radar signal processor, the range compression consists of a correlation (or matched filtering) of the radar channel signal with the heterodyne channel signal delayed for each range resolution cell. The performance of the matched filter depends on the quality of the heterodyne channel signal. Ideally, one would like the signal to be as clean as possible, i.e. free from corruption. Unfortunately, the heterodyne signal will be spoiled by many factors, which include receiver noise, propagation distortions, multipath, clutter, and interference. At best, one might get a heterodyne signal from a line-of-sight direct path relatively free from interference, multipath and clutter. In this case, only the noise in the heterodyne channel corrupts the signal. Retzer and Thomas [11, 12] have comprehensively investigated the effect of an imperfect heterodyne signal on the synchronisation for bistatic radar. They showed that matched filtering losses are negligible for the heterodyne channel signal having reasonably high SNR.

The power budget for the heterodyne channel is actually a communication link budget. In the operational SS-BSAR system, a directional or omni-directional antenna could be used for receiving the satellite signal directly over a synchronisation link (SL). The received signal power is calculated by taking the product of the power density ρ of the transmitting signal on the earth's surface and the effective area A_e of the receiving antenna. The noise power referred to the system input (the antenna terminals) within the system is defined by $P_n = kT_sB_n$, where T_s is the system noise temperature and B_n is the noise bandwidth of the system. For an N-transducer cascade, the system noise temperature is given [4] by

$$T_s = T_a + \sum_{i=1}^{N} \frac{T_{e(i)}}{G_i} \tag{2.12}$$

where T_a is the antenna noise temperature, $T_{e(i)} = T_o(F_{n(i)} - 1)$ is the effective input noise temperature of the *ith* cascaded component and G_i is the available gain of the system between its input and the input of the *ith* cascaded component (see Chapter 5 for the receiver architecture). The SNR before signal processing (at the input of the correlator/matched filter) is calculated approximately by the equation

$$\frac{S}{N} = \frac{\rho A_e}{kT_s B_n} \tag{2.13}$$

If the power density of the signal, in this expression, is the minimum value expected, the resulting SNR should be the minimum observable SNR at the input of the correlator. If such calculations yield a low SNR less than 10 dB, it implies that the received heterodyne signal is almost buried under the system noise at this point. This heterodyne channel signal can't be used directly for the correlation with the radar channel signal.

For GNSS, a noiseless replica signal can be locally generated as the signal structure and the spreading codes are fully known. However, this locally generated signal still needs to be synchronized (in delay, Doppler shift and phase) with the satellite signal received at the heterodyne channel to keep all the information necessary for further signal processing (see Chapter 4 for more details regarding the synchronisation).

For a spread-spectrum coded signal, such as the one used in GNSS, the duration of the spreading code is much longer than the duration of the pulses used in other satellite systems. Hence there is a SNR improvement factor due to coherent integration

processing of this long spreading code. This improvement is achieved between the antenna output and the discriminator input of the synchronisation algorithm. It can then be expressed as

$$\frac{SNR_{OUT}}{SNR_{in}} = T_c B \tag{2.14}$$

where the bandwidth B is the chip rate of spreading code and T_c is the coherent integration time. For example, for the GLONASS C/A-code, B is 511 kHz and T_c is 1 ms, which is the length of one C/A code, so that the integration processing introduces 27 dB SNR improvement. This SNR gain will increase to 40 dB when the Galileo E5a/b or GPS L signal considered. For other satellite systems, the product of the signal bandwidth and the coherent integration time (normally equals to the duration of pulse) is one and no SNR gain is obtained due to the integration. This is the inherent advantage of a GNSS signal for synchronisation. This follows from the fact that navigation signals were designed to be optimal for remote synchronisation.

In general, a typical synchronisation algorithm (tracking loops) requires a minimum of 10 dB SNR at the input of its discriminator. For example, with 40 dB SNR gain obtained by integration of the Galileo E5 signal (1 ms integration time), a minimum of -30 dB SNR will be required at the output the heterodyne channel antenna. For other satellites (ASTRA, Inmarsat 3, Iridium), the replica signal cannot be generated locally. This is due to the random nature of the information modulated on the transmitting signal. In this case, the minimum required SNR at the output of the heterodyne channel antenna is to be at least 10 dB to achieve low matched filtering loss. Figure 2.10 below shows a graph

"loss in match filtering (y-axis)" versus "SNR in the heterodyne channel (x-axis)" for various expected SNR in the radar channel. This result is helpful in demonstrating the required 10 dB SNR in the heterodyne channel for a noise reflected GNSS signal.

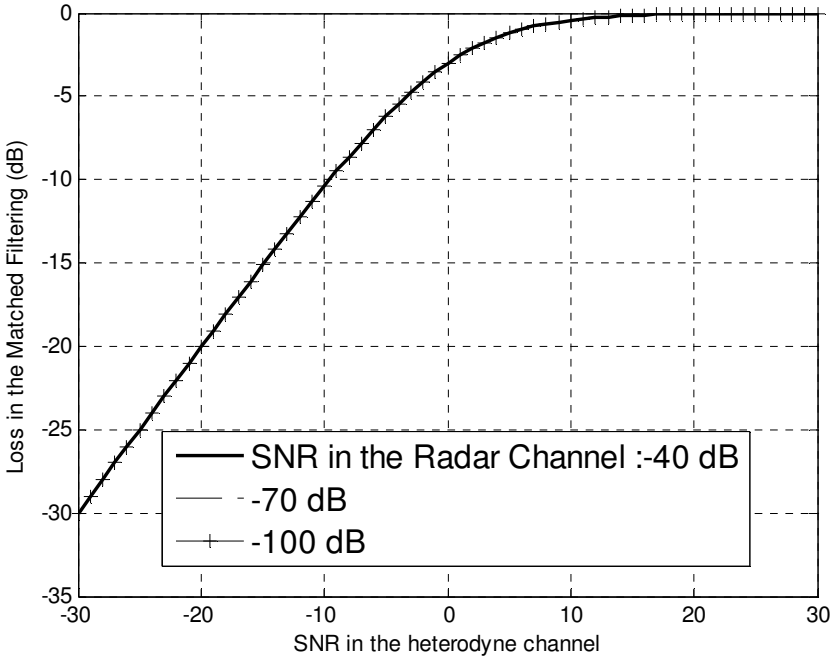

Figure 2.10: *the Match Filtering Losses vs. the Heterodyne SNR*

So the effective size A_e of this heterodyne channel antenna is proportional to the minimum SNR required for synchronisation. As mentioned above, the period of the code sequence used in communications satellites is much less than that of pseudo-random sequence transmitted by the navigation satellites. If utilizing the same signal bandwidth, synchronisation with a communications satellite will require a larger size antenna than using a navigation satellite.

Table 2-6: *Antenna Size vs SNR in the Heterodyne Channel*

Transmitter/Signal	A_e (m^2)	Required SNR (dB)
Galileo E5	0.001	-30
GPS L5	0.001	-30
GLONASS C/A	0.02	-17
ASTRA	0.15	10
Inmarsat 3	0.3	10
Iridium	0.04	10

Using transmitter parameters from Tables 2-4, 2-5, and Equation 2.13, Table 2-6 shows the minimum size of the heterodyne channel antenna as a function of required SNR at the heterodyne channel. The higher SNR in the heterodyne channel required for synchronisation purposes is achieved at the expense of increased antenna size. It should be noted that the calculations required to generate above table does not take in to account a number of practical problem such as propagation and receiver losses. In real situations we can expect a further increase in the antenna size. So we will have to use high gain directional antenna (narrow beam) for heterodyne signal reception for the other three satellite systems, this again will introduce an extra requirement on steering the antenna to track the satellite position to maintain it within the beam during the formation of the synthetic aperture.

2.4.3 The Radar Channel

The SNR of the radar channel is calculated for the period of aperture synthesis, considering targets radar cross section (RCS) independent of frequency and angle. A

suitable formula for monostatic SAR was derived in [4]. Indicating that the expression for SNR after range and azimuth compression, for an active bistatic SAR, the radar equation can be written as

$$\frac{S}{N} = \frac{P_t G_t}{4\pi R_T^{\,2}} \cdot \frac{A_{er}\sigma_B}{4\pi R_R^{\,2}} \cdot \frac{\tau_i}{\tau_o} \cdot \frac{1}{KT_s B_n} \cdot PRF \cdot T_c \cdot \eta \tag{2.15}$$

in which most of symbols have their common meanings, A_{er} is the effective area of THE radar channel antenna, σ_B is THE target bistatic radar cross section and η is the loss factor. In our case $\frac{P_t G_t}{4\pi R_T^{\,2}} = \rho$ is the power flux density on the earth's surface. The ratio of the uncompressed signal duration (τ_i) and the compressed signal duration (τ_0) is the SNR improvement due to range compression of the image formation algorithm. $PRF \cdot T_c = N$ is the number of azimuth samples integrated during the integration time of aperture synthesis (which is the gain in SNR due to the azimuth compression). If we assume the system loss factor as η and the receiver system noise bandwidth and the transmitting signal bandwidth are matched, so that $B_n \times \tau_0 = 1$ and taking into account $\tau_i \times PRF = 1$, an expression for the bistatic SAR SNR can be simplified as

$$\frac{S}{N} = \rho \cdot \frac{A_{er}\sigma_B}{4\pi R_R^{\,2}} \cdot \frac{1}{KT_s} \cdot T_c \cdot \eta \tag{2.16}$$

If a geostationary satellite is used or a quasi-monostatic geometry is considered for a moving satellite case, as discussed in section 2.3, for a fixed azimuth resolution $\Delta_{az} = D = \frac{\lambda R_R}{L_c} = \frac{\lambda R_R}{V_R T_c}$, we can deduce that

$$T_c = \frac{\lambda R_R}{V_R \Delta_{az}} \tag{2.17}$$

hence

$$\frac{S}{N} = \rho \cdot \frac{A_{er}\sigma_B}{4\pi R_R} \cdot \frac{1}{KT_s} \cdot \frac{\lambda}{V_R \Delta_{az}} \cdot \eta \tag{2.18}$$

For any GNSS system, the power density of the transmitted signal is approximately uniform over the illuminated region of the earth's surface; the minimum power density values (ρ) are calculated, for the three GNSS systems in the section 2.4.1.

The dimensions of the aircraft's radar channel antenna are constrained by the size of the aircraft and by the radar performance requirements. Coverage of the observation area demands a reasonably large beamwidth in the range direction and the effective size of the antenna along the radar track governs azimuth resolution. It has been assumed that a maximum effective along-track antenna dimension of about 1 m is acceptable (the physical dimension possibly being larger to allow beam shaping), the maximum effective elevation (or depression) dimension being 0.5 m. Hence, for the example of bistatic SAR using a non-cooperative transmitter, the radar channel antenna with effective area $\Delta_{az} = D \approx 1m$ is used in the calculation.

The value of the loss factor is estimated to be η = 0.5 (taking into account the various mechanisms which cause loss - typically absorption, beam shape loss, polarisation loss and a processing loss due to filter mismatch). The system noise temperature T_s can be written as $T_s = T_a + \sum_{i=1}^{N} \frac{T_{e(i)}}{G_i}$, where T_a is the antenna noise temperature. Assume

$T_a = 290K$ when an antenna looks on the ground and the receiver noise figure F is 1.5 dB. The system noise temperature is considered to be $290 \times F = 410$ Kelvin.

Table 2-7: *Parameters for Power Budget Calculation*

Transmitter	PSD (dBW/m^2)	λ (cm)	A_e (m^2)	Δ_{az} (m)
Galileo	-126	25.2	0.5	1
GPS	-127	20.0		
GLONASS	-128	18.5		
ASTRA	-111	2.8		
Inmarsat 3	-123	18.3		
Iridium	-108	18.5		

Using the parameters in Table 2-7 and considering the typical aircraft speed of 200 m/s, Equation 2.18 can be rearranged as

$$\frac{S}{N} = \rho \cdot \frac{A_{er} \cdot \lambda}{4\pi\Delta_{az}} \cdot \frac{1}{KT_s} \cdot \eta \cdot \frac{\sigma_B}{R_R V_R} = k \times \frac{\sigma}{R_R V_R} \tag{2.19}$$

where $k = \rho \cdot \frac{A_{er} \cdot \lambda}{4\pi\Delta_{az}} \cdot \frac{1}{KT_s} \cdot \eta$. It may be convenient to consider the factor k explicitly as the product of four elementary factors associated with the target illumination, the receiver antenna performance, the noise power spectral density, and an overall loss factor. The first of these is more-or-less constant for a given satellite system. The second, associated with receiver antenna performance, may be simplified further if the antenna is rectangular since the azimuth beamwidth is the ratio of wavelength to the effective along-track dimension of the antenna. The power spectral density of thermal noise changes relatively

little, assuming a good LNA, but the density of man-made noise may change considerably depending on the nature of the target area. The overall loss factor depends in part on climatic conditions and to that extent may vary a good deal.

Using Equation 2.17 and 2.19, the required integration time and achievable SNR can be calculated for different target radar cross section and receiver-to-target distance. Some examples are presented in Table 2-8. We can see that, to obtain certain SNR, the minimum integration time is increasing while the receiver-to-target range increases.

Table 2-8: *Power Budget Calculation*

Target RCS (m^2)		50	50	200	200
R_R (km)		3	10	3	10
Galileo	T_c (s)	3.78	12.6	3.78	12.6
	SNR (dB)	15.7	10.5	21.7	16.5
ASTRA	T_c (s)	0.42	1.4	0.42	1.4
	SNR (dB)	18.1	12.9	24.2	18.9
Inmarsat 3	T_c (s)	2.7	9.2	2.7	9.2
	SNR (dB)	14.3	9.1	20.3	15.1
Iridium	T_c (s)	2.8	9.3	2.8	9.3
	SNR (dB)	29.3	24.1	35.3	30.1

Figure 2.10 (a) and (b) show that the system SNR varies with the target distance. Comparing four satellite systems, it can be seen that Iridium has the highest SNR due to its low orbit height; and the targets with 50 m^2 RCS can be detected at a range of 3 km using a Galileo satellite as the non-cooperative transmitter and 200 m^2 RCS targets at the range of 11 km, considering a 13 dB SNR detection thresholds.

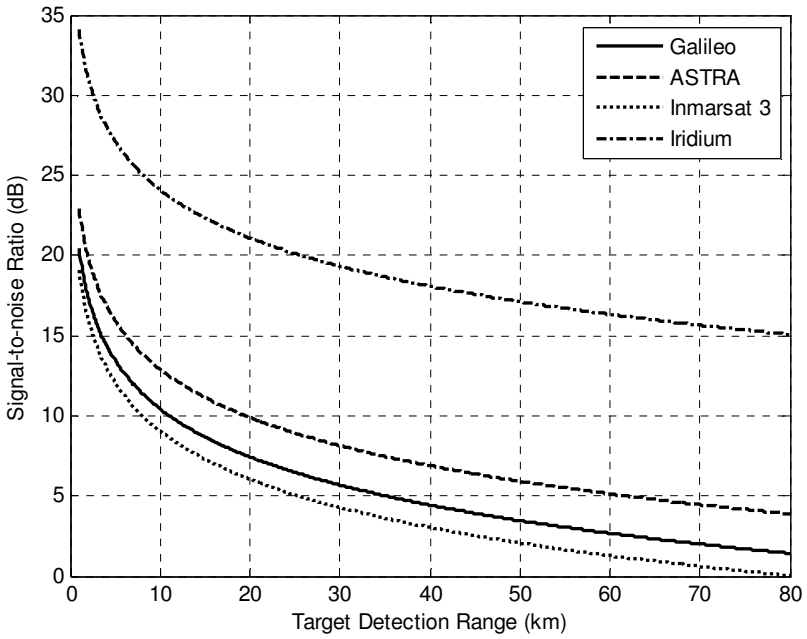

(a) For Target with 50 m^2 RCS

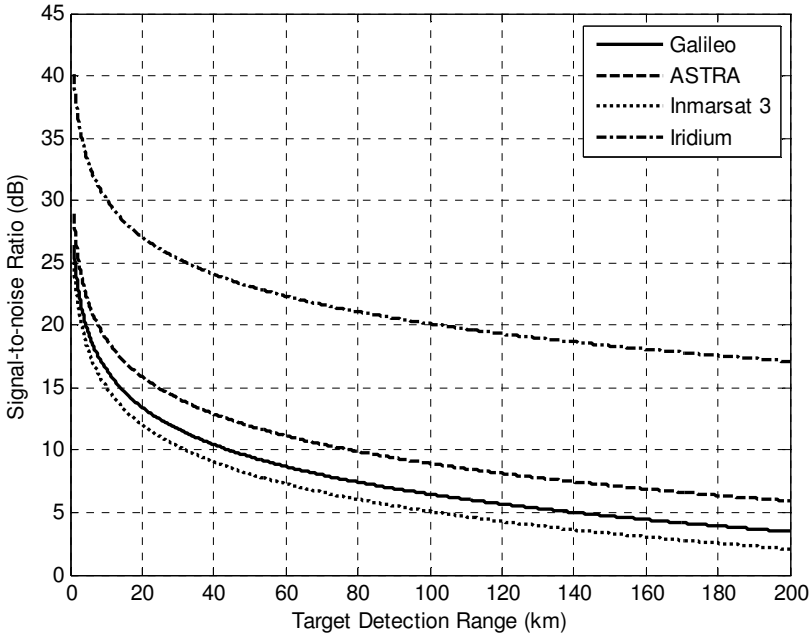

(b) For Target with 200 m^2 RCS

Figure 2.11: *SNR vs Target Detetion Range*

2.5 Summary

This chapter has discussed and compared the different candidates of non-cooperative transmitter for SS-BSAR. The analysis has been made on the basis of three important parameters: availability of transmitters, resolution and power budget. Four different types of satellite transmitters are considered; they are GNSS, ASTRA, Inmarsat, and Iridium.

The equations of bistatic resolution and its ground projection have been derived. Using the vector gradient method, iso-range and iso-Doppler contours have been plotted and the achievable resolutions have been calculated for two different bistatic geometries, parallel paths and non-parallel paths. The bandwidth of most GNSS navigation signals is under 10 MHz, which corresponds to 15 m, or lower, range resolution. For SS-BSAR using GNSS, the receiver parameters will mainly determine the azimuth resolution; and the finest ground range resolution may be obtained with quasi-monostatic topology.

It is highlighted that the GNSS satellite transmits about 10-20 dB less power compared to other satellites. However, it has an advantage of satellite diversity. Therefore one can choose the desired bistatic geometry for minimum range resolution loss. For example, Direct Satellite TV (DVB-S) broadcasting transmitters introduce about 20 dB stronger power flux density near the earth's surface compared to GNSS transmitters. However, geostationary satellites are fundamentally positioned above the equator and this requires a specific receiver trajectory for mapping a particular area and, in many or even most

situations, a vital loss in ground range resolution may take place due to the limited bistatic geometry.

It is also pointed out that for low match filtering loss, the heterodyne channel should have reasonably high SNR. It is shown that for broadcasting and communications satellites this is achieved at the expense of increased antenna size and potentially the antenna may be impractical to be mounted on an airborne platform. For GNSS one can locally generate the replica signal but it needs to be synchronized with the satellite transmitter. The synchronisation requires very low SNR (-30 dB) at the output of the heterodyne channel antenna. This makes it possible to use an omni-directional antenna for synchronisation with an airborne receiver.

Finally, it is concluded that overall a GNSS satellite is the best non-cooperative transmitter candidate for SS-BSAR. It provides a reasonable range resolution of ~ 3-8 m, allows satellite diversity and a target detection range of ~ 3-12 km for targets with 50 m^2 RCS.

References

1. Rodriguez-Cassola, M., et al., *Bistatic TerraSAR-X/F-SAR Spaceborne–Airborne SAR Experiment: Description, Data Processing, and Results.* Geoscience and Remote Sensing, IEEE Transactions on 2010. **48**(2): p. 781 - 794
2. Walterscheid, I., et al., *Bistatic SAR Experiments With PAMIR and TerraSAR-X—Setup, Processing, and Image Results.* Geoscience and Remote Sensing, IEEE Transactions on 2010. **48**(8): p. 3268 - 3279.
3. Okan, V., *GPS*, http://www.movingsatellites.com/.
4. Skolnik, M.I., *Radar Handbook*. 1990: McGraw Hill.

5. Willis, N.J., *Bistatic Radar*. 1991: Artech House.

6. Jones, H.M., *Presicted properties of bistatic satellite images*, in *IEEE National Radar Conference*. 1993. p. 286-291.

7. Cardillo, G.P., *On the use of the gradient to determine bistatic SAR resolution*, in *Antennas and Propagation Society International Symposium*. 1990. p. 1032-1035.

8. *Galileo Open Service Signal In Space Interface Control Document*. 2006, European Space Agency / Galileo Joint Undertaking.

9. *GLONASS Interface Control Document* 2002.

10. *GPS Interface Control Document*. 2002.

11. Retzer, G. *A concept for signal processing in bistatic radar*. in *IEEE International Radar Conference*. 1980.

12. Daniel, D. and J. Thomas, *Synchronization of Non-cooperative Bistatic Radar Receivers*. 1999, Syracuse University.

Chapter 3 GNSS Signals for SS-BSAR Application

3.1 Introduction

In the previous chapter, the potential non-cooperative transmitters for SS-BSAR were identified and compared, in terms of the availability, the resolution and the system power budget. The conclusion is that GNSS satellites have the advantage of large constellations and multiple visibilities. Also, they can provide reasonable range resolution and fair SNR after range and azimuth compression from SAR image formation.

However, GNSS signals are designed for the purpose of navigation and positioning, instead of radar applications. For most conventional monostatic SAR, the signals are transmitting in pulse mode without carrying extra modulated information. GNSS signals, instead, are transmitting in a continuous wave (CW) with modulated navigation information. The bandwidth of GNSS signals is often much smaller than that of conventional SAR signals.

This chapter will provide an analysis of the available GNSS signals from the SAR application point of view. Its generation, reception and power spectrum will be discussed. More importantly, the correlation property of GNSS signals will be studied and analysed to support the development of synchronisation and image formation algorithms. For SS-BSAR, the potential range resolution not only depends on the bandwidth of the ranging signal but also on the relative motion between the transmitter,

receiver and target. A method will be proposed in this chapter to improve the range resolution by combining the bandwidth of GNSS signals.

3.2 GNSS Signal Frequency Bands

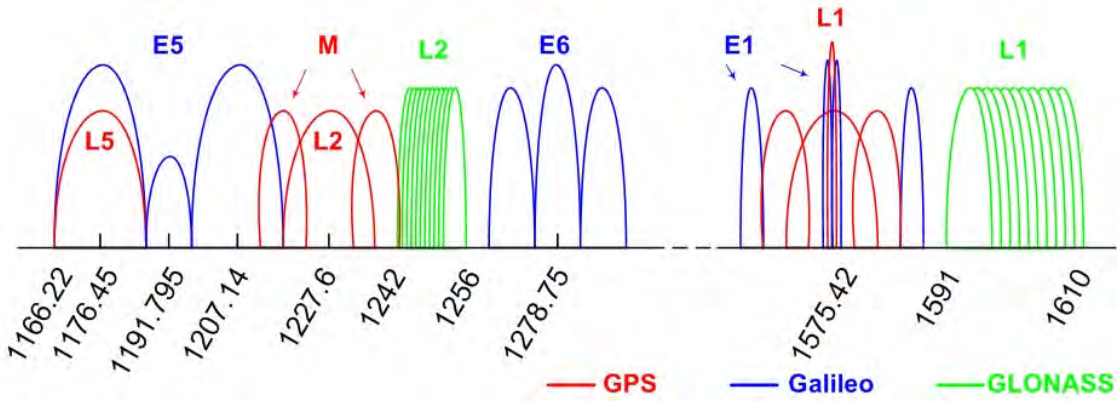

Figure 3.1: *GNSS Signals Frequency Bands*

Figure 3.1 presents the frequency bands for three major GNSS systems. It includes both the current GNSS signals and the future available signals. From Figure 3.1 we can see that GNSS frequency bands are crowded with signals from each constellation and sometimes the spectrum of adjacent signals overlap. Due to the modulation scheme, it has no effect for the navigation and positioning. However, this may introduce in-band interference for radar applications and affect the system SNR.

Galileo has a number of navigation signals modulated in three carriers: E5, E6 and E1. They are indicated in blue in Figure 3.1. Three independently usable signals are permanently transmitted by all Galileo satellites. The E5 link is further sub-divided into two RF links, E5a and E5b, covering the total bandwidth (E5) of ~ 51 MHz. All Galileo

satellites will use the same frequency bands and make use of the code division multiple access (CDMA) technique. Spread spectrum signals will be transmitted, including different ranging codes per signal, per frequency, and per satellite. Most Galileo signals come in pairs: a data (navigation message) signal and a data-free signal. For example, the E5b signal consists of two signals: E5b-I and E5b-Q. They are aligned in phase and consequently have the same Doppler frequency. For further details please refer to section 3.3 and the document [1].

The GIOVE-A and GIOVE-B spacecrafts are the first two Galileo testing satellites nominally providing signals on two out of the three carriers E5, E6 and E1 at a time, in the combinations E1-E5 or E1-E6. These two satellites will be used as the non-cooperative transmitter for SS-BSAR imaging experiments. The details of the experiments are presented in Chapter 5.

GPS modernization will introduce new navigation signals: a second civil signal in L2, a new carrier L5 and a new military signal M-code in L1 and L2 (shown in red in Figure 3.1). The main benefits of the new L5 signal include the improvement of signal structure for enhanced performance with: high power (-154.9 dBW), wider bandwidth (24 MHz), longer spreading codes in the navigation message and a data-free code to enhance the signal performance. An essential element of GPS modernization involves sharing or the dual use of the current L band spectrum by multiple signals that provide an enhanced radio navigation service for civilian and military users.

L1 and L2 signals of GLONASS are indicated in green in Figure 3.1. It provides two navigation signals: C/A code and P-code, which have 511 kHz and 5.11 MHz spreading code rate separately. GLONASS adopts the frequency division multiple access (FDMA) technique. There is also a modernization scheme for the current GLOSNASS constellation with new navigation signals. More information can be found in [2].

Existing GPS, a classic example of CDMA systems, currently employs non-return-to-zero (NRZ) waveforms on the spread spectrum codes. It is well known that NRZ waveforms concentrate the energy towards the centre of the band at the carrier frequency. The band region away from the centre of the frequency band is not used efficiently. The power spectral density (PSD) of NRZ signals follow a typical sinc function, which has nulls at the multiples of the spreading code chip rate in a CDMA system.

The Galileo signals and the planned modernized GPS signals will inherit improved performance compared to the existing GPS signals. One of the improvements is the introduction of the binary offset carrier (BOC) modulation. Binary offset carrier modulations offer two independent design parameters: subcarrier frequency and spreading code rate. These two parameters provide the freedom to concentrate signal power within specific parts of the allocated band to reduce interference with the reception of other signals. Furthermore, the redundancy in the upper and lower sidebands of BOC modulations offers practical advantages in receiver processing for signal acquisition, code tracking, carrier tracking, and message demodulation.

The binary offset carrier (BOC) modulation provides a simple and effective way of moving signal energy away from the band centre, offering a high degree of spectral separation from conventional NRZ or phase shift keyed (PSK) signals, whose energy is concentrated near the band centre. The resulting "split spectrum signal" effectively enables frequency sharing, while providing attributes that include simple implementation, good spectral efficiency, high accuracy, and enhanced multipath resolution [3]. Therefore, the combination of binary offset carrier and NRZ schemes in a given GNSS frequency band improves the bandwidth utilization beyond what only one signalling scheme can do.

A BOC(m, n) signal is created by modulating a sine wave carrier with the product of a pseudorandom noise (PRN) spreading code and a square wave subcarrier, each having binary ±1 values. The parameter m stands for the ratio between the subcarrier frequency and the reference frequency f_o = 1.023 MHz, and n stands for the ratio between the code rate and f_o. Thus, BOC(15,10) means a 15.345 MHz subcarrier frequency and a 10.23 MHz code rate. The special case of BOC(n, n) is equivalent to Manchester code. The transmitting signal is the product of the carrier, spreading code, binary offset carrier, and the navigation message. Traditionally, at the reception end, the RF hardware removes the carrier and the correlators remove the binary offset carrier code, leaving the navigation message and the residual frequency (Doppler shift) to be extracted or measured by a processor. More information is introduced in Chapter 4 regarding the GNSS signals reception process.

From Figure 3.1, it can be seen that there are three navigation signals that have the code rate of 10.23 MHz (the highest in all GNSS signals), which is equivalent to a 15 m range resolution in monostatic or quasi-monostatic SAR topology. They are GPS P-code on L1 and L2, the new GPS L5 signal and the signals carried by Galileo E5a/b. Because GPS P-code is an encoded signal that is mainly for military use and due to the unavailable of the L5 signal, Galileo E5 is the only signal available for a SS-BSAR imaging experiment. The next section will give a description of its generation, reception and power spectrum.

3.3 GNSS Signals Generation and Reception

Galileo introduced the innovative signal structure Alternate Binary Offset Carrier (15, 10) (or AltBOC (15, 10)) on its E5 signal, which aims to provide the advantages of multipath effect reduction and narrow band interference rejection. However, conventional GNSS receiver techniques are designed for a BPSK modulated signal. When the conventional design is adopted by Galileo signal processing, it will experience signal loss because of poor tracking loop (i.e. Delay Lock Loop (DLL)) stability due to the wider main lobe of the Galileo signal frequency spectrum and the ambiguous secondary peaks on the Galileo signal Autocorrelation Function (ACF).

The advantage of the AltBOC signal is that it provides spectral isolation between the two upper and lower components of the same composite signal. This signal makes it possible to retain the binary offset carrier implementation simplicity, while permitting the differentiation of the spectral lobes. The idea of Alternate binary offset carrier

modulation is used to perform the same process as binary offset carrier modulation but the sub-carrier used is a "complex" sub-carrier (see Figure 3.2). In that way, the signal spectrum is not split up, but only shifted to higher frequencies. Shifting to lower frequencies is obviously also possible.

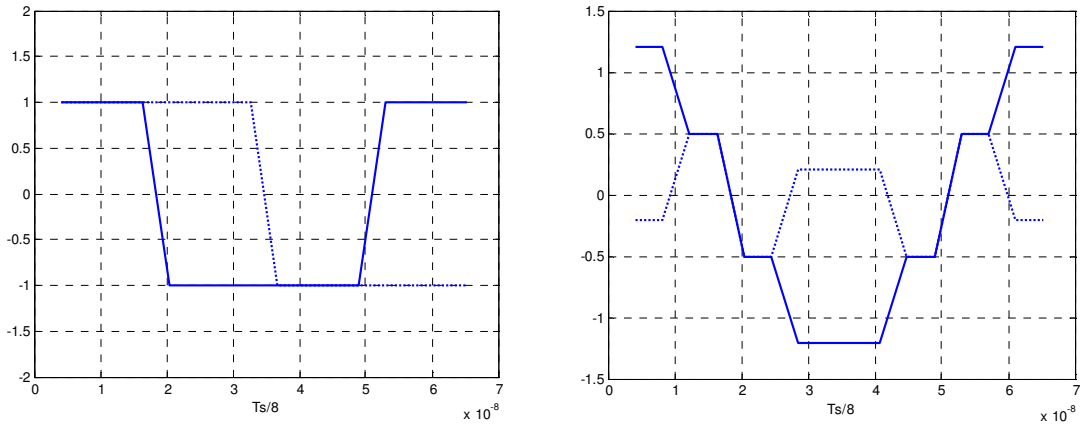

(a) Square wave sub-carrier for BOC (b) Complex sub-carrier for AltBOC

Figure 3.2: *Sub-Carrier*

However, the shifted signal doesn't have a constant envelope and thus may be distorted within the satellite payload due to non-linear amplification. That's why an innovation was proposed in [4] in order to create a constant envelope signal which is as close as possible to the AltBOC signal. The innovation introduces new terms which can be compared to intermodulation products. The expression of the new signal that has been obtained is called constant envelope AltBOC. It is actually a classical 8-PSK modulation with a non-constant allocation of the 8 phase-states.

3.3.1 Signal Generation

For GNSS signals using BPSK modulation, the expressions can be given for the power normalized complex envelope $s_X(t)$ (i.e. base-band version) of a modulated signal $S_X(t)$ (band-pass). Both expressions are described in terms of in-phase and quadrature components in the equations below

$$S_X(t) = \sqrt{2P_X}\left[s_{X-I}(t)\cos(2\pi f_X t) - s_{X-Q}(t)\sin(2\pi f_X t)\right] \tag{3.1}$$

$$s_X(t) = s_{X-I}(t) + js_{X-Q}(t) \tag{3.2}$$

where P_X is the total available power, s_{X-I} and s_{X-Q} are the in-phase and quadrature components, which are the product of the spreading code and the navigation bits and f_X is the carrier frequency. To compare this to the generation of Galileo E5 AltBOC(15, 10) modulation, Figure 3.3 below gives an example of the modulation scheme for GLONASS signals. The L1 signal consists of a quadrature C/A code and P-code; and L2 signal only has a P-code.

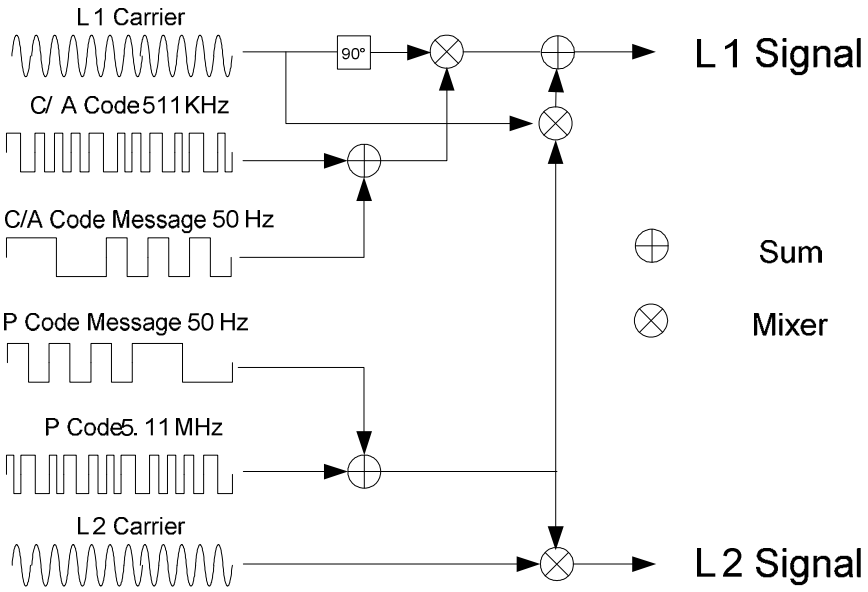

Figure 3.3: *GLONASS Signals Modulation Scheme*

The bandpass version expression for the GLONASS L1 signal can be written as

$$S_{L1}(t) = \sqrt{2P}\left[C(t)D(t)\cos(2\pi f_{L1}t) + P(t)D(t)\sin(2\pi f_{L1}t)\right] \tag{3.3}$$

where $C(t)$ and $P(t)$ are the spreading codes, and $D(t)$ is the navigation message. Its 5.11 MHz P-code can be used as the ranging signal for SS-BSAR applications. GPS signals can be generated and expressed with the same modulation scheme and expression given above.

The wideband Galileo E5 signal is then generated using the AltBOC modulation with a side-band sub-carrier, which can be written as [1]

$$
\begin{aligned}
s_{E5}(t) = & \frac{1}{2\sqrt{2}}\left(s_{E5a-I}(t) + js_{E5a-Q}(t)\right)\left[sc_{E5-S}(t) - jsc_{E5-S}(t - T_S/4)\right] \\
& + \frac{1}{2\sqrt{2}}\left(s_{E5b-I}(t) + js_{E5b-Q}(t)\right)\left[sc_{E5-S}(t) + jsc_{E5-S}(t - T_S/4)\right] \\
& + \frac{1}{2\sqrt{2}}\left(\overline{s_{E5a-Q}}(t) + j\overline{s_{E5a-Q}}(t)\right)\left[sc_{E5-P}(t) - jsc_{E5-P}(t - T_S/4)\right] \\
& + \frac{1}{2\sqrt{2}}\left(\overline{s_{E5b-I}}(t) + j\overline{s_{E5b-Q}}(t)\right)\left[sc_{E5-P}(t) + jsc_{E5-P}(t - T_S/4)\right]
\end{aligned}
\tag{3.4}
$$

The respective definitions of the binary spreading sequences s_{E5a-I}, s_{E5a-Q}, s_{E5b-I} and s_{E5b-Q} are the product of the spreading codes and navigation message (for s_{E5a-I} and s_{E5b-I} only). The E5 spreading codes include the primary and secondary codes. The definition and generation of the spreading codes are included in Appendix A. The respective dashed support sequences $\overline{s_{E5a-I}}$, $\overline{s_{E5a-Q}}$, $\overline{s_{E5b-I}}$ and $\overline{s_{E5b-Q}}$ are product signals, as described in equation 3.5.

$$
\begin{aligned}
\overline{s_{E5a-I}} &= s_{E5a-Q}s_{E5b-I}s_{E5b-Q} & \overline{s_{E5a-Q}} &= s_{E5a-I}s_{E5b-I}s_{E5b-Q} \\
\overline{s_{E5b-I}} &= s_{E5a-I}s_{E5a-Q}s_{E5b-Q} & \overline{s_{E5b-Q}} &= s_{E5a-I}s_{E5a-Q}s_{E5b-I}
\end{aligned}
\tag{3.5}
$$

The parameters sc_{E5-S} and sc_{E5-P} represent the four-valued sub-carrier functions (see Figure 3.2 (b)) for the single signals and the product signals respectively.

$$
sc_{E5-S}(t) = \sum_{i=-\infty}^{\infty} AS_{|i|_8} \cdot rect\left(t - i\frac{T_S}{8}\right) \tag{3.6}
$$

$$
sc_{E5-P}(t) = \sum_{i=-\infty}^{\infty} AP_{|i|_8} \cdot rect\left(t - i\frac{T_S}{8}\right) \tag{3.7}
$$

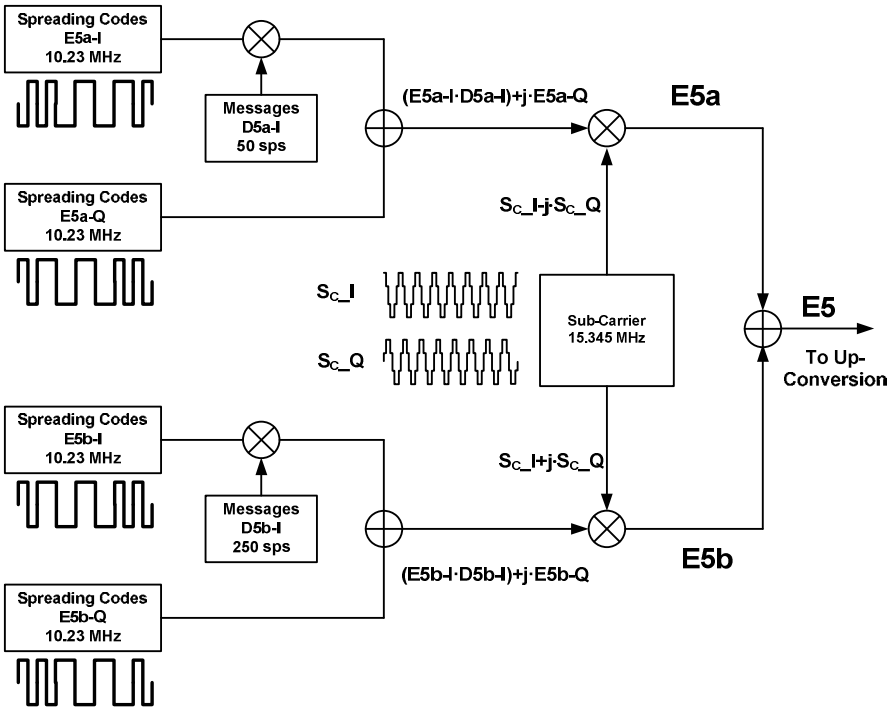

Figure 3.4: *Galileo E5 Modulation Scheme*

Figure 3.4 above gives the modulation scheme for Galileo E5. It can be seen that the full E5 signals consist of two signals and four codes, in comparison to two codes on the GPS/GLONASS L1 signal. All four codes can be used as the ranging signal for radar applications and the correlation of only data-free s_{E5a-Q} or s_{E5b-Q} codes support a simpler signal processing algorithm than data signals. However, usage of both I and Q signals will increase the received power, hence SNR. For example, combining the I and Q components of the E5b signal will improve the SNR by 3 dB compared to using E5b-Q; and the usage of all four codes results in 6 dB higher SNR. This is a significant increase as GNSS signals transmit relatively low signal power in terms of radar applications.

3.3.2 E5 signals reception

The multiplexing of the transmission for the E5a and E5b signals gives three alternative methods of processing the signal within the receiver architecture:

- E5a single sideband reception
- E5b single sideband reception
- E5 wideband reception

In order to simplify the processing route and to focus on the radar signal processing, single sideband reception is recommended for an SS-BSAR imaging experiment. The E5a or E5b signal can be received in a similar manner to a QPSK modulated signal according to the following

$$s_{E5a}^{r}(t)=\sqrt{2P_{E5a}^{r}}\begin{bmatrix} s_{E5a-I}(t-\tau_{E5a})\cos(2\pi(f_{E5a}-\Delta f_{E5a})(t-\tau_{E5a})+\phi_{E5a}) \\ -s_{E5a-Q}(t-\tau_{E5a})\sin(2\pi(f_{E5a}-\Delta f_{E5a})(t-\tau_{E5a})+\phi_{E5a}) \end{bmatrix} \tag{3.9}$$

where P_{E5a}^{r} is the E5a total received power, τ_{E5a} is the delay between transmission and reception for E5a, Δf_{E5a} is the carrier frequency offset and θ_{E5a} is the received phase.

After I-Q demodulation (output from receiver), its baseband components can be written as

$$I(t)=\begin{bmatrix} s_{E5a-I}(t-\tau_{E5a})\cos(2\pi\Delta f_{E5a}(t-\tau_{E5a})+\theta_{E5a}) \\ +s_{E5a-Q}(t-\tau_{E5a})\sin(2\pi\Delta f_{E5a}(t-\tau_{E5a})+\theta_{E5a}) \end{bmatrix} \tag{3.10}$$

$$Q(t)=\begin{bmatrix} s_{E5a-I}(t-\tau_{E5a})\sin(2\pi\Delta f_{E5a}(t-\tau_{E5a})+\theta_{E5a}) \\ -s_{E5a-Q}(t-\tau_{E5a})\cos(2\pi\Delta f_{E5a}(t-\tau_{E5a})+\theta_{E5a}) \end{bmatrix} \tag{3.11}$$

$$I+jQ(t)=\begin{bmatrix} \left(s_{E5a-I}(t-\tau_{E5a})-s_{E5a-Q}(t-\tau_{E5a})\right)\cos(2\pi\Delta f_{E5a}(t-\tau_{E5a})+\theta_{E5a}) \\ +\left(s_{E5a-I}(t-\tau_{E5a})+s_{E5a-Q}(t-\tau_{E5a})\right)\sin(2\pi\Delta f_{E5a}(t-\tau_{E5a})+\theta_{E5a}) \end{bmatrix} \tag{3.12}$$

This baseband complex signal is the actual input signal to the synchronisation algorithm described in Chapter 4. The parameters τ_{E5a}, Δf_{E5a}, and θ_{E5a} will then be tracked and used for local reference generation.

Nevertheless, the wideband E5 signal reception is required for the range resolution improvement proposed in section 3.5; and it can be processed in a correlation receiver which generates a local replica in accordance with an AltBOC signal format according to equation 3.4.

3.3.3 Power Spectrum Density

Galileo E5 signals apply AltBOC(15 10) modulation with subcarrier frequency $f_{sc}=15\times1.023MHz$ and chip rate $f_c=10\times1.023MHz$. Neglecting its dashed support sequences (intermodulation products), it can be simplified as (in comparison to equation 3.4)

$$\begin{aligned} x_{AltBOC}(t)=&[C_{E5aI}(t)\cdot D_{E5aI}(t)+jC_{E5aQ}(t)][sign(\cos(2\pi f_{sc}t))+jsign(\sin(2\pi f_{sc}t))]+ \\ &[C_{E5bI}(t)\cdot D_{E5bI}(t)+jC_{E5bQ}(t)][sign(\cos(2\pi f_{sc}t))-jsign(\sin(2\pi f_{sc}t))] \end{aligned}$$

(3.13)

where $C(t)$ are the spreading codes and $D(t)$ is the navigation message. To calculate the power spectrum density of a Galileo E5 signal, different terms of cross-correlation must be taken into account and analysed. The code sequences are independent, so the cross-correlation between two different codes is equal to zero. Consequently, all the cross-correlation terms in which the cross-correlation between two different codes, or different sub-carrier, are null. So the power spectral density of AltBOC(15 10) can then be written as the equation below according to [5]

$$G(f) = \frac{4}{\pi^2 f^2 T_c} \frac{\cos^2(\pi f T_c)}{\cos^2(\pi f \frac{T_c}{3})} [\cos^2(\pi f \frac{T_s}{2}) - \cos(\pi f \frac{T_s}{2}) - 2\cos(\pi f \frac{T_s}{2})\cos(\pi f \frac{T_s}{4}) + 2]$$

(3.14)

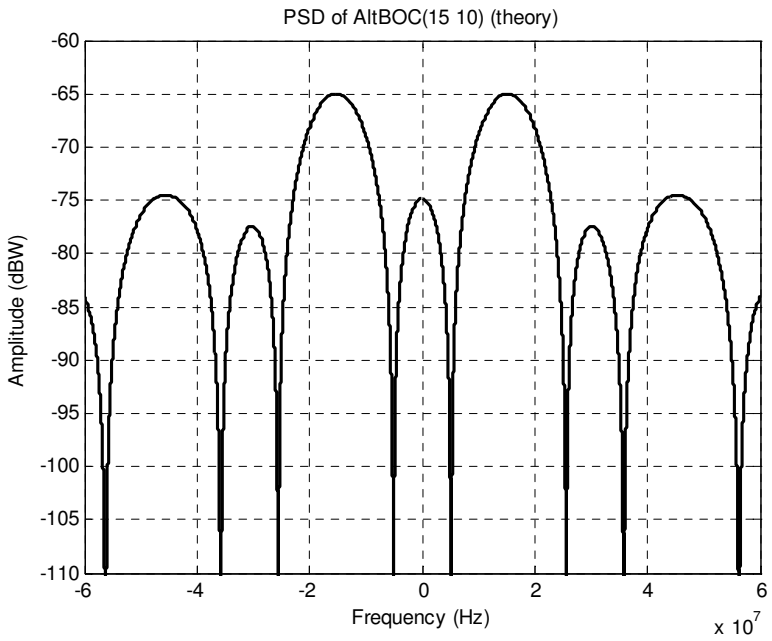

Figure 3.5: *Power Spectrum of AltBOC(15,10)*

Figure 3.5 plots the power spectral density (from equation 3.14) of constant envelope AltBOC(15, 10) modulation, which is utilized by Galileo E5 signals. It can be compared to the power spectral density of BPSK signal and other binary offset carrier signals plotted in Figure 3.6.

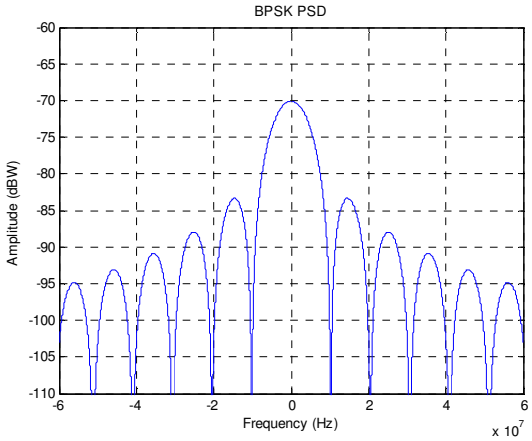

(a) Power spectral density of BPSK signal, P-code

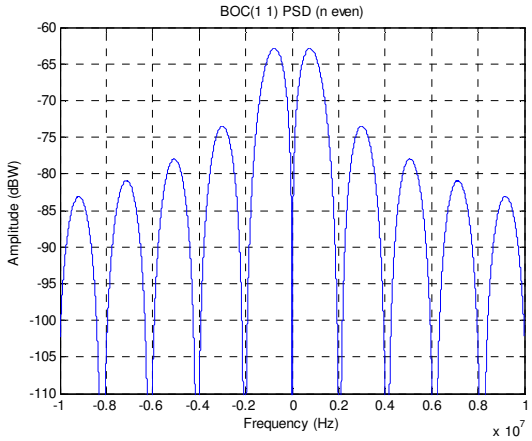

(a) Power spectral density of BOC(1, 1) signal, Galileo E1

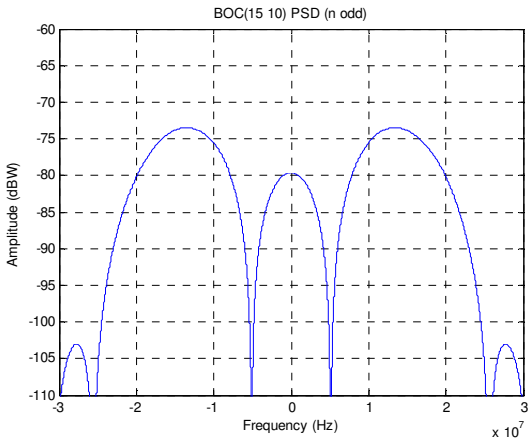

(c) Power spectral density of BOC(15, 10) signal

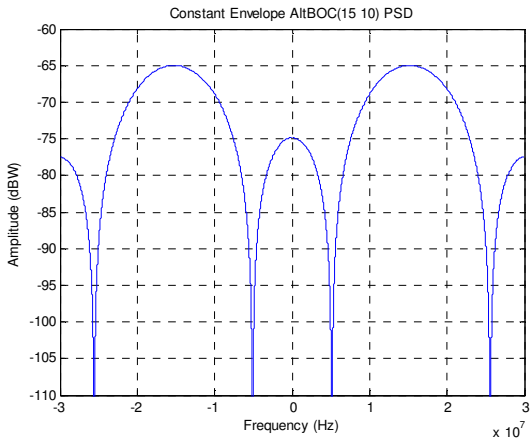

(d) Power spectral density of Galileo E5 signal (constant envelope AltBOC)

Figure 3.6: *PSD for Different Modulations*

3.4 Correlation Properties

The Pseudorandom Noise (PRN) codes are selected as the spreading sequences for the GNSS signals because of their characteristics. The most important characteristics of the pseudorandom noise codes are their correlation properties. These properties are described in [6]. Among them, two important correlation properties of the pseudorandom noise codes can be stated as follow:

- *Nearly no cross correlation* All the pseudorandom noise codes are nearly uncorrelated with each other. That is, for two codes C_i and C_k for satellites i and k, the cross correlation can be written as

$$r_{ik}(m) = \sum_{n=0}^{N} C_i(n) C_k(n+m) \approx 0 \qquad \text{for all m} \tag{3.15}$$

- *Nearly no correlation except for zero lag* All pseudorandom noise codes are nearly uncorrelated with themselves, except for zero lag. This property makes it easy to find out when two similar codes are perfectly aligned. The autocorrelation property for satellite k can be written as

$$r_{kk}(m) = \sum_{n=0}^{N} C_k(n) C_k(n+m) \approx 0 \qquad \text{for m} \neq 1 \tag{3.16}$$

The auto-correlation function (ACF) has a peak of magnitude

$$r_{kk,peak} = 2^L - 1 \tag{3.17}$$

where L is the number of states in the shift registers. In this case, L is equal to 13. The remaining values (sidelobe) satisfy the following inequality

$$\left|r_{kk}\right| \le 2^{(L+2)/2} + 1 \tag{3.18}$$

High auto-correlation peaks and low cross-correlation peaks can provide a wide dynamic range for signal acquisition. In order to detect a weak signal in the presence of strong signals, the auto-correlation peak of the weak signal must be stronger than the cross-correlation peaks from the strong signals.

Table 3-1: *Sidelobe Level of Pseudorandom Noise Codes*

Signal	Code Length (bits)	Sidelobe Level (dB)
Galileo E5a/b	10230	-40
GLONASS C/A	511	-54
GLONASS P-code	5110000	-66
GPS P-code	15345000	-72

The peak-to-sidelobe level of a pseudorandom noise code can be calculated from the equation below.

$$20\times\log_{10}(\frac{1}{N}) \tag{3.19}$$

For the full length PRN code and for the truncated code, it is derived from

$$20\times\log_{10}(\frac{1}{\sqrt{N}}) \tag{3.20}$$

Galileo E5a/b and GPS/GLONASS P-codes are generated from a truncated pseudorandom noise code. GLONASS C/A code is generated from the full length pseudorandom noise code. The sidelobe level of each code is given in Table 3-1 above.

Figure 3.7 below presents the auto-correlation function (ACF) of four GNSS signals using different modulations.

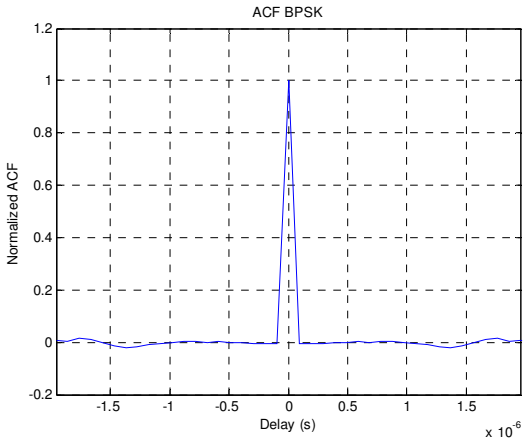

(a) ACF of BPSK signal

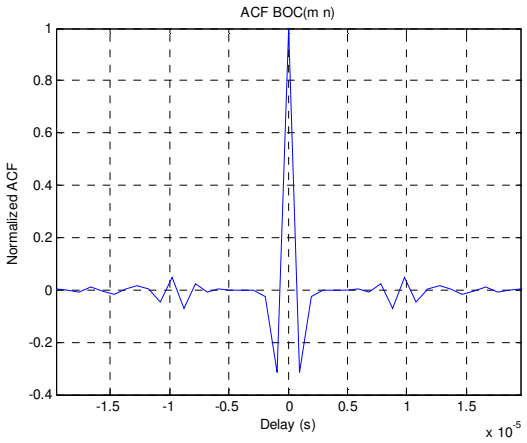

(a) ACF of BOC(1, 1) signal

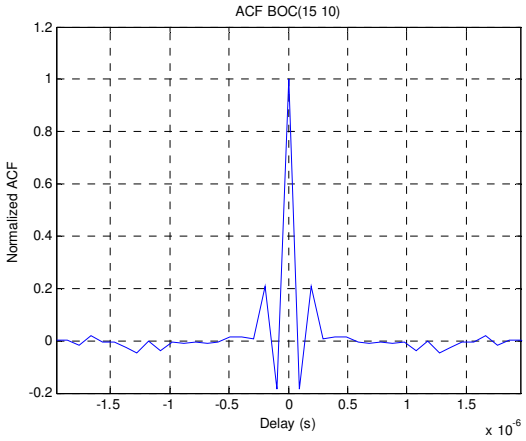

(a) ACF of BOC(15, 10) signal

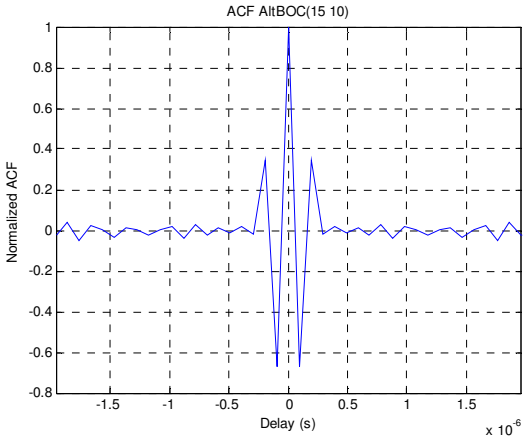

(a) ACF of AltBOC(15, 10) signal

Figure 3.7: *Auto-correlation function of BPSK and Different BOC Modulations*

It can be seen that a BOC modulated signal has multiple peaks in the auto-correlation function, in contrast to the single correlation peak of a BPSK signal. The number of negative and positive peaks in the auto-correlation function of a BOC signal is $2x-1$, where $x=\frac{2f_s}{f_c}$. For AltBOC(15, 10), $2x-1=2\times\frac{2\times15.345}{10.23}-1=5$; so the auto-

correlation function of a AltBOC(15,10) code has five peaks. The value of i-th peak is equal to

$$X_i = \frac{(-1)^i (x - |i|)}{x} \qquad for \quad i = 0, \quad \pm 1, \quad \cdots \pm (x-1) \qquad (3.21)$$

where $i = 0$ is the main peak.

Figure 3.9 shows the mainlobe of the auto-correlation function for BPSK and BOC signals in absolute value and decibel scale. The signal bandwidth is 10.23 MHz, and the width of mainlobe is defining the resolution ability of the spreading code for radar applications. It can be seen that the null-to-zero width of the mainlobe is 0.1 μs for BPSK signal and is equivalent to a 15 m range resolution in the monostatic SAR case. But the mainlobe of the auto-correlation function for a BOC signal has five peaks, which degrades the range resolution.

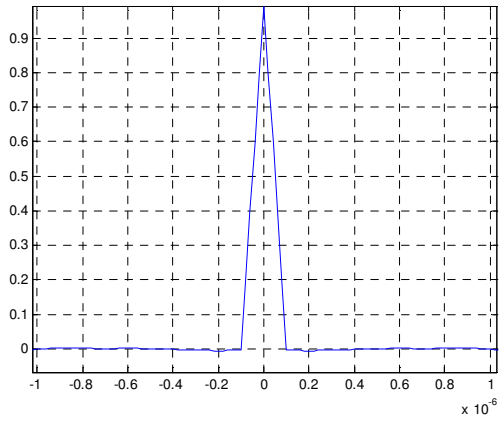

(a) Correlation peak for BPSK signal

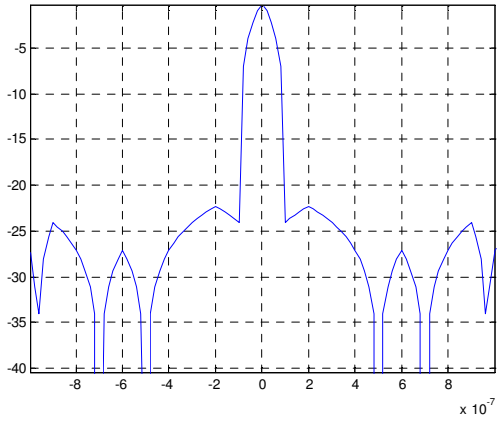

(b) correlation peak in dB scale

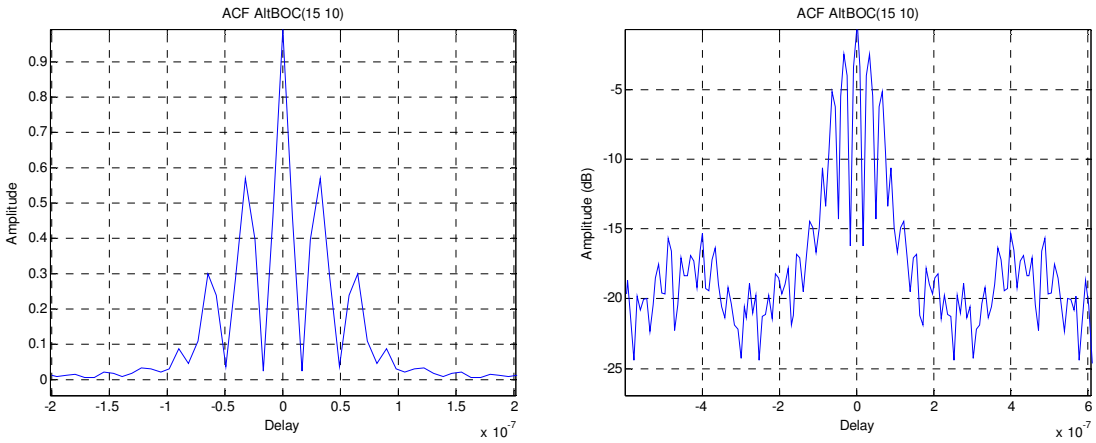

(a) Correlation peak of 10 MHz BOC (b) correlation peak in dB scale

Figure 3.8: *Mainlobe of Correlation Peak*

3.5 Resolution Enhancement

In this section, a method is proposed to improve the range resolution of GNSS signals by combining the frequency bands. The simulation results are shown for the practical example of the combined Galileo E5 band.

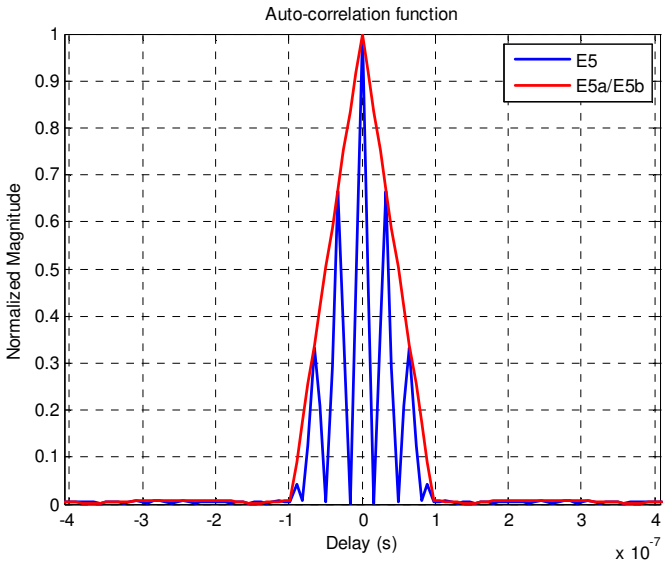

(a) correlation peak of E5a/b and full E5

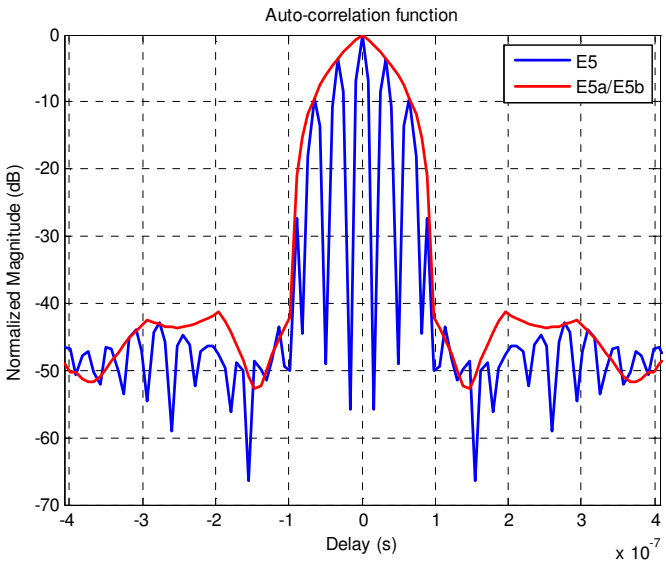

(b) correlation peak in dB scale

Figure 3.9: *Comparison of E5a/b and Full E5*

Figure 3.9 above presents the mainlobe of the auto-correlation function for E5a/b signals and the full E5 signal. If E5a/b is used as the ranging signal for SAR applications, its resolution ability is the same as the 10 MHz BPSK signal (Figure 3.8 (b)); and its sidelobe level is 40 dB. If full E5 is used, the main peak of the auto-correlation function is much smaller than 0.1 μs, but its resolution is still equal to 15 m as the multiple correlation peaks exist.

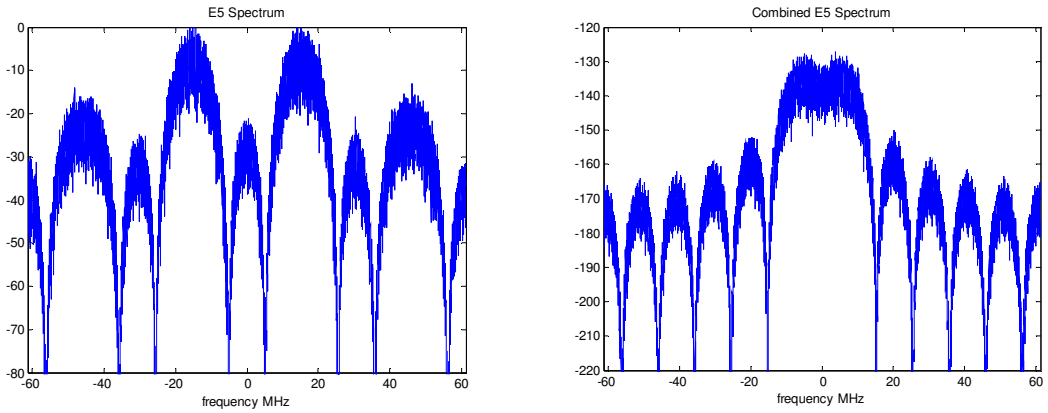

(a) simulated E5 spectrum (b) combined E5 spectrum (simulation)

Figure 3.10: *Shifted and Combined E5 Spectrum*

Figure 3.10 (a) plots the simulated E5 power spectrum. It is identical to the power spectral density of the E5 signal derived from equation 3.14 (Figure 3.5). The simulated E5 signal is generated according to the description in section 3.3. A method is suggested to shift the E5a/b bands towards the centre frequency, achieving higher bandwidth, hence a better range resolution. Figure 3.10(b) shows the power spectral density of a modified signal after the E5a/b bands are shifted by 10.23 MHz towards the zero frequency. It can be seen that the combined spectrum covers about 30 MHz bandwidth; and its envelope is smoother, hence a better correlation output.

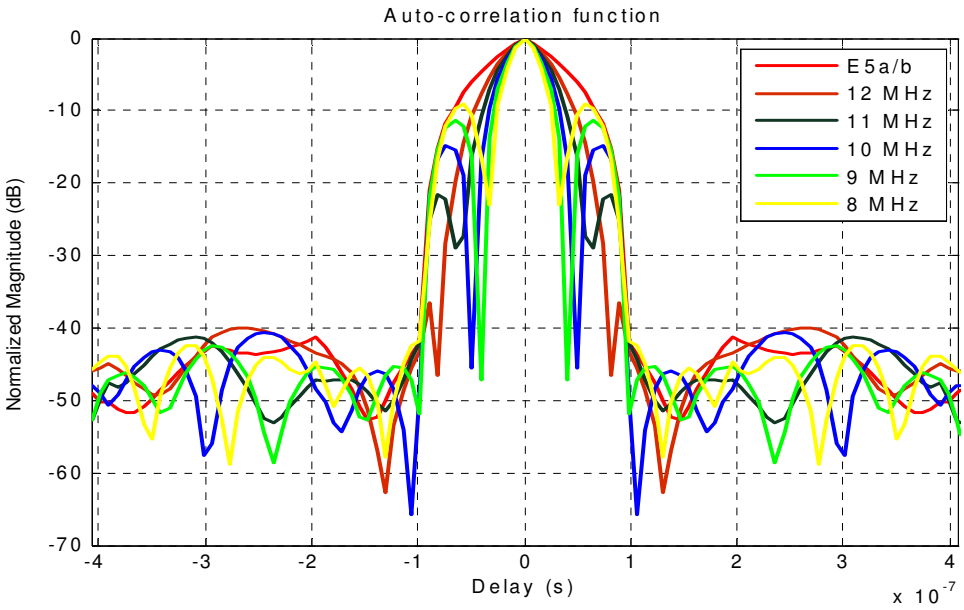

Figure 3.11: *Auto-correlation Function of the Combined E5 Spectrum by Different Shifts*

Figure 3.11 presents the auto-correlation function of the combined E5 spectrum, which is from converging the original E5 band by different frequencies. The mainlobe width becomes narrower as the shifting frequency reduces from 12 MHz to 8 MHz; but at the same time, the sidelobe level is decreasing to less than 10 dB, which consequently reduces the contrast of the SAR image. Balancing both mainlobe width and sidelobe level, 10.23 MHz is the optimal amount to combine the E5 band.

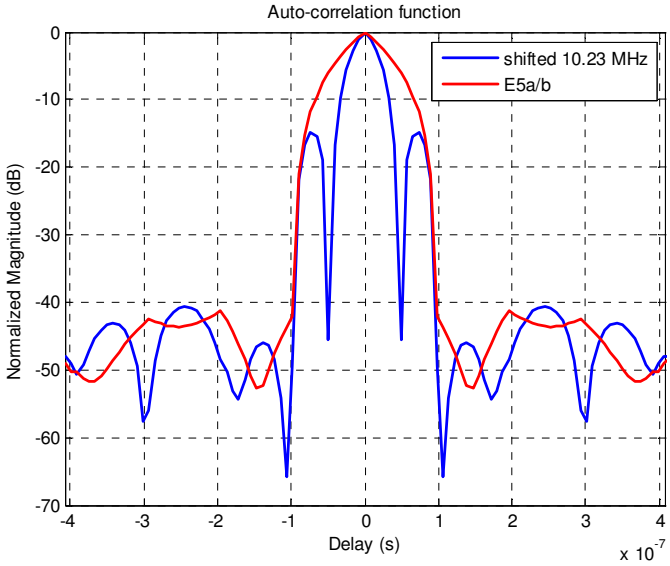

(a) ACF of E5a/b signal and combined E5

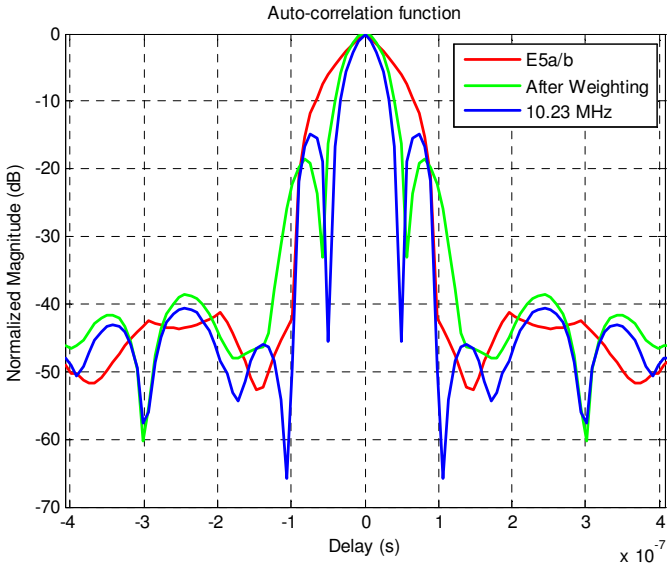

(b) ACF after weighting

Figure 3.12: *Resolution Ability of E5a/b and Combined E5 with Frequency Domain Weighting*

Figure 3.12 again shows the auto-correlation function of E5a/b and combined E5 (shifted 10.23 MHz). It can be clearly seen that the mainlobe width has been reduced to half of

the E5a/b auto-correlation peak mainlobe, hence the range resolution has improved from 15 m to 7.5 m. Figure 3.12(b) adds the results of weighting with a Kaiser window applied in the frequency domain. It suppresses the sidelobe and at the mean time broadens the mainlobe slightly. Looking at the frequency bands shown in Figure 3.1, a similar range resolution enhancement may be achieved with GPS L1 and L2 signals by combining the P-code and new M-code too.

Although the promising range resolution improvement can be expected by combining the full E5 bandwidth, the further study and simulation will be needed to fully support this claim. To analyse the range resolution, the CCF should be used instead of ACF. When combining the two signals, the constant phase jump from E5a to E5b needs to be taken into account. The phase jump in the reflected signal is different from the phase discontinuity in the locally generated reference signal. The two signals E5a and E5b are separated by 40 MHz and hence can have different Doppler shift. This Doppler shift needs to be estimated and compensated before the two signals could be combined in the real data processing. The above issues need to be addressed and confirmed by simulation and experimentation.

3.6 Summary

This chapter provides an analysis of the available GNSS signals for potential use in radar applications. New Galileo and modernized GPS signals are introduced and the advantage of binary offset carrier modulation has been identified. Generation, reception, and power spectrum have been discussed for different GNSS signals. Moreover, the correlation

properties of GNSS signals have been studied and analysed. A method has been proposed to improve the resolution by combining the bandwidth of the Galileo E5 signal. The preliminary results of the improved resolution are presented at the end of this chapter.

Reference

1. *Galileo Open Service Signal In Space Interface Control Document*. 2006, European Space Agency / Galileo Joint Undertaking.
2. *GLONASS Interface Control Document* 2002.
3. Betz, J.W., *Binary offset carrier modulations for radionavigation.* Journal of the institute of navigation, 2002. **48**(4): p. 227-246.
4. Godet, J., *Technical annex to Galileo SRD signal plans*, in *STF annex SRD 2001/2003 Draft 1*. 2001.
5. Rebeyrol, E., et al., *BOC power spectrum densities*, in *ION NTM 2005*. 2005: San Diego, CA. p. 769 - 778.
6. Gold, R., *Optimal binary sequences for spread spectrum multiplexing*. IEEE Transactions on Information Theory, 1967. **13**(4): p. 619-621.

Chapter 4 Synchronisation using GNSS Signals

4.1 Introduction

A crucial problem associated with bistatic radar is synchronisation between the transmitter and the receiver to allow for coherent signal processing. This includes: time synchronisation, the receiver must precisely know when the transmitter fires; phase synchronisation, the receiver and the transmitter must be coherent over extremely long intervals of time; spatial synchronisation, the receiving and transmitting antennas must simultaneously illuminate the same spot on the ground [1]. SAR imaging requires precise knowledge of the Doppler history, which in monostatic SAR can be estimated from the raw data. However, in an opportunistic bistatic system, the lack of phase lock between the transmitter and the receiver hinder a direct adaptation of monostatic methods. This is further aggravated by the lack of a common time reference between the BSAR platform position information and the acquired data.

In monostatic radar, high-frequency oscillator phase noise contributions over a very short two-way propagation time are negligible, while for bistatic systems, oscillator phase noise components of two frequency sources contribute to the phase shift. The effect of oscillator phase noise on BSAR was first discussed in [2] and further investigated in [3], which concluded that uncompensated oscillator jitter may cause a time-variant shift, spurious sidelobe, and a deterioration of the impulse response, as well as a low-frequency phase modulation of the focused SAR signal. Similarly, the impact of time synchronization errors would lead to unfocused images. In explicitly designed bistatic

radars, it is usual to derive all frequencies from a common reference, for example, by using GPS disciplined sources [4]. Another approach is to record the relative phase offsets between the oscillators, as it will be done in the TanDEM-X mission [5], which requires a two-way dedicated link. Once these offsets are known, they can be corrected in the data and image processing. However, if the receiver uses a non-cooperative source of opportunity, none of these strategies can be applied directly.

Instead, authors in [6] proposed a BSASR system with fixed receiver and spaceborne non-cooperative transmitter. Phase synchronization and pulse-repetition frequency (PRF) recovery are achieved using a dedicated link that receives a clean signal directly from the satellite. How to align the acquired data with the satellite orbit and how to estimate the Doppler centroid (DC) are studied. Similar synchronization problems, which arise in bistatic SAR missions have also been discussed in [7, 8] and solutions for the hybrid bistatic experiment with TerraSAR-X and PAMIR have been presented. Precise footprint synchronization is achieved by analyzing the amplitude progression of the satellite's signal in order to predict the arrival time of the main beam. The second synchronization task adjusts the receive gates to the transmit pulses which is achieved with a digital PLL.

In this chapter, the use of a dedicated synchronization link to quantify and compensate oscillator phase noise is investigated. The synchronization link itself may also suffer errors contributions from receiver noise, Doppler Effect, aliasing, interpolation, and filter mismatch. Several contributions such as the influence of the ionosphere or relativistic effects are neglected in the discussion to maintain the general overview of our approach.

4.1.1 Synchronisation for GNSS as NCT

In systems using co-operative transmitters, the transmitter and receiver can be designed to work together, with built-in means of synchronisation. However, in non-cooperative bistatic radar systems, the receiver has little or no knowledge of the transmitted signal, which increases the complexity of the synchronisation problem.

As mentioned previously, BSAR is subject to problems such as spatial synchronization, time synchronization, and phase synchronization. For the proposed SS-BSAR system using GNSS, time synchronization is more easily achieved with a CW navigation signal than the system transmitting a pulsed signal. There is no need for PRF recovery and pulse alignment. As GNSS satellites mostly adopt the global beam for transmitting, spatial synchronization is not a critical issue regarding the antenna footprint overlap. Hence, we only discuss phase synchronization in detail in this chapter.

The receiving part of the proposed SS-BSAR consists of two channels: the radar channel used for receiving the reflected signal from the target and the heterodyne channel used for synchronisation with the transmitter. As discussed in Chapter 2, the heterodyne channel signal in this case can't directly correlate with the radar channel signal, because of its low SNR (below the receiver noise). It is suggested that a locally generated replica should be used, whose parameters are fully synchronized with the heterodyne channel signal.

As indicated earlier, this synchronisation process may be possible if the GNSS signal is received directly on the heterodyne channel. Signals in the radar and heterodyne

channels are down-converted using a common local oscillator, in order to maintain the phase relationship between the two channels, and subsequently sampled using a common clock. A synchronisation algorithm has been proposed to apply to the stored heterodyne signal to extract all the information needed for local replica generation. It will be discussed in more detail in the following sections.

4.1.2 Equation of Received Signal

In this section, the equation of the received E5 signal at the heterodyne channel will be derived, and the discussion in section 4.2 and 4.3 will be based on it. It should be noted that, although we are considering a particular navigation signal, Galileo E5 in this chapter, the background theory and the methods of synchronisation are generic and could be used with other GNSS signals. The details for generation and modulation of a Galileo E5 signal are included in Chapter 3.

As mentioned in Chapter 3, due to the multi correlation peaks of AltBOC modulation, it is easier and more straightforward to process the E5a signal or the E5b signal separately than correlating the full E5 signal directly. Here, we consider the E5b signal as an example; the processing for E5a will be identical. Pseudorandom noise codes of the Galileo E5b signal are borne by carriers in phase-quadrature. The transmitted E5b signal at the input of the antenna can be written as:

$$S_{E5b}(t) = \sqrt{2P}\begin{bmatrix} C_{E5b-I}(t-\tau_s(t))D_{E5b-I}(t-\tau_s(t))\cos(2\pi f_c(t-\tau_s(t))+\phi(t)) \\ -C_{E5b-Q}(t-\tau_s(t))\sin(2\pi f_c(t-\tau_s(t))+\phi(t)) \end{bmatrix} \quad (4.1)$$

Considering single sideband reception of the E5b, the signal received in the heterodyne channel, after filtering, downconversion, quadrature demodulation, can be expressed as (for example of E5b):

$$S_I = C_{E5b-I}[t-\tau_s(t)]D_{E5b-I}[t-\tau_s(t)]\cos\left[2\pi f_s t+\phi(t)\right]+C_{E5b-Q}[t-\tau_s(t)]\sin\left[2\pi f_s t+\phi(t)\right] \tag{4.2}$$

$$S_Q = C_{E5b-I}[t-\tau_s(t)]D_{E5b-I}[t-\tau_s(t)]\sin\left[2\pi f_s t+\phi(t)\right]-C_{E5b-Q}[t-\tau_s(t)]\cos\left[2\pi f_s t+\phi(t)\right] \tag{4.3}$$

where $\sqrt{2P}$ is the envelope of E5b signal

$C_{E5b-I}(t)$ and $C_{E5b-Q}(t)$ represents the spreading code of E5b

$D_{E5b-I}(t)$ is the navigation message on E5b with a chip rate of 250 bps

f_c is the E5b carrier frequency

$\phi(t)$ is unknown phase variation

S_I and S_Q are the in-phase and quadrature signals at the demodulator output

$\tau_s(t)$ and f_s are, respectively, the delay and carrier frequency shift suffered by the signal from the satellite to the receiver.

The delay and frequency shift can be expressed as:

$$\tau_s(t) = \tau_d(t) + \tau_c(t) \tag{4.4}$$

$$f_s(t) = f_d(t) + f_{lo}(t) \tag{4.5}$$

where $\tau_d(t)$ is the varying delay due to satellite-receiver separation and $\tau_c(t)$ is the (varying) relative time shift, which occurs due to the difference between the timing of the receiver sampling clocks and the timing of the transmitting clock ($\tau_c(t)$ can be referred to as clock slippage or clock drift). The frequencies $f_d(t)$ and $f_{lo}(t)$ are, respectively, the Doppler shift due to the satellite and receiver motion and the difference between the signal's carrier frequency and the actual frequency output of the local oscillator ($f_{lo}(t)$ is affected by the stability of oscillator). We can see that the delay and the frequency shift are both functions of time. For example, the delay and frequency vary due to the changing distance between the transmitter and the receiver as well as due to the frequency drifts of the local oscillator.

4.1.3 Dynamics of Delay and Frequency Variation

From Equations 4.4 and 4.5, it is seen that both delay and frequency shift are functions of time. The total delay τ_s is the sum of delay due to the satellite-receiver separation and the time shift introduced due to unsynchronised clocks in the transmitter and receiver. Let us first calculate the maximum delay variation due to the transmitter and the receiver motion over an interval of one second. Figure 4.2 shows a simplified two-dimensional geometry used for calculation. The initial position of the Galileo satellite and airborne receiver is assumed to be (0 km, 23222 km) and (0 km, 0 km) respectively on the x-y plane. The satellite is assumed to be moving in a straight line (in short period of time) with a velocity of 4000 m/s in the +X direction, whereas the aircraft is moving in the negative X

direction with a velocity of 200 m/s. This indicates a rate of change of distance of 0.38 m/s, which corresponds to a delay variation about 1.3 ns per second.

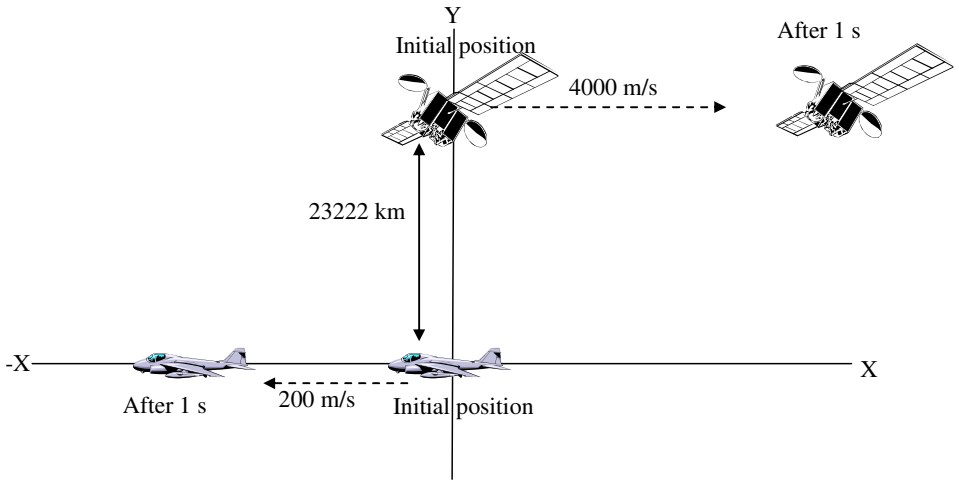

Figure 4.1: *Two Dimension Geometry*

The dynamics of the time-shift variation due to unsynchronised clocks depends on the stability of the sampling clock used in the receiver. In our system we are using a clock with a stability of 100 ppm. It was found experimentally that this clock gives an initial time shift $\tau_c(0)$ of approximately 0 ms and a time variation of about 2.4 μs/s. Therefore the total delay $\tau_s(0)$ is around 77 ms for 23222 km and the total delay variation is about 2.4 μs/s.

In Chapter 2 it is shown that the maximum Doppler shift due to the motion of GNSS satellites is about 4 kHz; the maximum Doppler shift due to the movement of a low-flying aircraft with a velocity of 200 m/s is about 1 kHz. Then a reasonable value for the expected maximum Doppler shift is about 5 kHz. Also the expected that maximum rate-of-change of the Doppler frequency due only to satellite motion is 1 Hz/s; its derivation is

given below. For our receiver we are using frequency synthesizers as the local oscillator to down-convert the received signal. It was found experimentally that these oscillators introduce some 0.5 kHz of frequency shift, which varies at the rate of ~ ±0.2 Hz/s. Therefore the total maximum frequency shift $f_s(0)$= 5.5 kHz. The total frequency variation is ± 1.2 Hz/s.

It should be noted that an accurate model for estimating the delay and frequency variation is beyond the scope of this section. Therefore the assumed delay and frequency variation may be different for another scenario or system. Nevertheless the assumed values of the variations give a good starting point for implementing the synchronisation algorithm.

Figure 4.2 shows a typical GNSS circular orbit around the earth, the average earth's radius being R_e (6368 km) and R_s the GNSS satellite orbit radius. The distance R_T from the satellite to the target area varies with respect to the satellite's elevation angle α; the greatest distance occurs when the satellite is at the horizon; it decreases with increasing satellite elevation angle and reaches a minimum at the zenith. The distance from the satellite to the airborne receiver will be little different from R_T, since a typical aircraft flight altitude is less than 20 km and the GNSS satellite orbit altitude is about 20,000 km.

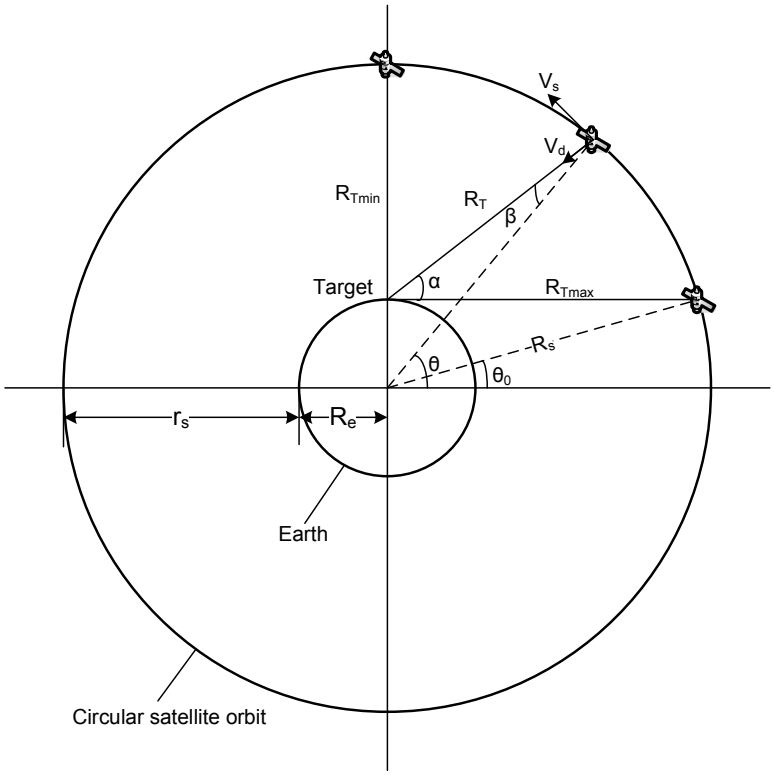

Figure 4.2: *Doppler frequency caused by satellite motion (courtesy of [9])*

An expression giving the relationship between slant range (R_T) and elevation (α) can be obtained from

$$R_s^2 = R_e^2 + R_T^2 - 2R_e R_T \cos(90 + \alpha) \tag{4.8}$$

$$R_T = R_e \left\{ \left[\left(\frac{R_s}{R_e} \right)^2 - \cos^2 \alpha \right]^{1/2} - \sin \alpha \right\} \tag{4.9}$$

The maximum slant range, occurring when $\alpha = 0$, is

$$R_{T\max} = \sqrt{R_s^2 - R_e^2} \tag{4.10}$$

The Doppler shift (for short observation intervals) is given by the following equation, which is plotted below in Figure 4.3 for a GLONASS satellite. For any lateral

displacement of the target from the ground track of the satellite, the maximum Doppler shift is observed at zero elevation.

$$f_d = \frac{V_d}{\lambda} = \frac{V_S}{\lambda}\frac{R_e \cos\psi \cos\alpha}{R_S} \tag{4.11}$$

where ψ is the angle between the satellite's ground track at the sub-satellite point and the terrestrial great circle passing through this point and the target position;

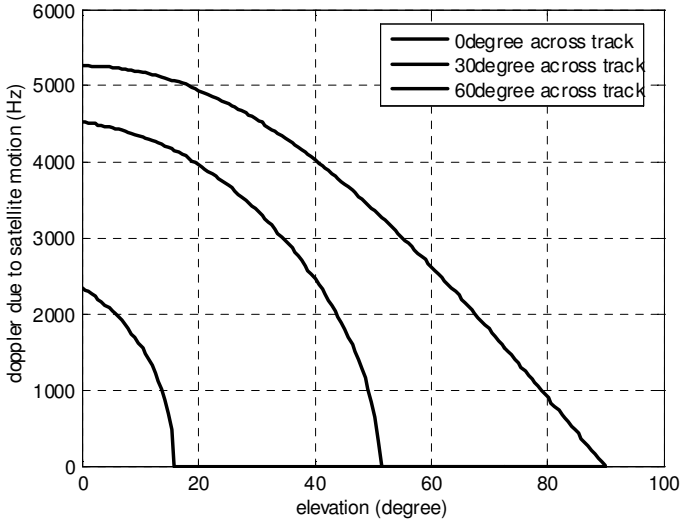

Figure 4.3: *Short Term Variation of Doppler Shift with Elevation for GLONASS*

Relevant parameters are given in the Table 4-1 for the GPS L1 channel, the GLONASS L1 channel and the Galileo E5 channel, the likely maximum Doppler referring to the Doppler at 10 degrees elevation with no target lateral displacement. The rate-of-change of the Doppler frequency is also important for the tracking of the GNSS signal. If the rate-of-change of the Doppler frequency can be calculated, the frequency update rate in the tracking algorithm can be predicted. However, the rate-of-change is not a constant over the satellite period.

The target is assumed to be displaced normally from the satellite's ground track by a great circle angle φ_T; the satellite is displaced (along the ground track) from the point of closest approach to the target by a great circle angle θ_T. The maximum rate of change of the frequency occurs at $\varphi_T = 0$ and $\theta = \pi/2$. The corresponding maximum rate of change of the Doppler frequency is [10]

$$\delta f_d \mid_{\max} = \frac{dV_d}{dt} \mid_{\max} \cdot \frac{f}{c} = \frac{VR_E d\theta / dt}{\sqrt{R_E{}^2 + R_S{}^2 - 2R_E R_S}} \cdot \frac{f}{c} \tag{4.12}$$

Constellation	GPS	GLONASS	GALILEO
Orbit Period	11 hrs 58 min	11 hrs 15 min	14 hrs 22 min
Orbit Altitude (km)	20180	19130	23222
Max Range from satellite to target on the earth's surface (km)	25785	24690	29300
Satellite Speed (m/s)	3874	3953	3643
Likely max. Doppler due to sat. motion (kHz)	4.88	5.26	3.07
Max rate of change of Doppler (Hz/s)	0.936	1.088	0.474

Table 4-1: *Doppler Shift Dynamics*

These two parameters will specify the synthetic aperture length and integration time appropriate to various altitudes for different types of aircraft. Detailed calculations for the potential resolution of SS-BSAR are given in section 2.3 using these typical values. From that we know that the rate-of-change of the Doppler frequency caused by the satellite motion is rather lower than due to receiver motion. It does not affect the update rate of the tracking of synchronisation significantly. If the receiver has an acceleration of 10 m/s^2 toward a satellite, the corresponding rate-of-change of the Doppler frequency can

be found from equation 4.12. The corresponding result is 53.3 Hz/s. comparing with the rate-of-change of the Doppler shift caused by the motions of the satellite; the acceleration of the receiver is the dominant factor. The operation and performance of a receiver tracking loop greatly depends on the dynamics of the receiver motion.

4.1.4 Proposed Synchronisation Algorithm

It is clearly seen from Equations (4.2) and (4.3) that the locally generated pseudorandom noise code needs to be synchronised with the received heterodyne signal in order to decode the navigation message and generate local replica for range compression. Figure 4.4 below shows a block diagram for the synchronisation algorithm proposed. For the example of the E5b synchronisation, it consists of:

- Acquisition, or coarse synchronisation using both in-phase and quadrature components of the E5b signal. It estimates the coarse frequency and delay, and extracts the secondary code.
- Frequency $f_s(t)$ tracking using the E5b-Q. It is the pilot signal of E5b and no navigation message is modulated. A least mean square algorithm will be applied to remove noise effects.
- The tracked frequency is then used to remove the Doppler shift from the received signal. The locally generated pseudorandom noise code is then fine delay synchronised to the input signal by curve fitting methods.

- Finally, the phase variation $\phi(t)$ is extracted and the fully synchronised local generated pseudorandom noise code is used to decode the navigation message on E5b-I.
- Range compression can be applied with the radar channel signal using a fully synchronized local reference.

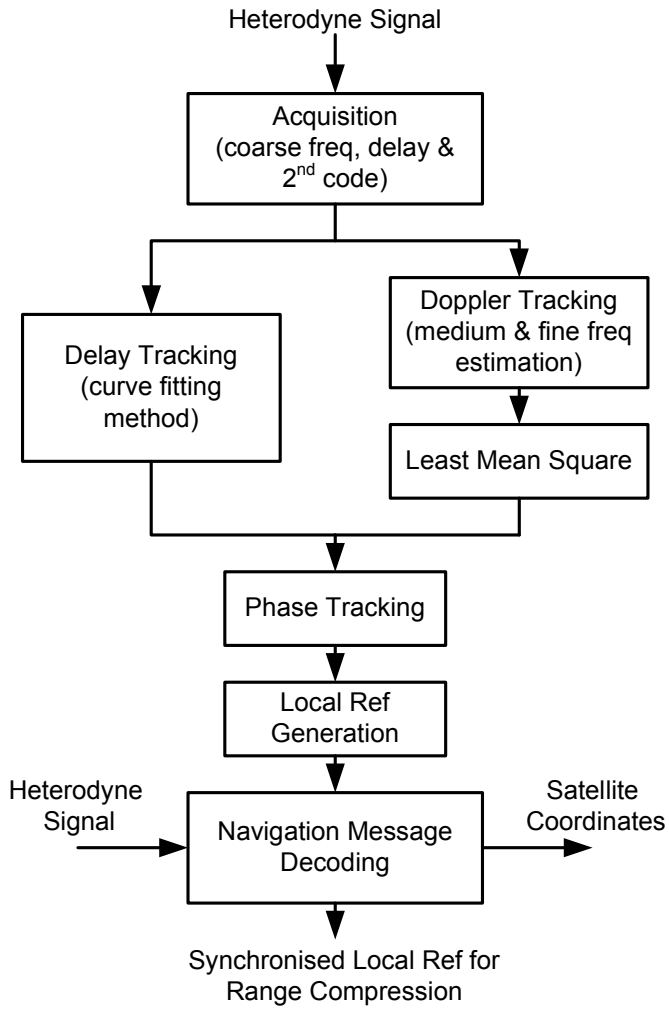

Figure 4.4: *Synchronisation Algorithm Block Diagram*

In the following two sections we will discuss the signal acquisition block and two tracking blocks in more detail. The performance of the tracking algorithm is analysed in terms of receiver & satellite dynamics and noise error. The results are supported by experimentation with Galileo satellites in section 4.4.

4.2 Signal Acquisition

In order to track the parameters and decode the information on Galileo E5b signals, an acquisition method must be used first to detect the presence of the signal. Once the signal is detected, the necessary parameters, such as the starting bit of the pseudorandom noise code (code phase) and coarse Doppler frequency will be obtained and passed to the tracking program. From the tracking program, information such as fine delay, fine Doppler and the navigation message can then be obtained.

The received signal S is a combination of signals from all n visible satellites. When acquiring satellite k, the incoming signal S is multiplied with the local generated pseudorandom noise code corresponding to the satellite k. The cross correlation between pseudorandom noise codes for different satellites implies that signals from other satellites are nearly removed by this procedure. To avoid removing the desired signal component, the locally generated pseudorandom noise code must by properly aligned in time, that is, have the correct phase.

Then the acquisition method must search over a frequency range to cover all likely frequency shifts. As mentioned earlier, the Doppler frequency shift will never exceed 5 kHz for a stationary or low speed receiver on earth; and approach as high as 10 kHz with a very high user velocity. Using a narrow bandwidth for searching means taking many steps to cover the desired frequency range and it is time consuming. Searching with a wide bandwidth filter will provide relatively poor sensitivity. In other words, there is a trade-off between speed and sensitivity. If the signal is strong, the fast, low sensitivity acquisition method can be used. If the signal is weak, the low-sensitivity acquisition will miss it, and therefore a high sensitivity method must be employed. If the signal is very weak, acquisition should be based on a long data length. From [9], it is sufficient to search the frequency in steps of 1000 Hz resulting in 41 different frequencies in the case of a fast-moving receiver and 21 in the case of a static receiver.

After mixing with the locally generated carrier wave, all signal components are squared and summed providing a numerical value. For each of the different frequencies all different code phases are tried. A search for the maximum value is performed. If it exceeds a determined threshold, the satellite is acquired with the corresponding frequency and code phase shift. Figure 4.5 below shows a typical acquisition plot for a visible satellite. The plot shows a significant peak, which indicates high correlation.

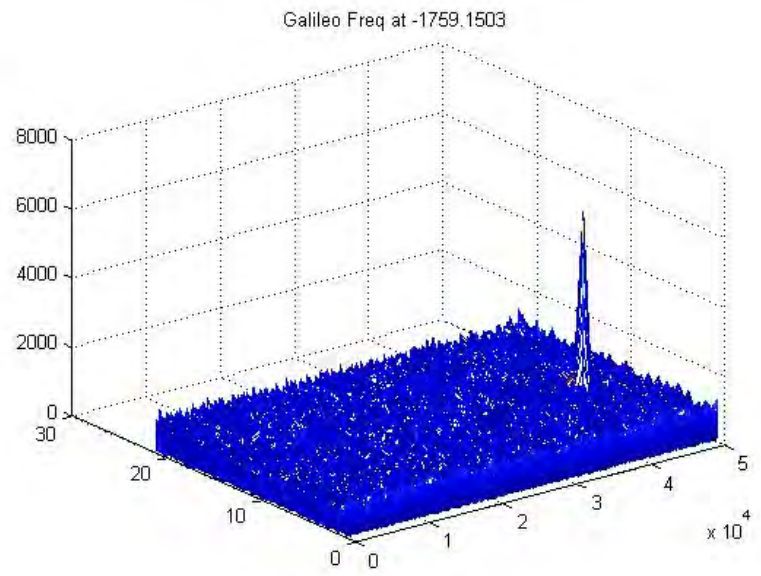

Figure 4.5: *Acquisition Result for GIOVE-A*

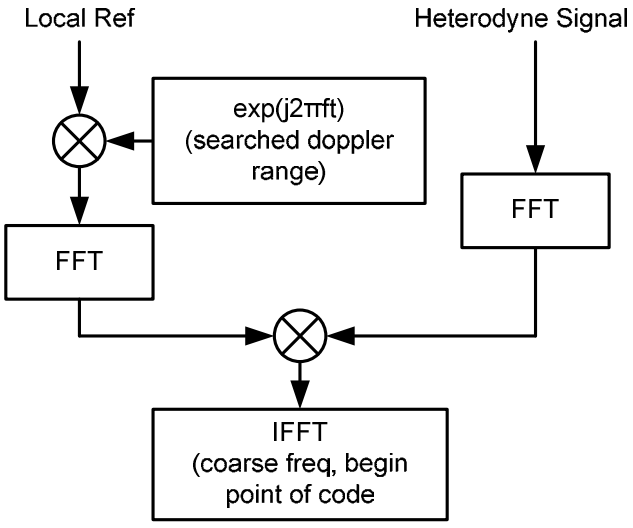

Figure 4.6: *Block Diagram (matched filter)*

The different acquisition techniques have been discussed in detail and compared, in terms of speed and sensitivity, in [9, 11]. Parallel code phase search acquisition (circular correlation) is suggested to apply for our case. The local pseudorandom noise code is multiplied by a locally generated carrier signal and transformed into the frequency

domain by fast Fourier transform (FFT). It's then multiplied with the outcome of the heterodyne signal with the FFT operation. The result of the multiplication is transformed into the time domain by an inverse Fourier transform. If a peak is present in the correlation, the index of this peak marks the pseudorandom noise code phase and coarse frequency of the incoming signal. The accuracy of the estimated frequency is similar to other acquisition methods. The pseudorandom noise code phase, however, is more accurate as it gives a correlation value for each sampled code phase. That is, if the sampling frequency is 50 MHz, a 1 ms code has 50000 samples, so the accuracy of the code phase can have 50000 different values instead of 10230 (for example of E5b-I/Q).

Now let us find the integration time required to implement the correlator, shown in Figure 4.6. The longer the integration time used, the higher the signal-to-noise ratio that can be achieved at the output of the correlator. However, the presence of the navigation data on the signal received from the satellite restricts the integration interval, unless this information is known or initially extracted from the signal. This is explained as follows:

The navigation message has a data rate of 50 bps on E5a-I (250 bps on E5b-I), whereas the E5a/b spreading codes have a bit rate of 10.23 Mbps and code length of 1 msec. Each navigation data bit is therefore 20 ms long, so that in 20 ms of data there can be one data transition at most. If there is a data transition in one 10 ms interval, the other 10 ms interval will not have one. Therefore, in order to guarantee there is no transition in the data, one of two consecutive intervals of 10 ms should be used; in practice both can be used since the one with no transition will provide better correlation than the other.

And due to AltBOC modulation on the E5 signal, there is one extra consideration needed for its acquisition, which is the secondary code. It splits the E5a and E5b spectrum to the opposite side of E5 carrier frequency. It has a similar effect as the navigation message on the acquisition and tracking algorithm. However, as the structure and length of this code is known, it is possible to be removed by the multiplication of its local replica as long as the code phase is aligned. For example E5b-Q, is 100 bits long with chip rate of 1000 Hz. 100 code phase transitions have to be completely tried to search the correct code phase for E5b-Q signal. Because there is only one 4-bit secondary code on E5b-I (remember E5b-I has navigation messages), the quickest way to search the correct secondary code phase is using E5b-I first then search E5b-Q; only 29 (4+100/4) different code phase transitions search will be necessary.

4.3 Signal Tracking

The acquisition provides only rough estimates of the frequency and code phase parameters. The main purpose of tracking is to refine these values, keep track, and demodulate the navigation message from the specific satellite. It consists of two tracking loops. First, the pseudorandom noise code is removed from the input signal and the frequency of the remaining CW is fine estimated; second, the estimated fine frequency variation is then used to remove the frequency shift from the heterodyne signal, Thereafter, fine code delay (phase) of the heterodyne signal can be found. Finally, the phase variation is tracked and the synchronised locally generated pseudorandom noise code can be used to decode the navigation message.

4.3.1 Fine Code/Delay Tracking

In this section two tracking methods will be discussed, the first being the conventional tracking loop [9, 12] and the second being the method known as block adjustment of synchronising signal (BASS). This method is suggested to be used for tracking the heterodyne signal in our case and is therefore discussed comprehensively.

The input signal is digitised at 50 MHz, so that every sample point is separated by 20 ns, and the coarse code phase (delay) estimate measures the beginning of the pseudorandom noise code with this resolution. For a more accurate estimate of the delay variation (for accurate clock recovery) additional processing is needed, as described below.

As in the block adjustment of synchronising signal algorithms, correlation is performed on consecutive blocks of input data. The selection of the integration time in this process is a trade-off between the requirements of the dynamics of delay variation and the SNR of the input signal. The criteria used for selecting the delay update, for the system under consideration, are described after discussion of the fine delay estimation algorithm.

In this section we are using a curve fitting method to estimate the fine delay as described by [9]. Figure 4.7 below shows the mainlobe of the correlation function within one chip of the pseudorandom code. Three correlations values are shown in this Figure: y_p is the coarse delay estimate (also known as prompt), y_e is the estimate obtained from the early code, and y_l the estimate from the late code. The time t is measured from the prompt

output to the early or to the late code output. We assume that y_p is t_p seconds from the ideal peak. A quadratic equation to model the correlation peak can be written as:

$$y = at^2 + bt + c \tag{4.13}$$

where y represents the correlation value and t represents time.

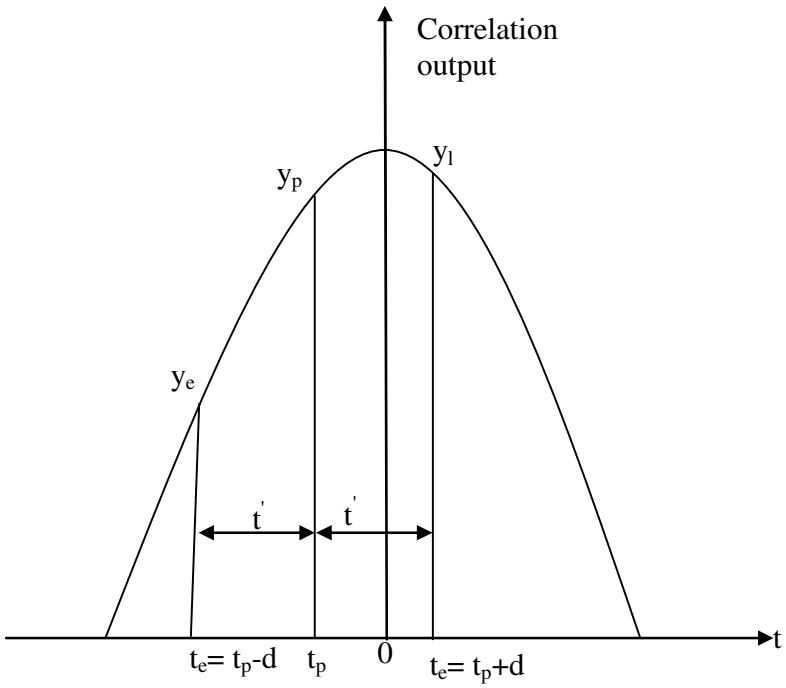

Figure 4.7: *Correlation Output of a pseudorandom noise Code*

This equation can be solved to obtain a, b, and c with three pairs of t and y values as:

$$\begin{bmatrix} y_e \\ y_p \\ y_l \end{bmatrix} = \begin{bmatrix} t_e^{\,2} & t_e & 1 \\ t_p^{\,2} & t_p & 1 \\ t_l^{\,2} & t_l & 1 \end{bmatrix} \begin{bmatrix} a \\ b \\ c \end{bmatrix} \text{ or}$$

$$\mathrm{Y} = \mathrm{TA} \quad \text{with}$$

$$\mathrm{Y} = \begin{bmatrix} y_e \\ y_p \\ y_l \end{bmatrix}$$

$$\mathrm{T} = \begin{bmatrix} t_e^{\,2} & t_e & 1 \\ t_p^{\,2} & t_p & 1 \\ t_l^{\,2} & t_l & 1 \end{bmatrix}$$

$$\mathrm{A} = \begin{bmatrix} a \\ b \\ c \end{bmatrix} \tag{4.14}$$

The solution can be written as:

$$A = T^{-1}Y \tag{4.15}$$

where T^{-1} is the inverse of matrix T. Once a,b,c from Equation (4.15) are found, the maximum value of y can be found by taking the derivative of y with respect to x and setting the result to zero. The result is:

$$\frac{dy}{dx} = 2at_p + b = 0 \quad \text{or} \quad \mathrm{t_p} = \frac{-b}{2a} \tag{4.16}$$

Thus, t_p is the desired fine delay estimate.

In the presence of noise it is impractical to use the t_p value from a 1 ms length of data. Although 1 ms integration time is enough for detecting the pseudorandom noise code, the

fine delay estimate t_p will fluctuate from its true value due to the presence of noise. For the system being considered, the delay estimate x_p is calculated every millisecond. Every 5 ms the t_p values are averaged to generate the final estimate of the delay. It was shown in section 4.1 that the delay variation is around 2.4 μs/s for the system considered here. It takes approximately 4.2 ms to shift the pseudorandom noise code by half the sample interval of 20 ns, which can justify this update rate. Note that the main contributor to delay variation is clock slippage and that the clock used in the experimental receiver does not exhibit very high frequency stability (only 100 ppm). The dynamics of the delay variation can be dramatically reduced if a very stable clock is used, allowing more values of t_p to be averaged to give a better delay estimate.

4.3.2 Fine Doppler Tracking

The purpose of the fine Doppler tracking algorithm is to estimate the carrier frequency of the input signal and; phase lock loops (PLL) or frequency lock loops (FLL) are often used. It requires two loops coupled together (one to strip off the pseudorandom noise code and the other to estimate the frequency). However, the implementation of the code and carrier tracking in the block adjustment of synchronising signal algorithm is different from the conventional tracking loop method. No initial phase adjustment is required, such as in the conventional phase-locked loop. The output from the acquisition algorithm can be used in reducing the computation time and ambiguities in estimating the frequency variation.

The BASS method operates on blocks of input data, the lengths of which depend on the SNR and the dynamics of the parameters to be tracked; block lengths of 6 ms are considered in this section.

The first step is to remove the pseudorandom noise code from the block of input data to produce a CW signal and this is followed by a Discrete Fourier Transform (DFT). The DFT frequency component with the greatest magnitude represents a coarse frequency estimate of the input signal frequency. A fine frequency estimate is obtained by comparing the phases of the frequency components identifying coarse frequency estimates in two consecutive data blocks. In the following we discuss the pseudorandom noise code removal and fine frequency estimation in detail.

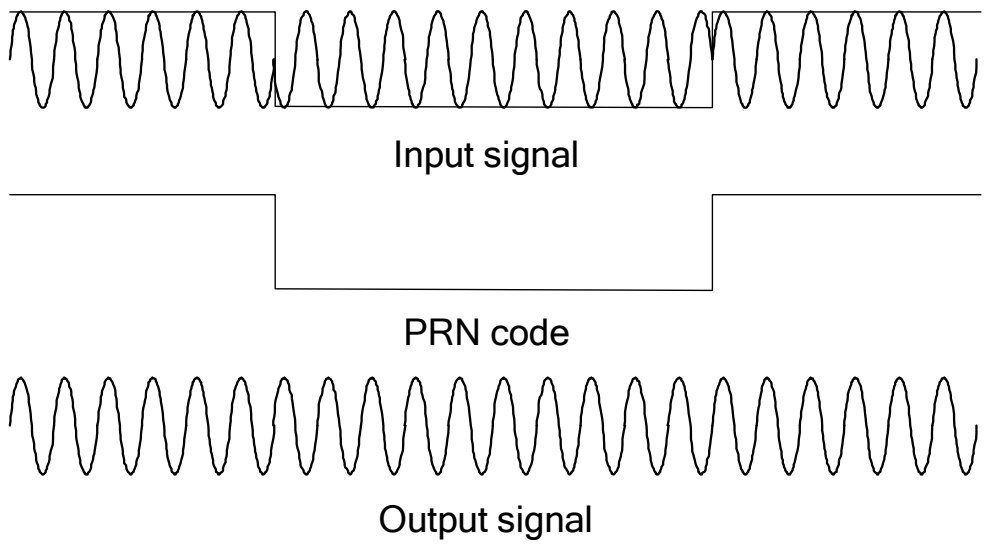

Figure 4.8: *pseudorandom noise Code Wipe-off*

Step 1: Stripping RPN code from the input signal

As mentioned earlier, the product of the pseudorandom noise code (with correct code phase) and the input signal produces a CW signal, as shown in Figure 4.8 above. The top plot is the input signal, which is a sinusoidal signal phase coded by a pseudorandom noise code. The bottom plot is a CW signal representing the result of multiplying the input signal and the pseudorandom noise code; the corresponding signal spectrum is no longer spread.

The frequency of the CW signal can be found from the Fast Fourier Transform (FFT) operation which, for an input data length of 1 ms, will have a frequency resolution of 1 kHz. A threshold can be set to identify strong components, the strongest giving a coarse estimate of the input frequency. As mentioned earlier, the signal is digitised at 50 MHz, so that 1 ms of data contains 50,000 data points and the corresponding FFT generates 50,000 frequency components. However, only the first 25,000 components contain useful information, the last 25,000 being complex conjugates of the first 25,000 points. The frequency resolution is 1 kHz and the total frequency covered by the FFT is 25 MHz, which is half of the sampling frequency. As discussed earlier, the expected maximum Doppler shift is about 5 kHz and the frequency shift of the local oscillator used is about 500 Hz so the total frequency shift is around 5.5 kHz. The frequency range of the FFT which is of interest is therefore only 6 kHz and only 6 frequency components need be calculated, using the discrete Fourier Transform (DFT). The choice of method depends on the speed of two operations.

The start of the pseudorandom noise code in the input data is unknown and, in order to find it, the input data must be multiplied point-by-point by a locally-generated digitized pseudorandom noise code, an FFT or DFT being performed on the product to find the frequency.

In order to search for a suitable 1 ms block of data, the input data stream must be progressively delayed with respect to the locally generated code, one sample interval at a time (50,000 shifts in all). Use of the FFT requires 50,000 operations each consisting of a 50,000-point multiplication and 50,000-point FFT. The output is 50,000 frames of data, each containing 25,000 frequency components (because only 25,000 frequency components provide information, the others being redundant) giving a total of 1.25×10^9 components in the frequency domain; the component with the highest amplitude among these can be considered as the desired result if it also crosses the 'adequate strength' threshold. Searching for the highest amplitude component can be time consuming but, since only 6 frequencies of the FFT output are of interest, the space to be searched can be reduced to 300,000 components. This approach allows the start of the pseudorandom noise code to be found with a time resolution of 20 ns (1/50 MHz), the associated frequency resolution being 1 kHz. It is clear that this process can be very time consuming; methods used to reduce further the number of frequency outputs are discussed below.

If one uses the initial estimate, from the acquisition program, of the relative time at which the pseudorandom noise code period begins, the number of frequency outputs can be

reduced dramatically. As discussed in section 4.1, the delay variation is around 2.40 μs/s (or 120 samples/second). If the delay of the pseudorandom noise code is continuously adjusted from one block of data to another, then one need not search through all 50,000 samples every 1 ms. Ideally a search through only 1-2 samples every millisecond is needed but, in the algorithm implemented, the search is through 6 samples every millisecond which accommodates sudden changes (if any) in delay variation. In this case the total number of frequency outputs is 36, which clearly reduces the computational load significantly.

Step 2: Fine Frequency Estimation

Use of the DFT (or FFT) to find fine frequency is inappropriate because a fine frequency resolution implies a long data record (a resolution of, say, 10 Hz requiring a data record of 100 ms) involving a large transform (a 100 ms. record requiring a 5000,000 point transform) which could be very time consuming. Besides, the probability of having a phase shift in 100 ms of data is relatively high.

The block adjustment of synchronising signal approach to finding fine frequency resolution is by phase measurement. Once the pseudorandom noise code is stripped from the input signal, the input becomes a (digitized) CW signal x(n), the DFT output X(k) of which can be written as:

$$X(k) = \sum_{n=0}^{N-1} x(n) e^{-j2\pi nk/N} \tag{4.17}$$

in which k identifies a particular frequency component and N is the total number of data points. The strongest frequency component in 1 ms of data at time m can be identified as $X_m(k_{max})$ The initial phase $\theta_m(k_{max})$ of the input can be found from the DFT output as:

$$\theta_m(k_{\max}) = \tan^{-1}\left(\frac{\mathrm{Im}(X_m(k_{\max}))}{\mathrm{Re}(X_m(k_{\max}))}\right) \tag{4.18}$$

where Im and Re represents the imaginary and real parts, respectively. Let us assume that at time n, a short time after m, the DFT component $X_n(k_{max})$ of 1 ms of data is also the strongest component, because the input frequency will not change rapidly during a short time. The initial phase angle of the input signal at time n and frequency component k_{max} is:

$$\theta_n(k_{\max}) = \tan^{-1}\left(\frac{\mathrm{Im}\left(X_n(k_{\max})\right)}{\mathrm{Re}\left(X_n(k_{\max})\right)}\right), \qquad -\frac{\pi}{2} < \theta < \frac{\pi}{2} \tag{4.19}$$

The two phase angles can be used to find the fine frequency as:

$$f = \frac{\theta_n(k_{\max}) - \theta_m(\mathrm{k}_{\max})}{2\pi(n-m)} \tag{4.20}$$

Figure 4.9 below diagrammatically represents Equation (4.20). This equation provides a much finer frequency resolution than the result obtained from the DFT. In order to keep the frequency unambiguous the phase difference $\theta_n(k) - \theta_m(k)$ must be less than 2π. If the phase difference is at a maximum value of 2π, the unambiguous bandwidth is 1/(n-m) where n-m is the delay time between two consecutive data sets.

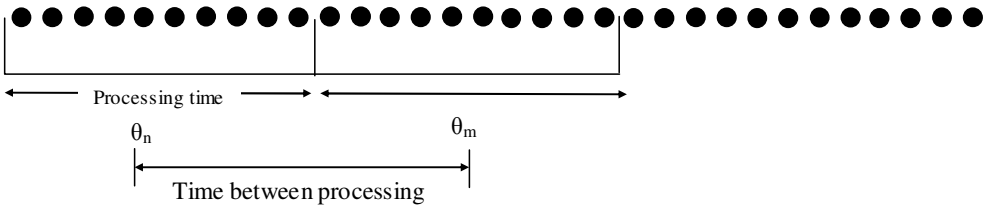

Figure 4.9: *Phase Angle from Two Consecutive Data Sets*

Although the basic approach to finding the fine frequency is based on Equation (4.20), there are several slightly different ways of applying it. If one takes the k_{max} frequency component of the DFT every millisecond, the frequency resolution is 1 kHz and the unambiguous bandwidth is also 1 kHz. In Figure 4.10 five frequency components are shown, separated by 1 kHz. If the input signal falls into the region between frequency components, the phase may be uncertain due to noise in the system, which may cause the input signal to be allocated to the wrong frequency bin.

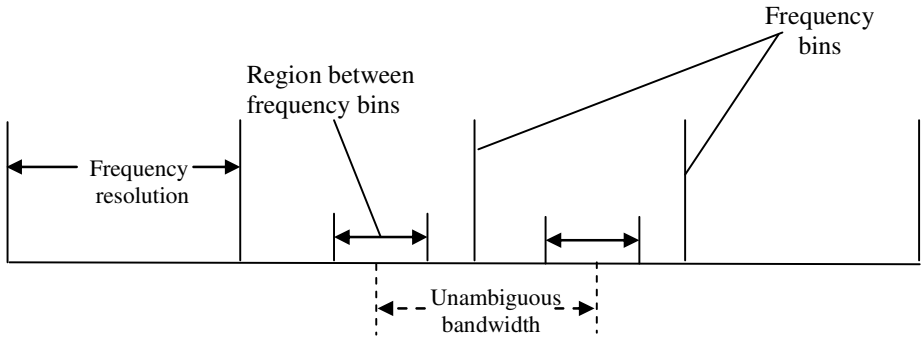

(a) Frequency separation

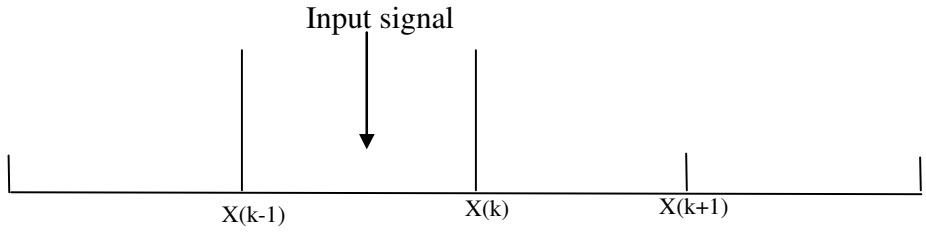

(b) Input signal

Figure 4.10: *Ambiguous Ranges in Frequency Domain (Courtesy of [9])*

One approach to eliminate the uncertainty is to speed up the DFT operation. If the DFT is performed every 0.5 ms, the unambiguous bandwidth is 2 kHz. With a frequency resolution of 1 kHz and an unambiguous bandwidth of 2 kHz, there will be no ambiguity problem in determining the fine frequency. However, this approach will double the number of DFT operations. In addition, decreasing the integration time by half will degrade the SNR by 3 dB.

The approach adopted in this section is to use the initial frequency estimate from the acquisition program. The acquisition algorithm described in section 4.2 searches the frequency band of the input signal with a step size of 1 kHz. The output of the

acquisition algorithm will give a rough indication as to whether the input frequency falls into the region between two frequency components of the FFT output. For example, if the frequency output of the acquisition program is 500 Hz, then the input signal falls into the region between FFT frequency components at 0 Hz and 1 kHz. One solution to this problem is to up-convert (in software) the signal by 500 Hz, before estimating the fine frequency. This ensures that the frequency of the input signal is close to one of the output frequency bins. Of course, 500 Hz should be subtracted from the resulting frequency estimate to obtain an appropriate value. If the DFT is used then the value of k used in Equation (4.19) should be kept close to the initial estimate provided by the acquisition algorithm.

The last point to be discussed is the conversion of the real and imaginary parts of X(k) into an angular measure (the two angles in Equation (4.20) will be obtained in this manner). Usually, phase angle is measured between $\pm \pi$ and the difference between two angles can be of any value between 0 and 2π. The maximum allowable difference angle is $2\pi/5$ (for 200 Hz); if the computed result is greater than $2\pi/5$, addition or subtraction of 2π results in a value, which must be less than $2\pi/5$. If noise is taken into consideration, the $2\pi/5$ threshold can be extended slightly, such as using $2.3\pi/5$, which means the difference must be equal to or less than this value. If the final value of the adjusted phase is still greater than this threshold, it means that there is a phase shift between two successive data sets and π should be subtracted from the result. Of course, the final angle should also be adjusted by adding or subtracting 2π to obtain a final result, which is less than the threshold.

One important point to be highlighted at this stage concerns the maximum frequency variation that the block adjustment of synchronising signal algorithm can track. Theoretically, for a 1 ms update interval, a frequency variation of up to 1 kHz/s can be tracked. For demonstration purposes, we assume a frequency variation of 50 Hz/s. Clearly this is a very high variation and it is not likely to occur in a practical system, however it will show that this update rate is enough for tracking any variation rate occurring in a real system.

4.3.3 Navigation Message Recovery and Reference Generation

Finally, in this section we will discuss a method of decoding the navigation message. Figure 4.11 below shows the method used to decode the navigation message. The estimated frequency is first used to strip the carrier from the received signal. After the frequency shift is removed, the locally generated pseudorandom noise code with correct code phase is multiplied with the I and Q components of the received signal. Thereafter the outputs of the multipliers are passed through low-pass-filters (LPF). The bandwidth of these low-pass-filters is matched with the navigation message rate of 250 Hz on E5b-I. The outputs of the low-pass-filters are expressed as:

$$Y_I = D_{E5b-I}(t)\cos\left[\phi(t)\right] \tag{4.21}$$

$$Y_Q = D_{E5b-I}(t)\sin\left[\phi(t)\right] \tag{4.22}$$

The phase φ(t) can be estimated from equations above as:

$$\phi(t) = \tan^{-1}\left(\frac{Y_Q}{Y_I}\right), \qquad -\frac{\pi}{2} < \phi < \frac{\pi}{2} \tag{4.23}$$

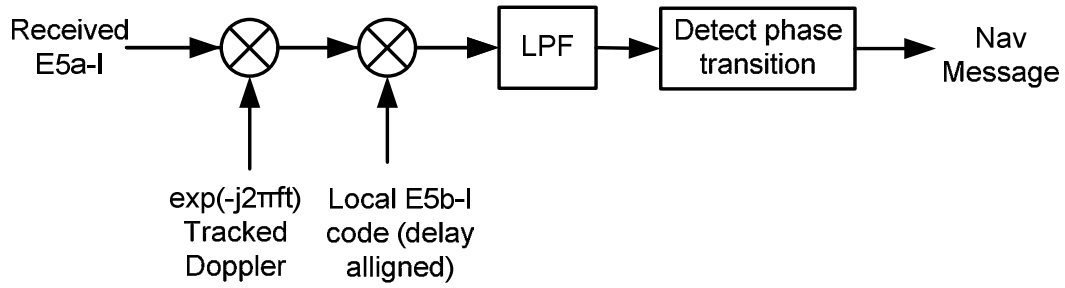

Figure 4.11: *Decoding the Navigation Message*

The output at LPF is the value of 1 and -1. Theoretically we could obtain a bit value for every millisecond of received data. For a bit rate 250 Hz, 4 consecutive values must by replaced by only 1. This conversion procedure is referred to as bit synchronisation. The first task of the bit synchronisation procedure is to find the time in a sequence where bit transitions occur. First, a zero crossing is detected. A zero crossing is where the output changes from 1 to -1, or vice versa. When a zero crossing is detected, the time of a bit transition is located. All bit transition times are known then, which is located 4 ms apart beginning from the first detected bit transition. When all navigation bits have been obtained, they must be decoded following the scheme defined in the Galileo Interface Control Document [13]

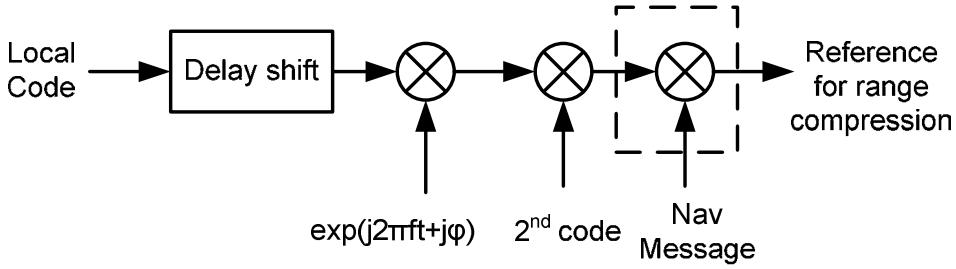

Figure 4.12: *Reference Generation for Range Compression*

With all information on hand, a local reference can be generated for range compression in further image processing. Figure 4.12 above give its block diagram, it is a replica of the heterodyne channel signal without noise present.

4.4 Experimental Verification

In this section we will experimentally confirm the synchronisation algorithm proposed and shown in Figure 4.4. To do this we consider the experimental set-up shown in Figure 4.13. To remind the reader, we briefly describe the data collection process below.

A direct signal from GIOVE-A (first Galileo testing satellite) was collected using an omni-directional antenna and a spiral helix antenna. The specification of antennas used is included in Appendix C. The GNSS receiver provides information on how many satellites are present, and their positions with respect to the receiver. The positional information of the satellites is then used in pointing the spiral antenna in the direction of the chosen satellite, in both elevation and azimuth directions.

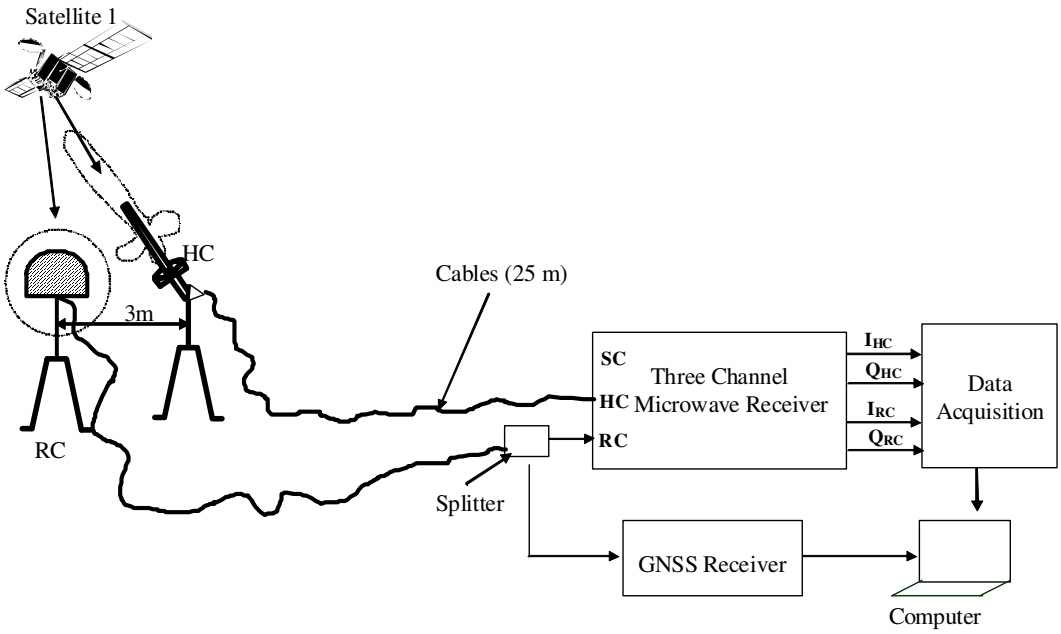

Figure 4.13: *Experimental Set-up for Synchronisation Verification*

Figure 4.14: *Photo of Experimental Set-up*

The signal from the satellite was directly received on two channels (radar channel and heterodyne channel). The radar channel antenna was a stationary omni-directional antenna and it was separated by some 3 m from the heterodyne channel antenna, which was a directional spiral antenna pointed towards the satellite. The receiver down-converts the signal and its baseband I and Q components are then stored on the hard drive of the computer over a 40 second interval. This topology results in negligible delay between the signals in the two channels, effectively giving a target at zero range.

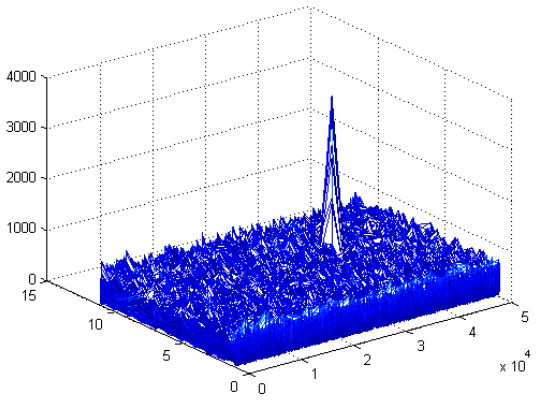

(a) Acquisition output

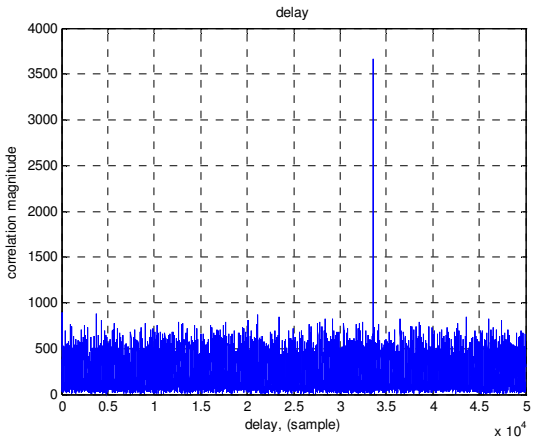

(b) Cross-section, delay

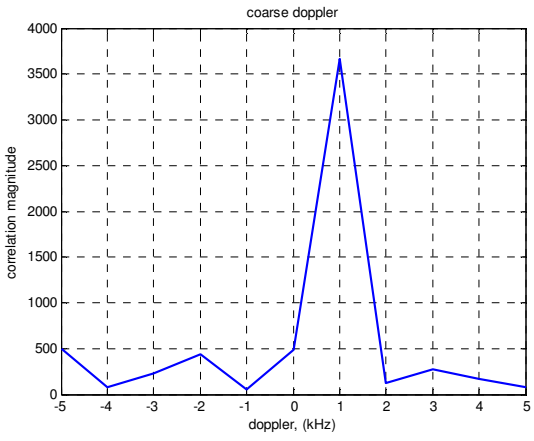

(c) Cross-section, coarse Doppler shift

Figure 4.15: *Acquisition Outputs*

Figure 4-15 (a) gives the acquisition output on 1 ms of stored heterodyne channel signal. It is a two dimension plot with a clear correlation peak, indicating the presence of GIOVE-A signal. The correlation peak value represents the signal magnitude. It is clearly visible and above a pre-determined threshold. Figures 4.15 (b) and 4.15 (c) show the cross-section of correlation peak in the time delay and frequency axis. The correct code phase is obtained up to one sample accuracy (out of 50000) and the coarse frequency resolution is clearly 1 kHz by searching +5 to -5 kHz.

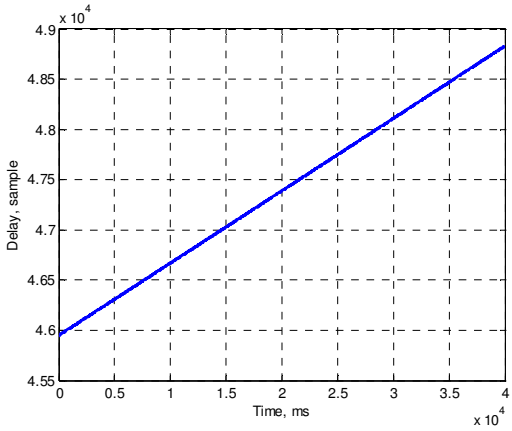

(a) Acquisition, delay

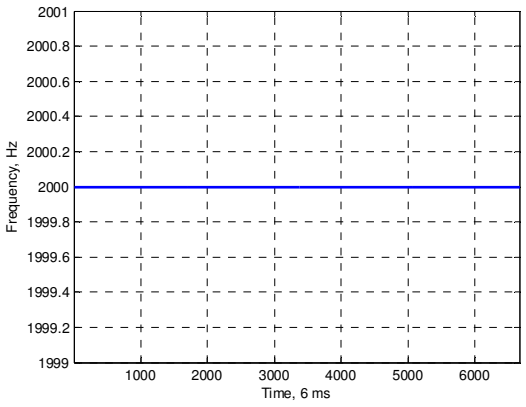

(b) Acquisition, coarse Doppler shift

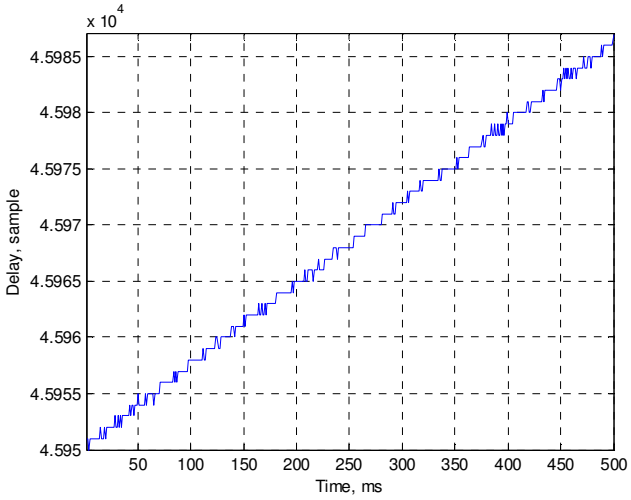

(c) Zoom view of delay

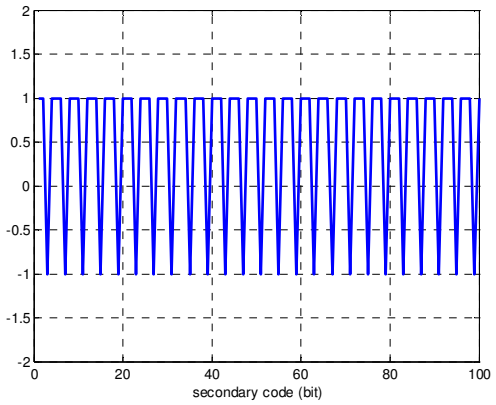

(d) 2nd code on E5b-I

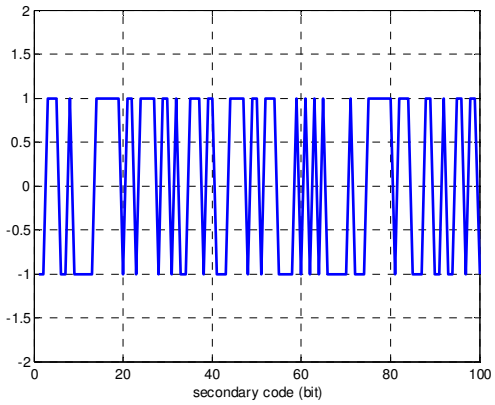

(e) 2nd code on E5b-Q

Figure 4.16: *Acquisition Outputs for 40 s Data*

Figure 4.16 give the coarse estimation of code phase and frequency over 40 seconds. Figure 4.16(a) represents the delay variation estimation obtained for each 1 ms data. The total delay variation is around 3000 samples over 40 seconds. The rate of delay variation is around 75 samples/s, which is equivalent to 1.5 μs/s in this case. Figure 4.16 (b) shows the coarse frequency output estimated by the FFT. The estimated coarse frequency is 2 kHz. Figure 4.16(c) zoom view of delay variation over the first 0.5 second. It is clearly seen that delay variation changes forwards and backwards randomly on the consecutive data. This is mainly due to clock drift and noise in the receiver. Figures 4.16(d) and 4.16(e) show the extracted secondary codes on E5b-I and E5b-Q respectively. It repeats every 100 ms for E5b-Q and every 4 ms for E5b-I. The tracking program could not apply for over 1 ms long data until the secondary code has been removed.

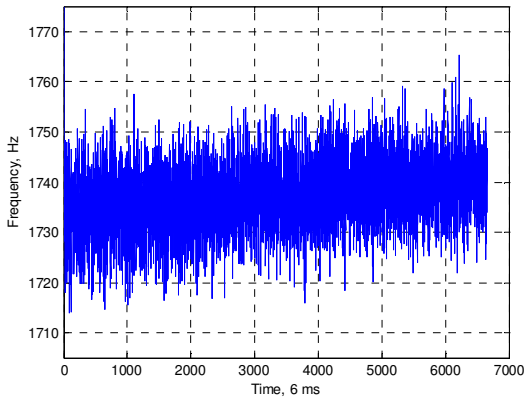

(a) Tracking, fine Doppler shit

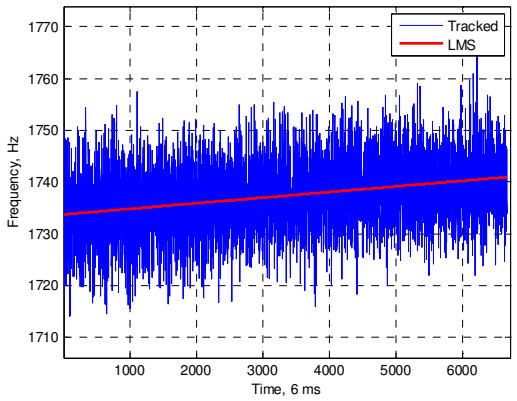

(b) Tracking, fine Doppler shit

Figure 4.17: *Doppler Shift Tracking Outputs*

Figure 4.17 shows the fine frequency tracking results, over 40 seconds, estimated by the block adjustment of synchronising signal algorithm. It generates a frequency output every 6 ms data. From Figure 4.17(a) it is seen that the range of frequency variation is around 30 Hz. This is because of low SNR at the input of tracking program. Figure (b) also gives a LMS result on the tracked frequency. It has a linear change at the rate of 0.2 Hz/sec, which is within our analytical prediction.

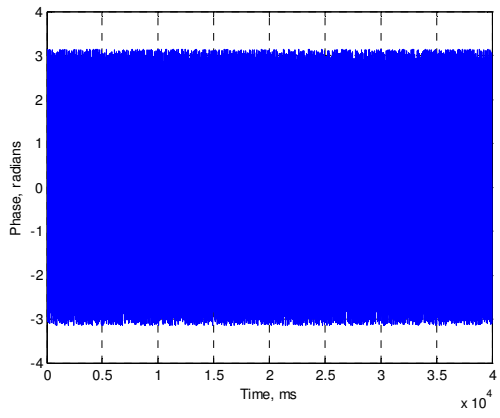

(a) Phase tracking output

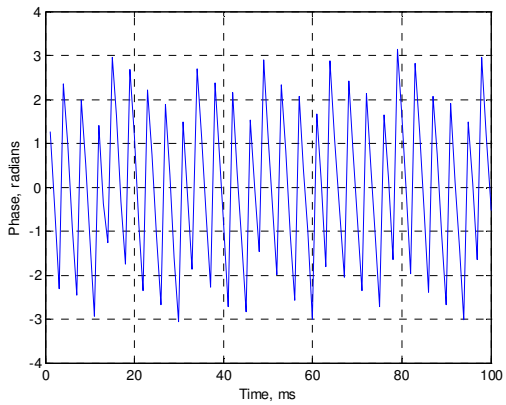

(b) Zoom view of phase

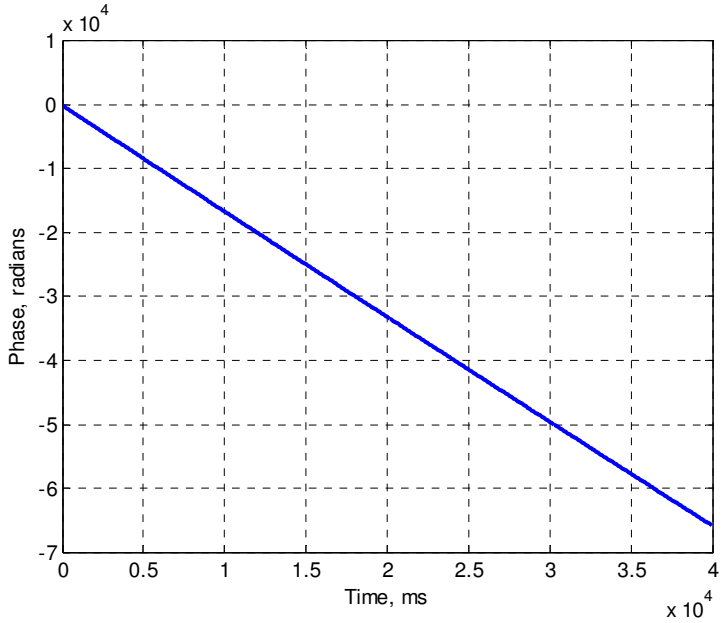

(c) Unwrapped phase

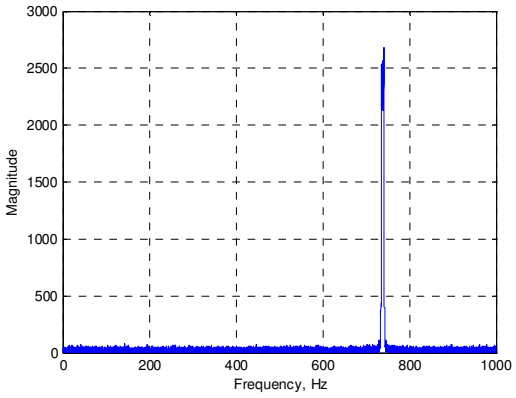

(d) Doppler spectrum from phase

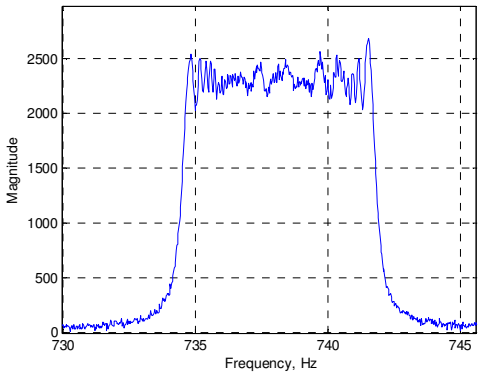

(e) zoom view of Doppler spectrum from phase

Figure 4.18: *Phase Tracking Outputs*

Figure 4.18 give the tracked phase output over 40 seconds. Figure 4.18(a) represents the phase variation estimation obtained for each 1 ms data, with zoom version in Figure 4.18(b). The tracked phase is wrapped within $+\pi$ and $-\pi$. Figure 4.18(c) gives the unwrapped result. Figures 4.18(d) and 4.18(e) show the frequency spectrum

reconstructed using the tracked phase. It covers the frequency ranging from 734 to 742 Hz; it need to be shifted by 1 kHz to corresponding to the actual Doppler shift shown in Figure 4.17. And also the passband of spectrum is having some fluctuation due to errors caused by noise. Ideally it should have a flat passband for a LFM signal.

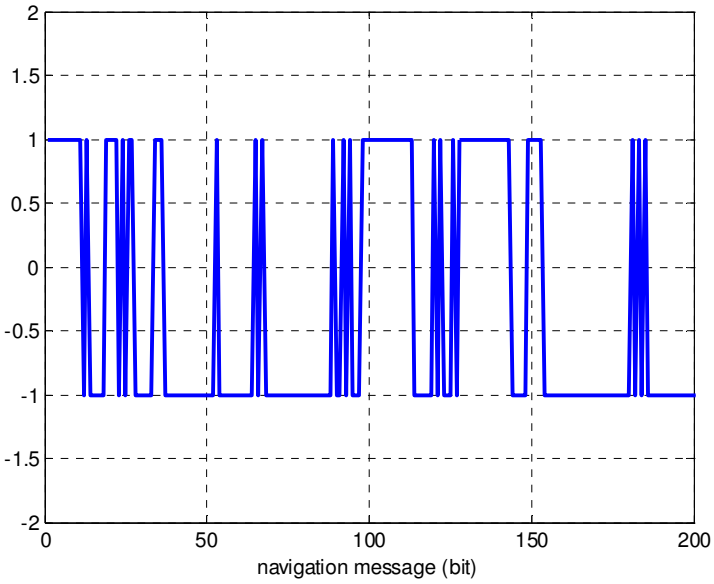

Figure 4.19: *Decoded Navigation Message*

Figure 4.19 shows the recovered navigation message from E5b-I. It plots the first 200 bits only, with each bit lasting 4 ms. This result confirms the proper functioning of our algorithm.

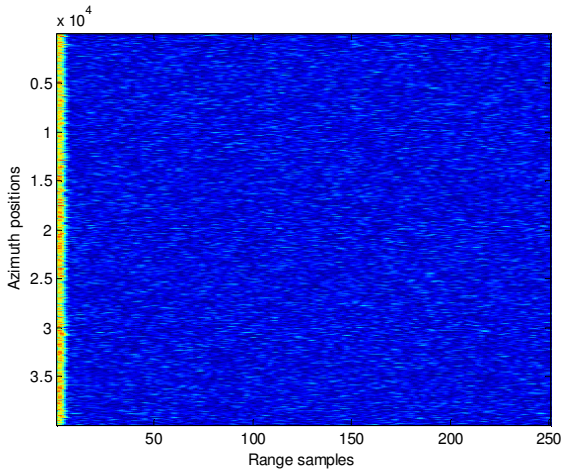

(a) Range compression of heterodyne data

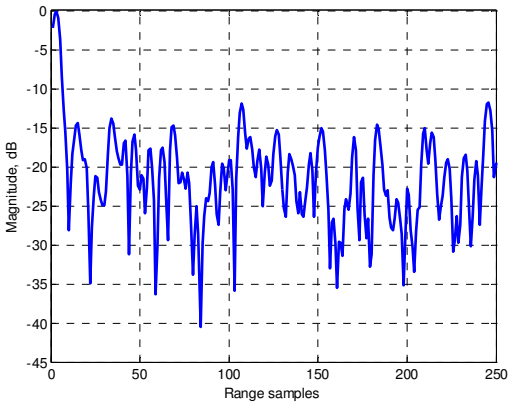

(b) Range cross-section

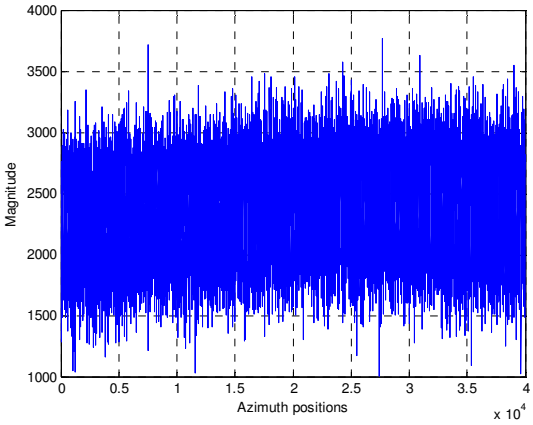

(c) Azimuth signal

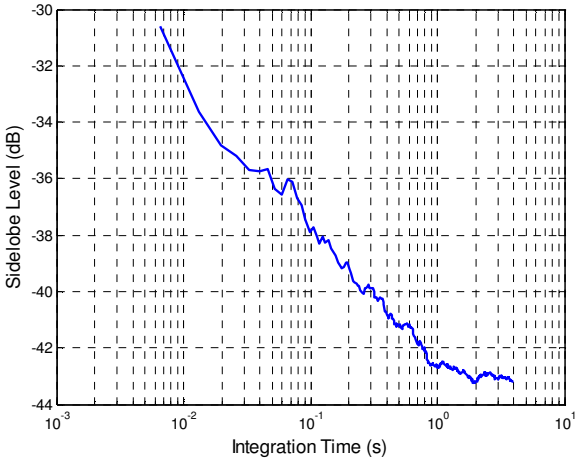

(d) the RMS sidelobe vs. the integration time

Figure 4.20: *Range Compression Results*

Figure 4.20 represents the correlation obtained between the proposed local reference shown in Figure 4.12, and the input heterodyne channel signal. For these results, only delay and frequency variation has been added to the local reference, without the phase information. It is seen that the algorithm gives a good compensation of delay variation and all correlation peaks are shifted to the first range bin. It confirms our tracking results and local reference generation method. Figures 4.20(b) and 4.20(c) give the cross-section in the range and azimuth axis for the first range bin. Figure 4.20(d) shows the RMS sidelobe versus the integration time. The maximum integration time is the duration of the aperture synthesis. This analysis would show that the synchronisation is valid over the entire image formation duration. It demonstrates that the proposed algorithm is functioning satisfactorily and good enough over the entire integration interval.

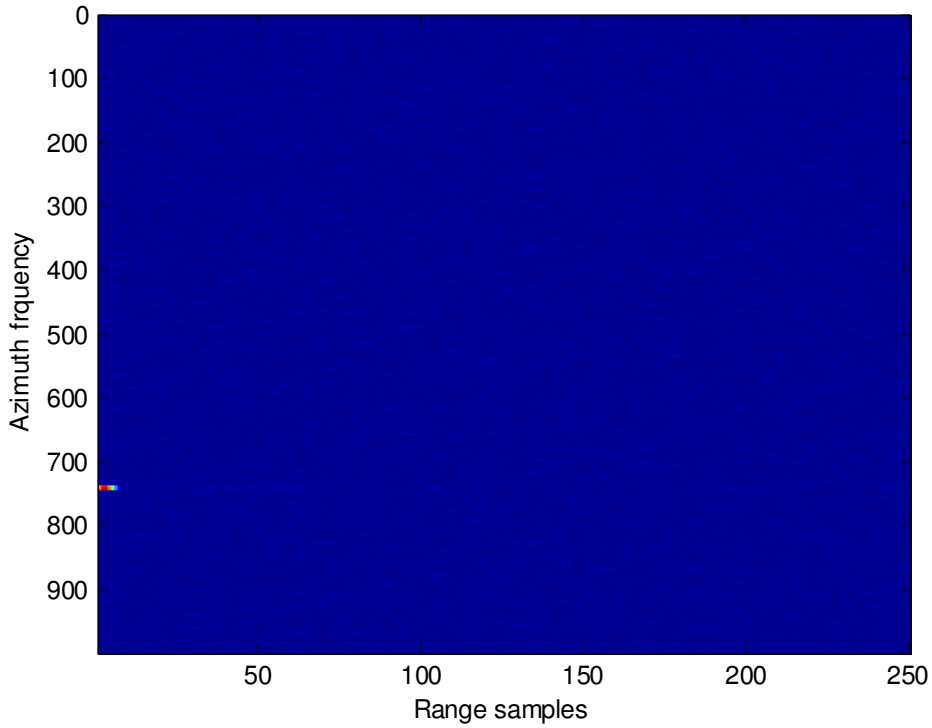

(a) FFT output

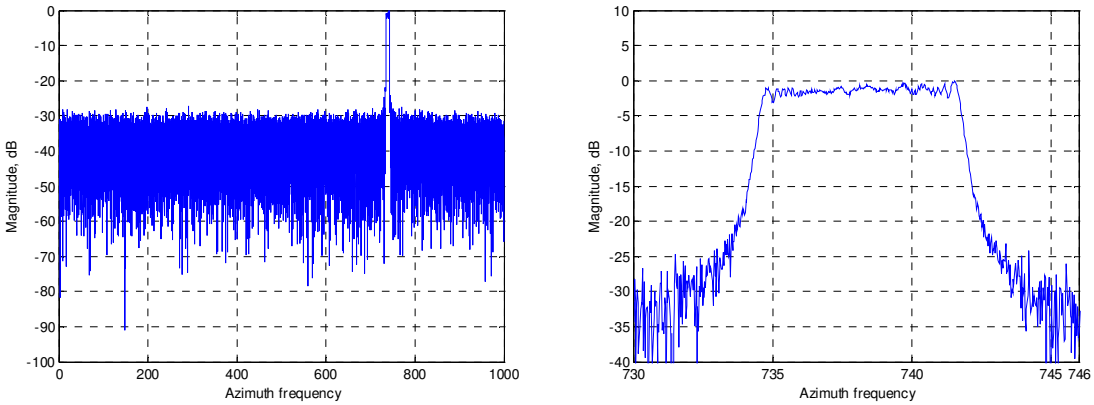

(b) Azimuth cross section (c) zoom view

Figure 4.21: *FFT of Range Compression Results*

Figure 4.21 represents the FFT output of range compression results. Figures 4.21(b) and 4.21(c) show the azimuth cross-section of the FFT output and its zoomed view. The spectrum of azimuth signal at the first range bin is coincident with the Doppler spectrum shown in Figure 4.18 (e). This again confirms the proper functioning of the proposed synchronisation and range compression algorithms.

4.5 Summary

In this chapter we discussed the synchronisation issues specifically for SS-BSAR using GNSS satellites. The synchronisation algorithm was verified using computer modelling and experimentation. The performance of the algorithm was also analysed in terms of varying signal dynamics and in the presence of noise.

It was pointed out that one of the key advantages of using GNSS transmitters is that it is possible to locally generate an ideal noiseless reference signal, as the transmitted pseudorandom noise codes are fully known. However, this is not possible when using other transmitters of opportunities (such as ASTRA, Iridium etc), as the transmitted information is random. The other advantage of a locally generated reference signal is that one can reject interference from other satellites. It was suggested that for GNSS signals the block adjustment of synchronising signal algorithm can be applied to track the parameters, such as fine delay and Doppler variation. The proposed range compression algorithm uses a locally generated reference signal modulated with tracked parameters, secondary codes and navigation messages. Experimental results of the synchronisation and range compression algorithm were presented and explained.

References

1. Willis, N.J., *Bistatic Radar*. 1991: Artech House.
2. Autermann, J.L., *Phase stability requirements for a bistatic SAR*, in *IEEE National Radar Conference*. 1984. p. 48 - 52.
3. Krieger, G. and M. Younis, *Impact of oscillator noise in bistatic and multistatic SAR.* Geoscience and Remote Sensing Letters, IEEE, 2006. **3**(3): p. 424-428.
4. Wang, W.Q., *GPS-based time and phase synchronization processing for distributed SAR.* IEEE Trans. Geosci. Remote Sens., 2009. **45**(3): p. 1040-1051.
5. Nies, H., O. Loffeld, and K. Natroshvili, *The bistatic aspect of the TanDEM-X mission*, in *Geoscience and Remote Sensing Symposium IEEE International*. 2007. p. 631 - 634.
6. Lopez-Dekker, P., et al., *Phase Synchronization and Doppler Centroid Estimation in Fixed Receiver Bistatic SAR Systems.* Geoscience and Remote Sensing, IEEE Transactions on 2008. **46**(11): p. 3459 - 3471
7. Espeter, T., et al., *Synchronization techniques for the bistatic spaceborne/airborne SAR experiment with TerraSAR-X and PAMIR*, in *Geoscience and Remote Sensing Symposium, 2007. IGARSS 2007. IEEE International* 2007. p. 2160 - 2163.

8. Espeter, T., et al., *Progress of Hybrid Bistatic SAR: Synchronization Experiments and First Imaging Results*, in *Synthetic Aperture Radar (EUSAR), 2008 7th European Conference on* 2008. p. 1 - 4.
9. Tsui, J.B., *Fundamentals of Global Positioning System Receivers: A software Approach*. 2000: John Wiley & Sons Inc.
10. Cherniakov, M., et al., *Bistatic Synthetic Aperture Radar with Emitters of Opportunity*. 2006, Unversity of Birmingham: Birmingham.
11. Borre, K., et al., *A Software-defined GPS and Galileo Receiver - A single-Frequency Approach*. 2007, Boston: Birkhauser.
12. Peterson, R.L., *Introduction to Spread Spectrum Communications*. 1995: Prentice Hall.
13. *Galileo Open Service Signal In Space Interface Control Document*. 2006, European Space Agency / Galileo Joint Undertaking.

Chapter 5 Experimental Hardware

5.1 Overview

To confirm system feasibility and investigate the system performance of the proposed SS-BSAR, experimentation methodologies have been proposed and a set of experiments have been planned and executed for real data collection. For these purposes, appropriate radar hardware and a receiver have to be designed and built.

This chapter presents a description of the hardware involved in the SS-BSAR experiments. The main experimental hardware is:

- Antennas and front-end, including the heterodyne channel antennas, the radar channel antennas, an antenna for a GPS receiver, and the RF front-ends attached to the antennas.
- A radar receiver with three receiving channels, which can be modified to receive GLONASS L1 signals or Galileo E5a/b signals respectively.
- A data acquisition subsystem, consisting of one six-channel ADC, a sampling clock, data acquisition card, and host PC.
- Other subsystems, including a power supply unit, two frequency synthesizers used as a local oscillator and one commercial dual-frequency differential GPS/GLONASS receiver to store the platform's position information.

In the following sections, the different requirements will be analysed for the heterodyne channel antenna and the radar channel antenna. An RF front-end design is compared

with different arrangements. It is suggested that the architecture of the radar receiver uses two stage down-conversion to collect complex data with in-phase and quadrature (I-Q) channels. In order to maximise the dynamic range of the ADC the total required gain for the amplification chain is calculated based on Galileo E5 signal reception. The impact of the quantization scheme and the sampling frequency will also be discussed; and different hardware testing set-ups will be introduced and discussed in section 5.3 with extensive testing results included in the Appendix.

5.2 Experimental Hardware Development

5.2.1 Antennas and Front-end

For the proposed SS-BSAR system, two receiving channels will be used, for the direct signal synchronisation and the reflected signal imaging. Two antennas will be required, as one looks at the sky and the other one points to the ground target area. There are different requirements for these antennas due to the different purposes.

First of all, a right-hand circularly polarized (RHCP) antenna will be used in the heterodyne channel (receiving a direct GNSS signal) and a left-hand circularly polarized (LHCP) antenna will be used in the radar channel (receiving a reflected signal from the target area) to decrease the level of direct path interference from the satellite. This is because all GNSS satellites are using a right-hand circularly polarized antenna for navigation signals transmission.

Ideally, the heterodyne antenna should cover a wide spatial angle to receive the maximum number of signals. The suggested requirement is to receive signals from all GNSS satellites about 10 degrees above the horizon. The reason behind this is to have the flexibility to form the optimal bi-static/multi-static topology and the capability for advance SAR applications, such as single pass interferometry and radiogrammetric 3-D surface mapping. Furthermore, the antenna should have a uniform gain over this very wide spatial angle. If an antenna has a large gain variation from zenith to azimuth, the strength of the received signals will not be consistent. In a CDMA system like GNSS, it is desirable to have comparable signal strength from all the received signals. Otherwise, the strong signals may interfere with the weak ones and make it difficult to detect them. Also, the heterodyne channel antenna should reject or minimise the multipath effect. It is caused by reflecting from the ground, or buildings, that add to the direct path signal. The reflection of a right-hand circularly polarized signal is a left-hand circularly polarized signal. A right-hand circularly polarized receiving antenna has a higher gain of the signals received from the satellites, and a lower gain for the reflected signals because the polarization is in the opposite direction. One common multipath effect is the reflection from the ground below the antenna. Therefore, an ideal heterodyne channel antenna should have a low back lobe. Some techniques such as a specially designed ground plane can be used to minimise the multipath from the ground below.

For the radar channel antenna in the SS-BSAR, its selection is mainly dependent on the platform restriction and the imaging requirements. Its beamwidth is decided by the SAR operation mode and the size of the target area. It could be a wide beamwidth antenna

covering the whole imaging area or a narrow beamwidth antenna for a strip-map SAR mode. Both mechanically steered antennas and electronic phase arrays can be used depending on the platform and other requirements. Its gain will then be limited by its size and beamwidth. One thing to notice is that there is no need for antenna footprint synchronisation between the transmitting antenna on the GNSS satellite and the receiver's radar channel antenna. It is simply because all GNSS signals are transmitted by the global beam and cover the entire part of the earth's surface that is visible to the satellite.

(a) Antennas: patch antenna, helix antenna, GNSS antenna

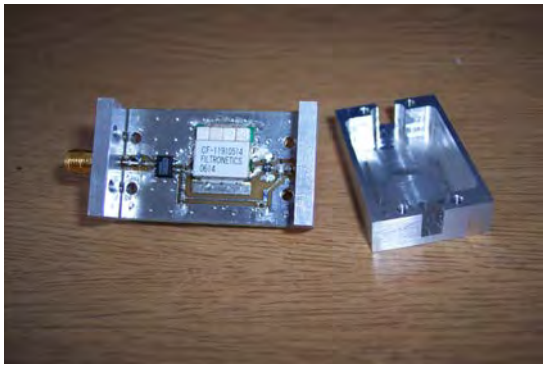

(b) RF front-end

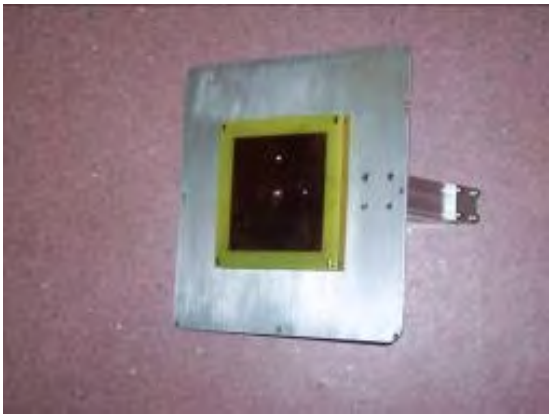

(c) Flat PCB patch design

(d) Heterodyne channel antenna

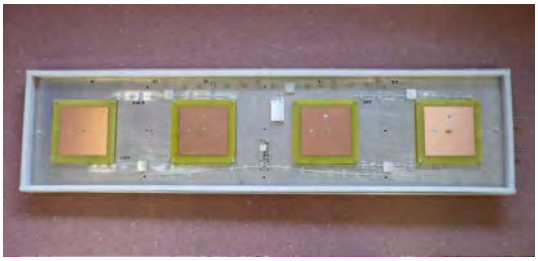

(e) Four element antenna array (radar channel antenna)

Figure 5.1: *Antennas and RF Front-end*

One common antenna design to receive a circular polarized signal is a spiral helix antenna, which inherently has a wide bandwidth. Another popular design is a microstrip antenna, which is sometimes referred to as a patch antenna. The advantage of the patch antenna is its simplicity and small size. Figure 5.1 displays the antenna selected and designed for the SS-BSAR using GNSS experiments, and Table 5.1 below gives its main parameters. More specifications can be found for the displayed antennas in Appendix C, and the application of these antennas will be discussed in Chapter 6 together with the experimental set-up description.

Table 5-1: *Antenna Parameters*

Antenna	Gain (dBi)	Beamwidth
Spiral helix antenna	16	30^{o}x30^{o}
Flat PCB patch antenna	9	65^{o}x66^{o}
GPS antenna	6	Omni-directional
Patch antenna array	14	65^{o}x15^{o}

In this chapter, an RF front-end refers to the first block connecting between the antenna and the long cable to the receiver. It can have one, or two, low noise amplifier (LNA) stages and one bandpass filter. There are many different ways to build an RF front-end.

The two important factors concerned are the total gain and filter installation. The first component following the antenna can be either a filter or an amplifier. Both arrangements have advantages and disadvantages. If the antenna is integrated with an amplifier, the first component after the antenna is the amplifier. Bandpass filters can be connected first and used to reject out-of-band signals and limit the noise bandwidth, but they would add insertion loss. If I-Q channels are used, filters may increase the difficulty of amplitude and phase balancing.

In general, the noise figure of a receiver can be expressed as (similar to noise temperature shown in equation 2.12)

$$F = F_1 + \frac{F_2 - 1}{G_1} + \frac{F_2 - 1}{G_1 G_2} + \cdots + \frac{F_N - 1}{G_1 G_2 \cdots G_N} \tag{5.1}$$

where F_N and G_N (i=1,2, …N) are the noise figure and gain of each individual component in the RF chain. If the amplifier is the first component, the noise figure of the receiver is low and is approximately equal to the noise figure of the first amplifier, which can be less than 2 dB. The potential problem with this approach is that strong signals in the bandwidth of the amplifier may drive it into saturation and generate spurious frequencies. If the first component is a filter, it can stop out-of-band signals from entering the input of the amplifier. However, the insertion loss of a narrowband filter is usually relatively high, about 2-3 dB. The received noise figure will be about 2-3 dB higher than the previous arrangement.

For the RF front-end design shown in Figure 5.1 (b), it has a first stage LNA (AM50-0002, 1.15 dB noise figure with 27 dB gain), followed by a RF bandpass filter (centre frequency at 1191 MHz with 51 MHz bandwidth for Galileo E5 reception) and a second stage RF amplifier with 15 dB gain. Its testing results and the datasheet for each component can be found in Appendix C.

5.2.2 Experimental Radar Receiver

The external views for the experimental hardware are shown in the figure below. All hardware and subsystems are installed into three standard 19-inch racks within one flight case. The top rack hosts the data acquisition subsystem with an output interface to a PC, the middle one is the microwave receiver, and the GPS receiver and other subsystem is inside the bottom rack. In the following sections, the block diagram of each rack will be provided and a description of it will be given.

(a) Front view, inputs to three receiving channels and data interface to PC

(b) Rear view, three pairs I/Q outputs and other inter-connection ports

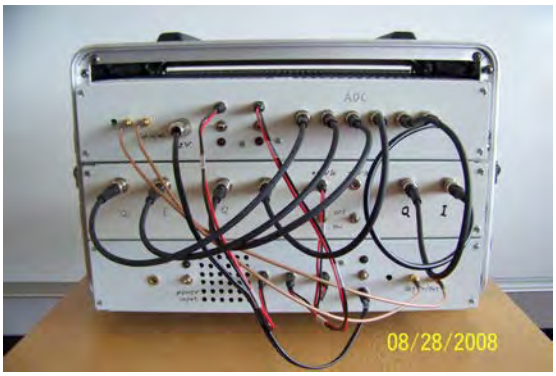

(c) Rear view with all ports connected

(d) Fully connected microwave receiver with a laptop for data collection

Figure 5.2: *Experimental Radar Receiver*

The function of a radar receiver is to amplify the radar echoes and to filter them in a manner that will provide the maximum discrimination between the desired echoes and undesired noise and interference. This microwave receiver (Figure 5.3) consists of three identical receiving channels: the heterodyne channel (HC), the radar channel (RC) and the spare channel (SC). A power supply and local oscillator interface is also included. The third channel (SC) is a backup and will be brought into use while conducting the interferometry experiment.

The proposed design for the microwave receiver is a two-stage down-conversion, as mentioned earlier. All three channels are designed to receive the Galileo E5 signal and convert it to baseband in-phase (I) and quadrature (Q) outputs. However, these channels could be modified to receive the GLONASS L1 signal as well. Details of this can be found in document [1].

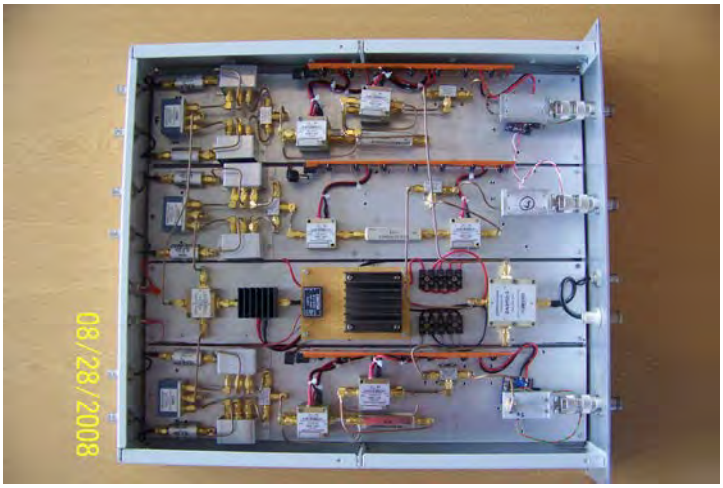

Figure 5.3: *Photo of Microwave Receiver*

Each receiving channel of the microwave receiver is divided into three parts (block diagram shown in Figure 5.4): the radio frequency (RF) part, centred on the E5 carrier frequency 1191.795 MHz, intermediate frequency (IF) part, centred on 140 MHz, and the baseband part with 10 MHz bandwidth. See Appendix G for a list of all the components used and the specifications.

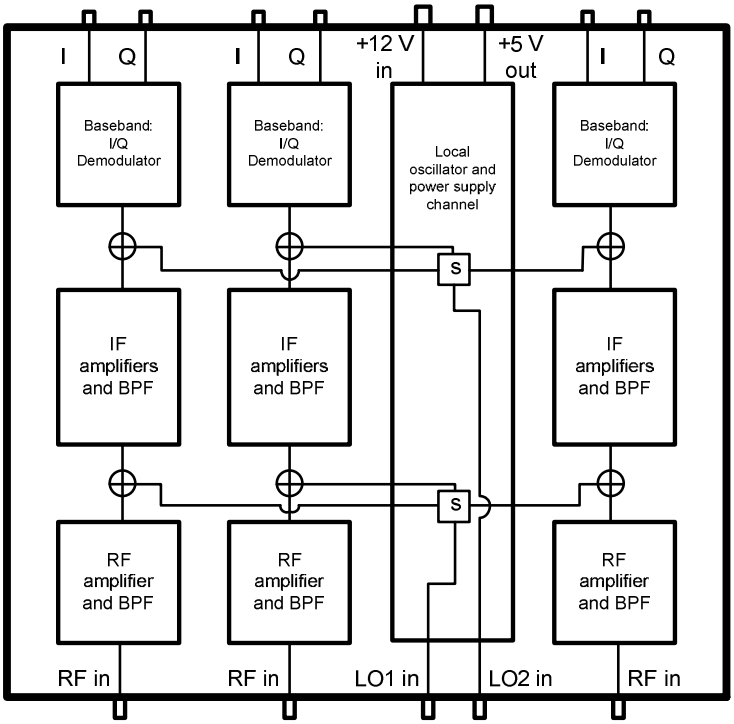

Figure 5.4: *Microwave Receiver Block Diagram*

The RF part includes a low noise amplifier (LNA1, the same as the one used in the front-end) connected to the front-end and the antenna through a coaxial cable, and a band-pass filter (BPF1), to suppress the strong interference from adjacent-frequency satellites. The IF part consists of a 140 MHz band pass filter (BPF2), four cascaded IF amplifiers (A1-A4) with a total estimated gain of 100 dB, and a 10 dB attenuator between the 3rd and 4th IF amplifier to avoid the last amplifier entering into the saturation and to improve the impedance matching between the components. The baseband part has an I/Q demodulator and two low pass filters (LPF1).

The received signal, after the initial RF amplification, is shifted to an intermediate frequency by mixing with a local-oscillator (LO1) frequency. Most amplification (~100

dB gain) will be applied at the IF stage. Not only is amplification at IF less costly and more stable than at microwave frequency, but also the wider percentage bandwidth occupied by the desired signal simplifies the filtering operation. In addition, the receiver can vary the LO1 frequency to follow any desired tuning variation of the transmitter without disturbing the filtering at IF. Ideal mixers in a receiver act as multipliers, which produce an output that is proportional to the product of the two input signals. Except for the effect of nonlinearity and unbalance, these mixers only produce two output frequencies, which are equal to the sum and the difference of the two input frequencies. After IF stage amplification and filtering, the IF signal is applied to a splitter and the resulting signals are mixed with two local oscillator (LO2) signals that are 90º apart in the phase. This process produces in-phase and quadrature output signals. After a low pass filter, the signal will be digitized and transferred to the computer hard disk through the data acquisition subsystem. Figure 5.5 shows the block diagram of the full receiving chain for two channels. It can be seen that two local oscillators, LO1 and LO2 are phase locked with the common frequency reference. This is critical for maintaining the coherence between the heterodyne channel signal and the radar channel signal.

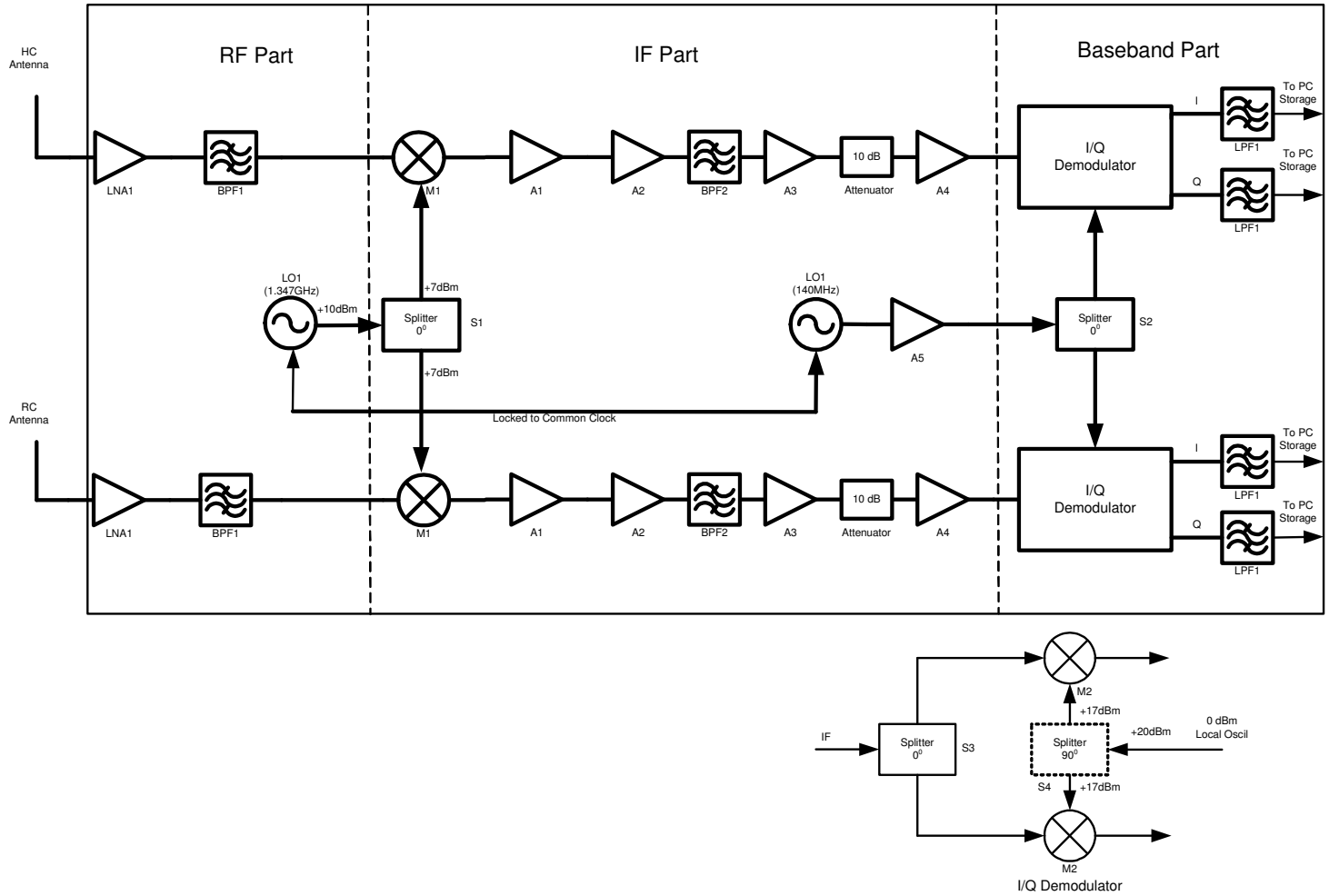

Figure 5.5: *Microwave Receiver Receiving Chain (2 channels shown)*

In this section the signal level and the required amplification will be discussed. The E5 signal level at the input of the front-end should be at least -155 dBW (-125 dBm), as discussed in Chapter 2. The available thermal noise power at the input of a receiver is

$$N_i = kT_sB \tag{5.2}$$

where k is the Boltzmann's constant, T_s is the temperature in Kelvin, B is the bandwidth of the receiver noise in hertz, and N_i is the noise power in watts. The thermal noise at room temperature where T_s=290 K expressed in dBm is -114 dBm/MHz ($10\times\log_{10}(kT_s)$, dBW/Hz).

For the heterodyne channel, the input to the receiver is an antenna pointing at the sky; the thermal noise is lower than room temperature, such as 50 K.

For the E5a or E5b signal, the null-to-null bandwidth is about 20.46 MHz. But the BPF1 (indicated in Figure 5.5) has a bandwidth of 51 MHz and in order for it to have the capability of receiving the full E5 (E5a and E5b) signal, the noise figure of LNA1 is 1.15 dB. Thus, the noise floor of the microwave receiver is at -97 dBm approximately. Supposing that the E5 signal is at -125 dBm at the input of RF front-end, the signal is 28 dB below the noise floor. One cannot expect to see the signal directly in the collected data.

The amplification needed depends on the analogue-to-digital converter (ADC) used to digitize the I-Q outputs. A simple rule is to amplify the signal to the maximum range of the ADC. However, this approach should not be applied to the GNSS signal, because the

signal is below the noise floor. If the signal level is brought to the maximum range of the ADC, the noise floor will saturate the ADC. Therefore, in this design the noise floor, rather than the signal level, should be raised close to the maximum range of the ADC. The maximum voltage to exercise the level of the ADC is about 3.8 V (LT1715) and the corresponding power is

$$P = \frac{3.8^2}{50} = 0.2888 \qquad watt = 24.6 \qquad dBm \tag{5.3}$$

It is assumed that the system has a characteristic impedance of 50 ohm. A simple way to estimate the gain of the amplifier chain is to amplify the noise floor to this level; thus, a net gain of about 122 dB (24.6+97) is needed. Since in the RF chain there are filters, mixer, and cable loss, the insertion loss of these components must be compensated with additional gain. The net gain must be very close to the desired value of 122 dB. Too low a gain value will not activate all the possible levels of the ADC. Too high a gain will saturate some components of the ADC and create an adverse effect.

For the receiving channel in Figure 5.5, the total amplification gain is 123 dB with 30 dB loss from mixers, filters and the attenuator. So the net gain is around 93 dB. However, with a 41 dB gain from front-end directly attached to the antenna, the total net gain is around 134 dB for the whole receiving chain. Please note that the calculation here does not include any cable loss, particularly the long cable used to connect the antenna with the receiver. The actual output level of the microwave receiver is around 700-800 mV which is enough to exercise the selected ADC.

There is one disadvantage that should be noted. For the I-Q demodulator, the 90-degree phase shift is introduced in the oscillator block. For a wide band receiver, the I-Q approach can double the input bandwidth with the same sampling frequency. However, the amplitude and phase of the two outputs are difficult to balance accurately, and the phase history of the input signal is vital for SAR image formation and needs to be measured accurately.

5.2.3 Data Acquisition Subsystem

Through the microwave receiver, the input signal is down converted into I-Q channels. The data collected through this approach are complex and the two sets of data are often referred to as real and imaginary. Since there are two channels, the Nyquist sampling is equal to the bandwidth of the input signal.

As discussed previously, the Galileo E5 signal is a CDMA signal. The dynamic range of a Galileo receiver need not be very high. An ADC with a few bits is relatively easy to fabricate and may operate at a high frequency. Another advantage of using fewer bits is that it is easier to process the digitized data. The disadvantage of using fewer bits is the degradation of the SNR. Spilker [2] indicated that 1-bit ADC degrades the SNR by 1.96 dB and a 2-bit ADC degrades the SNR by 0.55 dB. Chang [3] claims that the degradation is due to the number of bits of the ADC and is a function of input SNR and sampling frequency. A low SNR signal sampled at a higher frequency causes less degradation in a receiver. The GNSS signal should belong to the low SNR case because the signal is below the noise. At a Nyquist sampling rate, the minimum degradation is

about 3.01 dB and 0.72 dB for 1- and 2- bit quantizers, respectively. At five times the Nyquist sampling rate, the minimum degradation is 2.18 dB and 0.6 dB for 1- and 2- bit quantizers, respectively.

Although the sampling frequency discussed in this chapter is given a pre-defined mathematical value, the actual frequency used in the hardware usually has limited accuracy. The most important effect of sampling frequency inaccuracy may be the error in the pseudorange (fine code delay) measured, which has been discussed in section 4.3.

For the experimental hardware, the 1-bit quantization scheme is proposed. The purpose built data acquisition subsystem includes three components: an ADC board with six channels, one commercially available data acquisition card and a sampling clock. The ADC board first converts the analogue signal to a digital signal that can be accepted as the input of the data acquisition card. Due to the character of the received analogue signal, which is a pseudo-random sequence buried in noise, it is adequate to divide the voltage range of the signal into two discrete levels and to store it as a binary signal. The serial digital signal is subsequently sampled at a clock rate specified either by an on-board oscillator clock or by an external clock. For our experiments a sampling clock of 50 MHz is used in order to over-sample the Galileo E5a/b signal by a factor of ~5. A higher sampling rate could be used but it would need a high performance ADC and would increase the computation of signal processing significantly. Sampled digits are then transferred to the memory of the data acquisition card using a continuous FIFO mode.

Finally, using the appropriate software, this data stream is recorded on the computer hard disk for further processing. See Appendix E for further detail about this process.

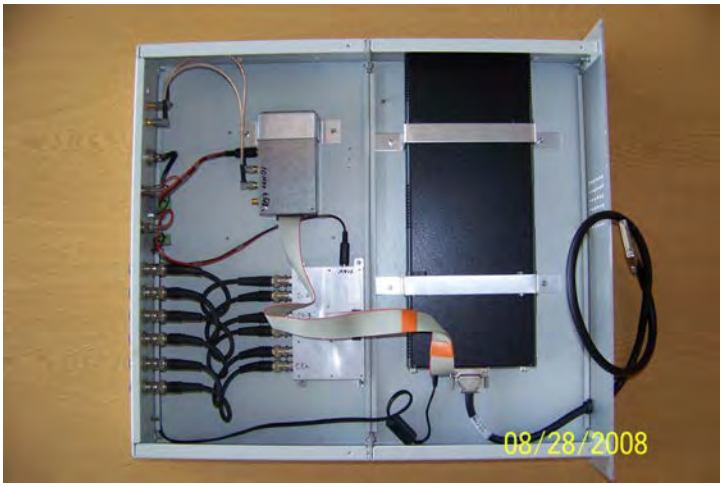

Figure 5.6: *Photo of Data Acquisition Subsystem*

Figure 5.6 above shows the contents of rack holding the data acquisition subsystem. Figure 5.7 below gives its block diagram. A 10 MHz frequency reference is taken out from the sampling clock and used to lock two local oscillators. Hence, the microwave receiver has one common reference, which is an OCXO with a frequency stability of ± 0.5 ppm. It is equal to the frequency accuracy of ±25 Hz for 50 MHz output.

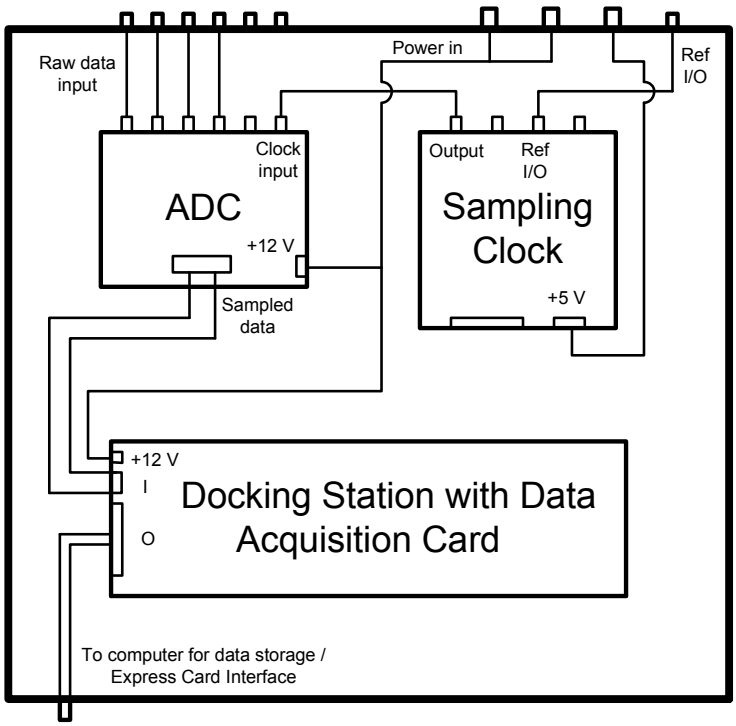

Figure 5.7: *Block Diagram of Data Acquisition Subsystem*

5.2.4 Other Receiver Subsystems

Figure 5.8: *Photo of Other Receiver Subsystems*

Figure 5.8 above shows the contents of bottom rack, which includes a commercial GLONASS/GPS receiver; two frequency synthesizers and power supply units.

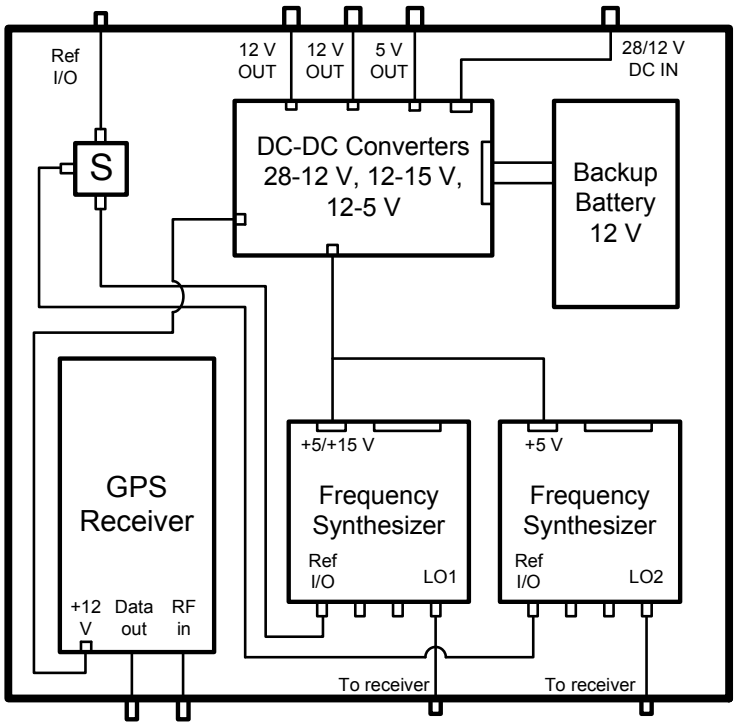

Figure 5.9: *Block Diagram of Other Receiver Subsystems*

Figure 5.9 above gives the block diagram. More details about the hardware in this block can be found in Appendices D and F.

5.3 Experimental Hardware Testing

To ensure proper operation and the collection of good data, all hardware had to be fully tested in the laboratory environment to prove its functionality. A set of testing set-ups will be discussed for antennas, the data acquisition subsystem and the microwave receiver respectively in this section.

5.3.1 Antenna Testing

Ideally the antenna radiation pattern should be measured in an anechoic chamber. However, due to the lack of availability of an anechoic chamber, a set of experiments have been performed in an open space to measure the gain and the beamwidth of the heterodyne and radar channel antennas. Figure 5.10 below shows the experimental set-up for antenna testing.

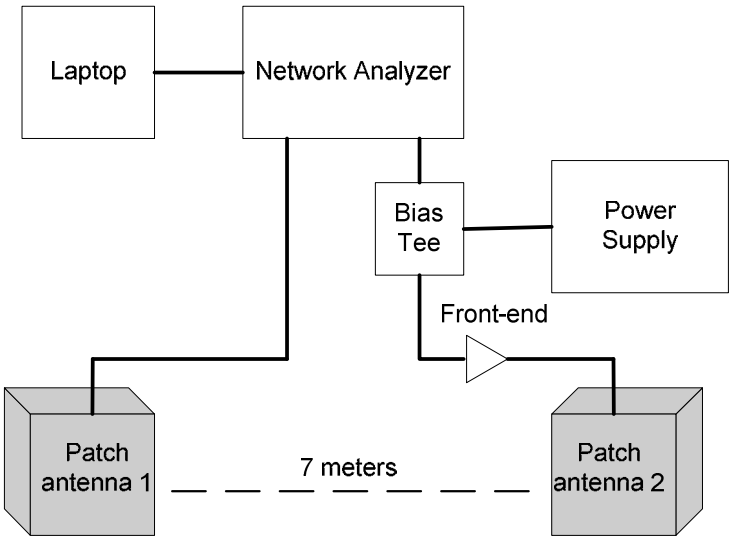

Figure 5.10: *Heterodyne Channel Antenna Testing Set-up*

For heterodyne channel antenna gain, S21 measurements have been made using a network analyser. Two identical patch antennas were installed with a separation distance of 7 metres, one for transmission and the other for reception. The network analyser calibration was carried out first and the input power level was adjusted to set the measured total transmission link gain (propagation loss, antenna gain, losses from cables etc.) to 0 dB.

For the radar channel antenna (4-element array) testing, an additional one-element patch antenna was used for transmission, with the antenna array being used for reception. The phase centres of the two antennas were set to the same height with a separation distance of 8 m. The antenna gain and beamwidth were found by rotating one antenna and taking the maximum and 3 dB readings of the received signal power from the spectrum analyser. The approximate beamwidth was then derived from the angle between the two 3 dB readings.

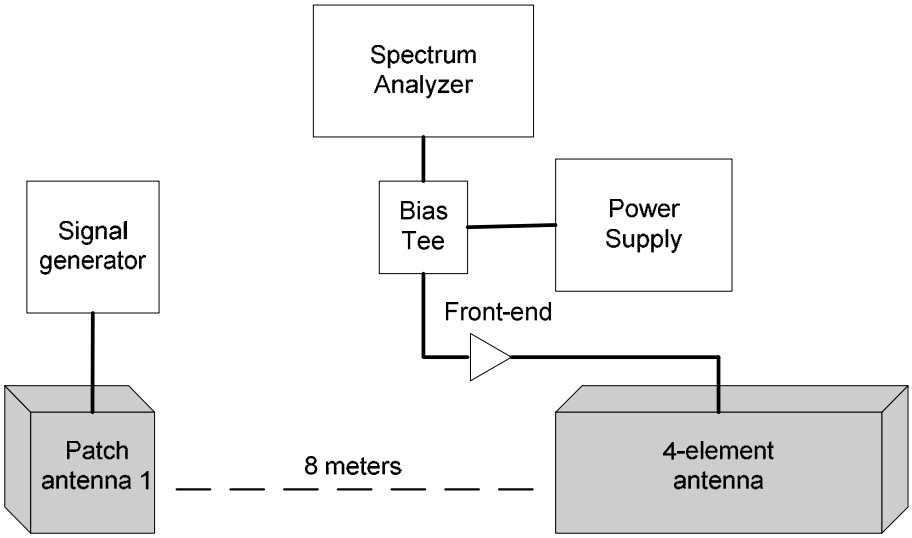

Figure 5.11: *Radar Channel Antenna Testing Set-up*

The testing results are included in Appendix C.

5.3.2 Data Acquisition Subsystem Testing

The data acquisition subsystem test consisted of testing the ADC board and the data acquisition card separately. The assembled subsystem was then tested with a sine wave and a square wave as inputs. The stored data was used to reconstruct the input signal

with MATLAB, allowing checks of the working frequency range and the lowest permissible input amplitude of the subsystem.

Figure 5.12 below shows a simplified test set-up. Preliminary tests start with a test of the ADC only. A 50 MHz signal generated using the satellite imitator is fed directly into the ADC and shown on the oscilloscope. A common clock is used to synchronize the satellite imitator and the sampling clock. Various signal levels have been generated to check the range of input voltages for the ADC.

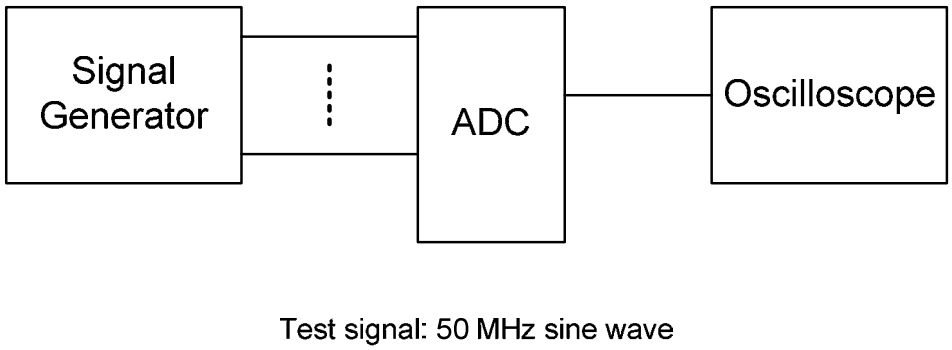

Figure 5.12: *ADC Test Arrangement*

Figure 5.13 below shows the testing setup for the whole data acquisition subsystem. With a baseband 10 MHz PRN sequence generated by an AMIQ generator, this analogue input signal has been converted to digital bits, sampled by the data acquisition card with a 50 MHz clock, and written into files on the hard disk. The stored data has then been divided into multiple files for each channel and the correlation with a locally generated PRN code has been used for a data integrity check.

The results for these two testing set-ups are included in Appendix E.

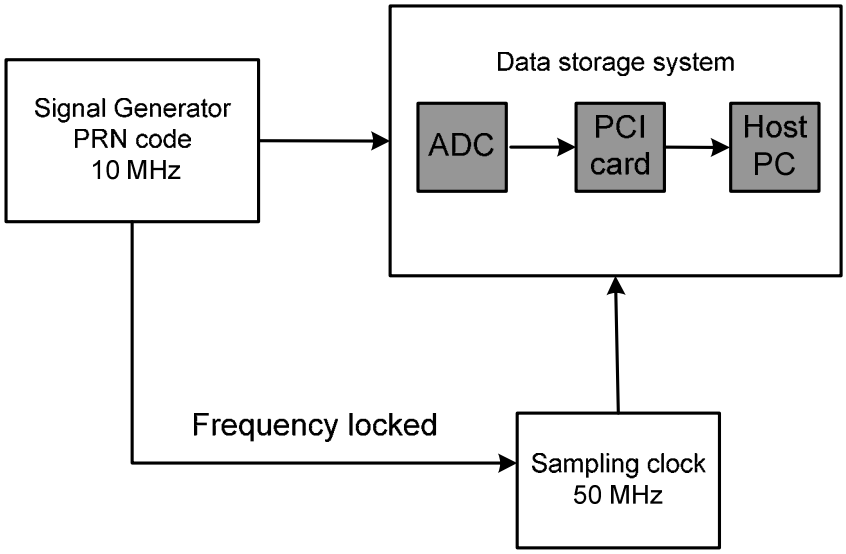

Figure 5.13: *Data Acquisition Subsystem Test Arrangement*

From the tests, we know that the internal interference of the ADC board and the impedance mismatch between the output of the ADC and the input of the PCI card are the potential sources of system degradation on bit error rate. Transmission line effects and environment noise, particularly on the clock and control lines, also require attention. It is advisable to use twisted-pair connections to the data acquisition card, each digital I/O signal line being twisted with a GND line, and to place a shield around the wires.

5.3.3 Experimental Microwave Receiver Testing

To ensure the full functioning of the assembled microwave receiver, the testing process is started from individual components, to connected blocks, and to the full receiving chain with noise and signals at the input. The testing mainly includes:

- RF parts testing: LNA and BPF
- IF parts testing: mixer, amplifier, BPF
- Baseband parts testing: splitter, mixer, BPF
- Test with noise – see noise RMS level on the oscilloscope
- Test with noise – record noise, investigate ACF and CCF
- Test with signals – see signal level (reduced gain scenario) on the oscilloscope
- Test with signals - record signal, investigate ACF, CCF

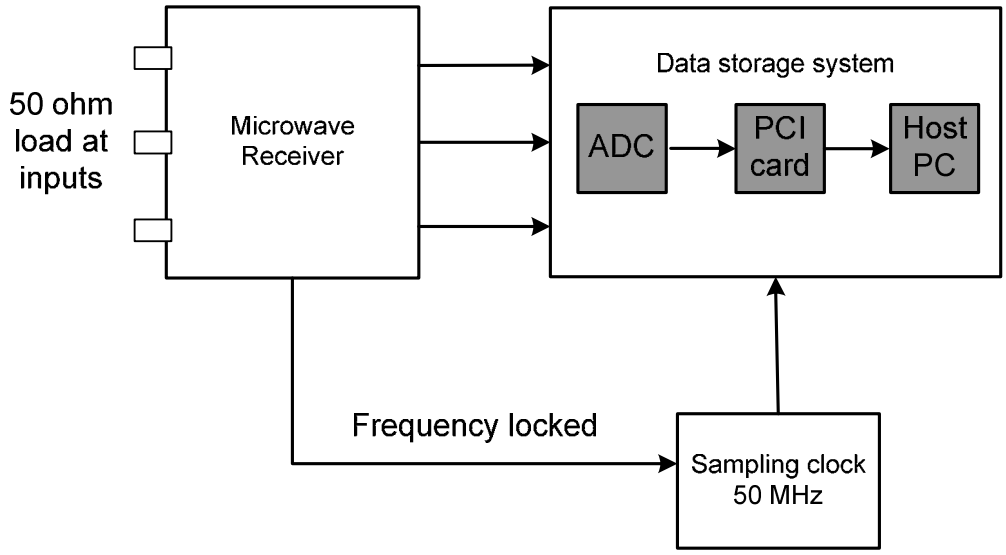

Figure 5.14: *Microwave Receiver Noise Testing*

Figure 5.14 above shows the diagram for receiver noise testing. No input signal will be applied and only a 50 ohm load is connected at the RF input of the microwave receiver. Only the receiver noise will appear at the input of the data acquisition subsystem and will be sampled and stored into the host PC.

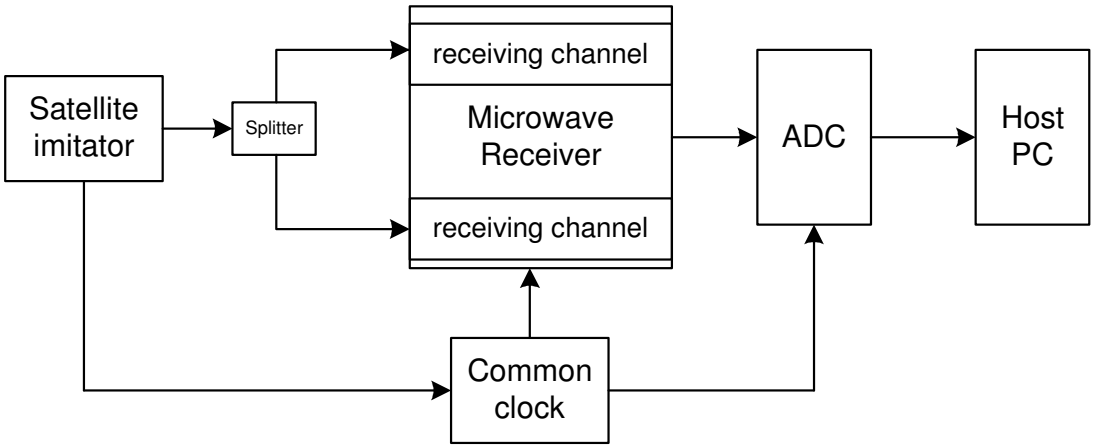

Figure 5.15: *Microwave Receiver Simplified Testing Arrangement*

Figure 5.15 shows a test set-up including the microwave receiver. A locally generated signal with 1191.795 MHz centre frequency and 10 MHz bandwidth will be applied at the RF input of microwave receiver. This is split and fed into the separate channels of the microwave receiver. Both the receiver noise and signal output will appear at the input of the data acquisition subsystem and will be sampled and stored into the host PC. The input signal level is set to higher than the nominal received Galileo E5 signal level as no front-end is used. A common clock is used to synchronize the transmitter and the receiver. Checking the stored data will verify the working of the microwave receiver.

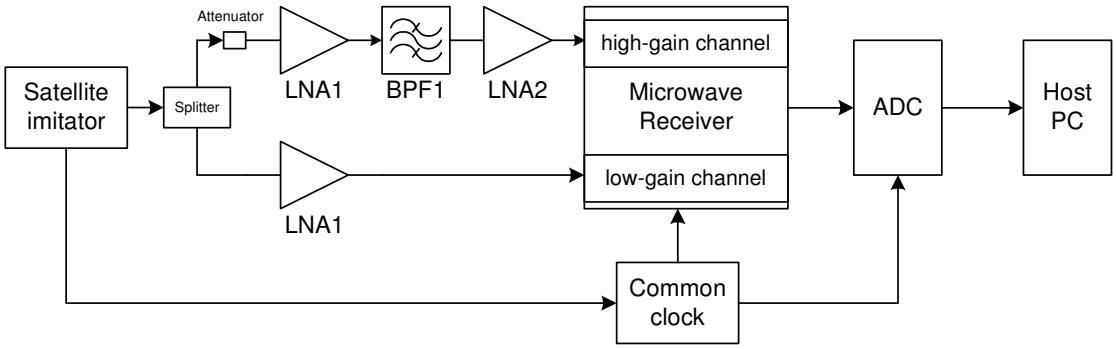

Figure 5.16: *Microwave Receiver Full Channel Testing Arrangement*

Figure 5.16 shows a full experimental testing arrangement, including all the components to be used in the outdoor experiments. A locally generated RF Galileo E5 signal is split, one copy going into a high-gain receiver channel (the radar channel) and the other going into the low-gain receiving channel (the heterodyne channel, with the gain reduced for testing purposes). The front-end is used with a high-gain channel and one low-noise amplifier LNA1 is used with the low-gain channel to compensate for the loss within the coaxial cables, which connect the satellite imitator and microwave receiver. The input signal level is set to the same as the nominal received Galileo E5 signal level. The full set of testing results are included and analysed in Appendix G.

5.4 Summary

This chapter discusses the development and testing of the hardware and the receiver involved in the SS-BSAR experiments. The heterodyne channel antenna should have a broad beam to receive signals from the zenith to the horizon. It should be right-hand circular polarized to reduce the reflected signals. The overall gain of the amplifier chain depends on the input voltage of the ADC. The overall gain is about 120 dB to receive Galileo E5 with the proposed hardware. The input signal is suggested to be down converted to baseband and then digitized, because it is simpler to build than direct digitization. The number of quantization bits is discussed, and one or two bits may be enough for GNSS signal recovery with a small degradation of receiver sensitivity. The impact of sampling frequency accuracy is also discussed. Finally, several experimental testing setups are presented to confirm the functionality of the designed hardware and

receiver. Further details on hardware specifications and the testing results are included in Appendices C-G.

Reference

1. Cherniakov, M., et al., *Bistatic Synthetic Aperture Radar with Emitters of Opportunity*. 2006, Unversity of Birmingham: Birmingham.
2. Spilker, J.J.J., *Digital communication by satellite*. 1995, Englewood Cliffs: Prentice Hall.
3. Chang, H., *Presampling filtering, sampling and quantization effects on the digital matched filter performance*, in *International Telemetering Confrerence*. 1982: San Diego, CA. p. 889-915.

Chapter 6 Experimentations and Parameters Estimation

6.1 Overview

This chapter consists of two main parts. The first part introduces the programme of experimentation, which leads to the ultimate objective of airborne SS-BSAR imaging. Experiment strategies and trials plans are designed to investigate the system feasibility of SS-BSAR using GNSS as a non-cooperative transmitter. The results from these experiments will establish potential system performance and allow the identification of possible applications for SS-BSAR.

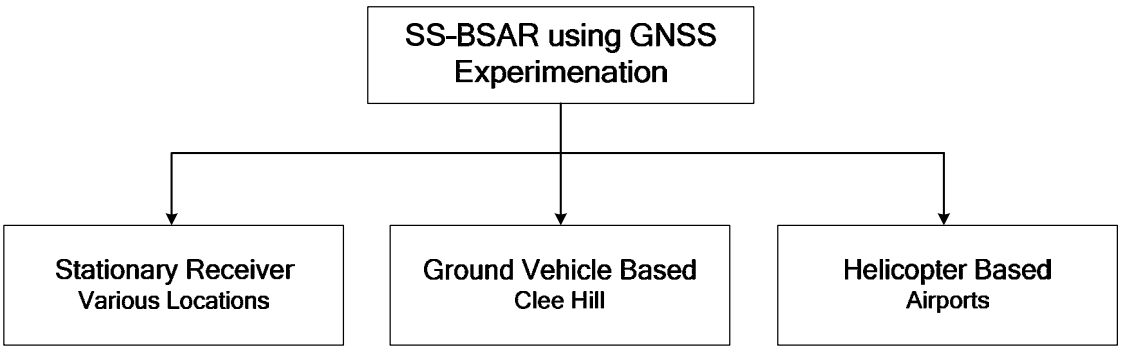

Figure 6.1: *Experimentation Methodology*

Figure 6.1 gives the overall experimentation methodology; it includes three stages: stationary receiver, ground moving receiver and airborne receiver. The program of work starts with the stationary receiver experiments and subsequent experiments with the receiver mounted on the ground vehicle and then an airborne moving platform. It has been established that when, in BSAR, both the transmitter and the receiver are in motion along their own trajectories. These two independent trajectories and associated speed vectors can be replaced with one effective trajectory and speed vector that characterize

the resolution ability of the system. This is an important conclusion that allows us to start experimentation with only the transmitter moving.

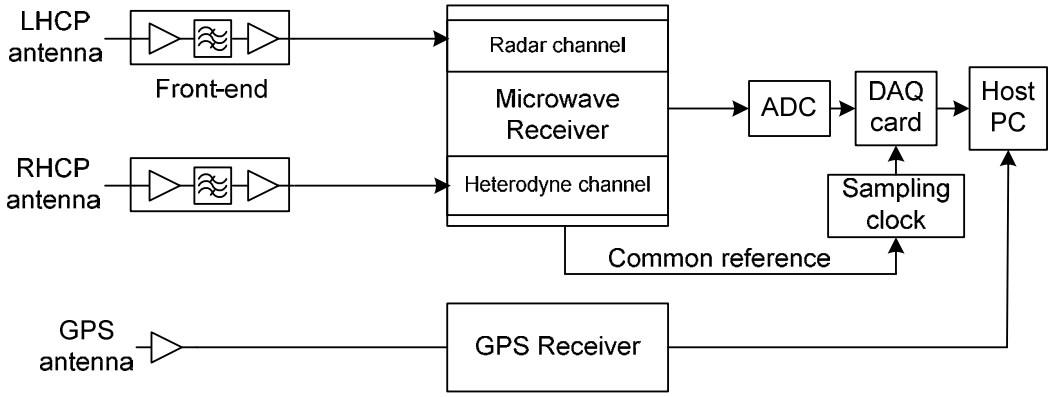

Figure 6.2: *Experimental Set-up for Imaging Data Collection*

Figure 6.2 presents the common experimental set-up using the hardware described in Chapter 5 for data collection. In addition to the radar channel, the receiver includes a navigation channel and a heterodyne channel, which uses an omni-directional antenna pointing at the satellite to receive the Galileo E5a/b signal directly. It allows generation of a synchronized local reference for correlation with echoes reflected from the target area. For the experiments with satellites, the first two Galileo testing satellites, GIVOE A/B have been used as the non-cooperative transmitter. Table 6-1 gives the parameters of one typical ranging signal; the relevant PRN code provides 10.23 MHz bandwidth and hence a range resolution of ~ 15 m (quasi-monostatic case).

Table 6-1: *Ranging Signal Parameters*

Ranging signal	Galileo E5b-Q
	Primary Code (1 ms long)
Carrier frequency	1207.14 MHz
Wavelength	0.2485 m
Chip rate	10.23 MHz
Received power	$3.99\times10^{-14} W/m^2$

The comprehensive experimental methodologies are described and discussed in sections 6.2 to 6.4, for each stage of the experiments. The actual experimental parameters and set-up block diagrams are also given. The potential resolution and signal-to-noise ratio for each experiment will be calculated. Experiment topologies involving a Galileo satellite are divided into quasi-monostatic SAR and bistatic SAR. A corner reflector (CR) has been built as the reference target; a number of houses within the target area will also be considered as radar targets. Separation of these reflectors will demonstrate the resolution ability of the radar and the signal-to-noise ratio obtained with corner reflectors having known radar cross-section may be used for power budget analysis.

The second part (section 6.5) discusses the parameter estimation problem for SS-BSAR using GNSS. Before applying the image formation algorithm to the experimental data, the parameters, such as the transmitter/receiver trajectories, Doppler shift and phase histories need to be estimated with pre-defined accuracy. Practical methods are proposed and compared for the transmitter/receiver parameter extraction and estimation. Two

specific problems, residual Doppler shift and motion compensation are briefly discussed. The parameter estimation results from the real experimental data are presented and discussed at the end of this chapter.

6.2 Stationary Receiver Experiments

6.2.1 Experiment Design

With the successful synchronisation experiments (discussed in Chapter 4), the proposed synchronisation algorithm has been verified. The SS-BSAR imaging experiments can be started. As the experimentation methodology indicated, the first stage is the experiment with stationary receiver and moving satellite. Only satellite motion will contribute the synthetic aperture. The main objective of this stage is to confirm the functionality of the full hardware system, including all antennas and receiving channels. Preliminary testing of the image formation algorithm will be carried out with the data collected, such as range compression and azimuth reference design. To be able to use a relative simple BSAR focusing algorithm, the quasi-monostatic topology is preferred for the stationary receiver experiment.

Figure 6.3 shows the layout of the experimental set-up in the quasi-monostatic SAR configuration. The quasi-monostatic SAR experiment, with a small bistatic angle, is an important stage leading to a more general study of the range resolution and cross-range resolution of bistatic SAR. The arrangement has three sections: the satellite, the receiving system and the observation area. As noted previously, the receiving system

comprises of a radar receiver having a radar channel and a heterodyne channel. Both channels' antennas are installed on the stationary platform, with one looking at the target area and one receiving the direct satellite signal. The preferred satellite position is at the relatively low elevation angle and on the extended line of target-to-receiver direction, in order to reduce the bistatic angle.

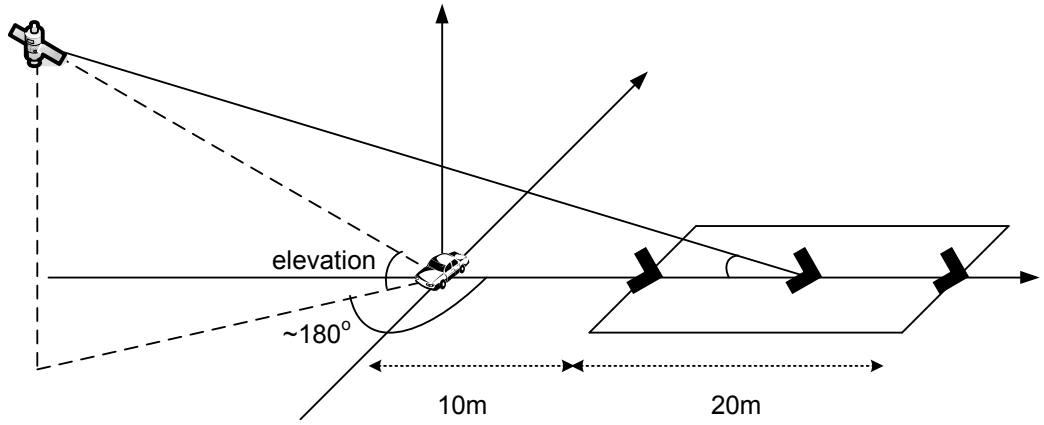

Figure 6.3: *Data Collection Geometry for Small Bistatic Angle*

In the observation area corner reflectors with different radar cross-sections are positioned at the different ranges to the receiver, separated by a range distance of 10-15 m to act as detectable targets. The purpose of these targets is to demonstrate the range resolution ability of the quasi-monostatic SAR, to calibrate the system power budget and to verify the correctness of the image formation algorithm. The corner reflector should have a sufficiently large radar cross-section, so that its range history and Doppler spectrum are visible during the image formation processing. Due to the low power density of the Galileo satellites on the earth, it is practically impossible to build a reflector which is strong enough to be seen at the output of the receiver hardware.

However, this reflector may possibly be detected after range compression, especially if it is situated close to the receiver (the transmitter's power density on the earth's surface can be assumed constant). Equation 6.1 can provide a measure of the target radar cross-section required over a particular integration time to give a sufficiently high SNR at the output of the range matched filter.

$$\sigma = \frac{SNR_{Rp}}{T_{\text{int}}} \times \frac{(4\pi)^2 R_R{}^2 k T_s}{P_D G_R \lambda^2} \tag{6.1}$$

Figure 6.4 shows the radar cross-section required to achieve a SNR of 13 dB at different receiver-to-target ranges. It can be seen that for a 1 ms integration time, a 2500 m^2 RCS corner reflector 100 m away from the receiver will provide 12 dB SNR. The calculation parameters are shown in Table 6.2 below.

Table 6-2: *Calculation Parameters*

Parameter	Symbol	Value
Receiver-to-target range	R_R	100-400 m
Receiver noise temperature	T_s	410 Kelvin
Gain of receiving antenna	G_R	16 dBi
Required SNR	SNR_{Rp}	13 dB
Integration time	T_{int}	1 ms

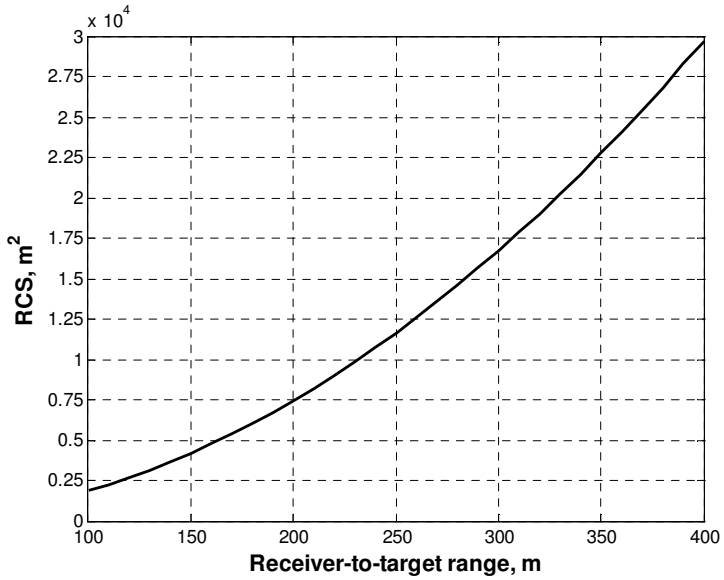

Figure 6.4: *Reflector Radar Cross-Section vs. Receiver-to-target Range*

The final point to note is that the required radar cross-section is in the direction of the receiver, not in the back-scattering direction. Moreover, it should be remembered that the bistatic equivalence theorem (bistatic radar cross-section is equivalent to the monostatic radar cross-section measured on the bisector of the bistatic angle) does not apply to complex shapes such as corner reflectors. The reflector should be oriented in a way that the receiver is within its major lobe width. The above means that the reflector type should have two parameters: relatively compact size to provide a high radar cross-section and a wide mainlobe. In terms of the mainlobe width, the ideal reflector type is the sphere; whereas, in terms of radar cross-section, the best solutions are the square and triangular corner reflectors. The equation below calculates the monostatic radar cross-section for triangular corner reflectors.

$$\sigma = \frac{4\pi a^4}{3\lambda^2} \tag{6.2}$$

where a is the characteristic dimension of the object. For the triangular corner reflectors, a is the length of its vertical side.

6.2.2 Imaging Data Collection

(a) Operation space

(b) Antenna installation

Figure 6.5: *Hardware Vehicle Installation*

(a) Stationary receiver experiment (site 1)

(b) Reference target – corner reflector

Figure 6.6: *Stationary Receiver – Reference Target*

Figure 6.5 above shows the photos of the hardware installation for the stationary receiver experiment. This is also the arrangement for the ground moving receiver experiment (discussed in section 6.3). Three antennas are separately installed on the roof of the vehicle; they are the LHCP helix antenna for reflected signal reception, the patch antenna for Galileo E5 direct signal reception and the GPS antenna for positioning. The parameters of these antennas can be found in Chapter 5 and Appendix C. The radar channel antenna is at a height of 3 m to the ground, with the beam centre looking horizontally. All three antennas are then connected through the cable to the receiver rack with a laptop for data recording.

Figure 6.6 shows the photos of the stationary receiver experiment arrangement. From Figure 6.6(a), we can see that one reference target has been placed 10 m away with respect to the stationary vehicle. It is then moved by 10 m increments each time to investigate the range resolution. Table 6-3 includes the satellite position information for different reflector distances. It can be seen that the satellite elevation is between 15–45 degrees, which is approximately equal to the bistatic angle in the quasi-monostatic topology. The triangular corner reflector has a 3-dB beamwidth of 40º around its symmetric axis [1]. So the corner reflector has been lifted by 59 cm (see Figure 6.6(b)), which changes its beam centre elevation from 45º to 8.5º. The height of radar channel antenna phase center is at 3 m and the closest range is at 11 m covered by a 30º antenna beam. The heterodyne channel antenna (patch antenna) has 60º beamwidth. It has been tilted with a pre-defined angle to align its beam center with the elevation of satellite.

Table 6-3: *Satellite Positions and Reflector Distance*

Distance	Elevation	Azimuth
10 m	34	52
20 m	32	53
30 m	16	54
45 m (site 2)	45	84

The azimuth and elevation angles of the satellite are measured with respect to the heterodyne antenna; however, it can be assumed that these measurements are the same as measurements made with respect to the corner reflector, due to the close proximity of the reference locations. The experimental imaging results are discussed in section 7.2 from two collected data sets.

Figure 6.7: *Stationary Imaging – Site 2*

6.3 Ground Moving Receiver Experiments

This section contains considerations regarding the SS-BSAR ground vehicle trial with the Galileo satellites acting as transmitters-of-opportunity. It includes the design considerations and concerns for the vehicle trial, such as the choice of a suitable location for experimentation, the potential range and cross-range resolution and power budget.

6.3.1 Experiment Design

This section investigates the resolution and the power budget for the SS-BSAR experiments using the Galileo satellites as transmitters and a ground moving vehicle as the receiver platform. The achievable resolution is calculated with the aid of receiver velocity and available aperture length. The power budget for targets at various distances and radar cross-section is investigated before and after application of the image formation algorithm.

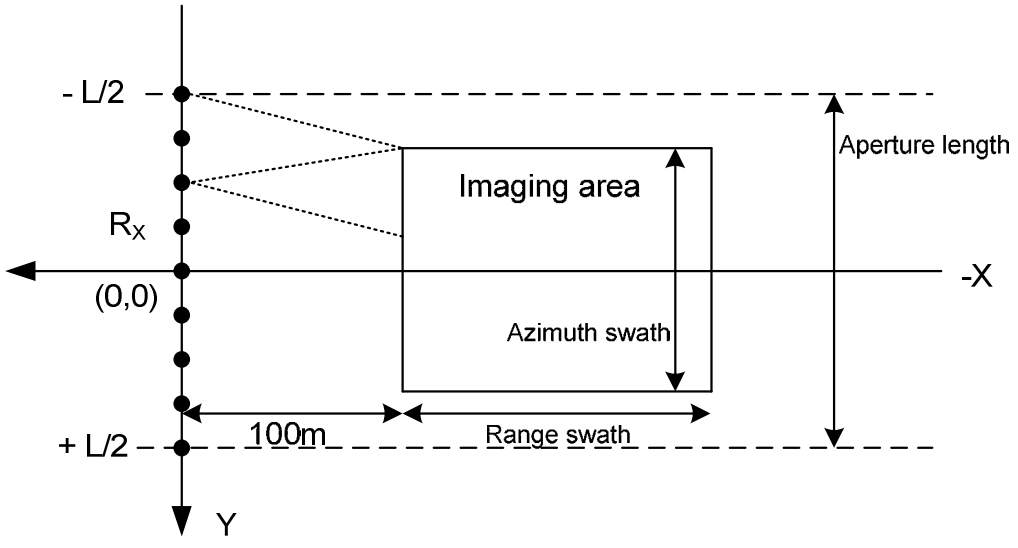

Figure 6.8: *Ground Moving Receiver Experiment Geometry (Receiver – Target Area)*

Figure 6.8 illustrates a typical SS-BSAR experiment geometry, with only receiver aperture and target area shown. The geometry is defined in the local reference frame, the origin locating at the mid-point of the receiver aperture. The moving receiver is travelling from –L to +L and defining the Y axis. The radar channel antenna is looking right and the target area is located at the –X axis. Targets encountered before the midpoint have a positive cross-range, whereas targets after the midpoint have a negative cross-range. The strip-map SAR mode is operating for the ground moving receiver experiments; hence the azimuth swath of observation area is slightly shorter than the available receiver synthetic aperture length due to the limitation of the antenna beamwidth. More information is given in Table 6.4.

- **Resolution**

For the bistatic SAR experiment, shown in Figure 6.3, the slant range resolution would be similar to the monostatic SAR case because of a small bistatic angle. For bistatic SAR experiments with a high-elevation satellite (Figures 6.8), the slant range resolution will degrade with increasing bistatic angle, according to equation 2.2. The slant range resolution along the direction of line-of-sight from the receiver to the target can be calculated by

$$\Delta_R = \frac{C}{2B} \cdot \frac{1}{\cos^2(\beta/2)} \tag{6.3}$$

Using Galileo E5 as the ranging signal, slant range resolution in the bistatic SAR experiment was expected to degrade from 30 m to 60 m when the bistatic angle increased from 0 to 45 degrees. While the bistatic angle is larger than 60 degrees, the resolution

will worsen significantly to a couple of hundreds of metres. So, such geometry should be avoided for the experimental data collection.

Because of the fixed antenna azimuth beamwidth coverage (~ 52 m at 100 m distance for the helix antenna with 30 degree beamwidth), the expected azimuth resolution in the quasi-monostatic SAR experiment varies, being proportional to the distance from the receiver to the target.

$$\Delta_{az} = \frac{\lambda R}{L_c} = 0.0048 \times R \tag{6.4}$$

Considering a target area between 100 m to 400 m from the aperture, the expected azimuth resolution will change from 0.48 m to 1.92 m. For the bistatic SAR experiment with a Galileo satellite, the azimuth resolution depends on the angular velocity of the satellite and also on the speed of the receiver. The cross range resolution, as given by equation 2.9, will be

$$\Delta_{CR} = \frac{\Delta_{azg}}{\sin(\alpha)} = \frac{\lambda}{T_c \cdot |\vec{\omega}_{Tr} + \vec{\omega}_{Rx}| \cdot \cos(\theta)\sin(\alpha)} \tag{6.5}$$

For the geometry of a small bistatic angle, considering a target at the distance of 250 m, the equivalent angular speed $|\vec{\omega}_{Tr} + \vec{\omega}_{Rx}|$ is 0.13^o per second, derived from the positions of the satellite transmitter and receiver during the synthetic interval, the azimuth resolution is about 1.7 m.

- **Signal-to-Noise Ratio**

Estimates of the power density of the Galileo E5 signal are given in section 2.4 and, based on these estimates, a density on the earth's surface of $3.99\times10^{-14}W/m^2$ is assumed. In ground vehicle experiments, a directional helix antenna with 16 dBi gain is used as the radar channel antenna, its effective area being $A_e=\frac{G\lambda^2}{4\pi}=0.2m^2$. For the signal-to-noise ratio in the radar channel, using the analysis in section 2.4, it can be written as

$$\frac{S}{N}=\frac{\rho A_e\lambda\eta}{4\pi KT_s\Delta_{az}}\times\frac{\sigma}{R_{rt}V_a} \tag{6.6}$$

where T_s is 410 K, Δ_{az} varies with range R_{rt}. Applying different parameters of each experiment to above equation, the expected SNR in the radar channel can be calculated. For example, the speed of the receiver is around 8 m/s and the azimuth resolution is about 2 m. For the experiments with the Galileo satellite, three different radar cross-sections (50 m^2, 100 m^2 and 500 m^2) are used for additional reference calculations, shown in Figure 6.9 below.

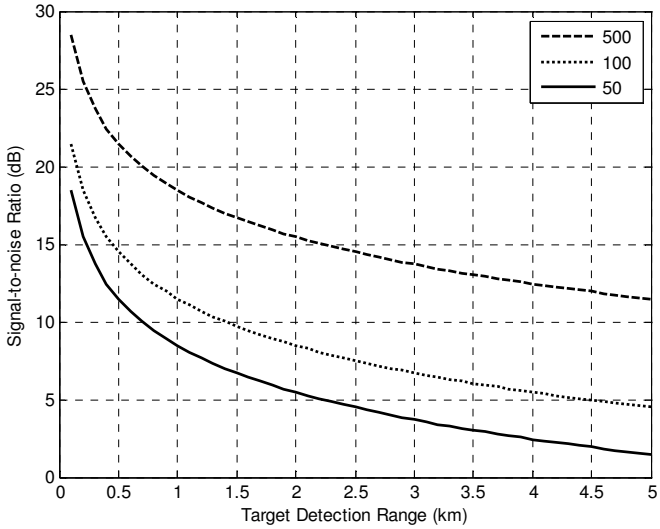

Figure 6.9: *Target Detection Range*

6.3.2 Imaging Data Collection

The second stage of the SS-BSAR experiments employs a moving receiver, the satellite and the receiver both then being in motion. Firstly, the radar antenna is mounted on a moving vehicle for antenna array synthesis, whereas the other antenna is looking to the sky, facing directly towards the satellite to receive the reference Galileo E5 signal.

During the formation of the aperture, GPS raw data is stored by the GPS receiver and converted to RINEX format, which contains three files. They are the ephemeris for GPS and GLONASS, and the observation file. From the real-time ephemeris, the satellite position could be calculated with a suitable algorithm. The receiver position could be derived from the observation file, which contains pseudorange and time information. More details are given in section 6.5

Customized data acquisition software also saves the starting and ending time of data collection, whilst the host PC time was synchronized to the internet. The time accuracy is up to ms level. However, the GPS receiver position is saved with respect to GPS time while collecting data, which is derived from the atomic clocks on the GPS satellites. There is 14-15 leap seconds difference between the GPS time and the host PC (UTC) time.

Due to our relatively low SAR resolution, particularly in the range direction, imaging of an urban area is not recommended. What is proposed is an imaging scene of an open field, which contains several, but sparsely oriented strong caterers, such as buildings and an aircraft.

Figure 6.10: *Target Area – Short Aperture*

The selected experiment site is located at Cleehill, Ludlow. The maximum distance that the vehicle can travel (the aperture length) is approximately 900 m along a relative straight road. The road is elevated relative to the imaging area, but its height is not constant. The change in height along the aperture is shown below in Figure 6.11. It can be seen that there is a big height variation in the synthetic aperture. We can, however, select a smaller aperture. In that case, the aperture length is 250-300 m. There are some potential targets in the area, at ranges between 100 and 800 m.

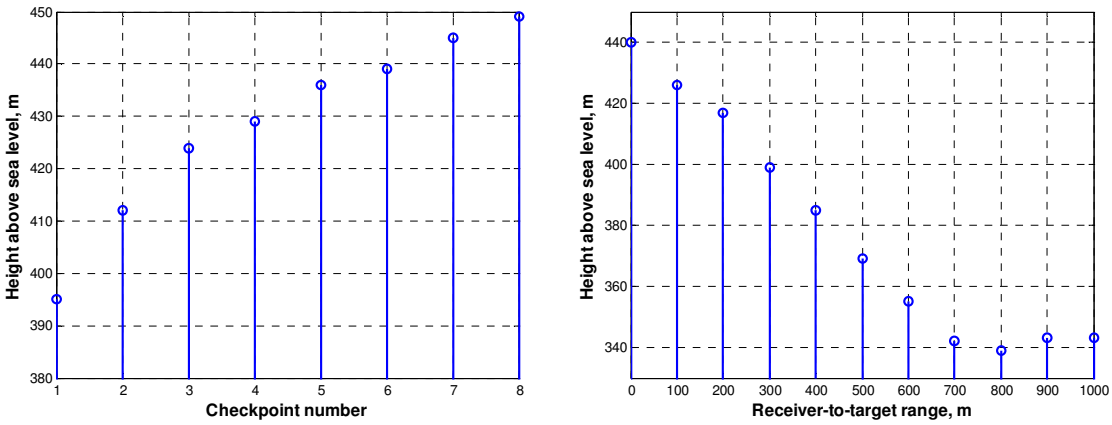

(a) Height profile along vehicle aperture (b) Range profile of target area terrain

Figure 6.11: *Terrain Profile of Target Area*

Using both GIOVE A/B satellites as transmitters of opportunity, a number of data sets were collected for SS-BSAR imaging. In the first set of data (collected at a recorded date and time) the bistatic angle was approximately 45.63° (quasi-monostatic configuration); whereas in the second data set (also collected at a recorded date and time) the bistatic angle was approximately 80.53°. The experimental parameters at the time of data

collection are shown in Table 6-4; illustrations of the data collection geometries are shown in Figures 6.10 and 6.12.

Table 6-4: *Experiment Parameters*

Parameter	Symbol	Value
Receiver-to-target ground range	R_R	100-800 m
Antenna altitude	h	3 m
Vehicle velocity	V	~ 8 m/s
Integration time	T_{int}	~ 30-90 s
Aperture length	L_c	~ 240-720 m
Gain of radar-ch antenna	G_R	16 dBi

Figure 6.12: *Target Area – Long Aperture*

Experimental imaging results will be given and discussed in section 7.3 for one set of data, which was recoded while both GIOVE A and B satellites were visible to the reviver. Hence two radar images could be generated from one data set collected from the same target area.

6.4 Airborne Receiver Experiments

6.4.1 Experiment Design

The aim of this section is to calculate parameters and define requirements for the helicopter-based SS-BSAR experiments. Three important parameters will be determined: range swath, azimuth swath and power budget.

Calculations on range swath will define the aircraft altitude and antenna tilt angle, as well as the absolute minimum/maximum ranges of observation. The azimuth swath will define the target observation time. All of the above parameters will be used to find the expected power budget for our experiment.

1) Range swath

The term "range swath" refers to the -3dB receiving antenna footprint on the ground in the range direction and involves the -3dB antenna beamwidth in the elevation direction. The antenna of the satellite transmitter illuminates a large part of the Earth's surface with an almost constant power density, so its influence on range swath can be neglected. As

mentioned previously, calculations on range swath define the aircraft altitude and antenna tilt angle, as well as the absolute minimum/maximum ranges of observation. Figure 6.13 below illustrates the relationships between these parameters.

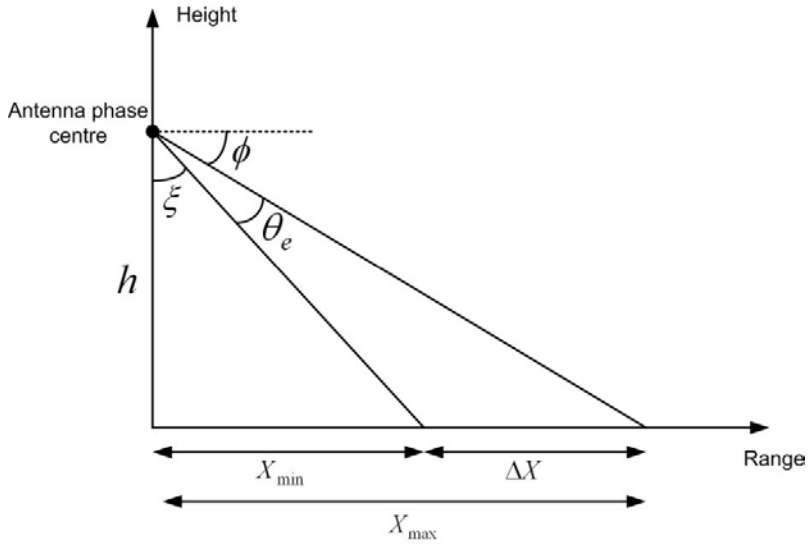

Figure 6.13: *Geometry for Range Swath Calculation*

In Figure 6.13, h is the altitude of the aircraft, ϕ is the tilt (look) angle of the antenna, θ_e is the -3dB beamwidth of the antenna in the elevation direction, ξ is the look angle at the minimum range of observation $X_{\min}$, $X_{\max}$ is the maximum range of observation and ΔX is the range swath. Correspondingly, the range interval of observation is $\Delta X = X_{\max} - X_{\min}$.

It is clear that by varying the aircraft altitude and the look angle, the minimum/maximum ranges of observation also vary. The value for θ_e in the calculations is $30°$, equal to the beamwidth of the experimental antenna used in the elevation direction. Note that these

ranges refer to ground ranges. For azimuth swath/power budget calculations we need to convert to slant ranges, i.e. take the aircraft altitude into account as:

$$R_{\min} = \sqrt{X_{\min}{}^2 + h^2}\ , \quad R_{\max} = \sqrt{X_{\max}{}^2 + h^2}\ , \qquad \Delta R = R_{\max} - R_{\min} \tag{6.7}$$

2) Azimuth swath

As soon as the start and final ranges of observation have been defined, the azimuth swath can be calculated. The geometry is shown in Figure 6.14. The variable θ_a denotes the 3dB beamwidth of the receiving antenna in the azimuth direction and ΔA is the azimuth swath at some slant range R from the receiver. To calculate the azimuth swath, we split the isosceles triangle in the figure in two right triangles. The azimuth beamwidth is set to $15°$, equal to that of our experimental antenna. From one of the two triangles, we get:

$$\tan\left(\frac{\theta_a}{2}\right) = \frac{\Delta A}{2R} \Rightarrow \Delta A = 2R\tan\left(\frac{\theta_a}{2}\right) \tag{6.8}$$

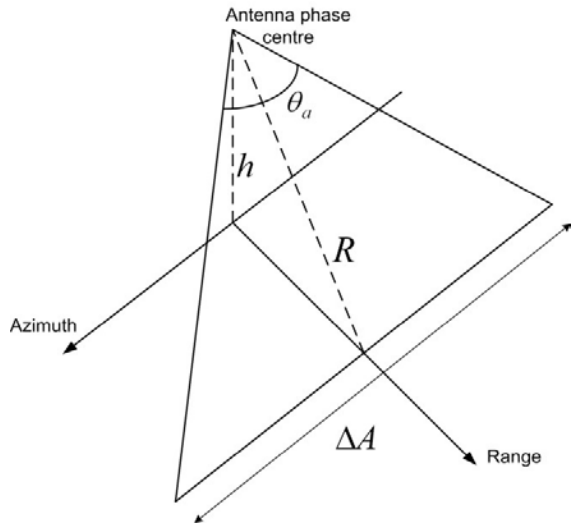

Figure 6.14: *Geometry for Azimuth Swath Calculation*

The experimental parameters at the times of data collection are shown in Table 6-5; illustrations of the data collection geometries are shown in Figures 6.15.

Table 6-5: *Experiment Parameters*

Parameter	Symbol	Value
Receiver-to-target ground range	R_R	500-3000 m
Antenna altitude	h	250 m
Vehicle velocity	V	10-100 m/s
Integration time	T_{int}	~ 30-60 s
Aperture length	L_c	~ 500-800 m
Gain of radar-ch antenna	G_R	14 dBi

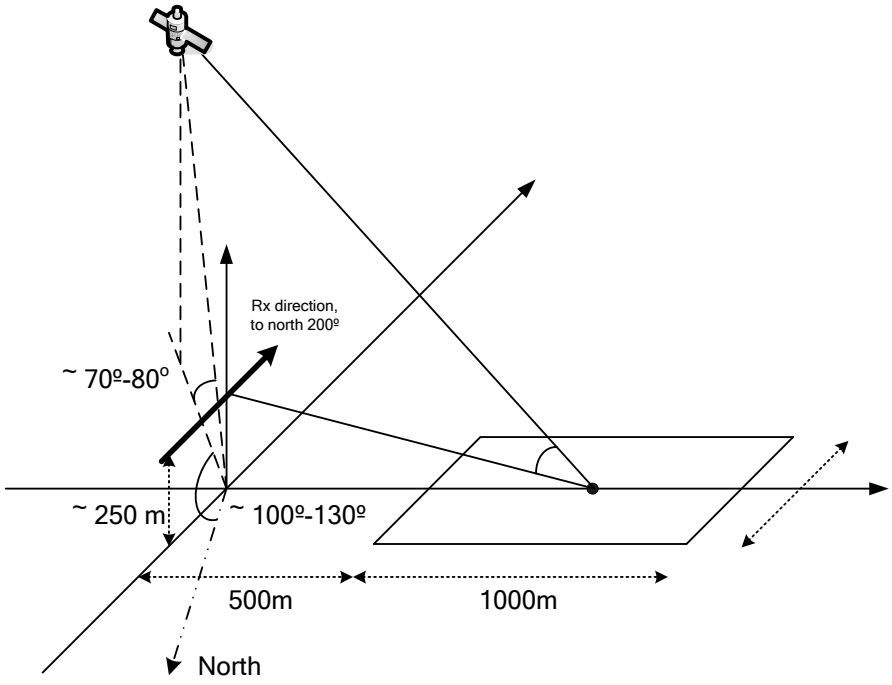

Figure 6.15: *Data Collection Geometry for Large Bistatic Angle*

Now it is useful to investigate up to what ranges we can detect targets of different radar cross-section. The velocity is set to 20 m/s (see section above) and T_{int} is equal to 1 ms. The other parameters are the same as the vehicle trial. So, a target with the 100 m^2 radar cross-section will be detected at the background of noise with SNRs of approximately 13.5 dB (1.6 km from receiver) or 16.5 dB (1 km from receiver). The power budget in this case is much tighter than that expected in the vehicle trials, but the system will provide a useful image.

From the analysis above, we can set the following specifications for the helicopter trials, in order to obtain an image of sufficient quality: 250 m aircraft altitude; 20 m/s aircraft velocity; 10-20 degrees receiving antenna inclination.

6.4.2 Imaging Data Collection

(a) Helicopter

(b) Receiver installation

(c) Operation space

(d) Heterodyne and GPS antenna

(e) Radar channel antenna array

Figure 6.16: *Hardware Helicopter Installation*

Figure 6.16 above shows the photos of hardware installation for helicopter based SS-BSAR experiments. One antenna array is used for reflected signal reception and installed inside the helicopter pod; the patch antenna for Galileo E5 direct signal reception and GPS antenna for positioning are installed inside the cabin. The parameters of these antennas can be found in Chapter 5 and Appendix C. The radar channel antenna is tilted at 15 degrees to the horizon. All three antennas are then connected through the cable to the receiver rack with a laptop for data recording. Photos of two target areas are shown in Figure 6.17 and 6.18. The runway, the hanger and the aircraft on the ground will be

used for detection. Experimental imaging results will be given and discussed in section 7.4.

Figure 6.17: *Target Area 1 – East Fortune Airfield*

Figure 6.18: *Target Area 2 – PDG Airfield*

6.5 Parameters Estimation

The formation of the synthetic aperture requires a coherent phase history to be maintained during the time it takes to synthesize the aperture. In fact, three specific factors impact the phase coherence of the two-dimensional SAR signal and introduce phase effects that influence the processing complexity and the resulting image quality. These factors are: propagation, source coherence (synchronisation between transmitted and reference signals) and motion compensation [2].

SAR imaging from space may encounter significant ionospheric dispersive effects resulting in phase errors in the range dimension which are caused by the frequency-dependant index of refraction. A variation in the integrated refractive index between the radar antenna and the targets also cause azimuth phase errors. Nevertheless the study of propagation effects on phase coherence of SAR signals is out of scope of this thesis. There are many excellent articles and books available for this topic [3-6].

For source coherence/synchronisation considerations, it is normal to generate a separate reference signal, at the appropriate time, using the coherent reference oscillator to maintain phase coherence in a monostatic SAR system. There are also simpler methods available for synchronisation between the transmitter and the receiver in the cooperative bistatic SAR systems. However, for SS-BSAR using GNSS as a non-cooperative transmitter, synchronisation is important and a specific chapter (Chapter 4) contributes to this issue in the thesis.

To generate a coherent synthetic aperture for fine azimuth resolution in a general SAR system, synchronisation accounts for relative motion between the transmitter/receiver and target over time. It can be derived from a deterministic path, measured motion using integrated sensors or signal derived estimation which uses autofocus techniques in processor or multiple prominent point processing (PPP) techniques. For the experiments described in the above sections, the relative motion estimation will be mainly derived from the deterministic path and measurements from integrated sensors. A description of signal based motion compensation can be found in [2]. Also there are many classical papers that discuss motion compensation with well-known algorithms for monostatic SAR [7-9]. However, for motion compensation in bistatic SAR there are fewer references available [10-12].

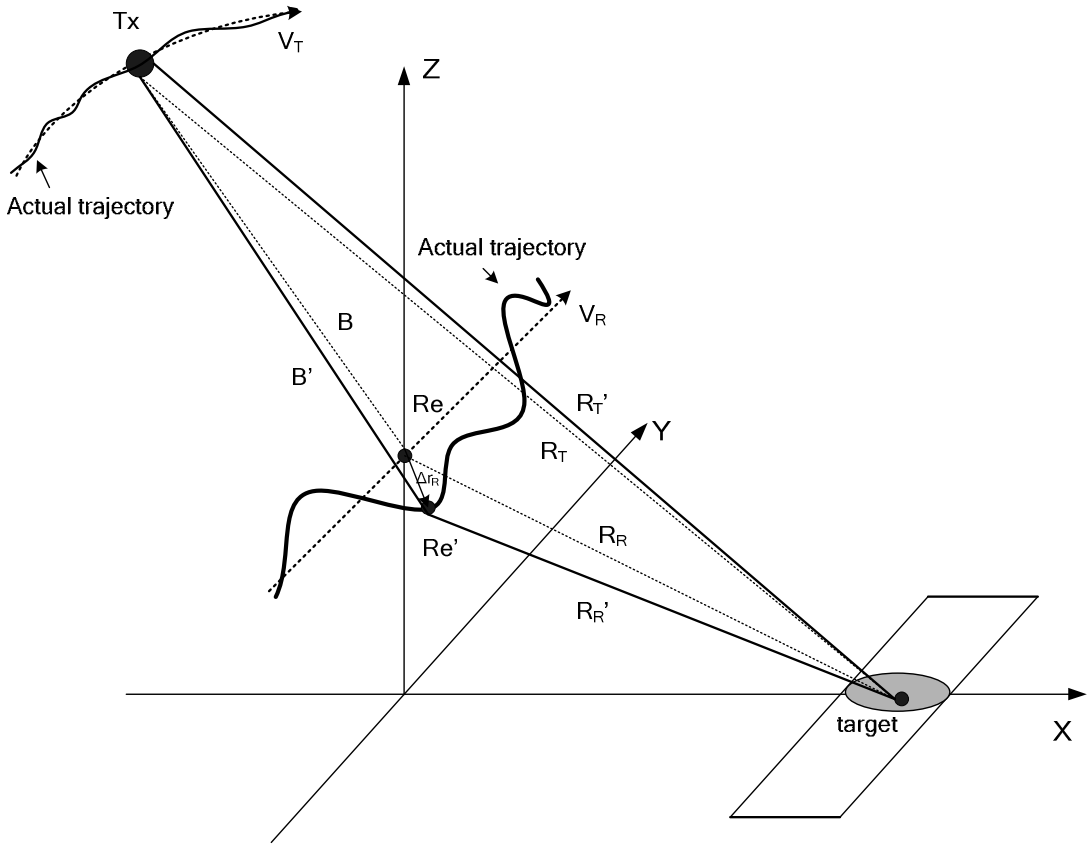

Figure 6.19: *Transmitter and Receiver Trajectories with Motion Errors*

In this section we will discuss the necessary motion parameters (position, trajectory and Doppler information) estimation and compensation to achieve the focused SS-BSAR image. Figure 6.19 above gives a typical example of SS-BSAR topology with the platform motion estimation errors. The actual trajectories of both transmitter and receiver are deviated from their nominal paths. Hence the Doppler shift and phase estimation will also contain intrinsic errors, which eventually affect the focusing of BSAR data.

Different methods are proposed for transmitter/receiver parameters extraction and the practical one is justified. Two problems, residual Doppler shift and low frequency motion compensation are briefly discussed. Techniques to compensate non-linear platform motion errors will be introduced and proved with the experimental results at the end of this section.

6.5.1 Platform Position/Location Estimation

- **Transmitter Trajectory Estimation**

A GNSS satellite, when used as the non-cooperative transmitter for SS-BSAR, has a trajectory that is normally a deterministic path and its geographic coordinates at the specific time can be extracted, calculated or estimated from different sources of information.

In general, GNSS satellites broadcast two types of navigation data, Almanac and Ephemeris. Almanac data contains coarse orbital parameters for all satellites in the constellation; Ephemeris data, by comparison, contains very precise orbital and clock corrections for each satellite. For our previous experiments using GLONASS [13] the real time ephemeris, received by a dual channel GPS/GLONASS receiver, were used to calculate GLONASS satellite's coordinates in ECEF (Earth-Center Earth-Fixed). The Cartesian reference frame and sufficient position accuracy has been used to obtain imaging results. However, the accuracy of the satellite trajectory derived from the

ephemeris, sometimes, is not enough for high resolution radar applications, for example, interferometric SAR.

To obtain the highest-precision civilian GNSS data and products, there is one international community, the international GNSS service (IGS) which can provide <5 cm accuracy for GPS satellite orbital position and about 15 cm accuracy for GLONASS satellite orbital position with known latency [14]. To compare, GNSS satellite broadcast data generally provides real time orbital accuracy of 100 cm and clocks accuracy of 5 ns RMS; final international GNSS service data provides orbital accuracy up to 2.5 cm and clock information within 75 ps RMS. However, the highest precise data can not be obtained in real time, instead 12-18 days latency is expected.

For the experiments described in sections 6.2-6.4, Galileo satellites have been used as the transmitter. The international GNSS service does not provide the service for the Galileo constellation yet; the ephemeris broadcasted from GIOVE A/B (first two Galileo testing satellites) is lacking in consistency at this stage. Another method is proposed and applied to meet the requirements, which is based on the prediction of GNSS satellite orbits. Nevertheless, for the operation of future SS-BSAR using GNSS, the real-time ephemeris is preferred in terms of the convenience and the international GNSS service data is most favoured for accuracy reasons. A brief description and explanation is given below for the method based on the orbital predication.

There are many different ways to mathematically describe the space orbit, but a number of schemes each consisting of a set of six parameters are commonly used in astronomy and orbital mechanics [15]. This is because the problem contains six degrees of freedom. These correspond to the three spatial dimensions which define position (the x, y, z in a Cartesian coordinate system) plus the velocity in each of these dimensions. These can be described as orbital state vectors, but this is often an inconvenient way to represent an orbit, which is why Keplerian elements are commonly used instead. A Keplerian orbit is merely an idealized, mathematical approximation at a particular time. Keplerian element parameters can be encoded as text in a number of formats. The most common of them is the NASA/NORAD two-line elements (TLE) format [15].

In our case, a computer program [16] is used with the two-line elements to compute the precise position of a satellite at a particular time. The reference frame of the resulting coordinates is the Earth-centred inertial (ECI) coordinates produced by the orbital model. The ECI coordinates are then converted to Earth-centred Earth-fixed Cartesian reference frame and finally transferred to local coordinates. The coordinate localization is realized through a 7-parameter transformation; more information regarding this issue is given in Appendix B. As the resulting satellite coordinates often have a 15 minute interval, an interpolation process will be necessary during the SAR imaging formation. Two references [17 and 18] should be considered for interpolation methods of GNSS satellite orbits. Considering the overall integration time of 30-60 seconds (for our experiments), the linear interpolation method is applied, which gives satisfactory outputs as verified by the testing results shown in section 6.5.4.

Unfortunately, the orbital data in the form two-line elements set does not provide any kind of accuracy information. According to [19], for a spacecraft in a typical Low Earth orbit, the accuracy that can be obtained is on the order of 1 km within a few days of the epoch of the element set. For GIOVE A/B satellites trajectories, real-world benchmarking results are acquired and analyzed in section 6.5.4. It is revealed that the coordinates derived from two-line elements data set can provide sufficient accuracy for the estimation of satellite motion and be used for SS-BSAR imaging formation.

- **Receiver Trajectory Estimation**

For high resolution SAR imaging, the radar position/velocity history is normally required with sub-meter precision. In our case, a dual frequency GPS receiver is integrated with the radar receiver hardware (Chapter 5). However, without differential GPS corrections, its real-time outputs can only provide meter-level receiver position data.

For our experimental data to achieve better estimation on receiver platform motion, a Precise Point Positioning method is proposed to improve the real time GPS outputs to centimetre accuracy. Precise Point Positioning is a post-processed GPS position estimation technique which generates a high precision autonomous solution. It is derived from a stored GPS receiver observation file combining with international GNSS service precise satellite orbit estimation, using non-differenced dual-frequency pseudorange and carrier phase [20]. The resulting position estimates are often referred to the WGS84

reference frame. However, these new WGS84 realizations are coincident with the International Terrestrial Reference Frame (ITRF) at about the 10 centimetre level. This means that one can consider that ITRF coordinates are also expressed in WGS84 at 10 cm level. The same coordinate localization is applied to the receiver coordinates. Hence both the transmitter and receiver trajectories can be presented in the one pre-defined local coordinate reference frame. It is also important to note that the quality of the GPS orbit and clock estimates, and consequently of the Precise Point Positioning derived positions, has improved from 10 cm and several nanoseconds in 1994 to about 2 cm and 0.1 nanoseconds in 2003.

Figure 6.20 below gives the block diagram of coordinate extraction process, which is actually applied to the experiment data. In summary, the Galileo satellite positions at the specific epoch are obtained by the prediction of its orbit using two-line elements data; the high-precision receiver positions are obtained by the Precise Point Positioning method using the stored GPS receiver observation file combining with the IGS precise GPS satellite orbit data. As a result, with high precision estimations of satellite and receiver trajectories, their velocity histories, Doppler shift and phase variation can be calculated for the transmitter-target-receiver geometry. For example, the Doppler shift between the satellite and the receiver (heterodyne channel) can be written as

$$f_{d_n} = \frac{\sqrt{(X_{S_n} - X_{R_n})^2 + (Y_{S_n} - Y_{R_n})^2 + (Z_{S_n} - Z_{R_n})^2} - \sqrt{(X_{S_{n-1}} - X_{R_{n-1}})^2 + (Y_{S_{n-1}} - Y_{R_{n-1}})^2 + (Z_{S_{n-1}} - Z_{R_{n-1}})^2}}{(t_n - t_{n-1}) \cdot C} \cdot f_0 \tag{6.9}$$

Satellite coordinates at position n: (Xs_n,Ys_n,Zs_n);

Receiver coordinates at position n: (Xr_n, Yr_n, Zr_n);

f_d: Doppler shift.

f_o: Carrier frequency.

C: Speed of light

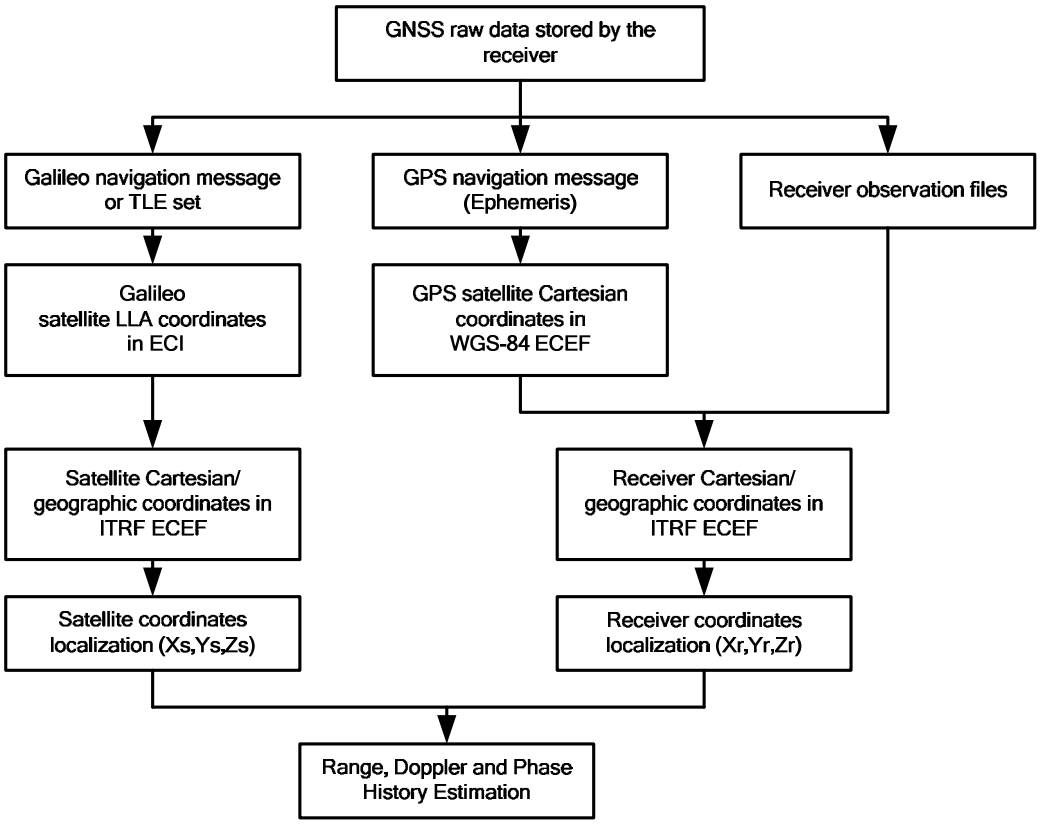

Figure 6.20: *Coordinates Extraction for Transmitter and Receiver*

One more thing is worth mentioning regarding receiver position. Although the resulting receiver coordinates have an accuracy of 2.5 cm, due to Precise Point Positioning processing, its update rate is 1 Hz from most GPS receivers. This means that the moving receiver position will be updated every one second; this is usually not adequate for the

estimation of high frequency motion errors. For example, the airborne platform is moving with high speed and rapid vibration, the phase centre of the antenna on the platform will suffer from high frequency motion errors. In such situations, the inertial measurement unit (IMU) and inertial navigation system (INS) are often required to provide short-term, high-frequency motion estimation. For the helicopter trials mentioned in section 6.4, the IMU/INS has not been used because of technical reasons. Its effect on the SS-BSAR image formation is uncertain and worthy of further study in the future.

6.5.2 The Problem of Residual Doppler Shift in SS-BSAR

Another problem associated with airborne SS-BSAR is the residual Doppler shift present between the heterodyne channel and the radar channel. This is due to the fact that the transmitter and receiver are both in motion, and in addition they are not co-located. This topology creates a difference in the angular velocity between the satellite-to-target path (radar channel) and the satellite-to-receiver path (heterodyne channel).

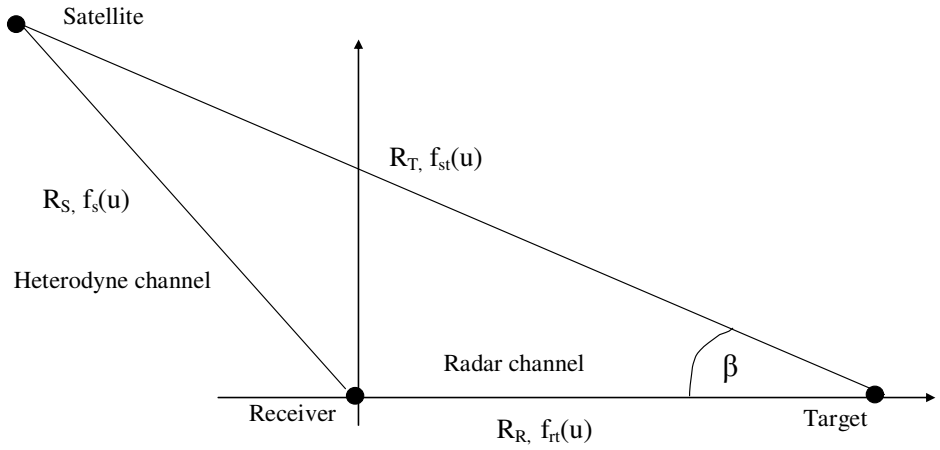

Figure 6.21: *Bistatic Triangle*

R_S: Satellite-to-Receiver range

R_T: Satellite-to-Target range

R_R: Receiver-to-Target range

$f_s(u)$: Doppler variation between satellite and receiver

$f_{st}(u)$: Doppler variation between satellite and target

$f_{rt}(u)$: Doppler variation between receiver and target (azimuth signature)

Figure 6.21 above shows the bistatic triangle for BSAR with the range and Doppler shift parameters. In the monostatic SAR, $f_{rt}(u)$ is the source of the azimuth signal and forming the azimuth resolution. However, this is not the case for BSAR because $f_s(u)$ is often not equal to $f_{st}(u)$. This residual Doppler shift ($f_{st}(u)$- $f_s(u)$) can be large enough to introduce a complete mismatch in the Doppler histories between the heterodyne channel and the radar channel. It could be space-variant and time-variant. It should be noted that this problem of a moving heterodyne channel is not only restricted to SS-BSAR using GNSS transmitters, but also a key problem of airborne SS-BSAR using any transmitter. In this section we will comprehensively discuss the problem of residual Doppler shift and how it affects the imaging algorithm. A method to estimate the residual Doppler shift will be described.

To describe the assumption made by the imaging algorithm, the received signal at the heterodyne channel can be expressed as:

$$s_h(t,u) = p\left(t - \frac{R_S(u)}{C}\right) \times \exp\left[-j2\pi\left(f_s(u)\right) t\right] \tag{6.10}$$

where *t* denotes fast time and *u* denotes slow (azimuth) time, *p* is the envelope of the ranging signal, *c* is the speed of light, $R_S(u)$ is the satellite-to-heterodyne range, varying with azimuth time u and $f_s(u)$ is the Doppler shift experienced by received heterodyne signal.

The signal received at the radar channel is given by:

$$s_r(t,u) = p\left(t - \frac{R_T(u)}{C} - \frac{R_R(u)}{C}\right) \times \exp\left[-j2\pi\left(f_{st}(u) + f_{rt}(u)\right) t\right] \tag{6.11}$$

where $R_T(u)$ and $R_R(u)$ are satellite-to-target and receiver-to-target range respectively, $f_{st}(u)$ is the Doppler shift due to the satellite motion relative to the target at coordinates (x_{ta}, y_{ta}) and $f_{rt}(u)$ is the Doppler shift due to the receiver motion relative to the target. This Doppler shift $f_{rt}(u)$ forms the main azimuth signature for image formation.

For each aperture position, the range/delay $\frac{R_S(u)}{C}$ and Doppler shift $f_s(u)$ were found from the synchronisation algorithm (discussed in Chapter 4). During the range compression, range and Doppler shifts were then removed from the radar channel signal which was stored for that particular position. Hence, the signal returned from a single

point target at coordinates (x_{ta}, y_{ta}) after the range $R_S(u)$ and the corresponding Doppler shift $f_s(u)$ are removed, has the form:

$$\begin{aligned} s_{rh}(t,u) &= p\left(t - \left(\frac{R_R(u)}{c} + \frac{R_T(u)}{c} - \frac{R_S(u)}{c} \right) \right) \times \exp\left[-j2\pi \left(f_{st}(u) + f_{rt}(u) - f_s(u) \right) t \right] \\ &= p\left(t - \left(\frac{R_R(u)}{c} + \frac{R_{re}(u)}{c} \right) \right) \times \exp\left[-j2\pi \left(\Delta f_{re}(u) + f_{rt}(u) \right) t \right] \end{aligned} \tag{6.12}$$

$$R_{re}(u) = R_T(u) - R_S(u) \qquad \text{and} \qquad \Delta f_{re}(u) = f_s(u) - f_{st}(u) \tag{6.13}$$

It could be seen from the above equations that the terms $R_{re}(u)$ and $\Delta f_{re}(u)$ introduce a residual range migration and a residual Doppler shift. A method to estimate the residual Doppler shift in the heterodyne channel was experimentally verified using the GLONASS satellite [21]. The experimental results are given in section 6.5.4 using a Galileo satellite. In the above equations, the azimuth signature $f_{rt}(u)$ is formed by the motion of the radar channel antenna relative to the target. Therefore in the imaging algorithm, an appropriate azimuth filter is designed for each range bin accordingly. A detailed explanation of the imaging algorithm is outside the scope of this thesis and can be found in [22, 23].

6.5.3 Motion compensation

Motion compensation (MC) is another aspect of SAR phase coherence. For BSAR, motion compensation is required for two platforms, instead of one platform in the

monostatic SAR case. However, the objectives and the effects remain more or less same. High frequency motion errors cause a loss in dynamic range, i.e., degraded sidelobe and resolution loss. Low frequency motion errors cause geometric distortion and poor map accuracy [7]. Motion compensation will not be perfect, with a residual phase error remaining in the signal. In general, the minimum objective is to reduce motion-induced phase effects to a level that an autofocus algorithm can accommodate.

There are three types of relative motion, line-of-sight translational, rotational motion and motion of individual targets. The tolerable magnitude of uncompensated motion increases with radar centre frequency, because the phase error associated with an uncompensated distance varies inversely with wavelength. At a given wavelength, the tolerable uncompensated distance is relatively independent of azimuth resolution, but resolution does naturally impact the allowable velocity or acceleration measurement error, since the resulting motion error increases with aperture time. It is common practice to use $\pi/4$ radian as an acceptable level of uncompensated low-frequency, nonlinear phase errors in order to avoid significant deterioration in image quality. First order bistatic motion compensation can be expressed as

$$\varphi_{err} = \frac{2\pi}{\lambda}\left(R'(t) - R(t)\right) = \frac{2\pi}{\lambda}\Delta R(t) \tag{6.14}$$

$$f_D'(t) = \frac{V_R'(t)}{\lambda} + \frac{V_T'(t)}{\lambda} = \frac{V_R(t)}{\lambda} + \frac{V_T(t)}{\lambda} + \left(\frac{\Delta V_R(t)}{\lambda} + \frac{\Delta V_T(t)}{\lambda}\right) \tag{6.15}$$

The correction term is $\Delta f_D(t) = \frac{\Delta V_R(t)}{\lambda} + \frac{\Delta V_T(t)}{\lambda}$ to compensate for the shift of the azimuth spectrum.

Moreover, antenna phase centre position/motions create phase effects in the SAR signal history. The antenna is normally suffering short-tem fluctuations in three dimensions. Measurement of the antenna phase centre motion requires a position history with accuracy over both the short and the long terms. In practice, GPS provides high long term accuracy with poor data rate and noisy attitude. INS provides high short term accuracy with high data rate and accurate attitude resolution. So GPS/INS integration, using a Kalman filter is a sufficient solution for motion compensation in SS-BSAR application.

6.5.4 Parameter Estimation Results

In this section, parameter estimation results are discussed and analyzed based on one ground moving receiver experiment (short aperture), which is described in section 6.3. The results are provided for transmitter/receiver coordinates, velocities, Doppler shifts and phase histories. For satellite parameters, the outcomes are compared between predications using a two-line elements data set and broadcast satellite position. Motion compensation results are shown for the relative non-linear motion between the transmitter and the receiver platforms. It is clearly shown from these results that the proposed methods and techniques are sufficient and effective for parameter estimation from our experiment data.

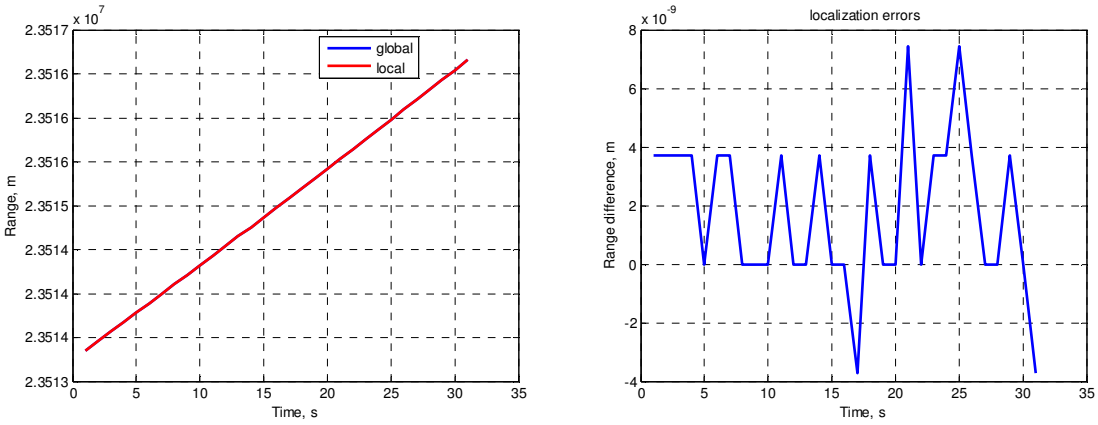

(a) baseline range (b) localization errors

Figure 6.22: *Coordinate Localization*

Figure 6.22 verifies the outputs of coordinate localization (refer to Appendix B). Figure 6.22(a) plots the range history between the transmitter and the receiver using the coordinates, both in the global reference frame and in the local frame. The range histories are almost identical and it can be seen from Figure 6.22(b) that the error in range history is on the order of 10^{-9} m because of the localization process. Then all estimation can be based on the local coordinates for Doppler shift, phase history etc.

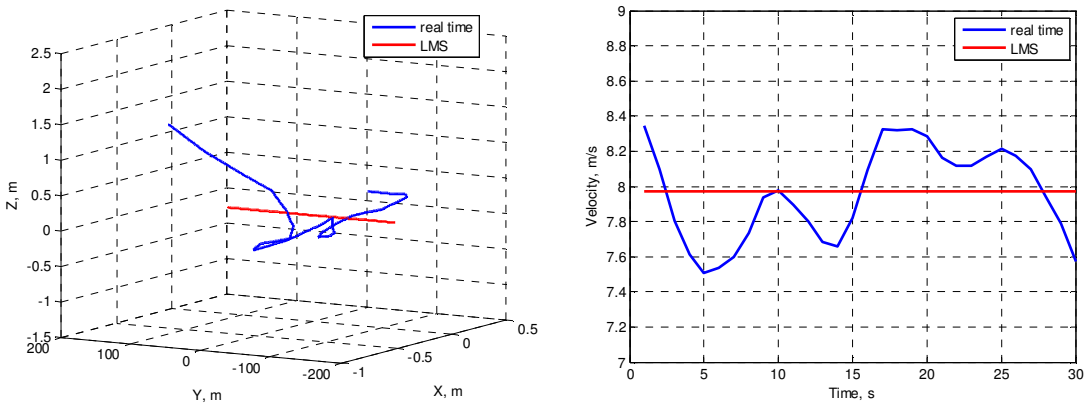

(a) receiver trajectory (b) receiver velocity

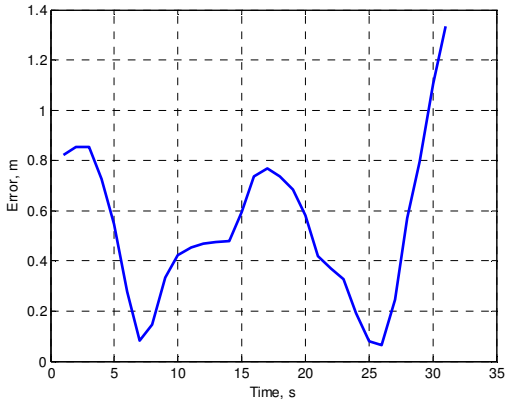

(c) baseline range error due to receiver estimation error

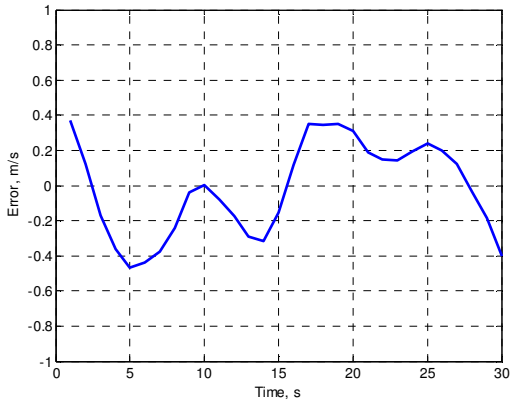

(d) receiver velocity error

Figure 6.23: *Receiver Parameters Estimation*

Figure 6.23 shows the result of the receiver parameters estimation from the Precise Point Positioning method proposed previously. It includes the receiver trajectory and velocity in the local reference frame. Figures 6.23(a) and 6.23(b) also give the least mean square outputs of estimated receiver path and velocity with a red line. It can be seen that least mean square receiver path has been defined as the Y-axis for the local frame in this case. Figure 6.23(c) presents the errors of bistatic baseline range estimation, due to receiver non-linear motion. Its maximum deviation is around 1.4 m from its nominal path and velocity error is around 0.4 m/s at the maximum (considering nominal speed ~ 8 m/s). Figure 6.23(d) shows the result of receiver velocity estimation errors and clearly reveals the acceleration and deceleration phase of receiver motion.

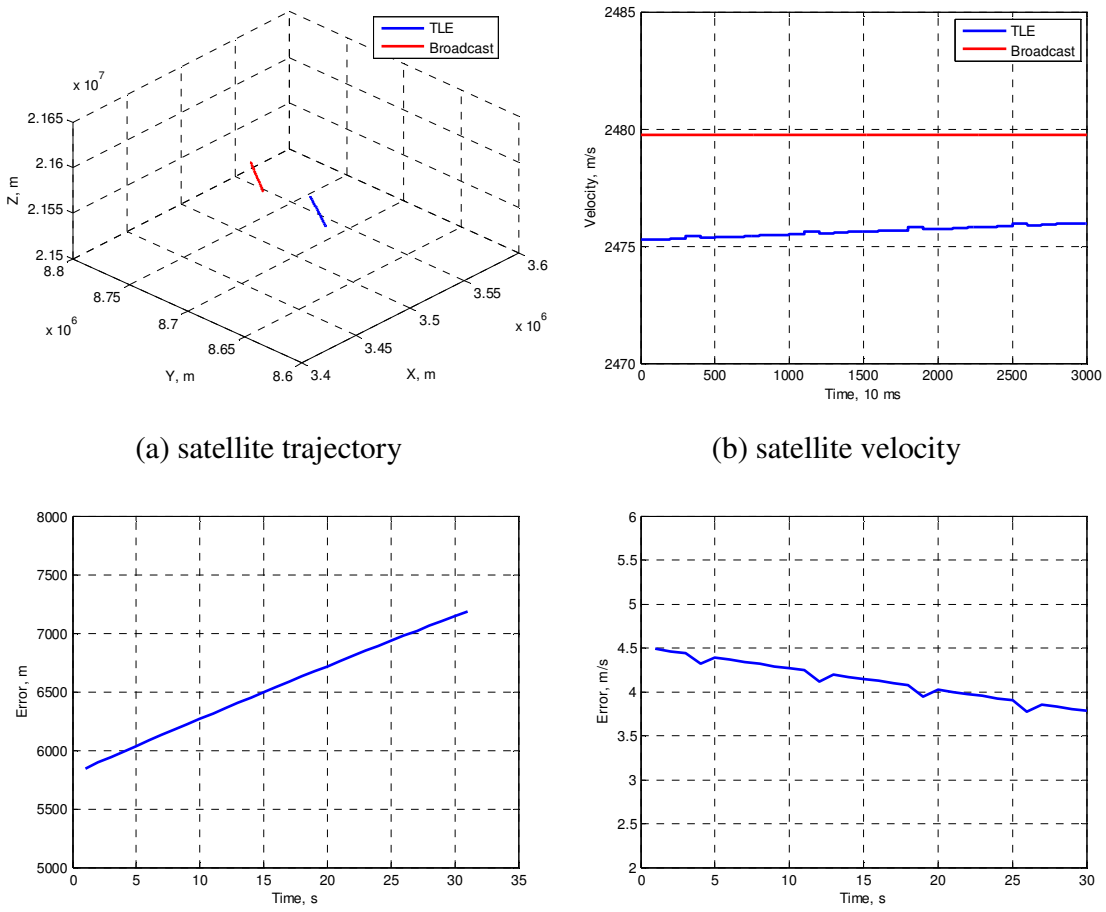

(a) satellite trajectory

(b) satellite velocity

(c) baseline range error due to satellite estimation error

(d) satellite velocity estimation error

Figure 6.24: *Satellite Parameters Estimation*

Figure 6.24 presents the result of satellite parameters estimation from the methods discussed previously. There are two sources of information used to extract GIOVE A/B satellite positions, the two-line elements data set and broadcast orbital data. Coordinates from two-line elements data set have 1 s interval and coordinates from broadcast data updates every 15 minutes, which have to be interpolated to a 1 s interval. Figure 6.24(a) plots the satellite trajectories using both coordinate data sets in the local frame. Two

results are separated far away and a constant shift is observed. Figure 6.24(b) plots the velocities derived from two different satellite paths. Velocity from broadcast data is almost constant over the 30 s integration time; velocity from the two-line elements data is varying slowly, in this case, increasing. Figure 6.24(c) presents the errors of bistatic baseline range estimation due to different satellite position estimations. This error is not constant and it varies from around 6000 m to 7000 m during the synthetic aperture. However, comparing to the Galileo satellite orbit height of 23000 km, the effect of this error may be neglected. Figure 6.24(d) shows the result of satellite velocity estimation errors and it is between 3.5 m/s to 4.5 m/s comparing to the average satellite speed of 2500 m/s. It will be shown from the results below that surprisingly, the two-line elements data provides a closer match to the parameters tracked by the synchronisation algorithm than the broadcast satellite position.

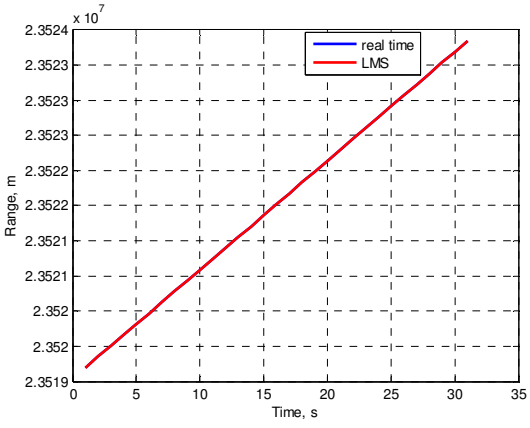

(a) baseline range history estimation

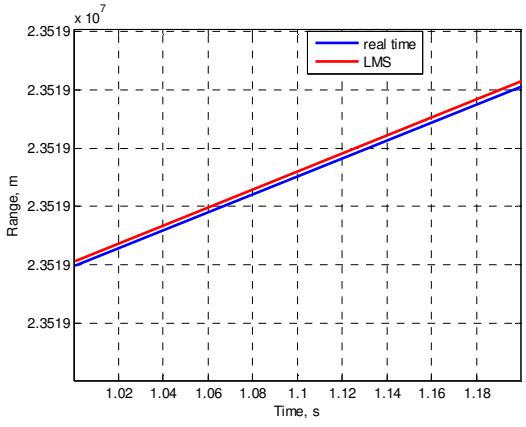

(b) zoom

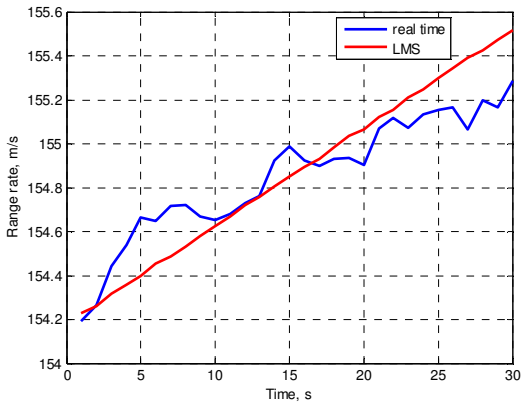

(c) range rate estimation

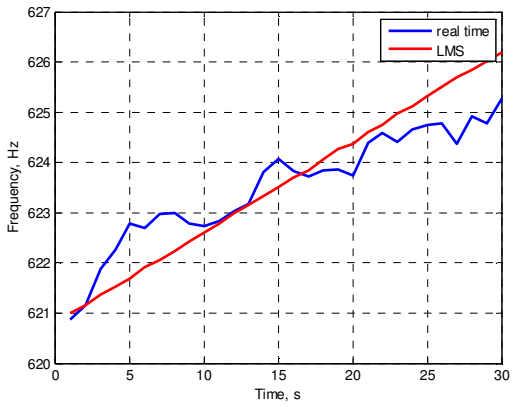

(d) Doppler shift estimation

Figure 6.25: *Baseline Range and Doppler History Estimation*

After the trajectories and velocities of the transmitter and receiver are estimated, Doppler shift could be calculated. Figure 6.25 shows the result of bistatic baseline range history, range rate and Doppler shift history estimation. The satellite positions derived from the two-line elements set is used; both real-time receiver positions and least mean square output of the receiver positions are used for comparison. Figure 6.25(a) shows the bistatic baseline range history using real-time and least mean square output of the receiver paths. This is slightly different from the plot shown in Figure 6.22(a), which is derived from same coordinates but in a different reference frame. From Figure 6.25(b), it can be seen that there is a small mismatch. The range rate can then be easily calculated from the range history between the transmitter and receiver, (Figure 6.25(c)) and converted to the Doppler shift in the heterodyne channel. The same Doppler shift is also tracked by the synchronisation algorithm. There is about 5 Hz Doppler bandwidth for 30 s aperture time. From Figures 6.25(c) and 6.25(d), we can see that the range rate or Doppler shift derived from least mean square output of receiver positions is linearly changing (red line), but the real-time value is varying mainly due to the actual non-linear

receiver motion. It is important that the tracked Doppler shift in the heterodyne channel will also reflect this non-linear effect and possible motion compensation may be applied to it before range compression.

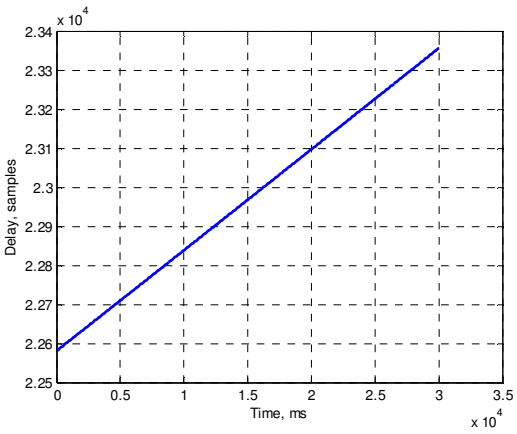

(a) Delay (code phase) estimation

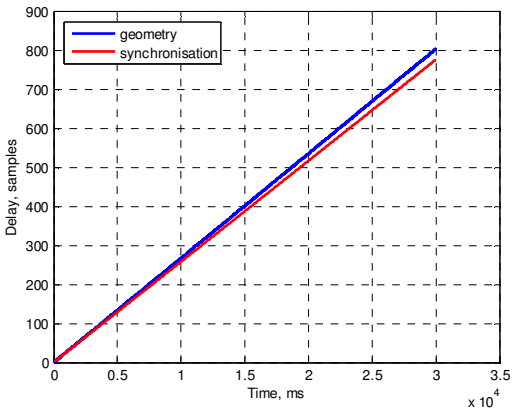

(b) Delay estimation (shift to 0)

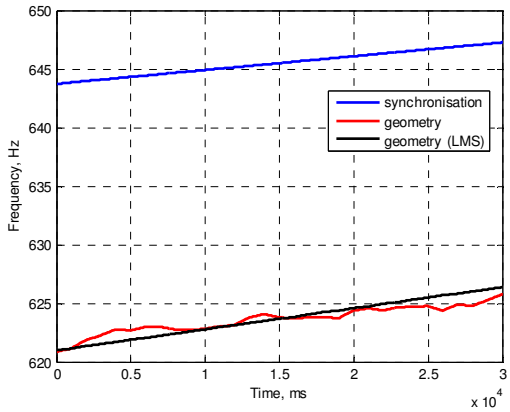

(c) Doppler shift estimations

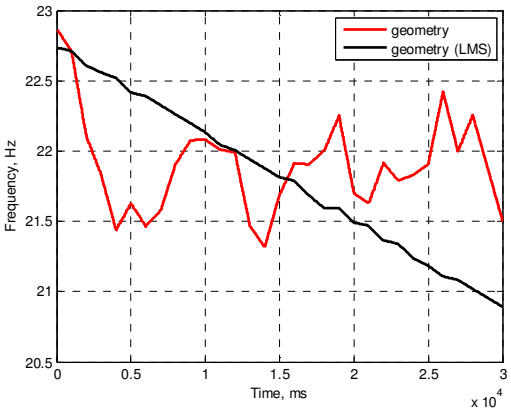

(d) Doppler shift estimation difference

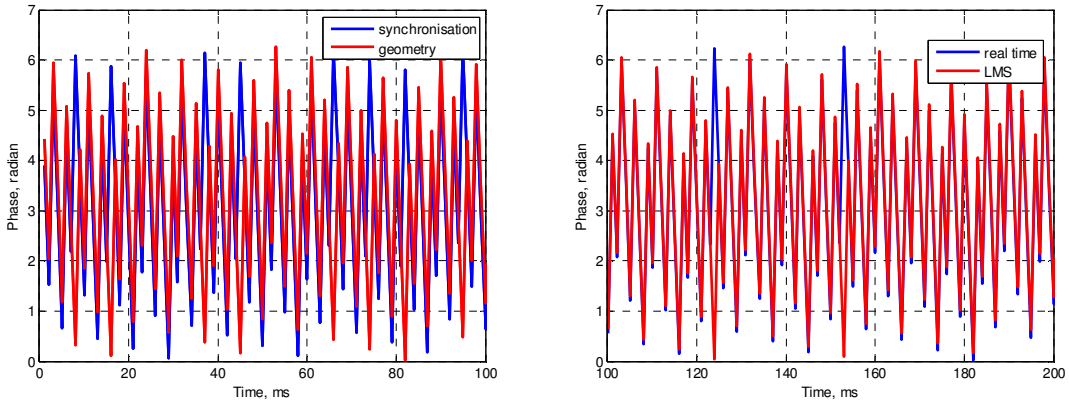

(e) phase history estimation (f) phase spectrum

Figure 6.26: *Comparison between Synchronisation Results and Parameters Estimation Results*

Figure 6.26 above provides the comparison between synchronisation results (Chapter 4) and parameters estimation results in the heterodyne channel. One is derived from the heterodyne channel signal and the other is derived from a geometrical approach.

Figure 6.26(a) plots the delay variation, which is derived from the baseline range history (Figure 6.25(a)). Figure 6.26(b) presents the comparison between this delay and the tracked delay (red line). The tracked value is from the delay-tracking loop of the proposed synchronisation algorithm. Both results are shifted to a start value of 0. Because the tracked value is a relative delay (code phase) measurement, it follows and extracts the change of delay without the information about the initial delay due to the transmitter-to-receiver range. One thing to mention here is that this initial delay could be found from the difference between the time of the signal being transmitted (included in the ephemeris) and the time of signal arrival. It can be seen that there is a divergence

between the two estimated delays, which is increasing with the time. This is mainly because the tracked delay not only presents the geometry motion between transmitter and receiver, but also includes the errors due to the propagation, local oscillator shifts, clock slippage etc.

Figure 6.26(c) shows the tracked Doppler shift and those from the geometry approach. The tracked Doppler shift are the values after least mean square fitting is applied to the actual Doppler shift tracking outputs. It is changing linearly without any non-linear component. However, the actual tracked Doppler shift is varying within about a 15 Hz range due to receiver noise (Figure 4.17). The other two plots in the figure are the same as Figure 6.25(d), which is the Doppler shift, estimated from the geometry coordinates. We can see a similar Doppler shift changing rate achieved by the two sources, but also there is a varying shift between the two sets of results, shown in Figure 6.26(d). The shift is ~ 22 Hz for this set of data, mainly coming from the clock offset between the transmitter and the receiver. Its value corresponds to the frequency accuracy ±25 Hz of the radar hardware (described in Chapter 5). So the difference between the two Doppler shift estimation techniques is mainly because of the frequency deviation of the local oscillator (frequency synthesizer) in the radar hardware. Figure 6.27 below will provide further proof for this assumption and the possible compensation that can be applied.

Figure 6.26(e) plots the phase variations (100 ms data) extracted by the tracking algorithm (blue line) and that derived from the range history (red line). Obviously the two estimated phases would not match each other as the two estimated Doppler shifts

have a varying shift. However, compensation schemes can be designed and tested using the frequency spectrum derived from these phases. Figure 6.26(f) presents the phase results derived from the range history, using real-time and least mean square output of receiver positions. It can be seen that the phases are almost overlapped with minor differences.

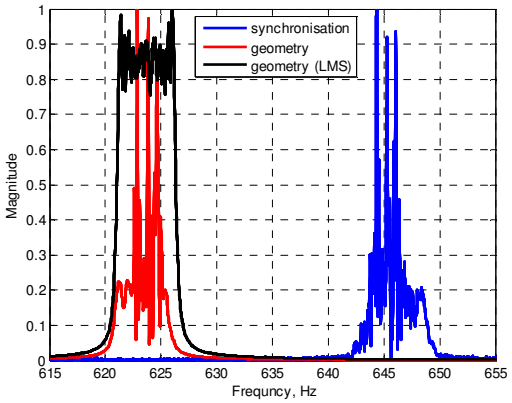

(a) phase spectrum

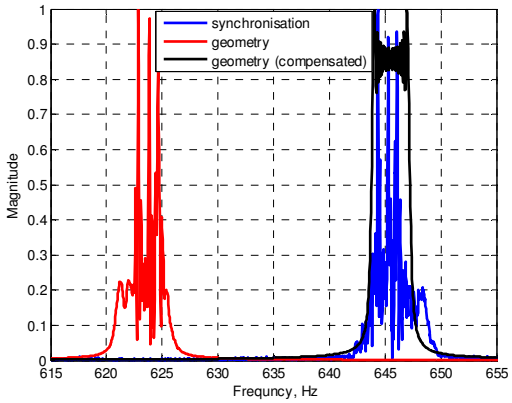

(b) phase spectrum

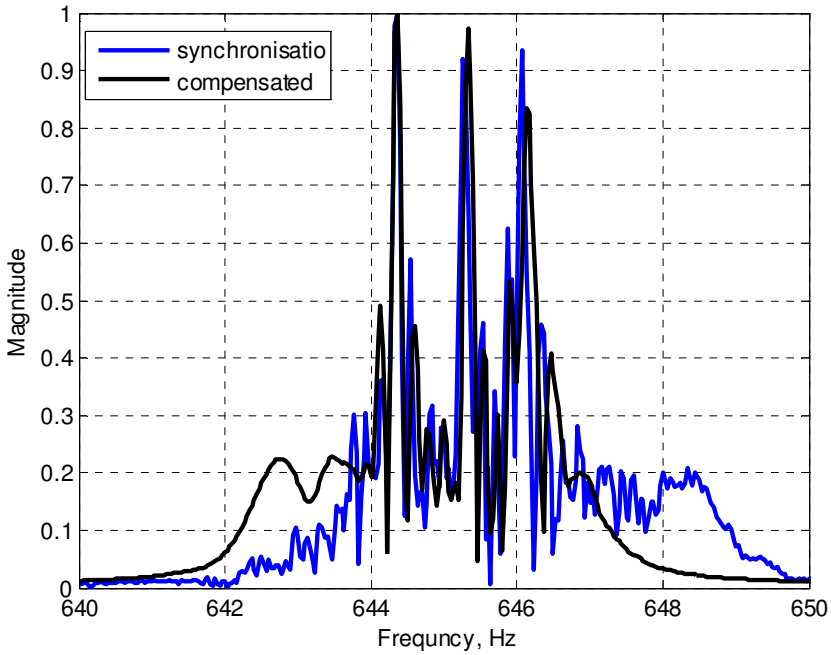

(c) phase spectrum (constant frequency shift compensation)

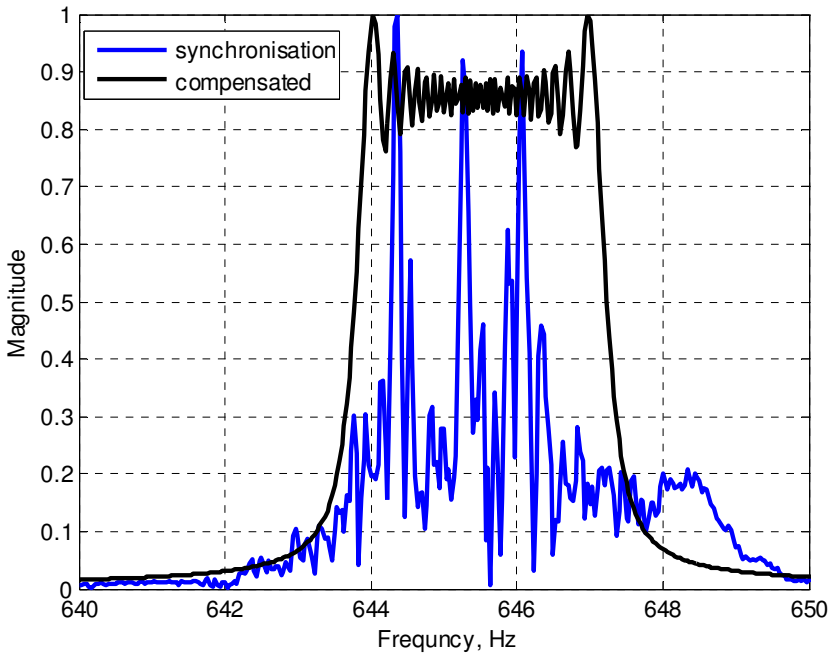

(d) compensated phase spectrum (zoom of (b))

Figure 6.27: *Motion Compensation (vehicle trial data)*

Figure 6.27 shows the frequency spectrum derived from the estimated phase variation and results of motion/phase compensation. Three phase spectrum are plotted in Figure 6.27(a), they are derived from the tracked phase (blue line) and the phase calculated from the transmitter/receiver range histories (red line from the motion between the satellite positions and real-time receiver positions; black line using least mean square output of receiver positions). These phases are actually corresponding to the Doppler shift in Figure 6.26(c), with the only difference in the tracked results. The tracked phase spectrum (blue line) presents the actual frequency/phase variation, but the Doppler shift in Figure 6.26(c) is the least mean square output. It can be seen that the tracked phase spectrum and the real-time geometry derived phase spectrum have similar patterns and fluctuations, for example, three high magnitude spikes. From these results, the tracking

(synchronisation) algorithm have been verified again; it clearly tracked and extracted the non-linear receiver motion.

Subsequently appropriate motion/phase compensation can be applied to both the directly received signal (heterodyne channel) and the reflected signal, for any undesired motion effects. Here we will only show the initial results of motion compensation applied to the heterodyne signal in SS-BSAR. Figure 6.27(b) again plots three phase spectrum, where the compensated phase spectrum is displayed as a black line. The proposed compensation is by shifting the red spectrum (geometry derived value) with the difference between the least mean square output of tracked Doppler shift and the geometry results, which is shown in Figure 6.26(d). It can be seen that a linear frequency modulated (LFM) signal (Figure 6.27(d)) is achieved after the phase compensation, hence the non-linear receive motion effect has been removed. Figure 6.27(c) shows the tracked phase spectrum and the geometry results compensated by a fixed value (21.5 Hz in this case). It can be seen that the two phase spectrum are not exactly the same, with small discrepancies due to the propagation or clock slippage, which is tracked by the synchronisation algorithm.

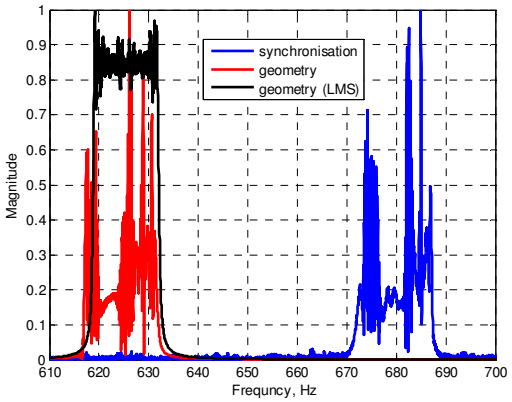

(a) phase spectrum (motion error compensation)

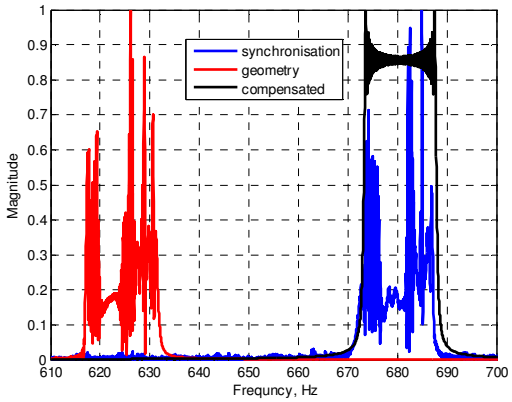

(a) phase spectrum (motion error compensation)

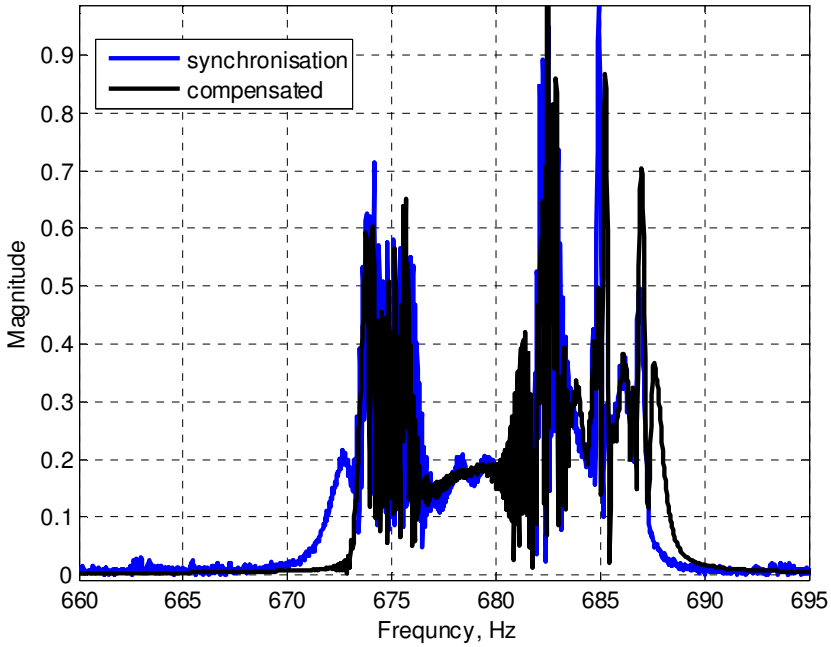

(c) compensated phase spectrum by fix frequency shift

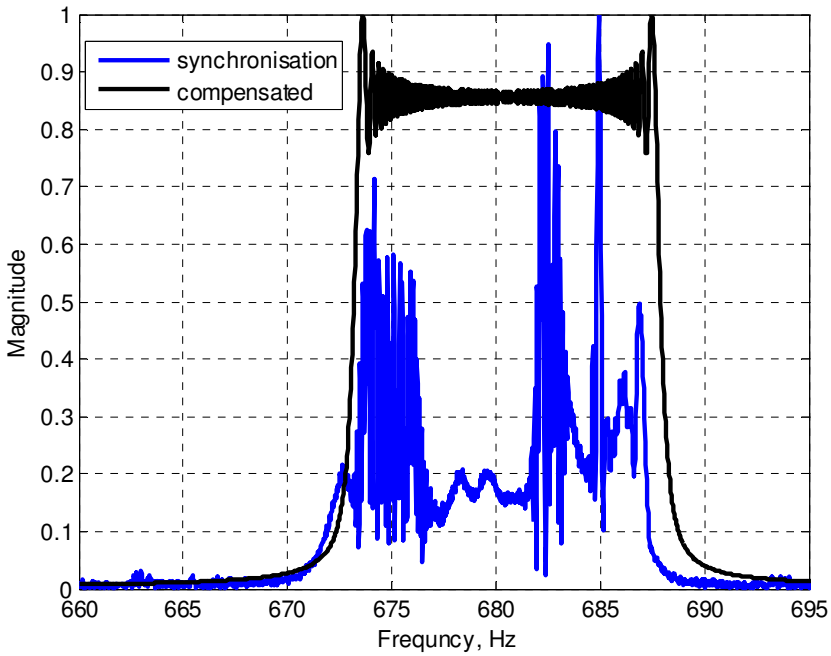

(d) compensated phase spectrum (zoom of (b))

Figure 6.28: *Motion Compensation (helicopter trial data)*

Figure 6.28 gives another example of motion/phase compensation. They are based on the helicopter trial data which is described in section 6.4. Similarly, three phase spectrum are plotted in Figure 6.28(a), they are derived from the tracked phase (blue line) and the phase calculated from the transmitter/receiver range histories (red line from the motion between the satellite positions and real-time receiver positions; black line using least mean square output of receiver positions). The tracked phase spectrum (blue line) presents the actual frequency/phase variation. It can be seen that the tracked phase spectrum and the real-time geometry derived phase spectrum have similar patterns and fluctuations, for example, multiple high magnitude spikes and a relative flat band around the centre. From these results, we can say that the tracking algorithm clearly tracked and

extracted the non-linear motion of the helicopter platform. Figure 6.28(b) again plots the compensated phase spectrum in a black line. It can be seen that a linear frequency modulated (LFM) signal (Figure 6.28(d)) is achieved after the phase compensation, hence the non-linear receive motion effect has been removed. Figure 6.28(c) shows the tracked phase spectrum and the geometry results compensated by a fixed value (56.3647 Hz in this case). It can be seen that the two phase spectrum are not exactly same, with a small discrepancy due to the propagation or clock slippage, which is tracked by the synchronisation algorithm.

6.6 Summary

This chapter consists of two main parts. The first part introduces the programme of experimentation leading to airborne SS-BSAR imaging. Experimental strategies and trials plans are designed to confirm the system performance. It has been divided into three stages: stationary receiver, ground moving receiver and airborne receiver. The actual experimental parameters and set-up block diagrams are also given.

The second part discusses the parameter estimation requirement for the proposed SS-BSAR system. Before applying the image formation algorithm to the experimental data, the parameters, such as, the transmitter/receiver trajectories, Doppler shift and phase histories need to be estimated with known accuracy. Two problems, residual Doppler shift and motion compensation are briefly discussed. The practical methods are proposed for transmitter/receiver parameter extraction and compensation. The estimation results from the real experimental data are discussed at the end of the chapter.

References

1. Ruck, G.T., et al., *Radar Cross Section Handbook*. Vol. 2. 1970: Plenum press.
2. Carrara, W., R. Goodman, and R. Majewski, *Spotlight Synthetic Aperture Radar: Signal Processing Algorithms*. 1995: Artech House.
3. Banks, P.M. and G. Kockarts, *Aeronomy*. Vol. A and B. 1973, San Diego, Califorinia: Academic.
4. Bauer, S.J. and H. Lammer, *Physics of Earth and Space enviroments*. 2004, Berlin: Springer.
5. Kelley, M.C., *Ionospheric Plasma Dynamics*. 1989, San Diego, California: Academic.
6. Parks, G.K., *Physics of Space Plasma: An Introduction*. 2nd ed. 2004, Boulder, Colorado: Westview Press.
7. Kirk, J.C., *Motion Compensation for Synthetic Aperture Radar.* IEEE Transactions on Aerospace and Electronic Systems, 1975. **AES-11**(3).
8. Mims, J.H. and J.L. Farrell, *Synthetic Aperture Imaging with Maneuvers.* IEEE Transactions on Aerospace and Electronic Systems, 1972. **AES-8**(4).
9. Kennedy, T.A., *Strapdown inertial measurement units for motion compensation for synthetic aperture radars.* IEEE Aerospace and Electronic Systems Magazine, 1988. **3**(10): p. 32-35.
10. Nies, H., et al., *Parameter estimation for bistatic constellations*, in *Geoscience and Remote Sensing Symposium, 2005. IGARSS '05*. 2005. p. 1038-1042.
11. Nies, H., et al., *A Solution for Bistatic Motion Compensation*, in *Geoscience and Remote Sensing Symposium, 2006. IGARSS 2006. IEEE International Conference*. 2006. p. 1204-1207.
12. Zhenbo, Z., T. Ziyue, and J. Xingzhou, *Research on Bistatic SAR Motion Compensation*, in *Radar, 2006. CIE '06. International Conference*. 2006. p. 1-4.
13. Cherniakov, M., et al., *Bistatic Synthetic Aperture Radar with Emitters of Opportunity*. 2006, Unversity of Birmingham: Birmingham.
14. Dow, J.M., R.E. Neilan, and C. Rizos, *The International GNSS Service in a changing landscape of Global Navigation Satellite Systems.* Journal of Geodesy, 2009(83): p. 191–198.
15. Celestrak. Available from: http://celestrak.com/.
16. Okan, V., *GPS*, http://www.movingsatellites.com/.
17. Hofmann-Wellenhof, Lichtenegger, and Collins, *GPS: Theory and Practice*. 5th ed. 2001: Springer.

18. Schenewerk, *A brief review of basic GPS orbit interpolation strategies.* GPS Solutions, 2003(6): p. 265-267.

19. Kelso, T.S., *Validation of SGP4 and IS-GPS-200D Against GPS Precision Ephemerides*, in *17th AAS/AIAA Space Flight Mechanics Conference*. 2007: Sedona, AZ.

20. *GPS Point Positioning Service CSRS - Precise Point Positioning (PPP).* Available from: http://webapp.csrs.nrcan.gc.ca/index_e/products_e/online_data_e/online_data_e.html.

21. Saini, R., R. Zuo, and M. Cherniakov, *Problem of Signal Synchronisation in SS-BSAR based on Global Navigation Satellite Emissions - Experimental Results.* IET Proceedings Radar, Sonar and Navigation, 2009. **4**(1): p. 110 - 125.

22. Antoniou, M., M. Cherniakov, and C. Hu, *Space-Surface Bistatic SAR Image Formation Algorithms.* Geoscience and Remote Sensing, IEEE Transactions on 2009. **47**(6): p. 1827 - 1843.

23. Antoniou, M., R. Saini, and M. Cherniakov, *Results of a Space-Surface Bistatic SAR Image Formation Algorithm.* Geoscience and Remote Sensing, IEEE Transactions on 2007. **45**(11): p. 3359 - 3371

Chapter 7 Experimental Results and Image Analysis

7.1 Image Formation Overview

In this section, a conceptual description of two BSAR image formation algorithms will be provided, which have been applied to the experimental data. However, before proceeding with our analysis, it is important to describe the structure of the BSAR collected data, to explain the need for and the purpose of SAR image formation algorithms in general, and to provide a brief background of general methods used for SAR signal compression.

The raw SAR data, collected during aperture synthesis, are assumed to be recorded in two dimensions. The first one is defined as the fast-time (or range-time) dimension; it is associated with propagation delays between signal transmission and echo reception. The second is defined as the slow-time (or azimuth-time) dimension; this is used in the specification of the radar's position during array synthesis. The reason for this notation is that the signals' propagation speed (the speed of light) is much faster than the speed of the transmitter/receiver platforms. Conceptually then, data collection proceeds as follows: In each radar position (corresponding to an instant in slow-time), the radar stops, transmits a pulse, records the pulse's echoes from the imaging area over a pre-defined time interval in the fast-time domain, and then advances to the next position. This is commonly known as the stop-and-go assumption.

Now, if we consider a single point target within an imaging area, the transmitter-to-target-to-receiver time, and hence the target's apparent range from the radar, varies as the radar moves from one position to another (i.e. it varies with slow-time). If the range variation is greater than the system's range resolution, this effect is known as range cell migration (range cell migration) and needs to be corrected, since the signal's energy is now distributed along several range bins. After range cell migration correction, the signal's energy is concentrated in one range bin, corresponding to the target's range of closest approach to the radar. Correction of range cell migration is an integral part of SAR signal processing, and the way it is performed often constitutes the main difference between some SAR algorithms.

Once the SAR data have been collected from the observation area and demodulated by the coherent microwave receiver, it is the purpose of SAR processing to produce an image by mapping target echoes from within that area into an evenly spaced (x, y) output grid. The x-coordinate represents 'forward' range (perpendicular to the synthesized array) and the y-coordinate represents lateral range, otherwise known as cross-range. The targets' forward ranges can be found from the relevant signal propagation delays, to and from the radar (fast-time information); their lateral ranges can be found from their azimuth phase signatures (slow-time information).

Whereas some of the monostatic SAR algorithms have previously existed for decades, interest in BSAR algorithms has risen only in the last few years. BSAR algorithms exist

which process data, partially, in the time domain but, as far as the author is aware, a generalized, entirely frequency domain, precision BSAR algorithm (such as the RDA, range cell migration, CSA) is not yet available. Here "generalized" means an algorithm which is able to process data collected with the transmitter and receiver flying in non-parallel flight paths, with unequal velocities.

A plan view of a general BSAR data collection geometry is shown in Figure 7.1. The transmitter and receiver are moving along the paths with velocities V_T, V_R, respectively, so that their synthetic aperture lengths during the data collection time are unequal. The cross-range direction y is defined to be the same as the receiver's moving path, and the range direction x is perpendicular to y. For a point target at coordinates (R_{R0}, y_0), the instantaneous transmitter-to-target and receiver-to-target slant ranges $R_T(u)$ and $R_R(u)$ are given by:

$$R_T(u) = \sqrt{{R_{T0}}^2 + {V_T}^2 (u_{T0} - u)^2} \tag{7.1}$$

$$R_R(u) = \sqrt{{R_{R0}}^2 + {V_R}^2 (u_{R0} - u)^2}\ , \tag{7.2}$$

where R_{T0}, R_{R0} are the transmitter's and receiver's slant ranges of closest approach to the target, occurring at slow-times u_{T0}, u_{R0}, with $y_0 = V_R u_{R0}$.

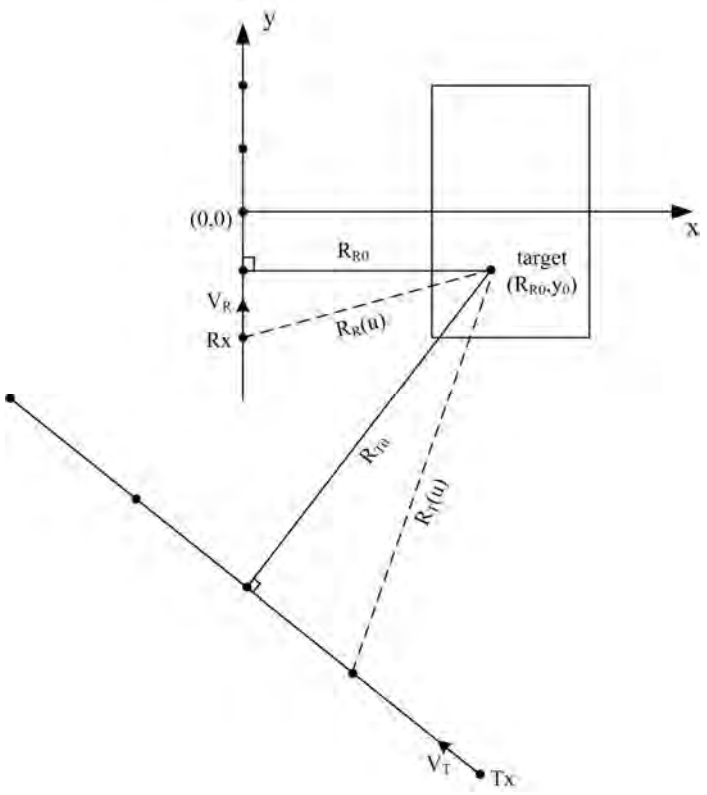

Figure 7.1: *General BSAR Geometry (2D view)*

Assuming the target is within the transmitting and receiving antennas' mainlobe for the whole integration time, then after baseband demodulation, the received signal from this point target is given by:

$$s(t,u) = p\left[t - \frac{R_T(u)}{c} - \frac{R_R(u)}{c}\right]\exp\left\{-j2\pi f_c\left[\frac{R_T(u)}{c} + \frac{R_R(u)}{c}\right]\right\} \tag{7.3}$$

where the azimuth signal's envelope has been omitted. From Equation 7.3, we see that the round trip two-way propagation delay of the monostatic signal has been replaced by

the two-path (transmitter-target and target-receiver) time delay in the bistatic signal; the different time delay, and delay variation, implies different signal phase, and phase variation. The slant ranges of closest approach are different for the transmitter and the receiver. Moreover, since the transmitter and the receiver move in different trajectories and their aperture lengths are different, $R_T(u)$ and $R_R(u)$ vary differently with slow-time. As a result, the total range cell migration is the sum of two individual and different range cell migrations, one due to the transmitter's motion, the other due to the receiver's. As far as phase variation across the aperture is concerned, we see from Equation 7.3 that this is the sum of two independent and different modulations, one due to the transmitter's motion relative to the target, and one due to the receiver's.

As in the monostatic case, the most straightforward way to process the signal in (7.3) is by two-dimensional matched filtering in the time domain. Note that each received fast-time sample corresponds to the range sum $R_T + R_R$, however we want each output grid point in the image to represent range and cross-range respect to the receiver. Therefore, for each output grid point (R_{R0i}, u_{Rj}), i.e. for each target at these coordinates, the transmitter-to-target and receiver-to-target range histories are given by:

$$R_{T(i,j)}(u) = \sqrt{{R_{T0i}}^2 + {V_T}^2 (u_{Tj} - u)^2} \tag{7.4}$$

$$R_{R(i,j)}(u) = \sqrt{{R_{R0i}}^2 + {V_R}^2 (u_{Rj} - u)^2}\ , \tag{7.5}$$

where R_{T0i}, R_{R0i} are the transmitter's and receiver's slant ranges of closest approach to the target, occurring at time u_{Tj}, u_{Rj}. Then the filter's response for the particular grid point can be written as:

$$s_0(t,u) = p\left[t - \frac{R_{T(i,j)}(u)}{c} - \frac{R_{R(i,j)}(u)}{c}\right]\exp\left\{-j2\pi f_c\left[\frac{R_{T(i,j)}(u)}{c} + \frac{R_{R(i,j)}(u)}{c}\right]\right\} \quad (7.6)$$

and the matched filtering operation is given by:

$$f(R_{R0i}, u_{Rj}) = \sum_t \sum_u s(t,u) \times s_0^{*}(t,u), \quad (7.7)$$

where the double sum is over all the available values of (t,u).

The similarity between (7.7) and the monostatic matched filtering operation is evident. However, there are some fundamental differences. In the monostatic case, in order to calculate the filter's response at a particular grid point, we need only to calculate the round-trip range of closest approach (of the radar to the target) and the corresponding azimuth time. Image formation calculations are straightforward, since the sample spacings of the output grid in the range-time and azimuth-time dimensions coincide with the sample spacings of the received signal (input to the SAR processor), and they are uniform. For the bistatic case, in order to calculate the filter's response at a particular output grid point, we need to find both the transmitter's and the receiver's ranges of closest approach and their corresponding azimuth times. This means that, for each output point, most of the parameters need to be recalculated. Furthermore, as mentioned

previously, the range (fast-time) sampling of the received signal now corresponds to the range sum $R_T + R_R$ so that, if the range samples of the output grid are to correspond to R_R then, because there is a non-linear relationship between R_R and R_T, the range sample spacing will be uneven.

The basic problem in deriving a generalized frequency domain algorithm for BSAR is the difficulty in obtaining an azimuth Fourier transform. Applying a range FT on the signal given by (7.6) we obtain:

$$s(f,u) = P(f)\exp\left\{-j2\pi(f+f_c)\left[\frac{R_T(u)+R_R(u)}{c}\right]\right\} \tag{7.8}$$

To obtain the signal's form in the two-dimensional frequency domain, we need to apply azimuth Fourier transformation to the signal given by (7.8). For BSAR, a relationship between azimuth time and azimuth frequency has been found "hard" or "impossible" to calculate. This is the main impediment to the derivation of a generalized, exact frequency domain BSAR algorithm. Without a relationship between azimuth time and frequency, neither the envelope nor the phase of the BSAR signal can be derived in the azimuth frequency dimension. As a result, neither range cell migration correction nor azimuth compression can be attempted in this dimension.

The Range-Doppler algorithm

Range-Doppler algorithm (RDA) has been applied to the experimental data, collected for stationary receiver experiment (described in section 6.2). The reason for this is the simplicity of its implementation; and the experimental topology is quasi-monostatic with small bistatic angle. The SAR compression in the range-Doppler algorithm is performed using two independent one-dimensional filters. It therefore assumes that the range and azimuth frequencies are independent. Its main feature is the approximation of the instantaneous slant range given in (for monostatic case):

$$R(u) = \sqrt{R_0{}^2 + V^2 u^2} \approx R_0 + \frac{V^2}{2R_0} u^2, \tag{7.9}$$

where the range history has been expanded into a Taylor series around the point $u = 0$, keeping the first two terms. To make this approximation means that higher order terms are insignificant, and this can only hold if $R_0 >> Vu$. This is more commonly known as the parabolic approximation. Making this approximation has two effects. The first one is that the problem of range cell migration correction can be solved efficiently in the range-time, azimuth-frequency (or range, Doppler) domain, from which its name stems. The second is that the phase of the azimuth signal model now has a quadratic form, implying a linear frequency modulated (LFM) signal, which simplifies its analysis and the design of an appropriate azimuth filter. However, it is noted that all these simplifications are the results of an approximation, so the algorithm, even though significantly faster than both of the previous processing methods, cannot yield the same precise results.

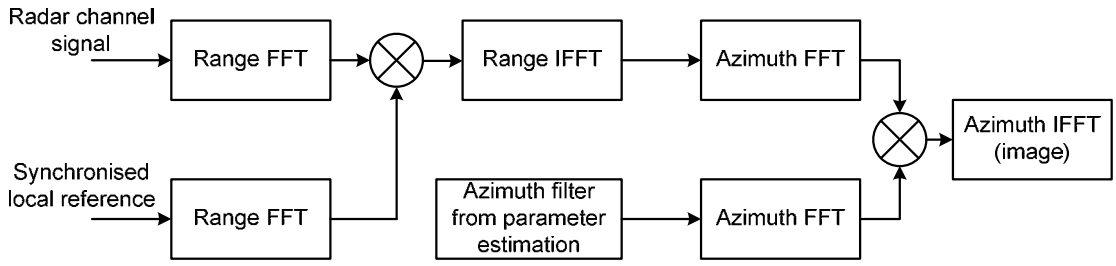

Figure 7.2: *Block Diagram for Range-Doppler Algorithm*

Figure 7.2 gives the block diagram for standard range-Doppler algorithm. As the first stage of SS-BSAR image formation, we will apply it to the stationary receiver experimental data. The image results obtained are shown in section 7.2.

The first step of processing is range compression of the received SAR signal. It is implemented by the correlation of radar channel signal with the synchronized local reference. The local reference is the replica of heterodyne channel signal but with high SNR. Its generation has been discussed in section 4.3 (Figure 4.12). After the data have been compressed in range, they are converted to the range-time, azimuth-frequency domain. This is where the range cell migration correction can be implemented. For monostatic SAR, it has been established that targets at the same range, but different cross-ranges, share the same range cell migration curve in this domain. The amount of range cell migration to correct is known, and because of the parabolic approximation, this range cell migration turns out to be range and Doppler-dependent. However, for bistatic SAR, the range cell migration is more complicated and space-varying. A few assumptions have to be made to apply monostatic range cell migration correction methods to bistatic SAR data. For a stationary receiver with a relatively small target area

and quasi-monostatic topology, an approximation is to consider that the range cell migration is range-invariant, so that all targets experience the same range cell migration as the target at the imaging scene centre. In this case, the range cell migration correction can be implemented by a range FFT, linear phase multiply and range IFFT. This method, however, imposes a limit on the range interval of observation. After range cell migration has been corrected, azimuth compression is performed. The principle is the same, but since the parabolic approximation has been assumed, the equations for the received and reference azimuth signals should be recalculated. The output of the azimuth compression yields the complex image of the observation area.

Bistatic Back-Projection Algorithm

In this section a conceptual overview of the generalized bistatic back-projection algorithm (BBPA) algorithms will be presented. It has been applied to the experimental data obtained from ground moving and airborne receiver experiments. Two image results are shown and analyzed in section 7.3, which is from one target area, simultaneously illuminated by two Galileo satellites.

The bistatic back-projection algorithm operates only partially in the frequency domain, thus suffering from inefficiency problems. Interestingly, however, it appears that the first generalized algorithm for bistatic SAR was a modification of the back-projection algorithm. Its principle of operation is very similar to that of the monostatic back-projection algorithm, the only difference lying in the calculation of the transmitter-target-

receiver propagation time delay which is used in the interpolation step. A block diagram of the BBPA is shown in Figure 7.3, followed by appropriate discussion.

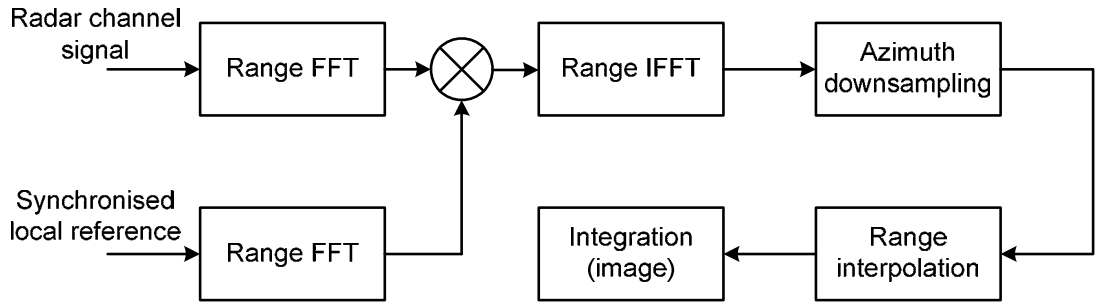

Figure 7.3: *Block Diagram of BBPA*

It can be seen that, conceptually, the BBPA is the same as its monostatic counterpart. The first step in the algorithm is the standard range compression performed in the range frequency domain. This step performs the summation over all the available discrete samples t_i of equation (7.3). If the range-time match-filtered signal at the grid point (R_{R0i}, u_{Rj}) is denoted again by $s_M \lfloor t_{ij}(u), u \rfloor$, the range compression output is:

$$f\left(R_i, u_j\right) = \sum_u s_M \left[\frac{R_{T(i,j)}(u) + R_{R(i,j)}(u)}{c}, u \right] = \sum_u s_M \left[t_{ij}(u), u \right], \tag{7.10}$$

then $t_{ij}(u)$ in this case is given by:

$$t_{ij}(u) = R_{T(i,j)}(u) + R_{R(i,j)}(u), \tag{7.11}$$

with $R_{T(i,j)}(u)$, $R_{R(i,j)}(u)$ given by (7.4), (7.5). As in the monostatic case, this means that, in practice, the discrete fast-time samples of $s_M(t,u)$ must be interpolated to recover $s_M\lfloor t_{ij}(u),u\rfloor$. The only difference is in the calculation of $t_{ij}(u)$.

If range cell migration exists after range compression, it is seen from (7.10) that the SAR signal energy is distributed along a number of range bins. However, a corrective process is suggested and stated explicitly in [1]: "to form the target function at a given grid point, one could coherently add the data at the fast-time bins that correspond to the location of that point for all synthetic aperture locations u" (i.e. execute the azimuth time summation of (7.10)). In practice, this is done by an interpolation in the range time domain, so as to recover $s_M\lfloor t_{ij}(u),u\rfloor$ from the discrete fast-time samples of $s_M(t,u)$. The back-projection algorithm owes its name to this concept. For each aperture position, the back-projection algorithm traces the range-processed data back (back-projection) in the range time domain to isolate the return of a reflector at a given point in the image output grid.

The actual implementation steps, applied the experimental data for bistatic back-projection algorithm, are the following:

- Fast time domain matched filtering, $s_M\left[t(u),u\right]$
- Fast time frequency domain interpolation by zero padding, $s_M\lfloor t_{ij}(u),u\rfloor$
- Create the image matrix $f\left(x_i,y_j\right)$ with local coordinates

- For fixed $f\left(x_i, y_j\right)$ and one azimuth position, find $t_{ij}\left(u\right)$
- Change the azimuth position, repeat the above step and sum $\sum_u s_M\left[t_{ij}\left(u\right), u\right]$

The bistatic back-projection algorithm suffers the same inefficiency problems as the back-projection algorithm. A more efficient version of the bistatic back-projection algorithm has also been developed [2]. We will briefly describe its main principle. Let us use the term "projection" to define the location of the target's cross-correlation function in fast-time, for a single sampling point in the receiver's aperture, after range compression and range time interpolation (according to Figure 7.3). If we have N samples in the receiver's aperture, we need to back-project N projections of the target to reconstruct it. This means that if we have an imaging grid of NxN points, we need to back-project N projections for each of the N^2 pixels, so the total computational cost is N^3. The efficient version of the bistatic back-projection algorithm states that images that are half the size of the original image can be reconstructed from half the number of projections [3].

With this in mind, let us go back to our previous example. Suppose we split our imaging grid into four sub-images. Each sub-image has N/2xN/2 points. For each pixel in the sub-image, we only need to back-project N/2 projections. The total computational cost for each sub-image is now $N^3/8$, and for the whole image it is $N^3/2$. This means that by splitting the image into four sub-images, we have reduced the computational cost by a factor of two. Decomposing the image recursively, and back-projecting using half the

number of projections for the smaller sub-images, the total computational cost reduces further.

However, there is a problem in using this algorithm when the carrier frequency of the transmitted signal is high. Even for the standard back-projection algorithm, the range time interpolator must be accurate enough to recover the samples of $s_M\left[t_{ij}(u),u\right]$ correctly. If the upsampling factor of the interpolator is insufficient, phase errors are introduced which could be significant. This upsampling factor was found to be proportional to the carrier frequency of the transmitted signal. This means that as the carrier frequency increases, our imaging grid at the output of the interpolator must have more samples in the range time direction. In that case the interpolation step, as well as the azimuth summation step (in whatever way it is performed), make the back-projection algorithm and the bistatic back-projection algorithm inefficient.

7.2 Experimental Image Results – Stationary Receiver

This section presents the experiment image results, obtained from stationary receiver experiments. The data used was collected on 04.11.2009, with GIOVE-A satellite as the transmitter. One corner reflector (CR) has been used as the reference target at the distance of 45 m to the stationary receiver. The experimental set-up and other parameters for the data collection have been included in section 6.2.

The results from two data sets will be introduced below; the two data sets are 30 s and 120 s long (total integration time) respectively. One data set was recorded at 12:56:34

GMT and the other one was recorded at 12:57:55 GMT. The results shown below, Figures 7.4 and 7.5 include the synchronisation results (delay, Doppler shift and phase tracking outputs), heterodyne channel focusing results and radar channel azimuth compressing (imaging) results. Each result will be comprehensively described and explained.

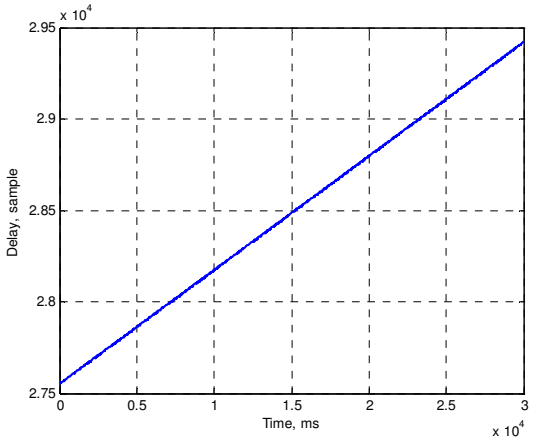

(a) delay

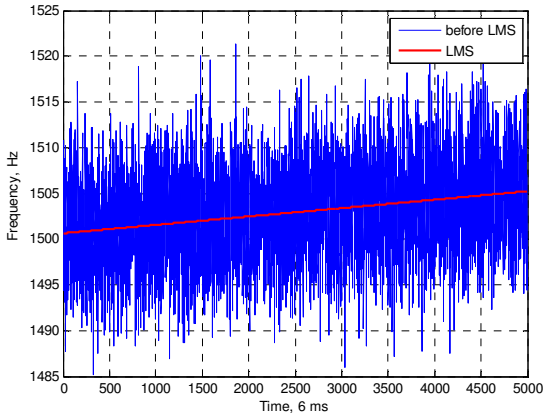

(b) Doppler shift

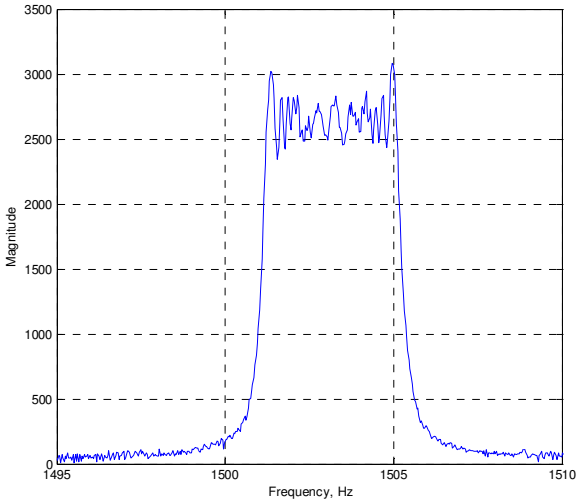

(c) phase history

Figure 7.4: *Synchronisation Outputs*

Figure 7.4 above shows the synchronisation outputs for the 30 s data set. It includes the delay tracking output, Doppler tracking output and phase tracking output. These parameters will be used for the local reference generation for further image formation processing. The detail of the synchronisation algorithm and local reference generation has been discussed in Chapter 4. From Figure 7.4(c), the Doppler bandwidth is about 5 Hz for 30 s observation.

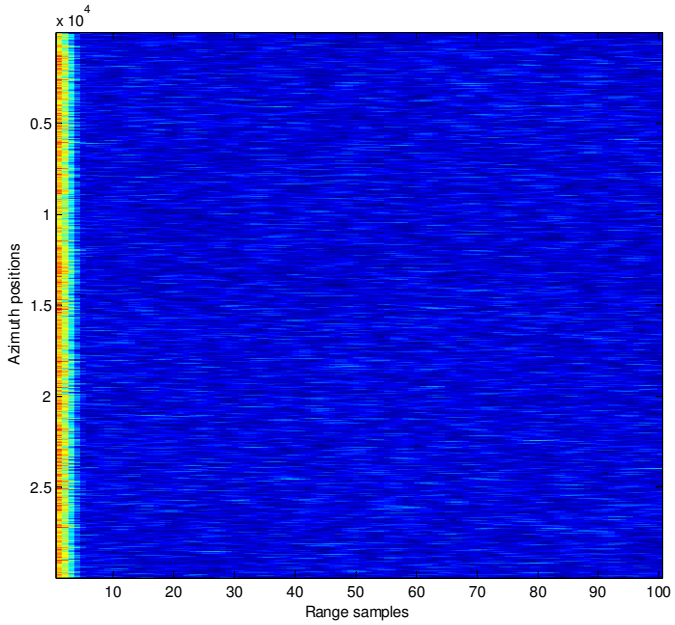

(a) Range compression of heterodyne channel data

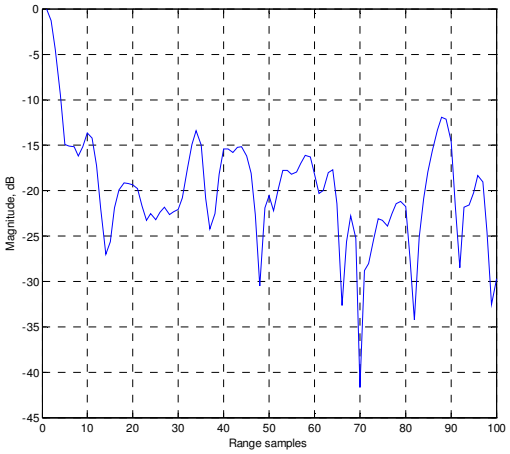

(b) Range cross-section

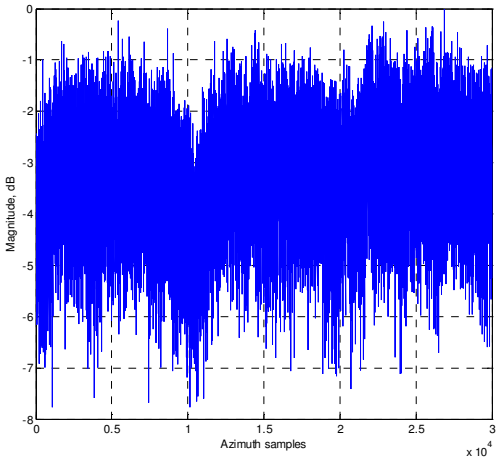

(c) Azimuth frequency

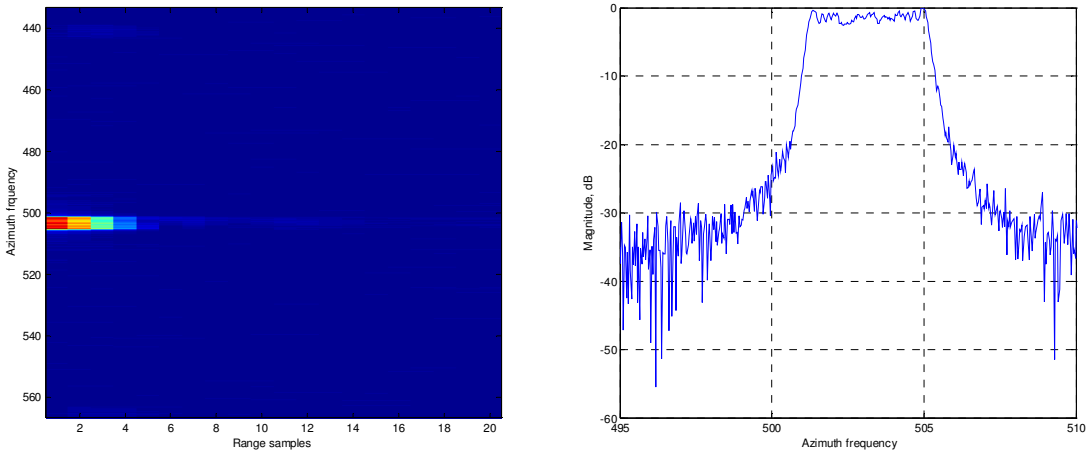

(d) FFT of range compression output (e) azimuth frequency

Figure 7.5: *Heterodyne Channel Range Compression Results*

Figure 7.5 above gives the heterodyne channel range compression results. This step is used to establish whether the local reference signal created after synchronisation and used for compressing the radar channel data in range is correct. The main concern was whether the reference signal contains the correct Doppler/phase. For Figure 7.5(a), the X-axis is the range sample, the first 100 range bins are shown; the Y-axis is the azimuth sample, 30000 azimuth samples (1ms/sample) are equivalent to 30s azimuth integration time. It can be seen that data in heterodyne channel were compressed using a reference signal which contained the tracked signal delay, but not the tracked Doppler/phase. Its range and cross-range cross-section are given in Figures 7.5(b) and 7.5(c).

At each cross-range position, target energy is concentrated at the first range bin, indicating that the tracked signal delay is correct. Selecting all samples at this range bin and taking a Fourier Transform, yields the Doppler spectrum of the heterodyne signal (Figure 7.5(e)). The result of azimuth FFT on range compression output is shown in

Figure 7.5(d). By comparing Figure 7.5(e) and Figure 7.4 (c), the two phase spectrum are identical, hence both the local reference generation method and range compression have been verified. We can then proceed to compress the heterodyne signal in azimuth using the tracked phase.

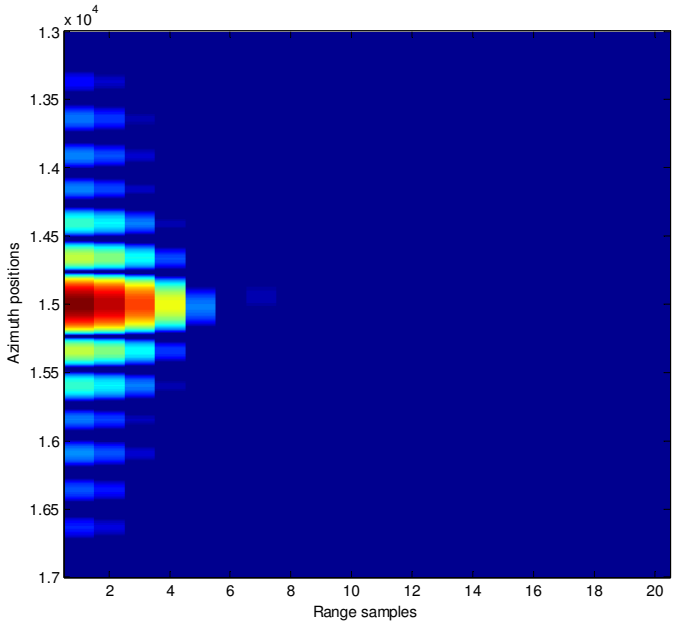

(a) Focusing of heterodyne data (azimuth compression)

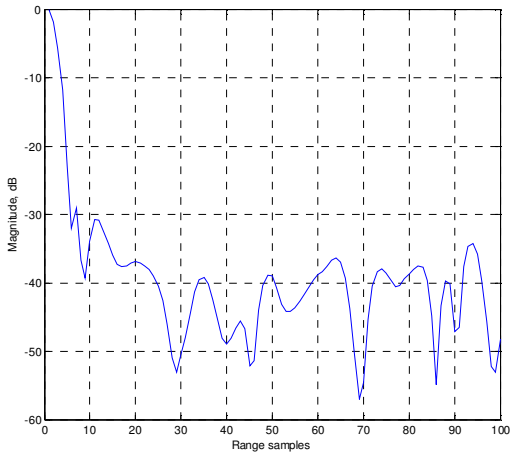

(b) Range cross-section

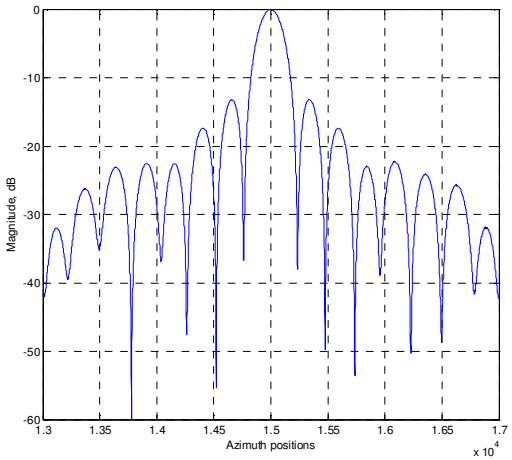

(c) Cross range cross-section

Figure 7.6: *Heterodyne Channel Focusing*

Figure 7.6 shows the focusing results of the heterodyne channel data. The tracked phase (Figure 7.4(c)) is used to form the azimuth filter as discussed previously. It can be seen that the heterodyne channel has been properly compressed, both in range and in azimuth. A sinc function, like point spread function, has been obtained (Figure 7.6(a)). The mainlobe width of the correlation peak in range is equal to 5 range samples, corresponding the 10 MHz ranging code sampled by 50 MHz. A cross-section of the compressed output along the azimuth direction is shown in Figure 7.6(c). We can now proceed to compress the radar channel signal in range and in azimuth.

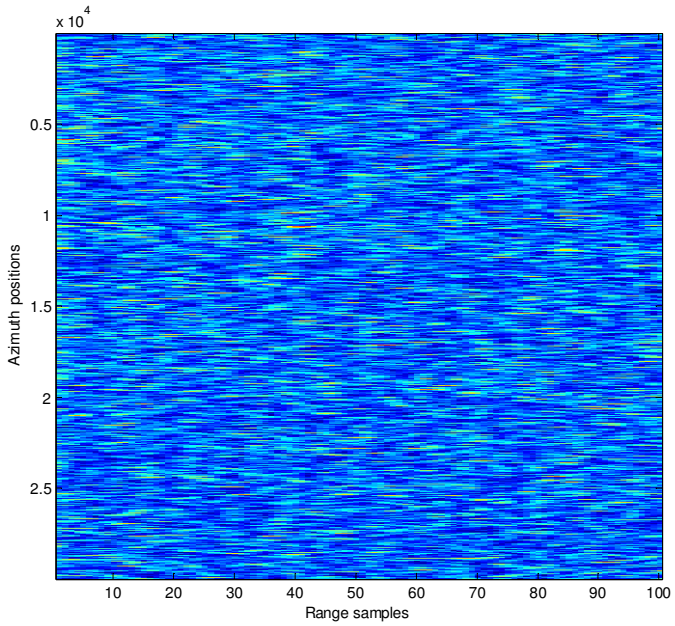

(a) Range compression of radar channel data

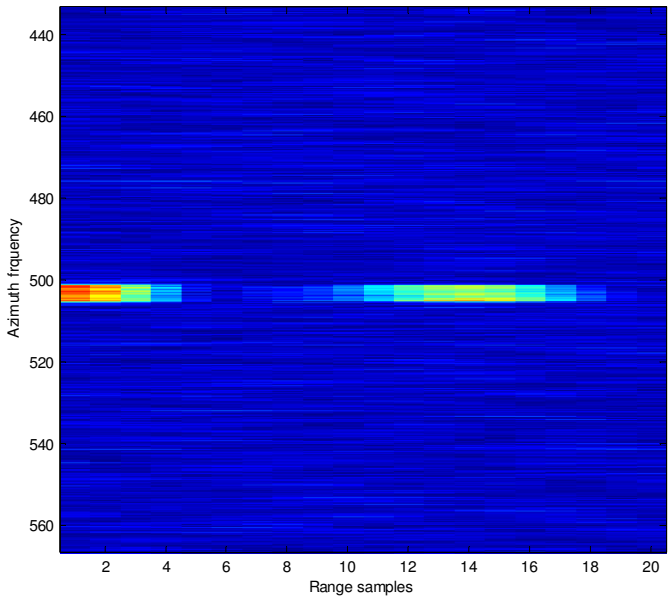

(b) azimuth FFT

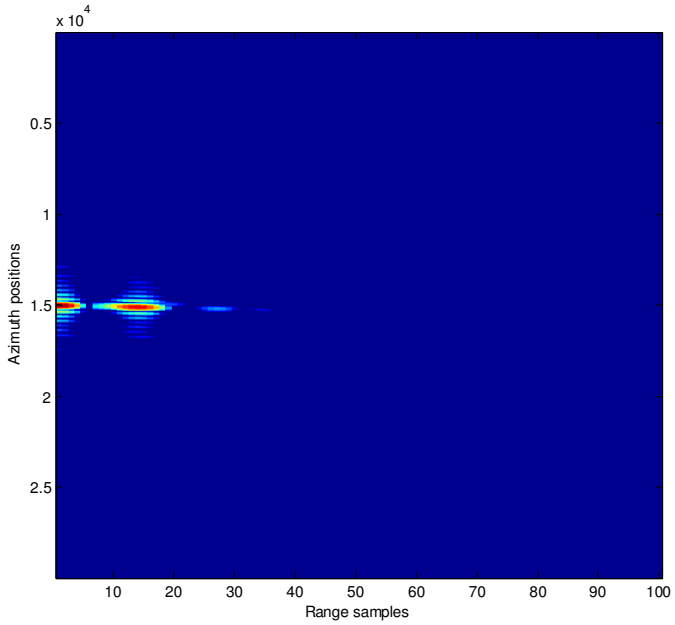

(c) azimuth compression (imaging)

Figure 7.7: *Corner Reflector Imaging Results*

Figure 7.7 gives the imaging results from the stationary receiver experiment for corner reflector detection. It is obtained by compressing the radar channel data using a simplified range-Doppler algorithm. One critical assumption has been made, which is the azimuth history of the corner reflector (45 m to receiver) is equal to the phase history tracked in the heterodyne channel. This is true because the transmitter-to-target range of 23000 km contrasts to the 45 m receiver-to-target range.

Figure 7.7(a) presents the range compression output of radar channel signal. It can be seen that the SNR is relatively low with no obvious correlation because it is a reflected signal. However, as soon as an FFT is applied to this output, two frequency spectrums (Figure 7.7(b)) can be identified in the range time-azimuth frequency domain. Using the tracked phase as an azimuth filter, the azimuth compression has been formed.

From Figure 7.7(c), we can see that two point target like reflections are clearly shown. The first point spread function is identified as the direct interference in the radar channel (compare to Figure 7.6(a)), which is received by the sidelobe of radar channel antenna. The second point spread function is identified as the reflection from the corner reflector; it appears at the 14^{th} range sample, which is equal to the slant range of 84 m to the receiver. This is because the slant range here is actually the bistatic range, which is the sum of the receiver-to-target range and the difference between the transmitter-to-target and the transmitter-to-receiver ranges. In this experimental set-up, it is approximately twice (90 m) the receive-to-target range, considering the small bistatic angle. The colour

scale of the radar image is in dB, where 0 dB represents the pixel with the highest intensity. The dynamic range of the image has been artificially clipped to 30 dB.

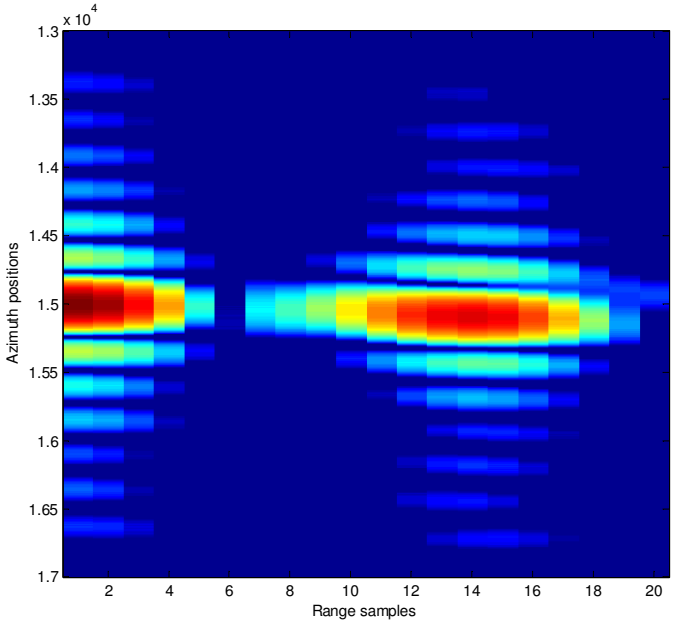

(a) zoom (corner reflector image)

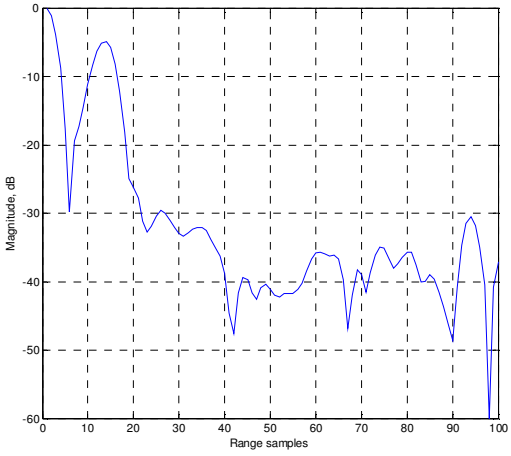

(b) Range cross-section

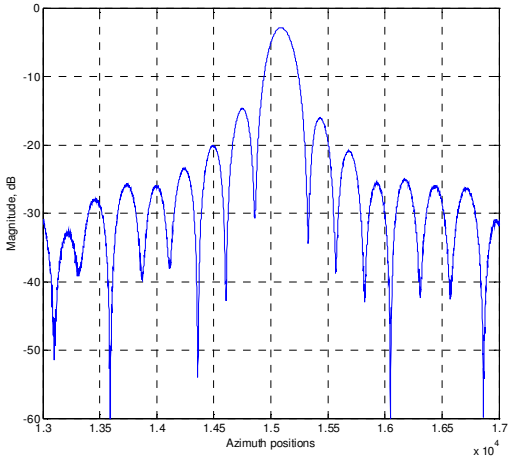

(c) Cross range cross-section

Figure 7.8: *Corner Reflector Imaging Results*

Figure 7.8 presents the zoom plot of corner reflector image with its cross-sections.

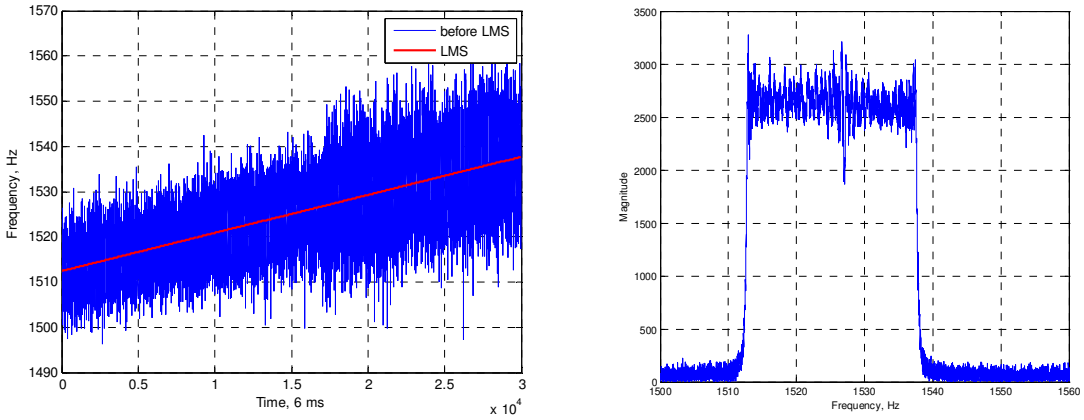

(a) Doppler shift

(b) phase history

Figure 7.9: *Synchronisation Outputs*

Figure 7.9 above shows the synchronisation outputs for the 120 s data set. From Figure 7.9(b), the Doppler bandwidth is about 25 Hz for 120 s observation. We should expect the improvement in azimuth resolution for this data, comparing to the 30 s data.

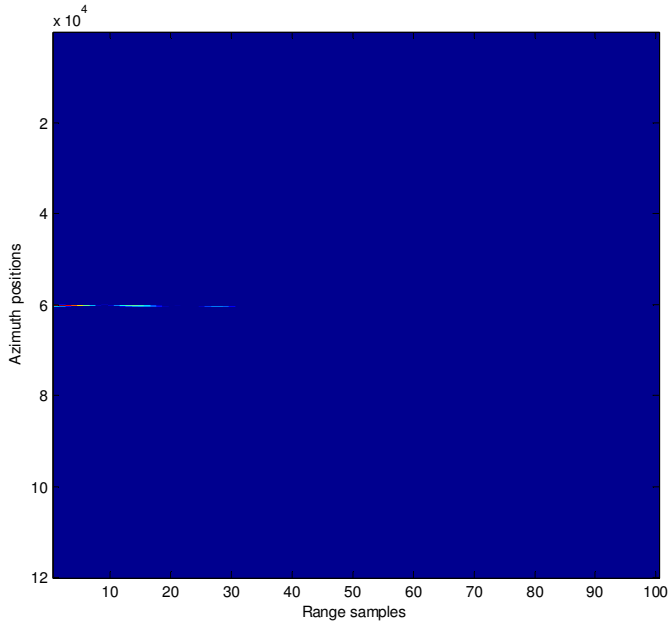

(a) azimuth compression output (imaging)

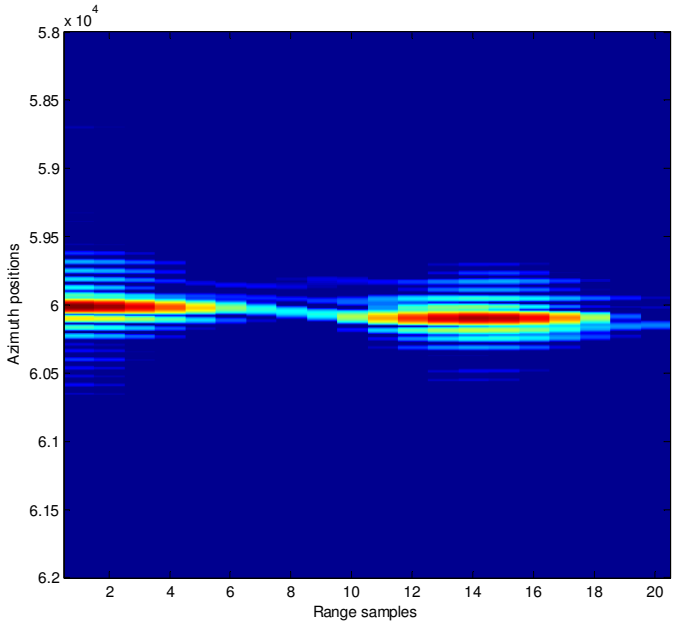

(b) zoom (corner reflector image)

Figure 7.10: *Corner Reflector Imaging Result 2*

With the same processing procedures applied to 120 s data, Figure 7.10 gives another imaging result from the stationary receiver experiment for corner reflector detection. Y-axis of Figure 7.10(a) indicates 120000 azimuth positions this time. Again, we can see that two point target like reflections are clearly shown. The second point spread function appears at the 14^{th} range sample too, which is equal to the slant range of 84 m to the receiver. The colour scale of the radar image is in dB, where 0 dB represents the pixel with the highest intensity. The dynamic range of the image has been artificially clipped to 30 dB.

Figure 7.11 below shows the range and cross-range cross-sections of second point spread function of both images (30 s and 120 s). It is clearly seen that SNR has improved and finer azimuth resolution has been achieved by using a longer integration time.

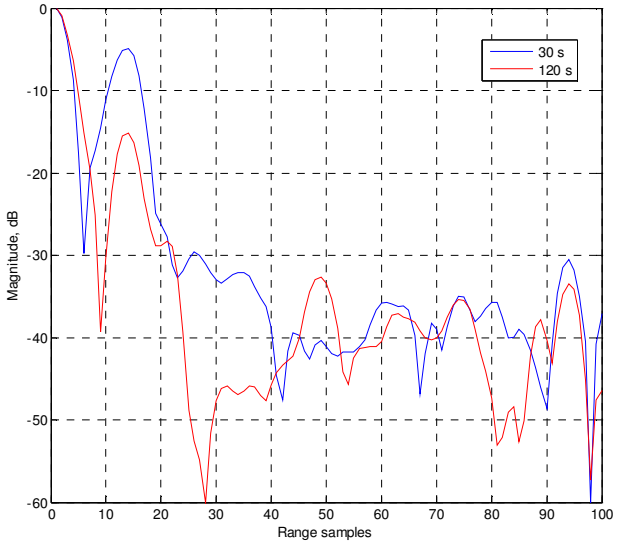

(a) Range cross-section

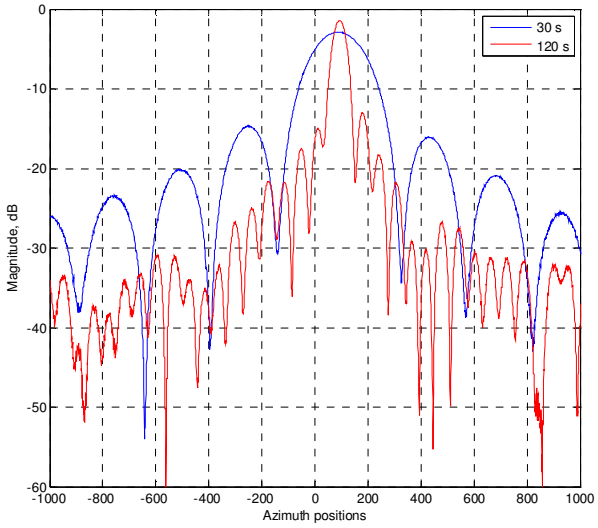

(b) Cross range cross-section

Figure 7.11: *Range and Cross Range Cross-sections*

7.3 Experimental Image Results – Ground Moving Receiver

This section presents the experiment image results, obtained from the ground moving receiver experiments. The data used was collected on 22.12.2008, with both GIOVE-A and GIOVE-B satellites signals received. The experimental set-up and other parameters, such as the target area analysis, have been included in section 6.3. The separated houses shown in Figure 6.10 are used as the targets for detection.

Galileo satellites adopt a CDMA scheme; one recorded data set can contain the signals from all visible satellites. So, two images can be generated with one receiver aperture from both GIOVE A/B satellites. The two image results will be introduced below; the data length is 30 s and it was recorded at 10:18:18 GMT. The results shown below include heterodyne channel focusing results and radar channel azimuth compressing (imaging) results. The description and explanation of each result will be comprehensively discussed.

To implement the full bistatic back-projection algorithm described in section 7.1, we also need to verify whether the instantaneous ranges (transmitter-target, receiver-target and transmitter-receiver) calculated from our extracted transmitter and receiver positions are correct. The parameter estimation results are included and discussed in section 6.5.4 for this particular data.

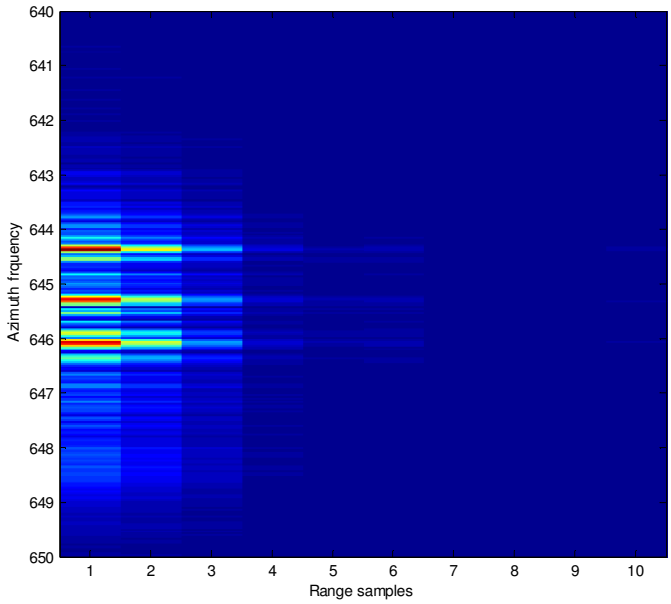

(a) FFT output of range compression for heterodyne data

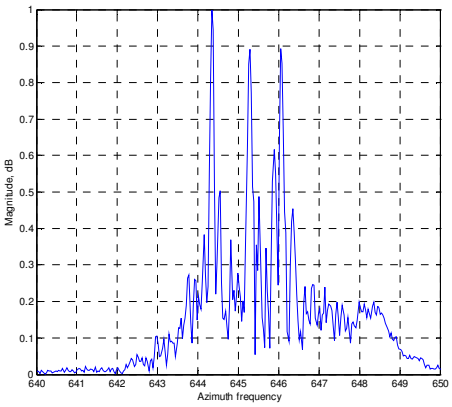

(b) azimuth frequency cross-section

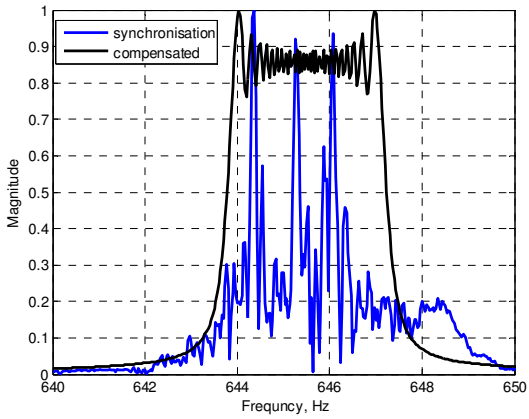

(c) tracked and compensated phase spectrum

Figure 7.12: *Heterodyne Channel Range Compression Results*

Figure 7.12 presents the range compression output of the radar channel signal. Following the same procedures used for the stationary receiver data, the result of azimuth FFT of range compression output is shown in Figure 7.12(a). By comparing Figure 7.12(b) and Figure 6.27(d) (repeated here in Figure 7.12(c)), the tracked phase spectrum and azimuth

frequency of FFT output are identical, hence both local reference generation method and range compression have been verified. We can then proceed to compress the heterodyne signal in azimuth using the tracked phase.

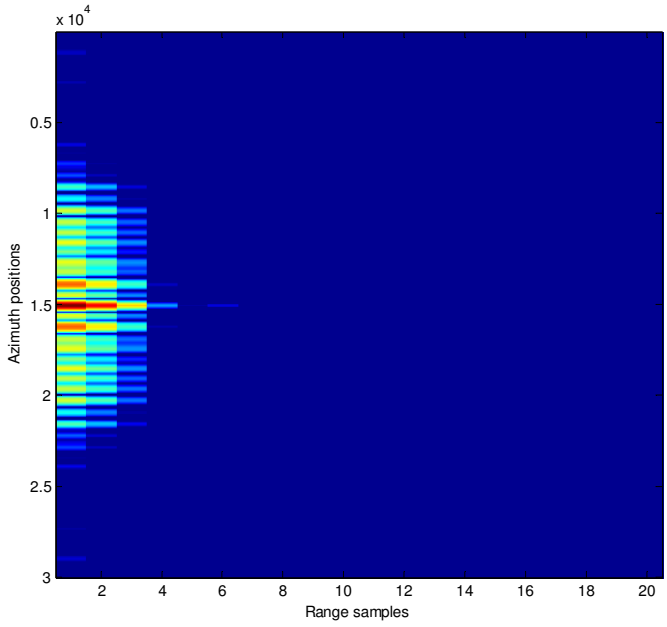

(a) Focusing of heterodyne data (azimuth compression)

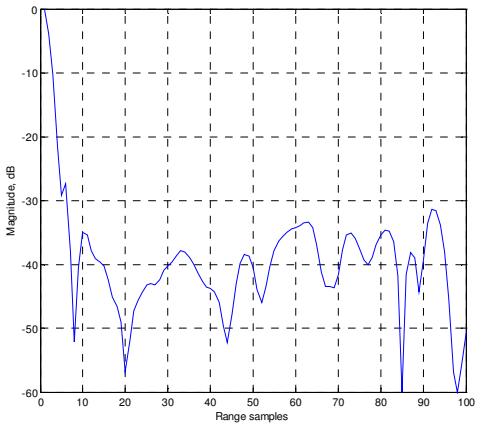

(b) Range cross-section

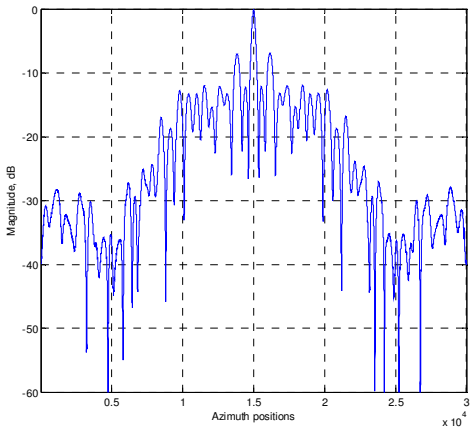

(c) Cross range cross-section

Figure 7.13: *Heterodyne Channel Focusing*

Figure 7.13 shows the focusing results of the heterodyne channel data. The tracked phase (Figure 7.12(b)) is used to form the azimuth filter, as discussed previously. It can be seen that the heterodyne channel has been compressed both in range and in azimuth. A cross-section of the compressed output along the azimuth direction is shown in Figure 7.13(c). Comparing to Figure 7.6(a), the result is slightly defocused, mainly due to the fluctuating phase spectrum, which is derived for non-linear receiver platform motion. A compensation method has been proposed in section 6.5.4. We can now proceed to compress the radar channel signal in range and in azimuth.

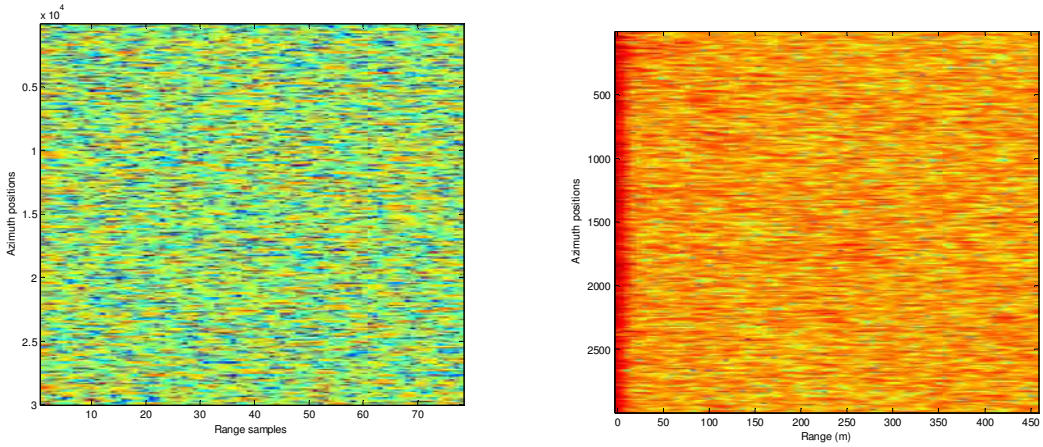

(a) before azimuth down sampling

(b) after azimuth down sampling

Figure 7.14: *Range Compression of the Radar Channel Data*

Figure 7.14 above gives the range compression output of the radar channel data. It can be seen that the direct interference becomes visible after azimuth down sampling, which is equivalent to azimuth integration.

Figure 7.15 below shows the interpolation results after range compression. For this data, 50 times interpolation has been applied and range cross-section remains the same.

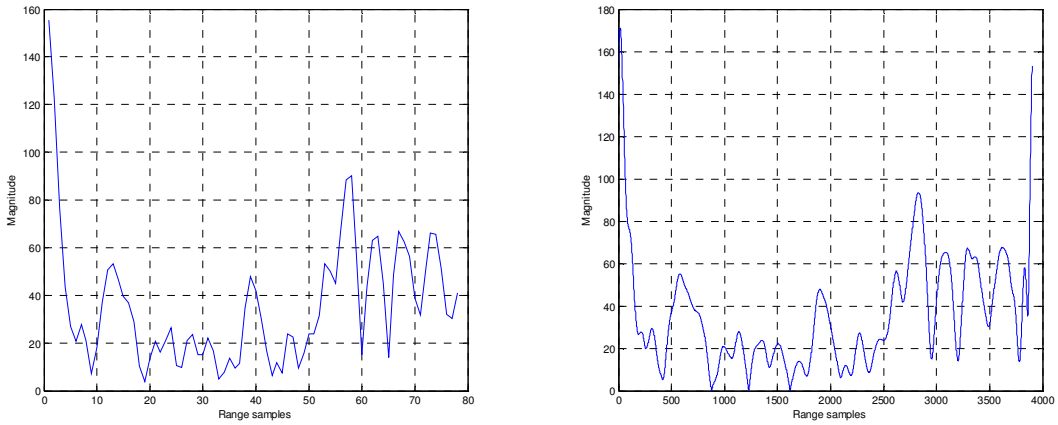

(a) Before range sample interpolation (b) After range sample interpolation

Figure 7.15: *Range Interpolation Results*

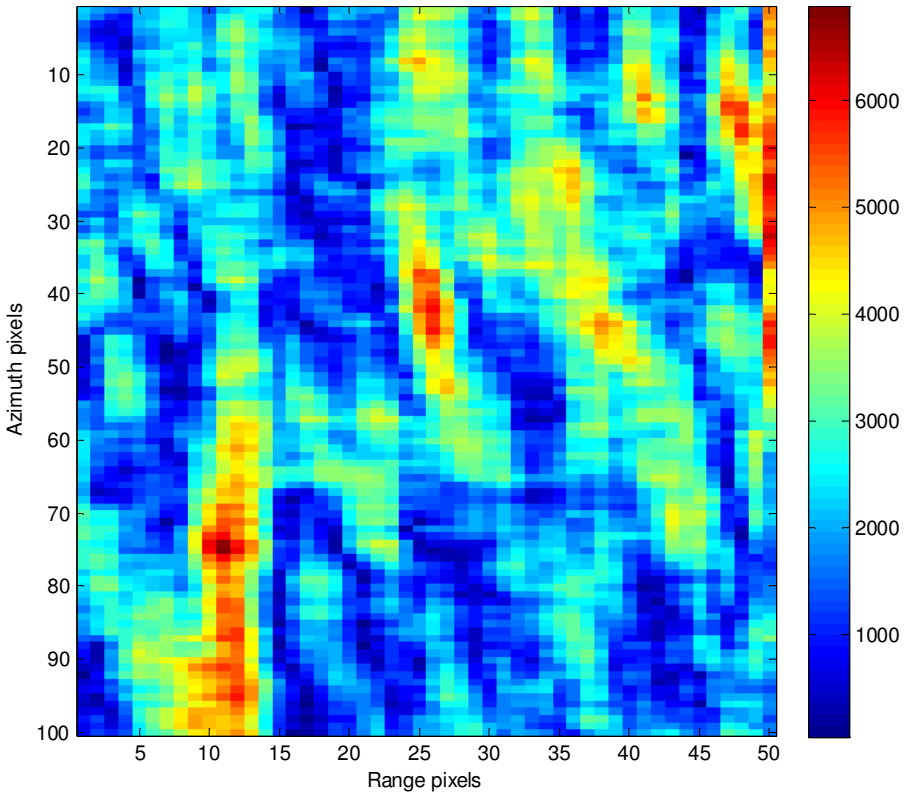

Figure 7.16: *Moving Receiver Imaging Result – GIOVE A*

A SAR intensity image using GIOVE-A satellite is shown in Figure 7.16. The Radar image covers the target area of 300 m x ~180 m, with pixel size 6 m x 1.8 m. The satellite photograph of the target area is shown in Figure 7.17. The receiver was mounted on a ground vehicle, moving along the road on the left in the figure. As can be seen in Figure 7.17, the dominant target is an extended structure towards the middle of the scene (at a range of approximately 250 m). From Figure 7.16, it can be seen that some strong reflections have been detected. Moreover, buildings on the centre and upper side of the imaging area are visible. The area surrounding these buildings is grassland and therefore

its intensity is lower. Parts of the forested area towards the site of the building can also be seen.

Figure 7.17: *Target Area – Separated Houses*

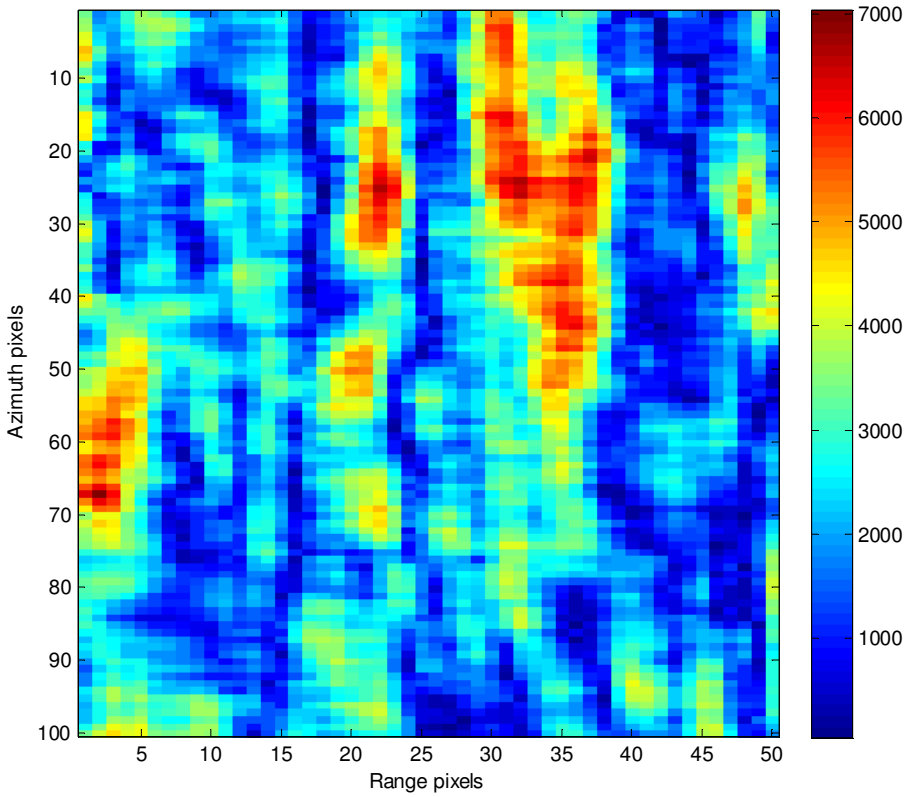

Figure 7.18: *Moving Receiver Imaging Result – GIOVE B*

Figure 7.18 presents the image result from the same data, but using the GIOVE-B satellite. Due to a different bistatic angle, the reflection properties of the target area are changed. Hence the image obtained is slightly different to the one from GIVOE-A.

At the moment, there are a few factors affecting image quality. One is the accuracy of the satellite positions, which introduces errors in the calculated instantaneous bistatic range; the other is the output of the synchronisation algorithm. The tracked Doppler of the direct transmitter-receiver signal contains a contribution from receiver motion errors, but this amount is unknown (due to the fact that a least-mean square algorithm is applied

to get an average estimate). Since this tracked Doppler is mixed with the transmitter-target-receiver Doppler, the mixed signal (and hence the final image product) contains motion errors too.

It is possible that the above factors are responsible for limiting the quality of the image in terms of contrast and proper focus. These limitations can only be overcome through step-by-step verification of the image formation algorithm, perhaps adding some modifications to it (e.g. an autofocus technique). Even so, it appears that an intensity image has been obtained which corresponds to the reflectivity of the inspected terrain.

Even though the radar reflectivity map can be associated with features of the imaging area, it was clear that there was a lot of room for improvement.

7.4 Summary

In this chapter, the structure of the BSAR collected data are described to provide a brief background of general methods used for SAR signal compression. Conceptual descriptions of two BSAR image formation algorithms are provided, which have been applied to the experimental data. The range-Doppler algorithm (RDA) has been applied to the experimental data and collected for the stationary receiver experiment. The image results are included in section 7.2, for a corner reflector detection. The reason for this is the simplicity of its implementation; the experimental topology is quasi-monostatic with small bistatic angle. The generalized bistatic back-projection algorithm (BBPA)

algorithms have been applied to the experimental data obtained from the ground moving and airborne receiver experiments. Two image results are shown and analyzed in section 7.3, which is from one target area, simultaneously illuminated by two Galileo satellites.

Reference

1. Soumekh, M., Synthetic Aperture Radar signal processing with Matlab algorithms. 1999: Wiley-Interscience.
2. Ding, Y., Synthetic Aperture Radar image formation for the moving-target and near-field bistatic cases. 2002.
3. Ding, Y. and D.C. Munson, A fast back-projection algorithm for bistatic SAR imaging, IEEE ICIP, 2002. 2: p. II-449 - II-452.

Chapter 8 Conclusions and Future Work

8.1 Conclusions

This thesis focuses on SS-BSAR using GNSS as the transmitter of opportunity. The main goal of this research is to investigate the feasibility of a BSAR system using spaceborne navigation satellites and verify its performance, such as spatial resolution and signal-to-noise ratio (SNR). Both stationary and moving receivers have been considered, and Galileo satellites have been used as the non-cooperative transmitter for the experimentation.

First of all, the proposed SS-BSAR system has been theoretically analysed for system parameters, such as the transmitter power, spatial resolution, power budget and the properties of the ranging signals. It is highlighted that the GNSS satellites transmit 10 dB less power compared to other satellites, such as TV broadcast vehicles. However, it has an advantage of satellite diversity and thus one can choose the desired bistatic topology for low resolution loss. It is concluded that overall a GNSS satellite is the most suitable, non-cooperative transmitter candidate for SS-BSAR. It provides a reasonable range resolution of ~ 8-15 m and a target detection range of ~ 3-12 km for 50 m^2 targets.

The most promising GNSS for the considered purpose are the EU Galileo satellites and the new GPS III satellites. These satellites can potentially provide a range resolution of about 8 m against 30 m for GLONASS. The Galileo E5 and new GPS L5 signals also

provide at least 6 dB more received power compared to the GLONASS L1 channel. Therefore one can expect a four times improvement in the maximum operational range.

As GNSS signals are designed for navigation purposes, one navigation signal (Galileo E5) has been studied analytically, in terms of radar applications. Its signal correlation property has been investigated by simulation and a technique has been simulated to combine the full E5 bandwidth and potentially improve the range resolution for a GNSS based SS-BSAR system.

Synchronisation, as an inevitable issue for a non-cooperative bistatic system, has also been investigated. In our case, phase synchronisation is the most important as the largely separated transmitter and receiver must be coherent over extremely long intervals of time. Synchronisation using a direct link signal has been proposed and the algorithm to extract the required information has been applied to the experimental data. The synchronisation experiment confirmed that a minimum 10 dB SNR is required in the heterodyne channel.

To obtain the experimental data for image formation and confirm the system analysis results, an experimental test bed for the proposed SS-BSAR system has been developed and tested with full functionality. Experimentation methodology has been planned and a number of experiments have been conducted, such as a synchronisation experiment, a stationary receiver experiment, a ground moving receiver experiment and an airborne receiver experiment. A set of data has been collected for radar imaging. To generate a

bistatic image, practical issues, such as parameter estimation (transmitter and receiver trajectory history) and motion compensation have also been comprehensively addressed. The solutions have been proposed and applied to experimental data.

Image formation algorithms for SS-BSAR, such as range-Doppler and back-projection algorithms have been studied and briefly discussed. As the development of focusing techniques for general bistatic topology is out of scope of this thesis, the full discussion of an image formation algorithm for SS-BSAR using GNSS can be found in the report [1]. Using the data from stationary receiver experiments, radar images have been generated with a corner reflector as the reference target. Using one data set from ground moving receiver trials, SAR intensity images from two satellites have been obtained simultaneously and analysed to some extents.

In term of publications, three journal papers have been published (author and co-author) and three papers have been presented at conferences with a number of co-authors during the PhD study period. The list of papers is included at the end of this Thesis.

8.2 Future Work

Based on the image results obtained from the ground moving receiver experiment, the recommendation for the next step is to investigate the current bistatic back-projection algorithm and improve the quality of the SAR image. As the images obtained do not reveal the correct location (both range and azimuth) of targets/houses within the

observation area, the possible causes should be examined. Except for faults in the image formation algorithm itself, other causes could be due to errors in estimated satellite positions or otherwise due to errors from the synchronisation outputs.

Moreover, the development of a frequency domain general BSAR image formation algorithm should be considered, as a bistatic back-projection algorithm lacks efficiency while processing airborne data from large target area.

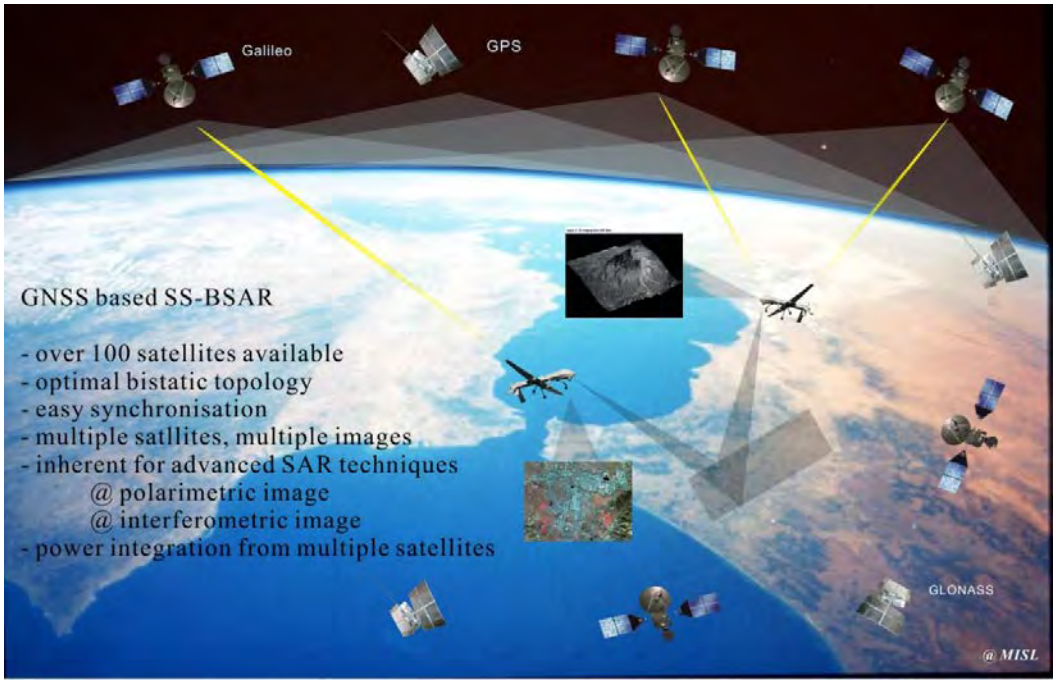

Figure 8.1: *Future of GNSS based SS-BSAR*

A few minor issues are also worth further analysis. One is the range resolution improvement by combining GNSS bandwidth. Answers need to be considered regarding how to apply the proposed method during the image formation process. Experimental

data may be collected to verify the simulation results shown in Chapter 3. The other problem is the motion compensation for SS-BSAR general topology, particularly for an airborne receiver platform. The current solution may be improved by applying data fusion to GPS and inertial navigation outputs.

Finally, Figure 8.1 gives an artistic view for the future of a GNSS based SS-BSAR system. With over 100 navigation satellites available in 10 years time and the inbuilt advantage of optimal bistatic topology and easy synchronisation, such systems have excellent potential for advanced SAR applications, such as polarimetric and interferometric image generation. Power integration from multiple satellites is also possible to improve the system power budget, which is the main disadvantage of such a system. Employing ultra low cost commercial GNSS receiver hardware, GNSS based SS-BSAR will be a viable and important solution for many remote sensing applications.

Reference

1. Cherniakov, M., et al., *Bistatic Synthetic Aperture Radar with Emitters of Opportunity*. 2006, Unversity of Birmingham: Birmingham.

Appendix A Galileo Spreading Codes Generation

The spreading codes for a Galileo E5 signal consist of a primary spreading code and a secondary code used for pilots and for signals with low data rate. The secondary code is used to modulate the primary code like a deterministic data modulation, to generate a total code length that is a multiple of the primary code length. With GIOVE-A and GIOVE-B, the primary spreading codes are generated as truncated combined M-sequences (maximum length sequence) that can be implemented using linear feedback shift register (LFSR) techniques. Secondary codes are short-memory stored pseudo random sequences. The code length to be used for each of the E5 signal components is the value stated in the table below.

Table A-1: *Spreading code lengths for GIOVE-A and GIOVE-B*

Channel	Chip Rate (Mcps)	Code Length (ms)	Code Length (chips)		Symbol Rate (sps)
			Primary	Secondary	
E5a-I	10.23	20	10230	20	50
E5a-Q	10.23	100	10230	100	No
E5b-I	10.23	4	10230	4	250
E5b-Q	10.23	100	10230	100	No

A.1 Spreading Codes Generation

The Galileo E5 primary spreading codes are generated by a tiered code construction. Register based primary codes used in Galileo are generated as combinations of two M-sequences, being truncated to the appropriate length, whereby a secondary code sequence is used to modify successive repetitions of a primary code. When considering a primary code with length N chips and an associated secondary code with length N_s chips, the first

chip of the secondary code in binary representation is used to control the polarity of the first epoch of the primary code sequence by exclusive-or combination, as shown in Figure A1 below. If applicable, data modulation is applied to the full code, again using the exclusive-or combination of code and data symbols.

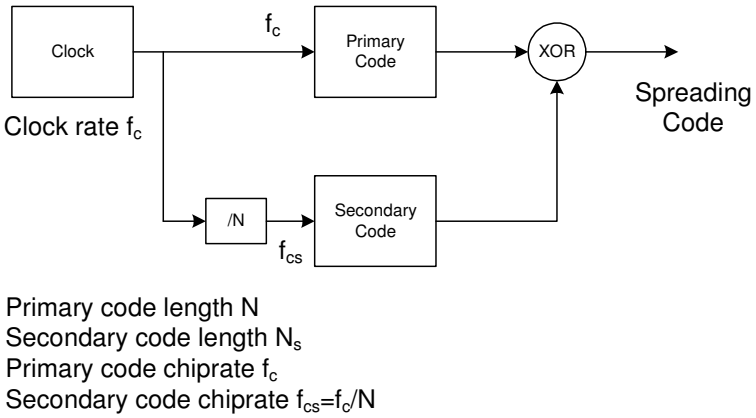

Figure A.1: *Code construction principle*

A.2 Primary Codes

Figure A2 below shows an example implementation of the linear feedback shift register method for generation of truncated and combined M sequences for the E5a-I signal.

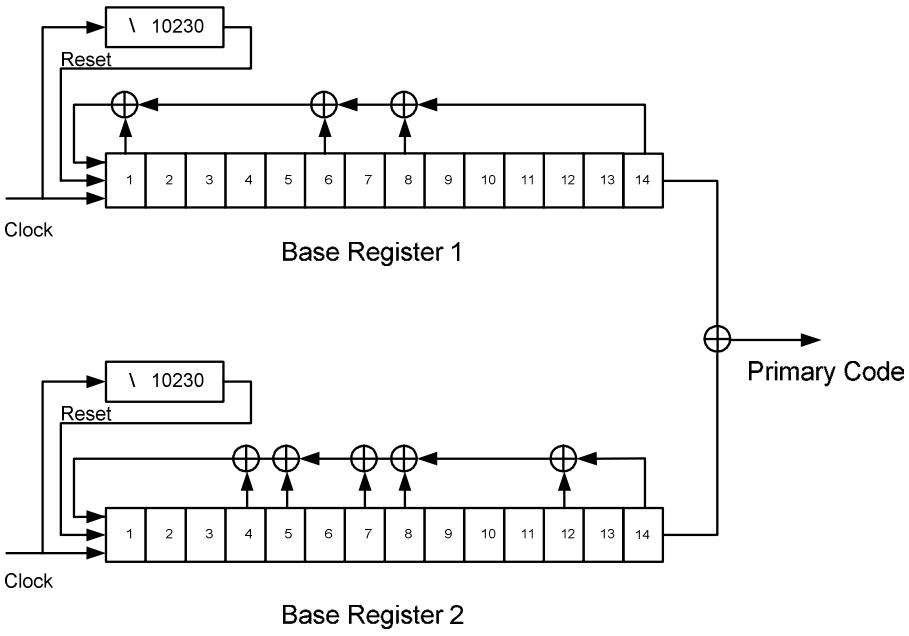

Figure A.2: *Linear shift register based code generator*

Two parallel registers are used: base register 1 and base register 2. The primary output sequence is the exclusive OR of register 1 and 2 outputs; the shift between the two sequences is zero. For truncation to primary code-length N, the content of the two shift registers is reinitialized after N cycles of the registers with so-called start-values. The start values for all base register 1 cells, in logic level notation, are "1" for all codes. The start values for all base register 2 cells are defined in Galileo Signal In Space Interface Control Document [1]. The E5a-I, E5a-Q, E5b-I and E5b-Q primary codes apply same principle, using the parameters defined in Table below.

Table A-2: *Primary code parameters*

Signal	Register	Feedback Taps	Register Length	Start Values
E5a-I	Base 1	1, 6, 8, 14	14	All "1"
	Base 2	4, 5, 7, 8, 12, 14	14	From specification
E5a-Q	Base 1	1, 6, 8, 14	14	All "1"
	Base 2	4, 5, 7, 8, 12, 14	14	From specification
E5b-I	Base 1	4, 11, 13, 14	14	All "1"
	Base 2	2, 5, 8, 9, 12, 14	14	From specification
E5b-Q	Base 1	4, 11, 13, 14	14	All "1"
	Base 2	1, 5, 6, 9, 10, 14	14	From specification

A.3 Secondary Codes

The secondary codes are fixed sequences with length defined in Table A-1 and more details can be found in the Galileo Signal In Space Interface Control Document [1]. For the 4 and 20 bit secondary codes the same code is used for all associated primary codes. For the 100 bit code, an independent secondary code is assigned for each primary code.

Appendix B Coordinate and Datum Transformations

Coordinate transformations are used to convert from one type of coordinates to another type of coordinates. Datum transformations are used to convert between a global coordinate and a local coordinate system. A geodetic datum defines the relationship between a global and a local three-dimensional Cartesian coordinate system. With both the transformations, we can convert the earth ellipsoids coordinates to target ellipsoids coordinates.

Two different coordinate systems are most commonly used to represent the earth ellipsoids: Cartesian coordinates (x, y and z) and geographic LLA coordinates (Latitude, Longitude and Altitude), which is a global coordinate system. Coordinate transformations can be applied to convert a global Latitude Longitude and Altitude coordinates to a global XYZ coordinates. With known coordinates of at least three points in both systems, a global Cartesian coordinates can be transferred to a local Cartesian coordinates using 7-parameters transformation, or called 3D similarity transformation.

B.1 Geographic – Cartesian (La, Lo, A) – (X, Y, Z)

One uses the formula

$$X = (N + H)\cos La \cos Lo$$
$$Y = (N + H)\cos La \sin Lo$$
$$Z = (N(1 - e^2) + H)\sin La$$

with *La* and *Lo* are Latitude and Longitude, *H* being the altitude and *N* being

$$N = \frac{a}{\sqrt{1 - e^2 \sin^2 La}} = \frac{a^2}{\sqrt{a^2 \cos^2 La + b^2 \sin^2 La}}$$

a, *b* are semi major and semi minor axes of the ellipsoid and *e* is the eccentricity of the earth.

B.2 7-parameters transformation

Given the three-dimensional of a point *P* in a Cartesian coordinate frame (*u, v, w*), the coordinates of this point in a different Cartesian coordinates frame (*x, y, z*) can be computed using the relation

$$\begin{pmatrix} x \\ y \\ z \end{pmatrix}_P = \begin{pmatrix} \triangle x \\ \triangle y \\ \triangle z \end{pmatrix} + (1+\delta s) \begin{pmatrix} 1 & \delta w & -\delta\varphi \\ -\delta w & 1 & \delta\varepsilon \\ \delta\varphi & -\delta\varepsilon & 1 \end{pmatrix} \cdot \begin{pmatrix} u \\ v \\ w \end{pmatrix}_P$$

with $\triangle x$, $\triangle y$, $\triangle z$: coordinates of the origin of frame (*u, v, w*) in frame (*x, y, z*);

$\delta\varepsilon$, $\delta\varphi$, δw : differential rotations around the axes (*u, v, w*), respectively to establish parallelism with frame (*x, y, z*);

δs : differential scale change.

Considering WGS84 or ITRF to be the (*u, v, w*) frame and local coordinates to be (*x, y, z*) frame, coordinates of a Galileo satellite or radar receiver platform can be transformed to local coordinates, once these seven transformation parameters are know.

Appendix C Antennas and Front-end

C.1 Spiral Helix Antennas

Table C-1: Spiral Helix Antenna Parameters

Model Number	Frequency (GHz)	Gain (dBi)	HPBW Az x El	Polarization	Dimension (mm)	Connector
AMH16-16L-02	1.1-1.7	16	30^o x 30^o	Left Hand Circular	1005 x 55	N-type (F)
AMH16-16R-02	1.1-1.7	16	30^o x 30^o	Right Hand Circular	1005 x 55	N-type (F)

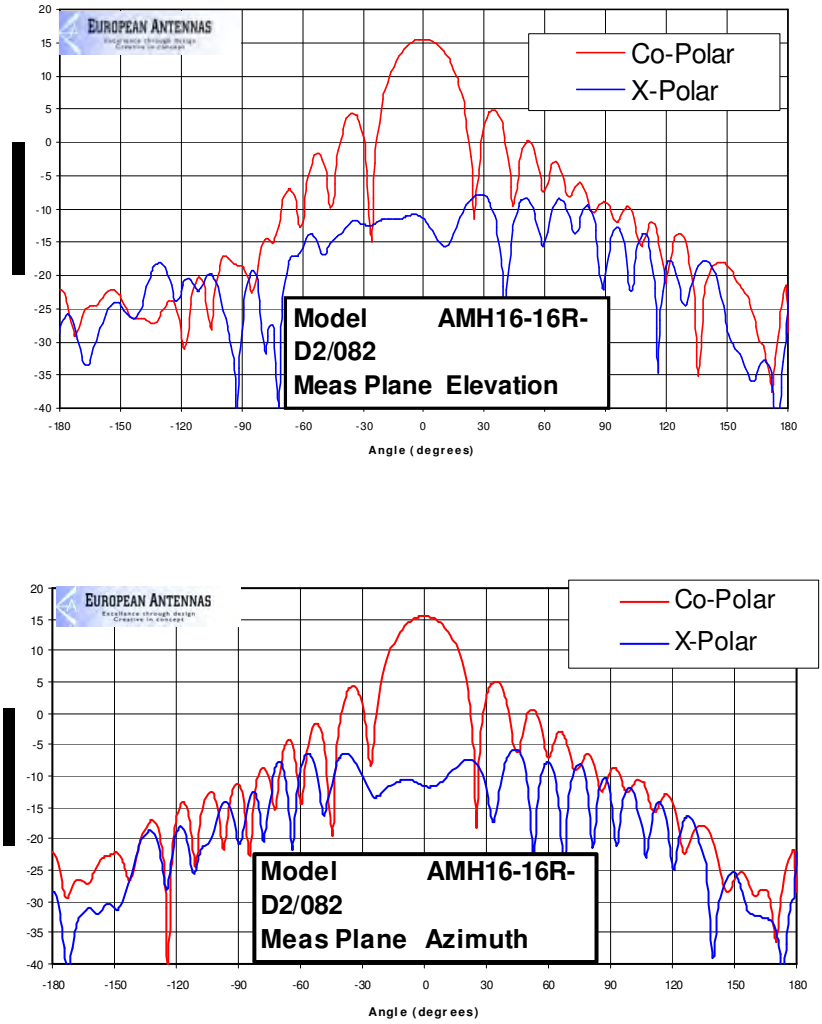

Figure C.1: *Radiation Pattern of Spiral Helix Antennas*

C.2 Flat PCB Patch Antennas

C.2.1 Heterodyne Channel Antenna

Specification

1) Working frequency 1192±25 MHz
2) Working polarization – right circular polarisation, additional polarization – left circular polarisation
3) Radome dimensions 260x260x25 mm

Antenna concept

The antenna (Figure C2 below) consists of two PCBs. The first single layer PCB is a quadrant radiating element (patch). The second double-layer PCB has a 90-degree power splitter for antenna feeding.

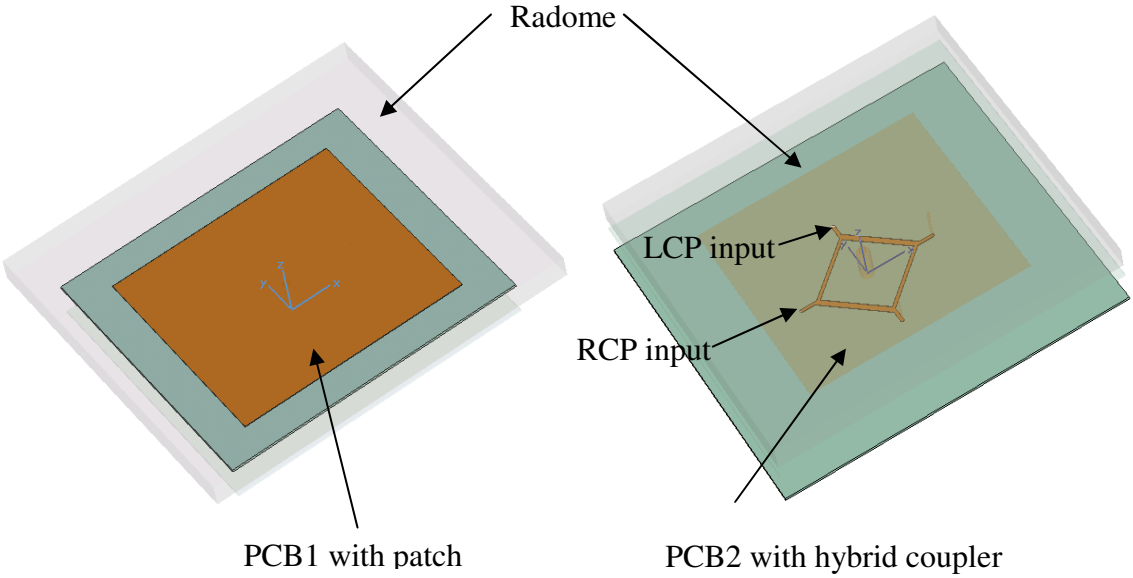

Figure C.2: *Heterodyne channel antenna concept*

The coupler's PCB2 is installed on a duralumin ground plate. Both PCBs are separated by 5 M3x10 mm spacers and screwed by M3 screws. Two feeding wires (1 mm copper) connect the coupler and patch being soldered to them. The total assembly of the antenna

is shown in the drawings Figure C.7. The antenna has two feeding points for right circular polarisation and left circular polarisation separately. The input connectors are SMA-type. The connectors unused must be loaded by a 50 Ohm standard SMA load. The Radome is attached to ground plate by 3x10 wood screws.

Calculated antenna parameters (for $\varepsilon = 4.6$*):*

Frequency, MHz	Gain, Left Circular Polarisation, dB	Gain, Right Circular Polarisation, dB	Axial ratio, dB
1167	-4.81	9.14	-0.584
1192	-3.47	9.18	-0.076
1217	-2.4	9.22	-0.151

Beam width (at 1192 MHz) is around 65^{o}x66^{o}.

Antenna bandwidth is 1.11-1.28 GHz (14.2%) at the VSWR=1.5 level.

Simulated antenna parameters are shown in Figures C3, C4 and C5 below.

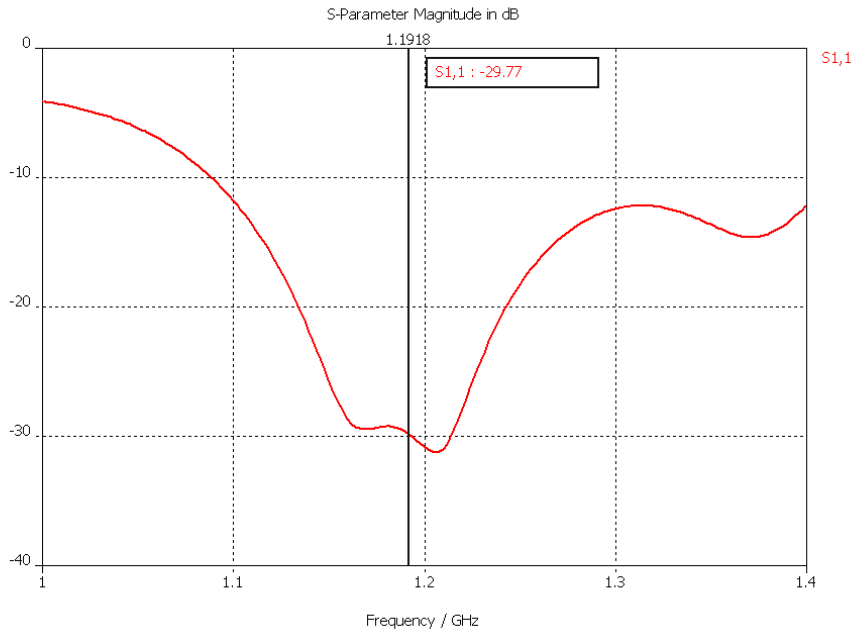

Figure C.3: *Return loss, S11*

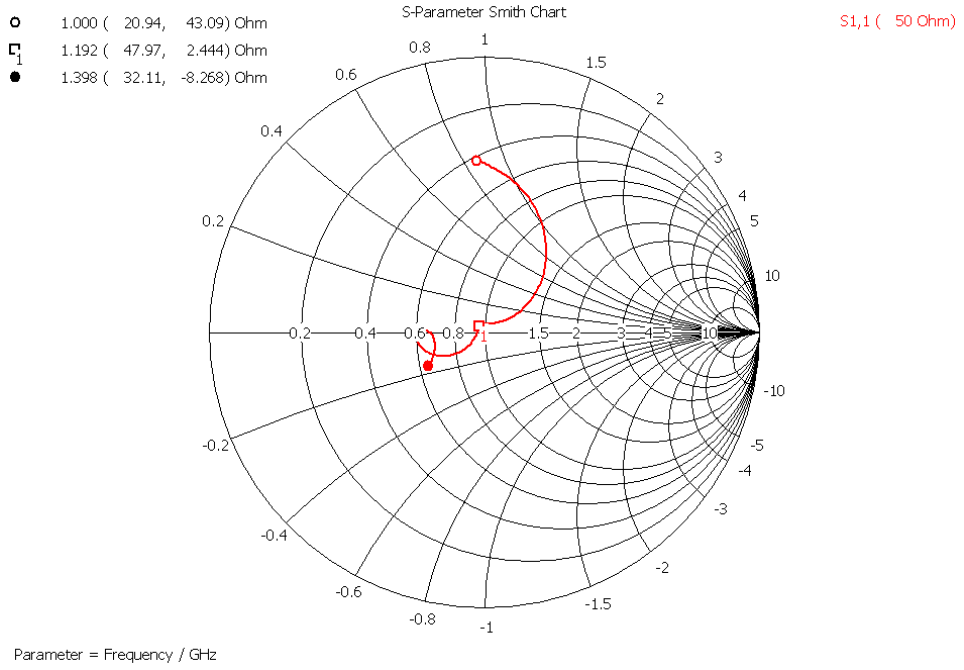

Figure C.4: *Impedance*

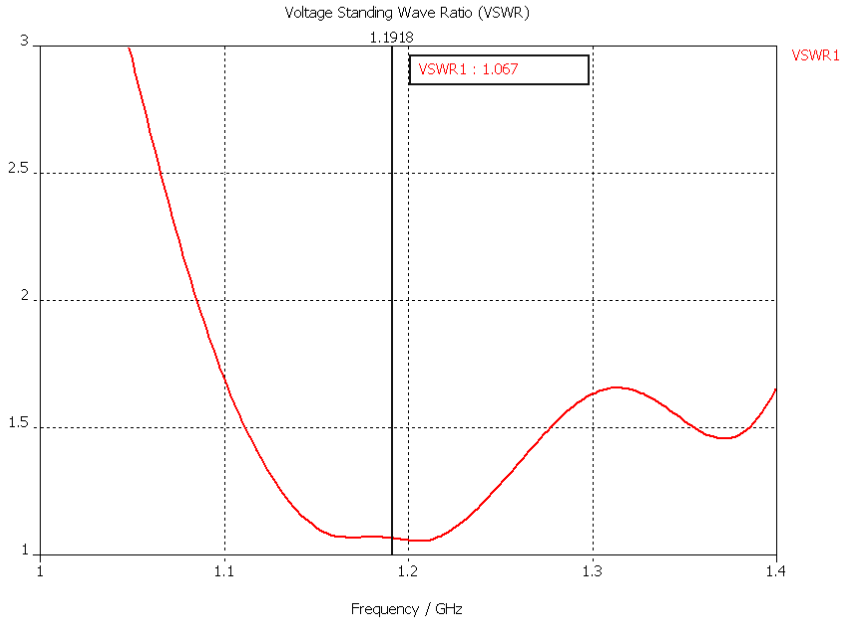

Figure C.5: *VSWR*

The drawings of PCBs with dimensions are shown in Figure C6 and C7 below.

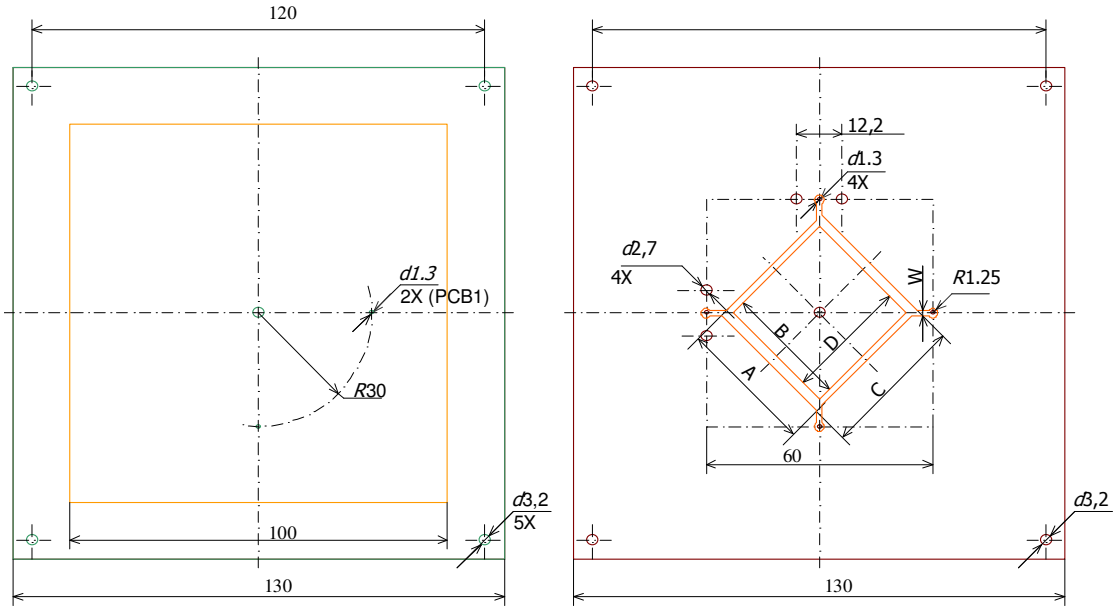

Figure C.6: *Antenna PCB layout*

PCB1 (one-side copper FR-4-0.8mm)

PCB size 130x130 mm

Patch size 100x100mm

PCB2 (two-side copper FR-4-0.8. One side – top – power splitter, other side – all ground)

Dimension (mm)	Variant 1	Variant2
A	35.6	33.5
B	32.4	30.5
C	37.7	35.6
D	32.3	30.4
W	1.6	1.5

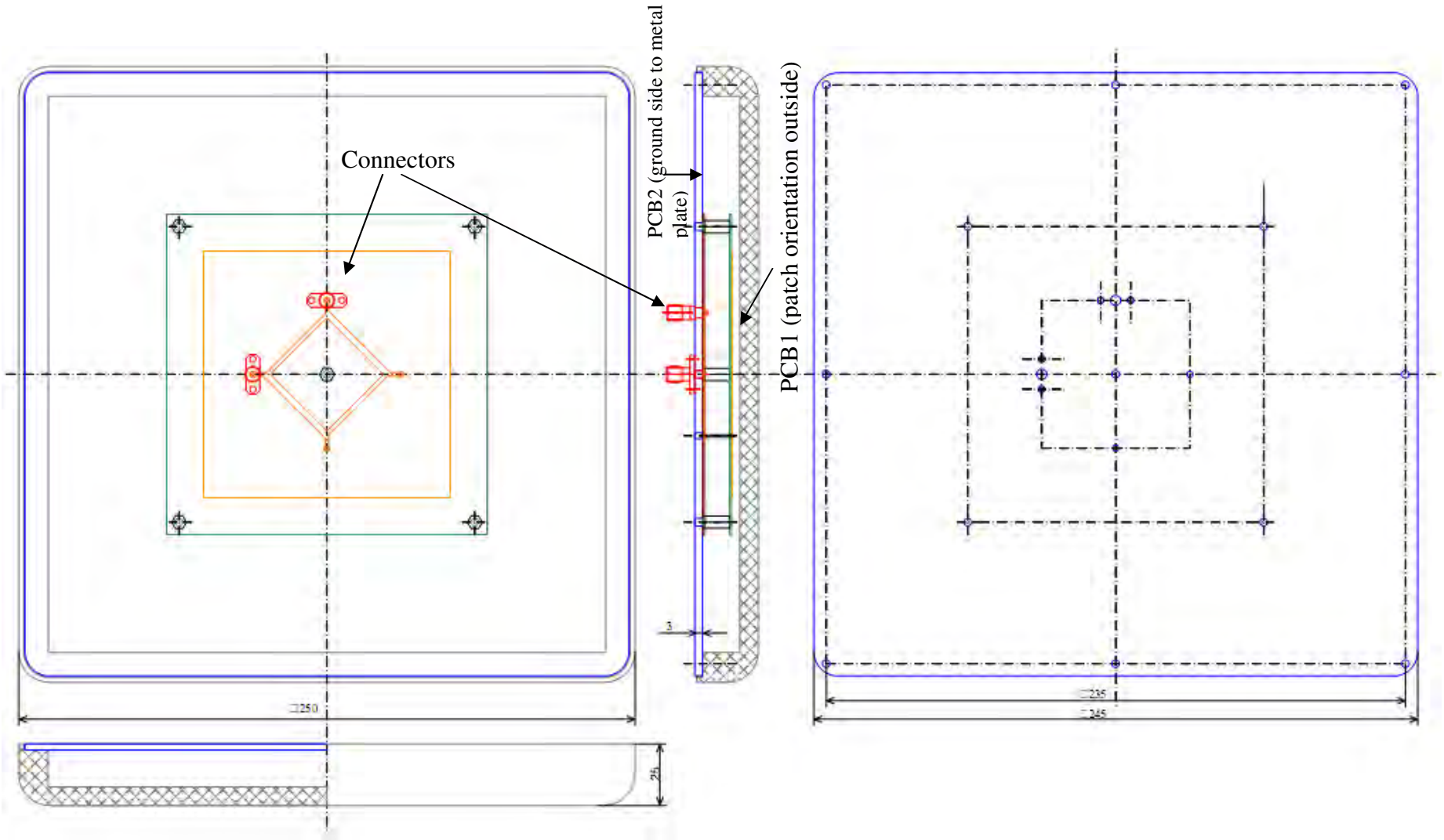

Figure C.7: *Heterodyne channel antenna assembly*

C.2.2 Radar Channel Antenna

The radar channel antenna used for the vehicle and the airborne trials is a four-element patch antenna. The design and specifications for each element are the same as the single element patch antenna used for the heterodyne channel.

Specification

1) Working frequency 1192±25 MHz
2) Working polarization – right circular polarisation, additional polarization – left circular polarisation
3) Beam width at 1192 MHz around 65^{o}x15^{o}.
4) Radome dimensions 1000x250x30 mm

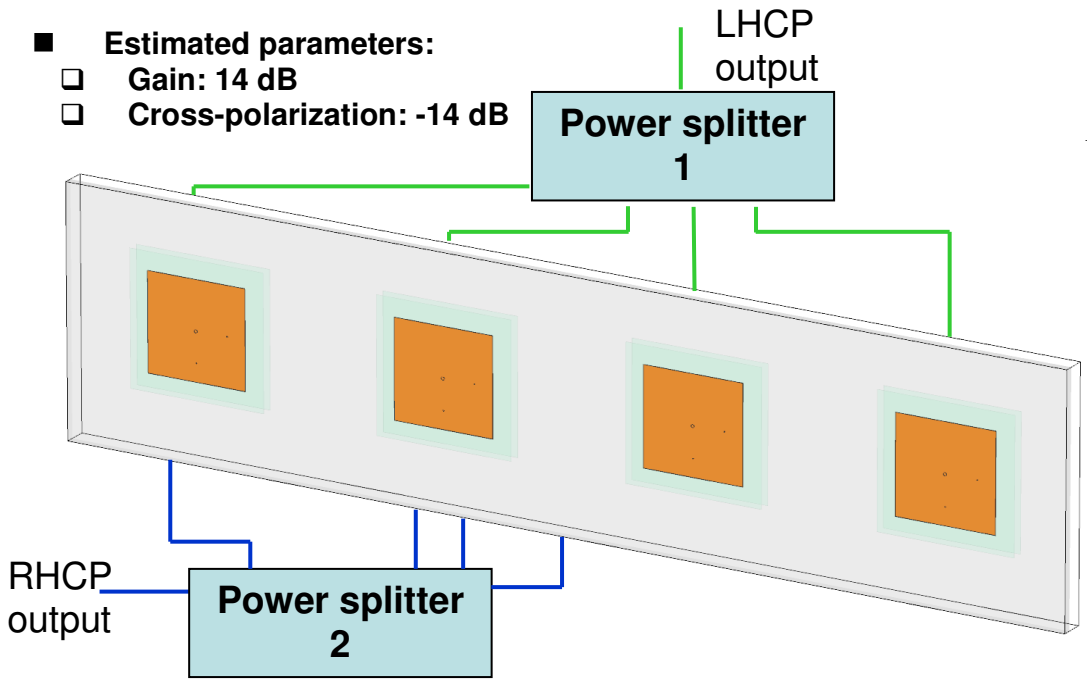

Figure C.8: *Radar channel antenna concept*

C.2.3 Patch Antennas Testing Results

A set of experiments have been conducted in open space to measure the gain and the beamwidth of the heterodyne and the radar channel antennas. Figures C.9 and C.11 below show the experimental set-up for the antenna testing. In order to measure the heterodyne channel antenna gain, S21 measurement has been made using a network analyzer. Two identical patch antennas were installed with the separation distance of 7 meters, one for transmission and the other for reception.

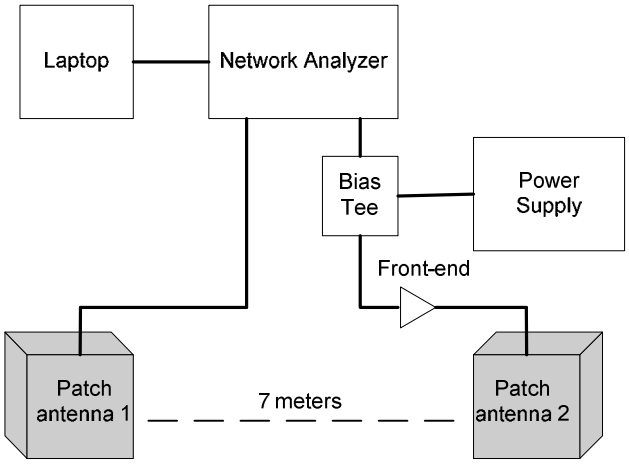

Figure C.9: *Heterodyne channel antenna testing set-up*

The calibration of the Network Analyser and connecting cables was conducted and the input power level was adjusted to set the measured total transmission link gain (propagation loss, antenna gain, losses from cables etc) to 0 dB. Figure C10 below show the testing results (S-parameters). Assuming a free space propagation loss model, the antenna gain is about 7.5 dB and close to the expected value of 9.18 dB at 1192 MHz.

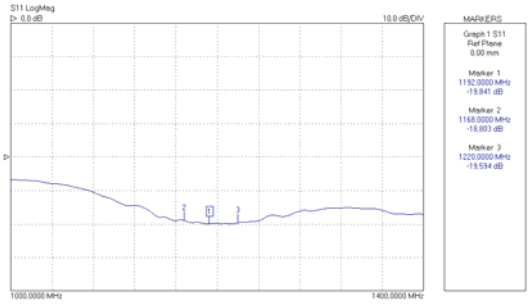

(a) return loss, S11

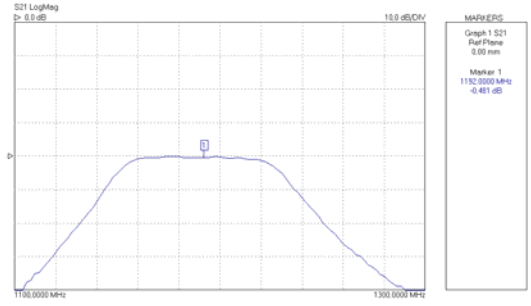

(b) insertion loss, S21, right CP

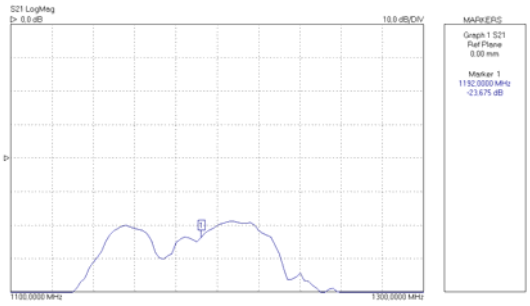

(c) insertion loss, S21, back of receiving antenna face to transmitting antenna

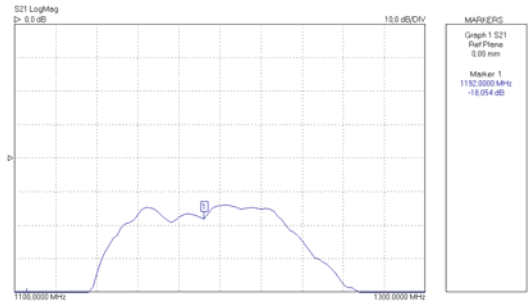

(d) insertion loss, S21, cross polarization

Figure C.10: *S-parameter results*

For the radar channel antenna (4-element array) testing, an additional one-element patch antenna was used for transmission, and the antenna array for reception. The phase centre of the two antennas was set to the same height with the separation distance of 8 m, and the antenna gain and beamwidth were found by rotating one antenna and taking the maximum and 3 dB readings of the received signal power from the spectrum analyser. The approximate beamwidth was then derived from the angle between two 3 dB readings. The measured beamwidth is approximate 75^{o}x15.5^{o} for both polarizations and matches well with the theoretical value of 65^{o}x15^{o}.

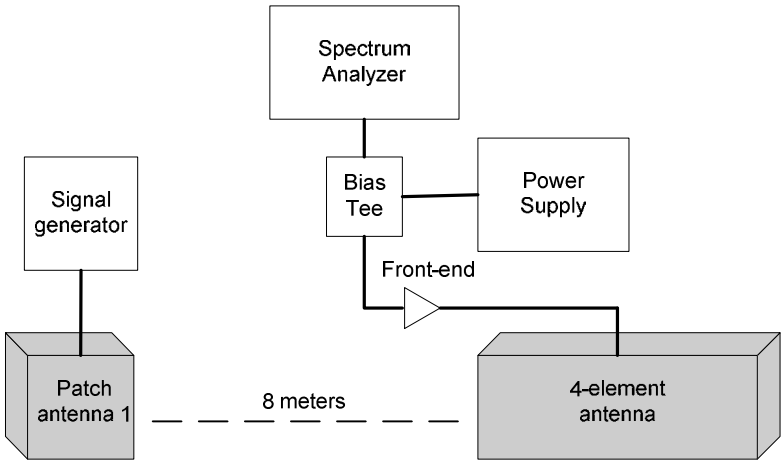

Figure C.11: *Radar channel antenna testing set-up*

C.3 GPS Antenna

The PG-A1 is a precision dual-frequency, dual-constellation antenna featuring an integrated ground plane to help eliminate errors caused by multipath. The PG-A1 was designed to accompany the Topcon modular receivers such as the Legacy-E, Legacy-H and Odyssey-RS.

Table C-2: *PG-A1 Specifications*

Frequency	GPS & GLONASS L1/L2
Gain	6 dBi, Omi-directional
Integrated UHF	No
Centering	Precision Micro Centre
Type	Microstrip on flat ground plane
Weight	492 g
Dimensions	141.6mm × 141.6mm × 52.7mm
DC voltage	+2.7 ~ +12 V; 25A @ 5.0 typ
LNA gain	30 ± 2 dB

Output	50 Ohm
Connector	TNC
Environmental	Waterproof
Operating temperature	-40°C~ +55°C
Shock Resistance	2-meter pole drop

C.4 RF Front-ends

An RF front-end, compatible with the Galileo E5 signals and the antennas described previously, has been developed. It has two variants; one consists of a first stage low noise amplifier (noise figure 1.15 dB), RF bandpass filter and 2nd stage amplifier, the other only has a first LNA and a RF bandpass filter. Figure C12 below show the testing results for the front-end blocks developed. The total gain of the front-ends is around 44 dB for 1st variant and 22 dB for 2nd variant.

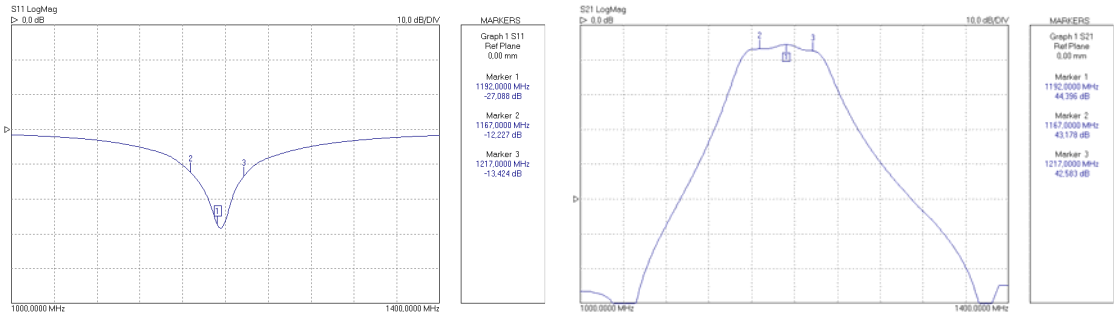

(a) input return loss, S11, block 1 (b) insertion loss, S21, block 1

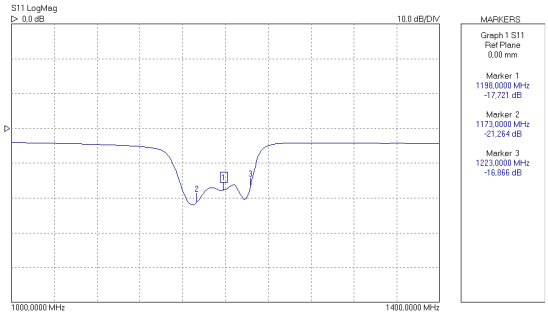

(c) output return loss, S22, block 1

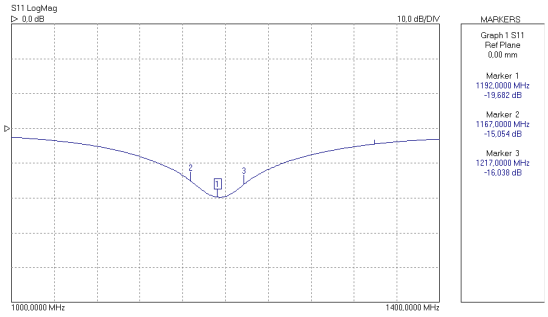

(d) input return loss, S11, block 2

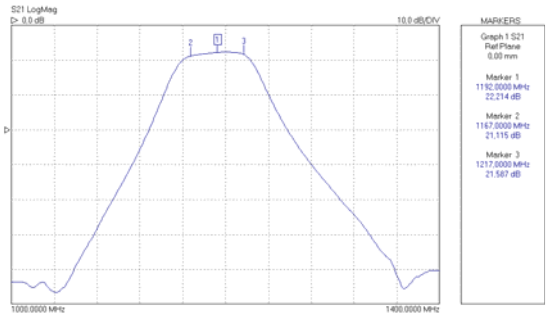

(e) insertion loss, S21, block 2

(f) output return loss, S22, block 2

Figure C.12: *Front-end S-parameters results*

Appendix D Frequency Synthesizer

LMDP_1500_0500_01

1. PRODUCT DESCRIPTION

The LMDP_1500_0500_01 is a small step size frequency synthesizer, which generates frequencies from 1000MHz to 2000MHz with less than 2.4 Hz resolution via 31 parallel data bits. The output signal is phase-locked to an internal 10 MHz TCXO with +/- 1ppm accuracy or an external 10 MHz reference. When an external 10 MHz reference (+1dBm min.) is applied to J1, the TCXO will be shut-off automatically and the output signal will be locked to the external reference.

2. SPECIFICATIONS

ELECTRICAL

Main Output (J4)

Frequency Range:	1000 MHz to 2000 MHz
Frequency Resolution:	2.3283 Hz
Frequency Accuracy:	Depending on the 10 MHz reference with an additional error of +/- 2.3283 Hz
Output Power:	+13 dBm +/-3 dB
Harmonic:	<-20 dBc
Spurious:	-45 dBc Typical.

SSB Phase Noise (*Fout* = 100 MHz, Internal 10 MHz)

@ 1 kHz Offset	-80 dBc/Hz
@ 10 kHz Offset	-90 dBc/Hz

Internal Reference:

Frequency:	10 MHz
Frequency Stability:	**+/-** 1 ppm

External Reference (J1):

Frequency:	10 MHz
Input Power:	+1 dBm minimum

Auxiliary Output (J2):

Frequency: 10 MHz Buffered from Int. or Ext. Ref.

Output Power: +3 dBm minimum

DC Input (JP1)

+5 VDC @ 900 mA typ. (1 A Max.)

+15 VDC @ 75 mA typ. (120 mA Max.)

LMDD_LF_300_01

1. PRODUCT DESCRIPTION

The LMDD_LF_300_01 is a direct digital synthesizer (DDS), which generates frequencies from 500 kHz to 300 MHz in less than 2.4 Hz resolution via 31 parallel data bits. The unit has a built-in 1 GHz clock. The 1 GHz clock is phase-locked to an internal 10 MHz TCXO with +/- 1ppm accuracy or an external 10 MHz reference. When an external 10 MHz reference (+1 dBm min.) is applied to J1, the TCXO will be shut-off automatically and the 1 GHz clock will be locked to the external reference.

2. SPECIFICATIONS

ELECTRICAL

Main Output (J4)

Frequency Range: 500 kHz to 300 MHz

Frequency Resolution: .23283 Hz

Frequency Accuracy: Depended on the 10 MHz reference with an additional error of +/- 0.23283 Hz

Output Power: +6 dBm +/-3 dB

Harmonic: <-20 dBc

Spurious: -45 dBc Typical.

SSB Phase Noise (*Fout* = 100 MHz, Internal 10 MHz)

@ 1 kHz Offset -105 dBc/Hz

@ 10 kHz Offset -115 dBc/Hz

Internal Reference:

Frequency: 10 MHz

Frequency Stability: **+/-** 1 ppm

External Reference (J1):

Frequency: 10 MHz

Input Power: +1 dBm minimum

Auxiliary Output (J2):

Frequency: 10 MHz Buffered from Int. or Ext. Ref.

Output Power: +3 dBm minimum

DC Input (JP1) +5 VDC @ 800 mA typ. (1 A Max.)

Testing Results and Frequency Setting

Figure D1 below shows the signal spectrum after programming the frequency synthesizer to the required frequency. For the Galileo receiver, the intermediate frequency is set to 140 MHz and the RF input is mixed with local frequency of 1347.14 MHz. The next page also gives the circuit diagram for the frequency programming board.

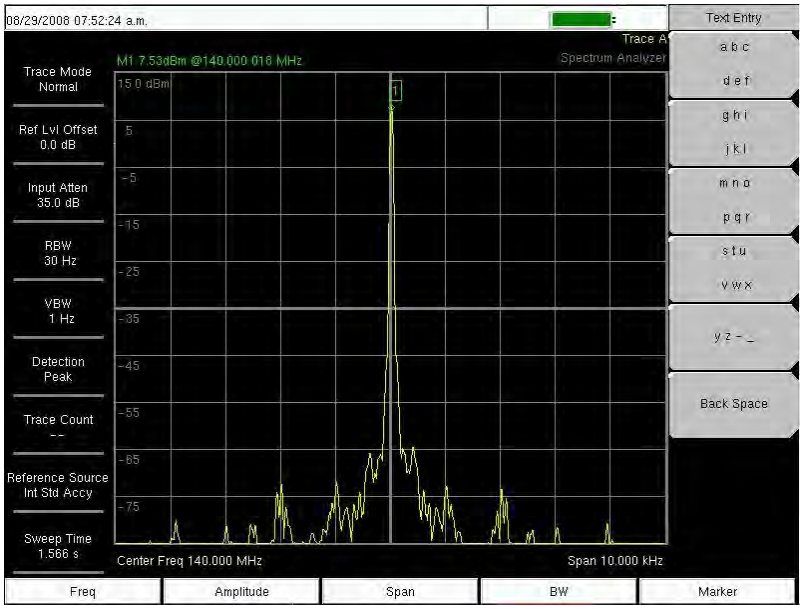

(a) 140 MHz, IF local frequency

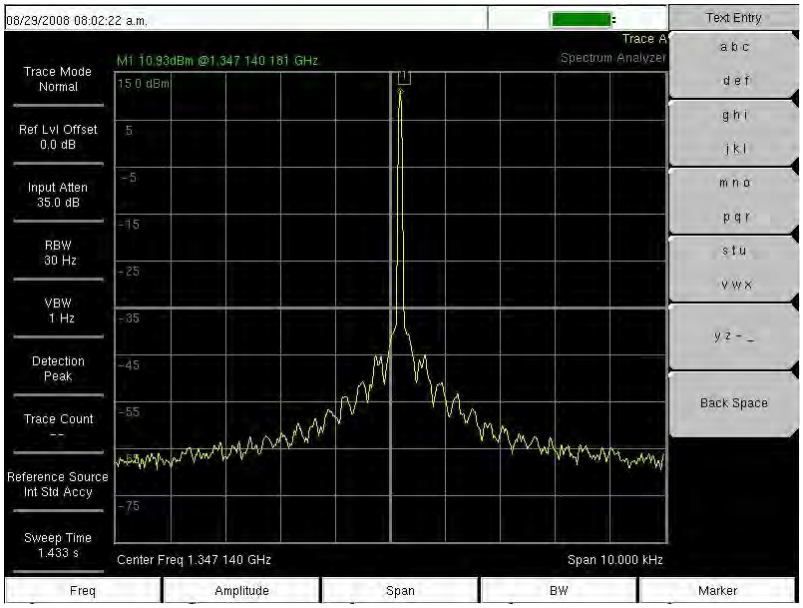

(b) 1347.14 MHz, RF local frequency

Figure D.1: *Frequency synthesizers output*

Figure D2 below shows the PCB diagram of frequency synthesizer setting board. It has 32 switches, controlling the 0-31 parallel data inputs (TTL high or low) to the frequency synthesiser. Extra circuitry is also included to indicate the status of the frequency setting.

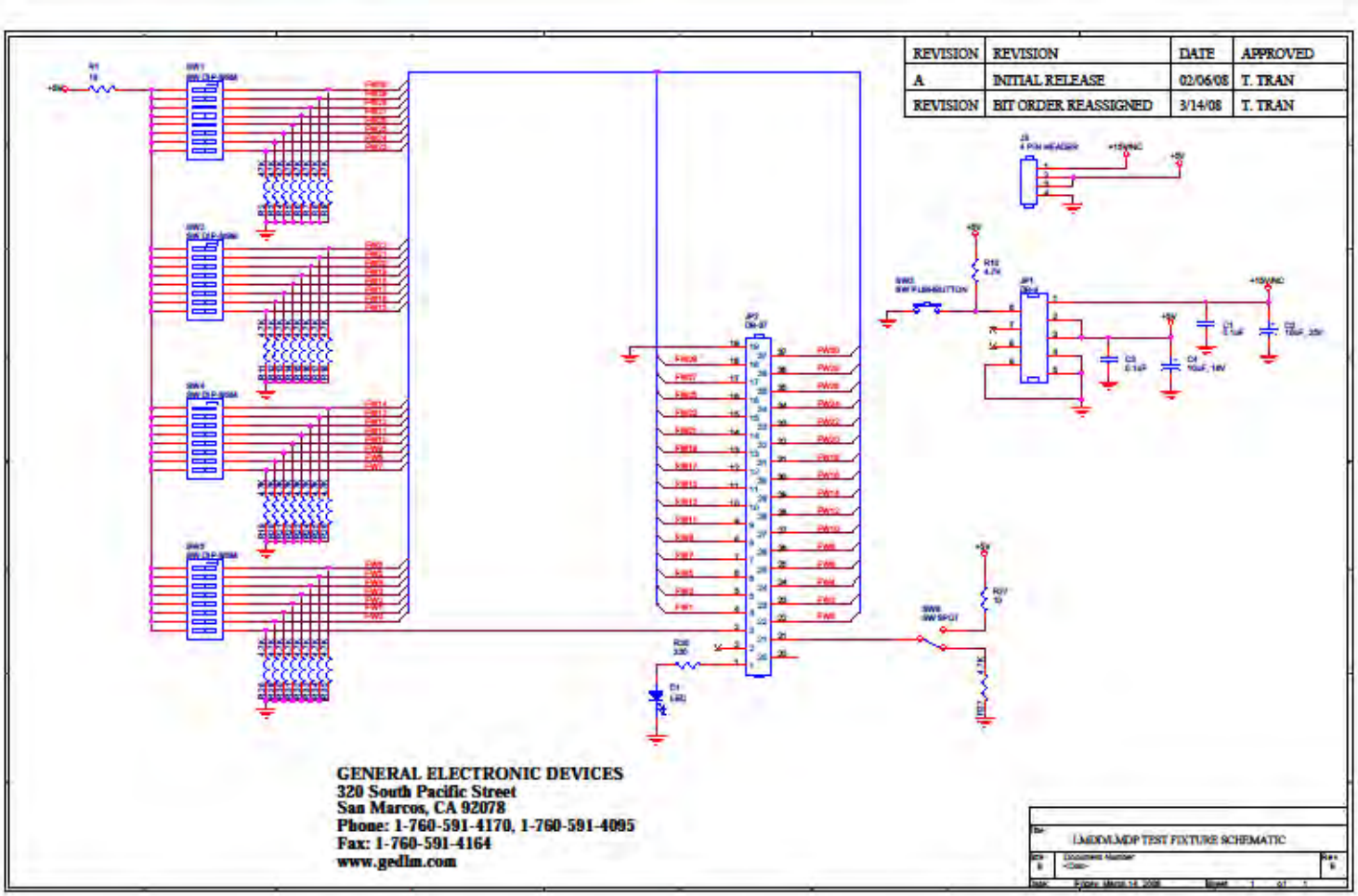
REVISION | REVISION | DATE | APPROVED
A | INITIAL RELEASE | 02/06/08 | T. TRAN
REVISION | BIT ORDER REASSIGNED | 3/14/08 | T. TRAN
GENERAL ELECTRONIC DEVICES
320 South Pacific Street
San Marcos, CA 92078
Phone: 1-760-591-4170, 1-760-591-4095
Fax: 1-760-591-4164
www.gedlm.com
GEDDM,MDP TEST FIXTURE SCHEMATIC

Appendix E Data Acquisition Subsystem

The data acquisition subsystem includes two parts: a purpose-built analog-to-digital convertor board (six channels) and a commercially available data acquisition card. The analogue signal at the output of the microwave receiver consists of a binary sequence buried under random receiver noise. The ADC board firstly converts this signal to digital bits that can be accepted as the input to the data acquisition card. This quantization scheme (1 bit resolution) is adequate because of the M-sequence property and since subsequent processing can accept the error rate involved. The digital bits are then sampled at a fixed frequency set by an on-board oscillator or an external clock, (we use here 50 MHz in order to over sample the Galileo E5a/b signal by a factor of 5). A higher sampling rate would need a faster ADC and would increase the computation burden of future signal processing. After sampling, the sampled digits are transferred to the memory of the data acquisition card using the continuous FIFO mode. Finally, using the customized software, this data stream is recorded onto the computer hard disk for further offline processing.

E.1 Analog-to-Digital Converter

The ADC used here is an ultra fast comparator (10 ns response time) with a voltage converter. The input and output of the comparator are connected with three resistors for impedance matching, and a set of capacitors is used for power supply bypassing.

Table E1 below gives the details of all parts used for ADC module and Figure E1 below gives the PCB diagram of the six channels ADC board.

Table E-1: *ADC Module Part List*

Position	Part number	Value	Case	Qty	Producer
C17,22-24,28,30-32,34	06033G104ZAT2A	0.1 uF Y5V 25V	603	20	AVX
C7,10,11,14,15,18,19-21	TPSA106K010R1800	10uF-10V	A	9	AVX
C25	TAJD476K025R	47uF-25V	D	1	AVX
C26,27,29,33	TCJB476M010R0070	47uF-10V	B	4	AVX
U1-3	LT1715CMS			3	Linear Tech
U4	L78M05CTD	5V Voltage regulator	DPAK	1	STM
U5	LM2662M	DC converter	SO-8	1	National Semiconductors
U6	SN74ALVC04D		SOIC-14	1	Texas Instruments
U7	MC33269D-3.3		SO-8	1	On Semiconductor
R1-24	MC 0.063W 0603 5% 100R	100 Ohm	603	24	Multicomp
VD1	MBRA140T	1A-40V Shottky	SMA	1	International Rectifier
X1	SMT 2.5MM POWER SOCKET			1	
X2	20 WAY STRAIGHT BOX HEADERS FCI RC			1	
XW1-6		BNC 50 Ohm PCB		6	

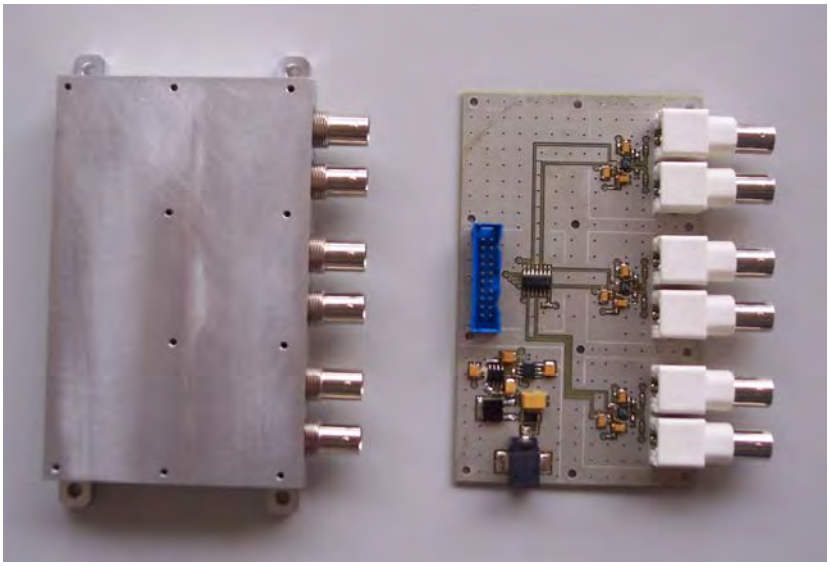

Figure E.1: *Photo of ADC (six channels)*

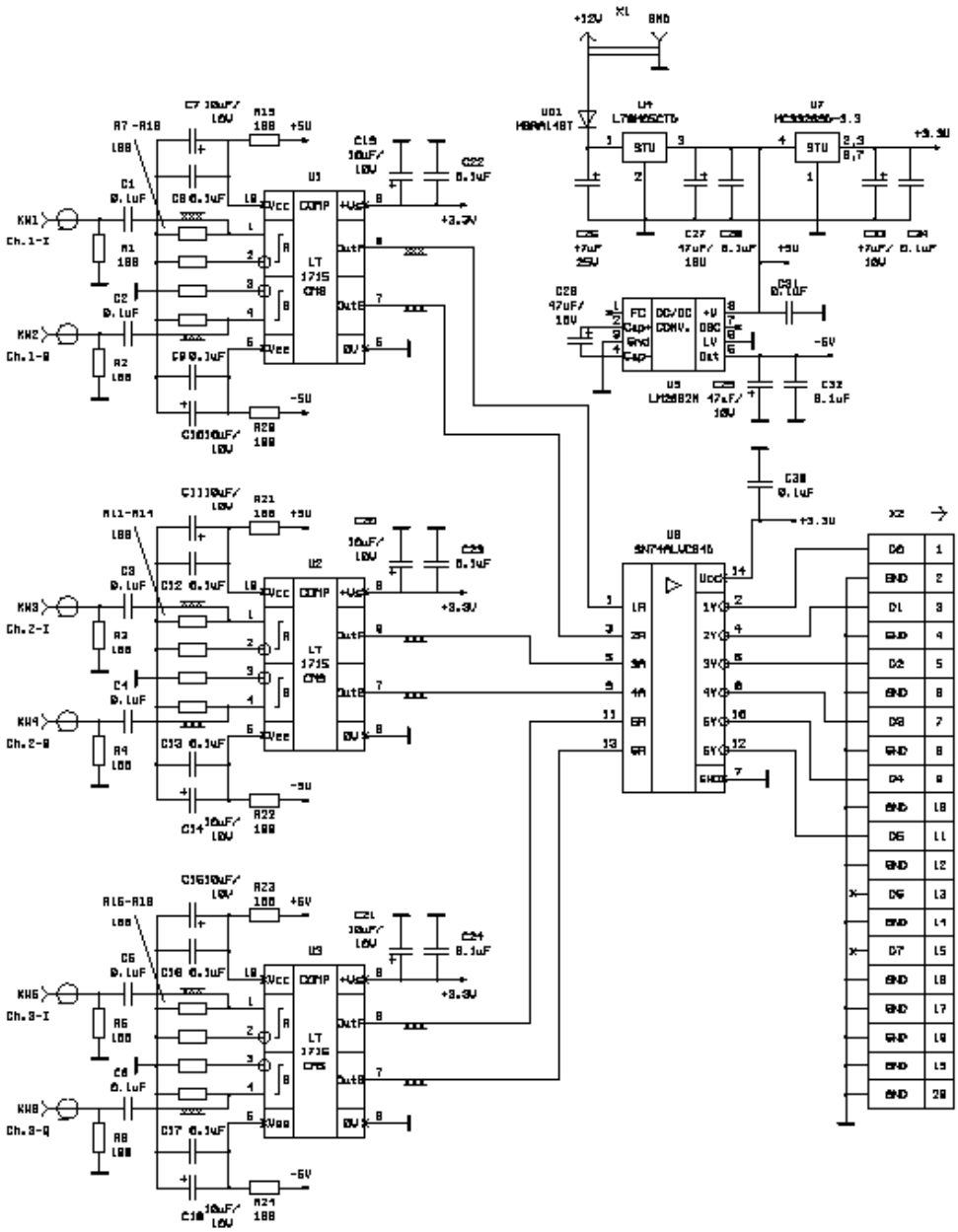

Figure E.2: *A/D Converter Circuit Diagram*

E.2 Sampling Clock

Table E-2: *Sampling clock module part list*

Position	Part number	Value	Case	Qty	Producer
C2, C4-C9	06033G104ZAT2A	0.1 uF Y5V 25V	603	7	AVX
C3	TPSA106K010R1800	10uF-10V	A	9	AVX
C1	TAJD476K025R	47uF-25V	D	1	AVX
U1	HCD311/BNDN	OCXO		1	Golledge
U2	L78M05CTD	5V Voltage regulator	DPAK	1	STM
U3	74AC04PC	Hex inverter	DIP-14	1	Fairchild
U4	74AC191PC	4-bit counter	SOIC-16	1	Fairchild
R1-4	MC 0.063W 0603 5% 100R	100 Ohm	603	4	Multicomp
VD1	MBRA140T	1A-40V Shottky	SMA	1	International Rectifier
X1	SMT 2.5MM POWER SOCKET			1	
X2	20 WAY STRAIGHT BOX HEADERS FCI RC			1	
XW1, 2	SMA 50 Ohm PCB end launch connector	19-70-TGG		2	MULTICOMP
F1, 2	PLP-10.7	10,7MHz LPF		2	Minicircuits

Table E2 above gives the details of all parts for the sampling clock module. The 50 MHz sampling clock is generated by the OCXO, and see its specification are given in the data sheet below.

E.3 Data Acquisition Card

- 1 bit to 16 bit digital I/O
- Special 1, 2 and 4 bit digital I/O mode (Mi.7005 only).
- 3,3 V and 5 V compatible TTL I/O
- 1 ks/s up to 125 Ms/s sample rate
- Up to 512 Mbyte memory
- Enhanced trigger possibilities
- Replay and record possible at the same time

Figure E.3: *Data acquisition card and docking station*

Options included

- FIFO mode
- External TTL trigger input/output
- External TTL clock input/output
- Pattern and edge trigger
- Pulse width trigger
- Basic memory: 16 Mbyte
- 1 to 4 bit memory efficient mode
- Input impedance selectable to 110 Ohm or 1 MOhm

The digital data acquisition card offers a resolution between 1 bit and 16 bits with a maximum sample rate of 125 Msamples/s. Each of the 16 1-bit resolution channels of the board can be separately programmed for input or output. The entire on-board memory of up to 16 Mbytes can be used for recording or replaying digital data or the board can be used in a FIFO mode, which is designed for continuous data transfer between a measurement board and the PC memory (up to 100 Mbytes/s) or hard disk (up to 50 Mbytes/s). The data stream is controlled automatically by the interrupt request on the driver. A sampling clock can be supplied from an external system using an external connector and it is possible to output the internally used sampling clock to synchronize external equipment. The internal standard synchronization bus allows synchronization of several boards.

E.4 Software for Data Acquisition

The customized data acquisition software applies the FIFO mode of the data acquisition card to record the data continuously, and transfer it to the hard disk directly. The on-board memory is used as a continuous buffer and the data must be read from the board with at least as high a speed as the speed of data collected in. If the data is read from the board more slowly, the hardware buffers will overrun and the FIFO mode will be stopped.

Figure E.3 shows the working schema of the FIFO mode. On the hardware side, the board memory is split into two buffers of the same length. These buffers can be up to half of the on-board memory in size. In addition to the hardware buffers, the software driver holds up to 256 software buffers of the same length as the hardware buffers (at

present 64 software buffers can satisfy the experiment usage, as confirmed by testing). Whenever a hardware buffer is full with data the hardware generates an interrupt and the software driver transfers the contents of this hardware buffer to the next software buffer that is available. While transferring the content of one hardware buffer to the PC, the other is filled as an automatic background process. After processing the data, the application software tells the driver that it can use the software buffer for data collection again. This two-stage buffering has a big advantages when running the FIFO at the speed limit.

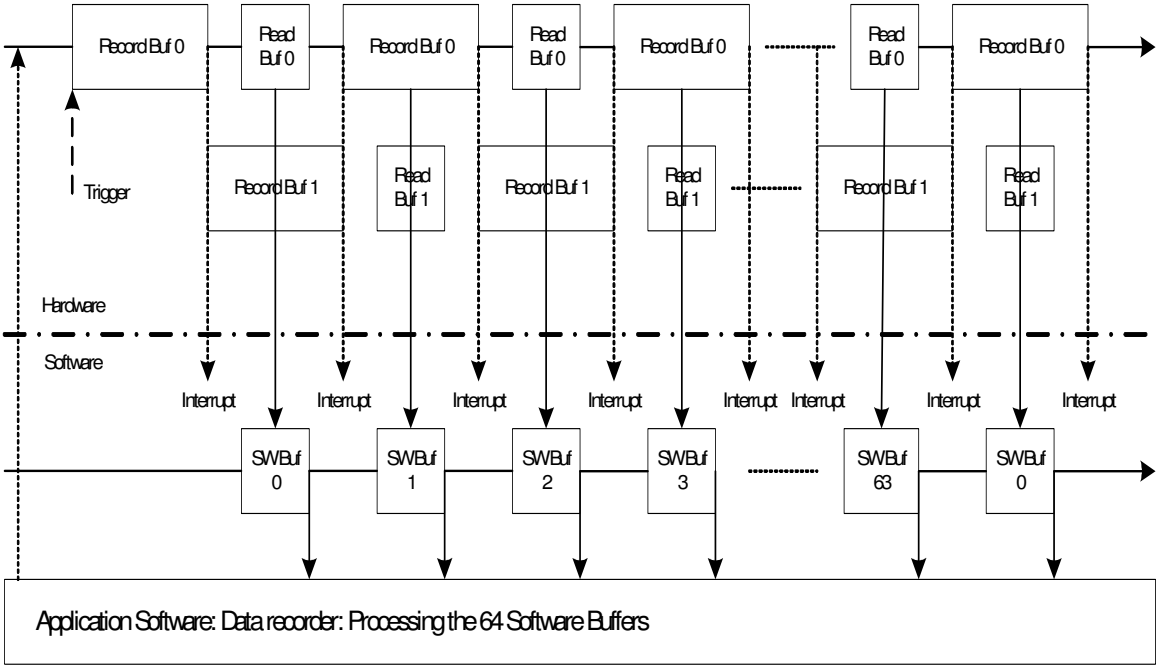

Figure E.4: *Read Scheme of FIFO Mode*

The software buffers greatly expand the acquisition time that can be buffered and protects the whole system against buffer overrun. However, one bottleneck with the FIFO mode is the PCI bus of host PC. The standard PCI bus is theoretically capable of transferring 32-bit long data at the frequency of 33 MHz, so that a maximum burst transfer of 132 Mbytes per second can be achieved. As several devices can share the PCI bus this maximum transfer rate is only available for a short transfer burst time

until new bus arbitration is necessary. In fact the continuous transfer rate is limited to approximately 100-110 Mbytes per second. The maximum FIFO speed one can achieve depends heavily on the PC system and the operating system and varies from system to system. The maximum sample rate supported by the data acquisition board depends on the working mode and the number of activated channels.

For the experimentation reported, 4-bit and 8-bit modes are used, these modes respectively allowing maximum sample rates of 125 MSamples/s (62.5 Mbytes/s) and 100 MSamples/s (100 Mbytes/s). Abundant tests indicated that best results were obtained when programming the buffer length to be a number of samples that can hold approximately 100 ms of data. Here we use 64 software buffers, the size of each being 16 kbytes. However, when operating near the speed limit of the PCI bus in the FIFO mode or when buffer overruns, it can be useful to have larger FIFO buffers. When the goal is a fast update in FIFO mode, smaller buffers and a larger number of buffers can offer better performance.

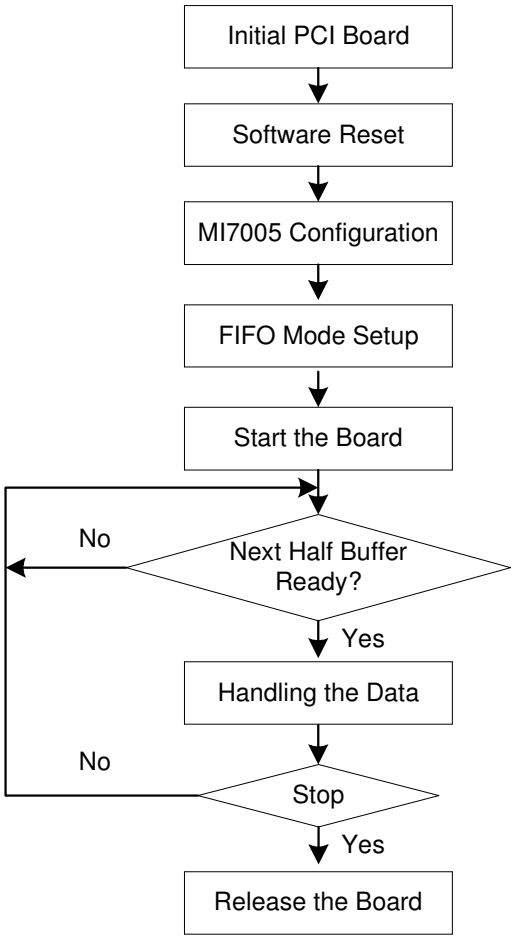

Figure E.5: *Data Acquisition Software Flowchart*

Figure E4 above shows the software flowchart of the customized data acquisition application, which employs the data acquisition board to record the data. First, the data acquisition board is initialized to get the board number and board type. Then the board configuration routine defines the working mode and allocates buffer memory, and the FIFO routine defines the clock source, the sampling rate, the trigger source and the input impedance etc. The software "start" command and "wait" command both wait for the signal that the next buffer has to be processed, this signal being generated by the software driver on receiving an interrupt from the board. The application counts all the software buffers that have been transferred and this number

can be read out from the driver to know the exact amount of data that has been transferred. Finally, after handling the data, the memory is cleared and the board released.

The file format of the data files generated by this process is described here. The whole of a file is a data block, and the data is written to the file in 16-bit binary format, with the lower byte first (little endian). For example, the value 0x1234 is written to disk with 34 first followed by 12. The total length of the data block depends on the data width and the total data count. Because the file is written in binary format, any binary file editor can be used to view it or functions designed for reading files can be used to get the file information and data values.

The software mentioned above stores the data as a single sequence, so it is necessary to extract the data supplied by the different channels from this sequence. By performing bit manipulation, each stored byte is extracted and divided into four or eight parts, each bit pair (associated with a particular channel) being saved individually. After this process, the raw data will have been split into four or eight files with identical size, each relevant to a different channel.

E.5 Data Acquisition Subsystem Testing

The data acquisition subsystem test consisted of testing the ADC board and the data acquisition card separately at the beginning; the assembled subsystem was then tested with a sine wave and a square wave as inputs, the stored data was used to reconstruct the input signal with MATLAB, allowing checks of the working frequency range and

the lowest permissible input amplitude of subsystem. Transmission line effects and environment noise, particularly on clock and control lines, also require attention. It is advisable to use twisted-pair connections to the data acquisition card, each digital I/O signal line being twisted with a GND line, and to place a shield around the wires.

Figure E6 below shows the testing setup for the whole data acquisition subsystem. With a baseband 10 MHz PRN sequence generated by AMIQ generator, this analogue input signal has been converted to digital bits, sampled by data acquisition card with 50 MHz clock, and written into files on the hard disk.

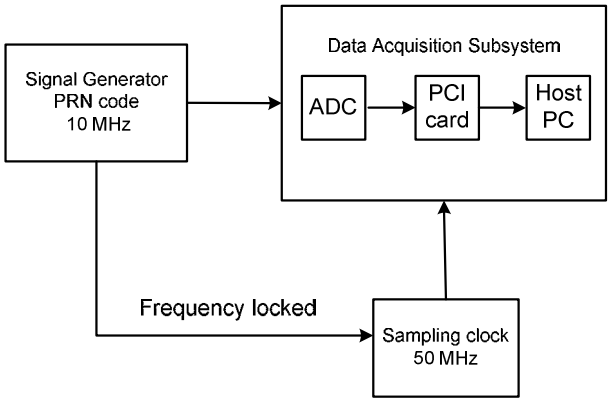

Figure E.6: *Experimental Set-up for DAQ Testing*

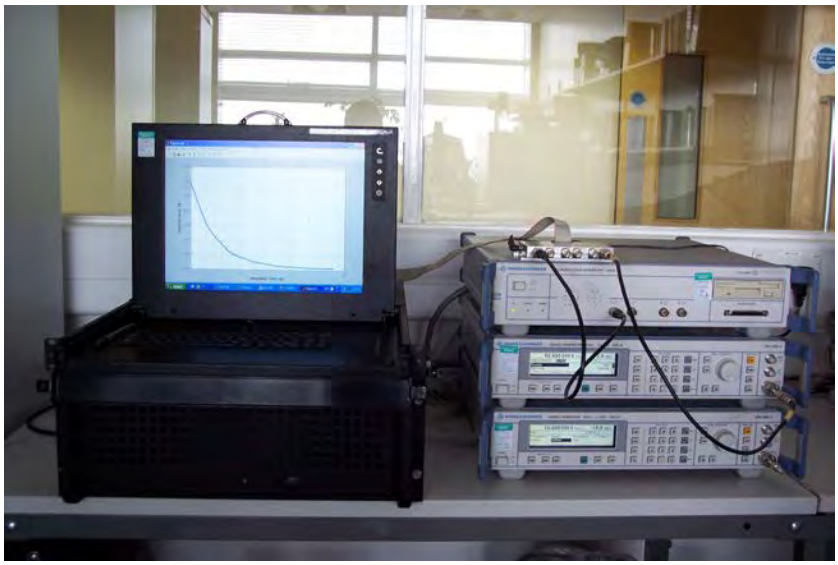

Figure E.7:*Photo of Experimental Set-up*

The stored data has then been divided into multiple files for each channel and the correlation with locally generated PRN code has been used for a data integrity check.

Figure E8 below show the correlation results. Figure E.8 (a) shows the mainlobe of the correlation peak between the stored data from one channel and the reference code; and Figure E.8 (b) shows the zoomed version. It can be clearly seen that the width of mainlobe is 0.1 us which corresponds to 10 MHz symbol rate. Figures E.8(c) and E.8(d) plot the sidelobe level of the correlation peak in both decimal and log scales. It reaches the expected theoretical value of -90 dB (as the PRN code is generated from 15 bit shift feedback registers). From these results the full function of data acquisition subsystem has been confirmed and it's ready for the further testing with the microwave receiver.

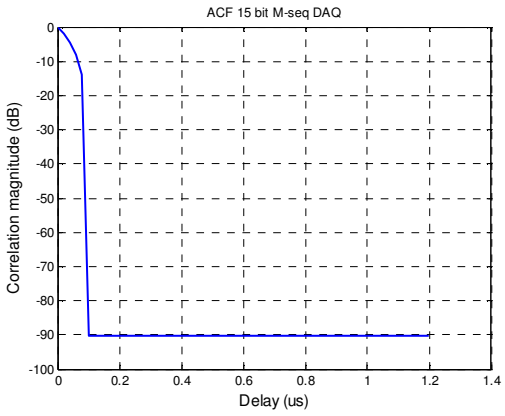

(a) correlation peak main lobe

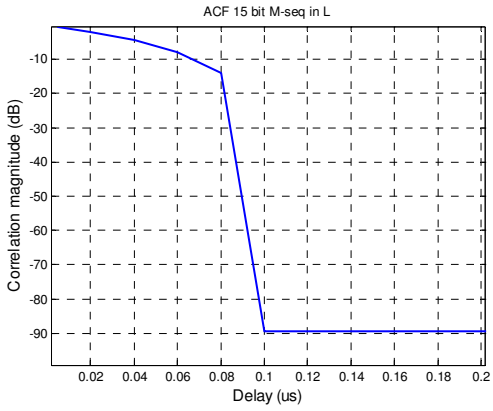

(b) zoom of (a)

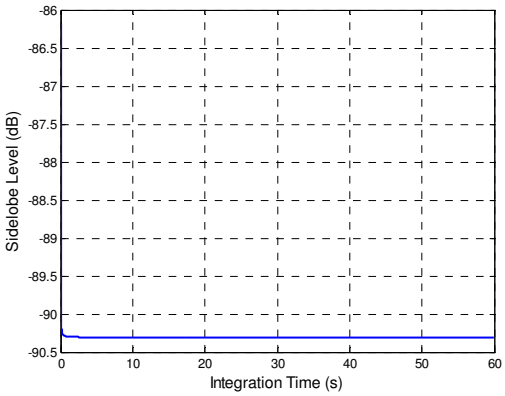

(c) correlation sidelobe level

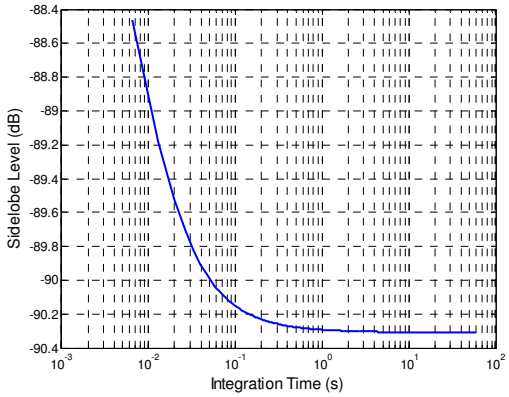

(d) log scale of (c)

Figure E.8: *Data Acquisition Subsystem Testing Results*

Appendix F GPS Receiver

The Legacy-E (Topcon) GNSS receiver is used in the radar. It based on a full function Euro Card design, which allows use of GPS and/or GLONASS L1 and L1/L2. The Legacy-E features dual frequency ability with GPS, or single with GPS+GLONASS signals. Based around a half Euro Card, it is one of the smallest high performance GPS units available on the market. A photo of the Legacy-E receiver and its antenna are shown below.

Brief specification:

- 1 x Legacy E GGD GPS+ Base Station
- 40 Super Channel Receiver
- L1+L2 GPS/GLONASS
- Advanced Multipath Reduction
- 96Mb Data Recording
- Base Case
- 7ah Battery / Charger
- PGA-1 GPS Antenna with cable
- Co-op Tracking (low elevation, under canopy)
- Base Case Complete
- Heavy Duty Wooden Tripod
- PC-CDU Lite Interface Software

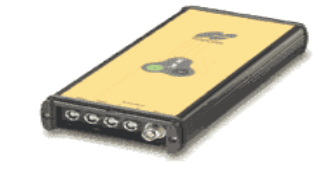

Appendix G Microwave Receiver – Testing Results

As discussed in Chapter 5, more details are given in this section for the hardware design and testing of the microwave receiver. Table G1 below lists the information for all microwave receiver components. Most of parts are off-the-shelf commercial products except the RF front end which is a customized designed and its specification included in Appendix C. In this Appendix, specifications for all other parts will be given and testing results for different blocks and the full microwave receiver will be presented and discussed.

A series of testing stages in the laboratory has been performed according the following categories:

1. Power supply test, DC and AC coupling
2. Local oscillator test, frequency synthesizer
3. IF and baseband blocks test, IF gain and quadrature demodulator distortion
4. Full receiver test with noise and input signal

Table G-1: *Microwave Receiver Parts List*

Component	Specifications	Model Number	Supplier
RF LNA1	See Appendix C		
IF Amplifiers A1—A4	F_l –F_u: 0.05-500 MHZ, Gain: 20 dB, NF: 5.3 dB	ZFL-500	Mini-circuits
Splitters S1	3-way 0^0, 1.0 -- 2.0 GHZ	ZA3PD-2	Mini-circuits
Mixers M1	LO/RF: 1-4.2 GHZ	ZX05-C42	Mini-circuits
IF Filter BPF3	F_c: 140 MHz, 1 dB BW: 55.8 MHz, Insertion Loss: < 1 dB	KR 2743	KR Electronics
Splitters S2	3-way 0^0, 1 -- 500 MHz	ZFSC-3-1	Mini-circuits
Splitters S3	2-way 0^0, 2 -- 1200 MHz	ZX10-2-12	Mini-circuits
Splitters S4	2-way 90^0, 120 - 180 MHz	ZMSCQ-2-180	Mini-circuits
Mixers M2	LO/RF: 0.5-500 MHZ, IF: DC-500 MHz	ZLW-1H	Mini-circuits
Amplifier A5	F_l –F_u: 0.01-1GHz	ZFL-1000VH	Mini-circuits
LPF1	Pass Band: DC-32 MHZ	SLP-30	Mini-Circuits

The process for these testing categories has been described briefly and the main results are noted below.

- Power Supply Test, DC and AC coupling

Given different input voltages applied to the DC-DC converter, the working range and the converter output voltage are established. From these results, the DC-DC converters work consistently and accurately over a wide range of input voltages. Using an AD-3521 FFT analyzer, it tests the AC coupling at the external power supply, the output of the DC-DC converter and the capacitor board to check the external interference and environment noise applied to the microwave receiver caused

by these components. Table G-2 below shows the AC coupling testing results. Although this interference extends into the working frequency range of the microwave receiver, the extremely low amplitude implies little effect upon the wanted signal.

Table G-2: *AC Coupling Test Results*

Power Supply Unit	Frequencies	Level
External Power Supply Input: 220 V AC, Output: 12 V DC	50 Hz	-68 dBV to –80 dBV
	66.4 kHz	-43 dBV
Internal DC-DC Converter Input: 12 V DC Output: 15 V DC	50 Hz	-80 to -102 dBV
	25 kHz	-107 dBV or less
	424 kHz	-36 dBm to –67 dBm
At capacitor board 15 V	424 kHz	-49 dBm to –70 dBm
Internal DC-DC Converter Input: 12 V DC Output: 5 V DC	410 kHz	-44 dBm

- Local oscillator test, frequency synthesizer

During the experiments using GLONASS, two synchronized Rohde & Schwarz signal generators are locked with a common clock and used as a local oscillator. During the experiments using Galileo, as the compact hardware is required for field trials, two frequency synthesizers have been used to replace the signal generators. The test procedure is to find the appropriate output level of the local oscillator using a spectrum analyzer, comparing with the working range of the power splitter and the ZFL-1000VH amplifier. Table G-3 below shows the output level from each point.

Table G-3: *Frequency Synthesizer Test Results*

Generator	Frequency	Output Level
Frequency synthesizer 1	1347.14 MHz	10 dBm
Frequency synthesizer 1	140 MHz	6 dBm
Power Splitters and LO 2 amplifier		
Component	Frequency of operation	Insertion loss/Gain
Power splitter 1(ZA3PD-2)	1347.14 MHz at the input	~ 6 dB
Power splitter 2 (ZA3PD-2)	140 MHz	~ 5.5 dB
Power splitter (ZMSCQ-2-90)	140 MHz	~3 dB
Local oscillator amplifier (ZFL-1000VH)	140 MHz	~ 22 dB

To match the working amplitude of the mixers perfectly, considering the loss of the power splitter and the amplifier gain, the output level of LO1 and LO2 will be set as 10 dBm and 6 dBm individually.

- In-Phase/Quadrature Demodulator Distortion (Baseband Block) Test

The goal of the testing is to check the amplitude unbalance between the in-phase and quadrature channels. See Figure G.1 below for the testing diagram. A 140 MHz sine wave is used as a IQ demodulator input, with the combined I/Q signals vectors shown on the screen of the two-channel oscilloscope.

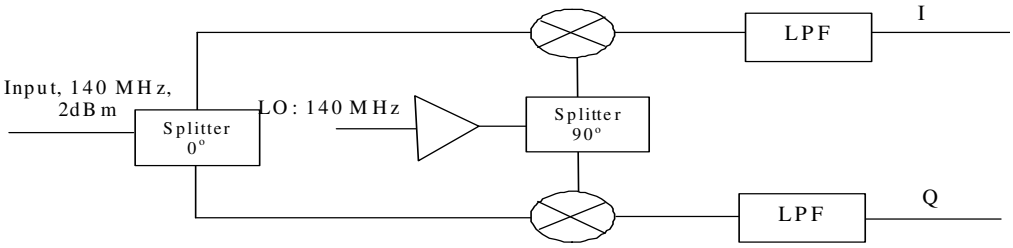

Figure G.1: *I/Q Demodulator Distortion Test Diagram*

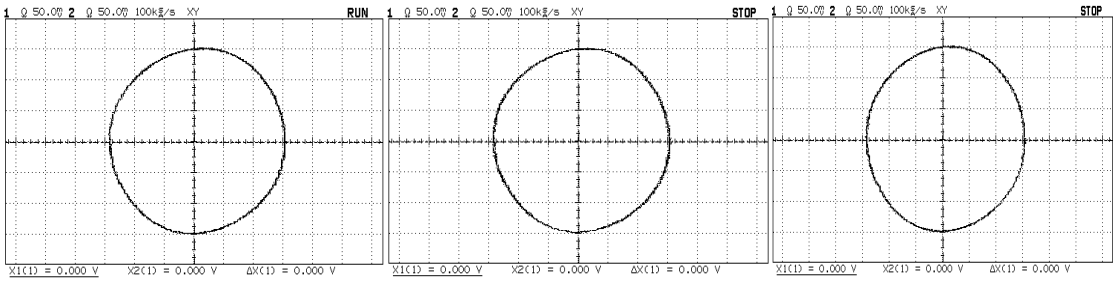

Heterodyne Channel **Radar Channel** **Low-gain Channel**

Figure G.2: *I/Q vectors*

In the diagram (Figure G.2) shown above the vertical and horizontal scales are equal. A nearly perfect circle is shown, indicating that the I and Q channels are balanced.

The goal of next testing phase is to check whether the microwave receiver can down-convert the input to baseband signal successfully. A 50-ohm load was connected to the input and the frequency response observed with a spectrum analyzer. The output spectrum after the IF bandpass filter and the entire IF amplifier has the centre frequency (140 MHz) and bandwidth (50 MHz), confirming the response of the IF filter.

The second step is to provide a BPSK signal as the input of the receiver and test the channels without IF amplifiers and without a SAW filter (to avoid IF amplifier saturation due to high gain). See Figure G.3 below for testing procedure. For the test, the signals are displayed and stored using the oscilloscope.

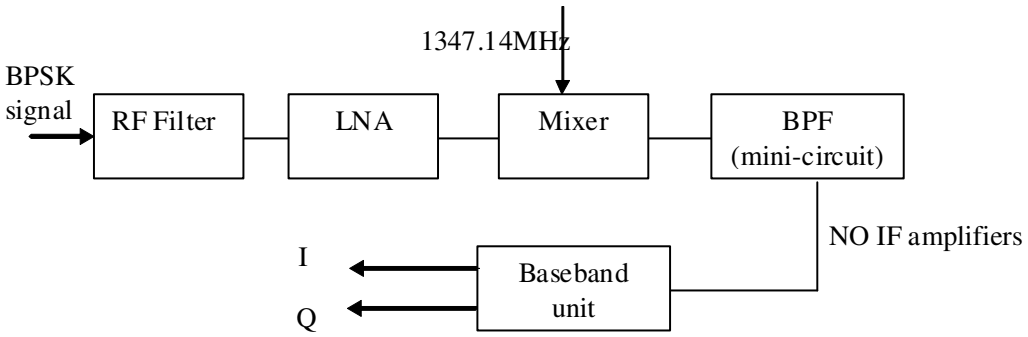

Figure G.3: *Test Diagram*

- Full receiver test with noise and input signal

Figure G.4 below shows the diagram for receiver noise testing procedure. No input signal will be applied and a 50 ohm load was connected at the RF input of the microwave receiver. Only the receiver noise will appear at the input of data acquisition subsystem, sampled and stored into the host PC.

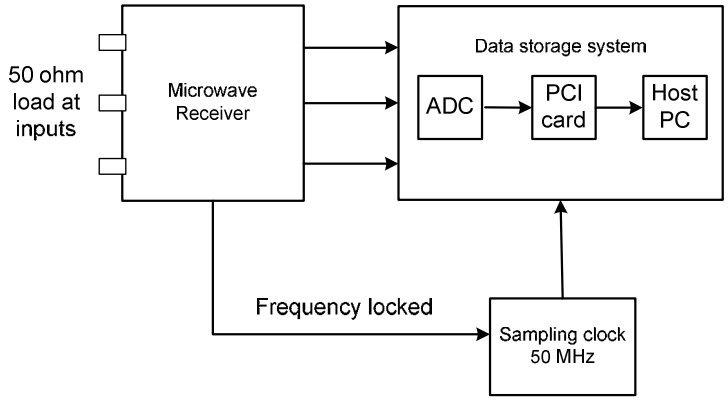

Figure G.4: *Receiver Noise Test Diagram*

Figures G.5 below show the correlation results. Figure G.5 (a) shows the mainlobe of auto-correlation peak of the receiver noise in channel R; and Figure G.5 (b) shows its

sidelobe level. Figures G.5 (c) and G.5(d) plot the similar results for channel H. Figures G.5(e) and G.5(f) plot the cross-correlation of the noise between two channels. From these results the receiver noise behaves as expected and no strong internal interference was detected.

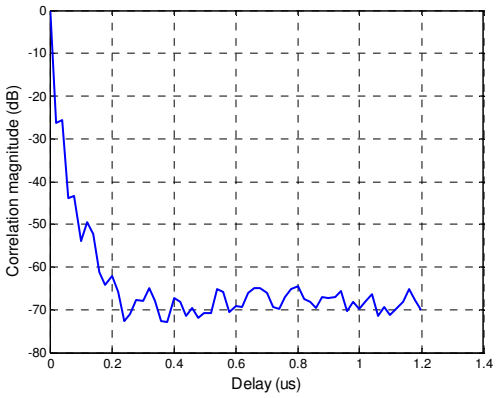

(a) ACF of noise in R-channel

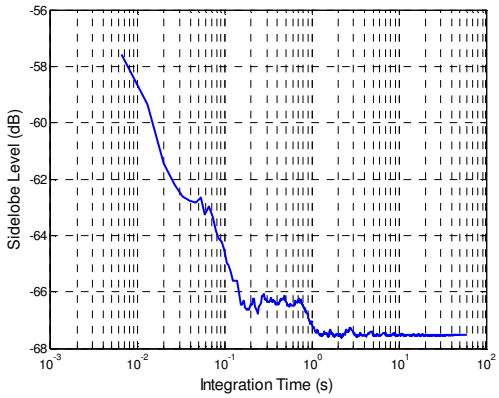

(b) sidelobe level of (a)

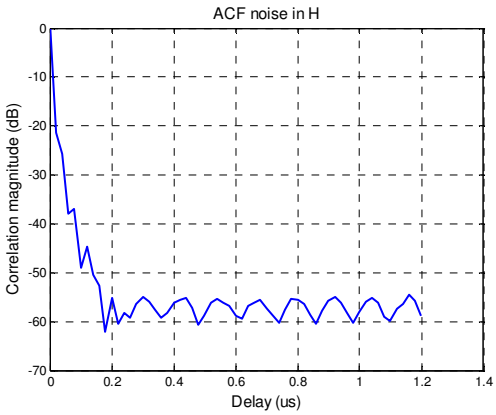

(c) ACF of noise in H-channel

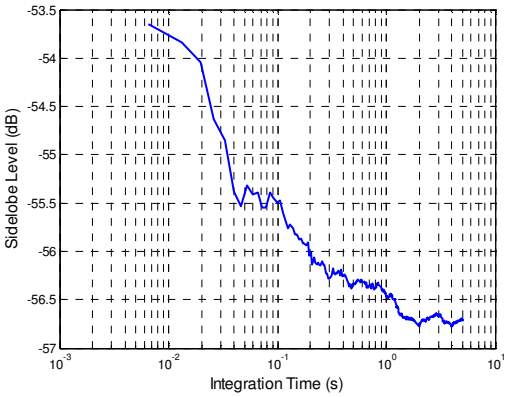

(d) sidelobe level of (c)

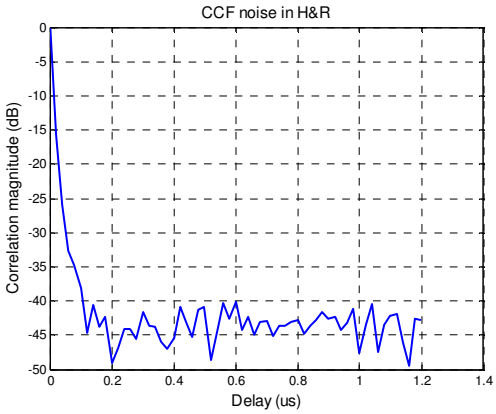

(e) CCF of noise between H and R channels

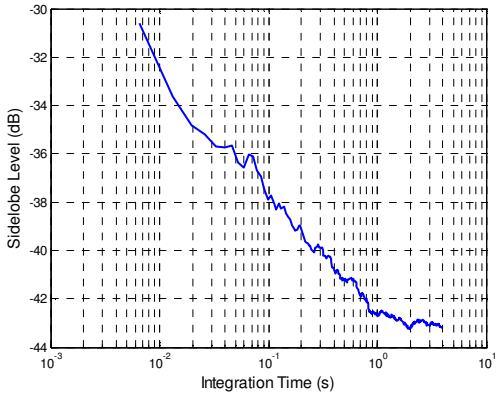

(f) sidelobe level of (e)

Figure G.5: *Receiver Noise Testing Results*

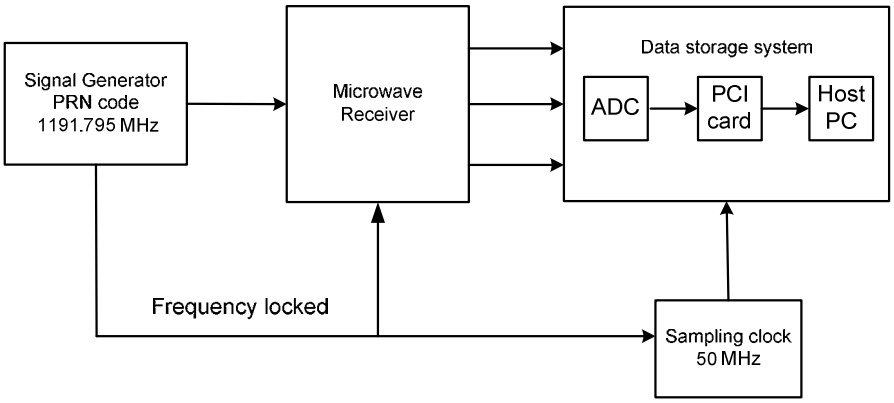

Figure G.6: *Test Diagram for Receiver with Input Signal*

Figure G.6 above shows the diagram for receiver input signal testing procedure. An input signal with 1191.795 MHz frequency and 10 MHz bandwidth will be applied at the RF input of the microwave receiver. Both the receiver noise and the signal output will appear at the input of the data acquisition subsystem, sampled and stored into the host PC.

Figure G.7: *Photo of Satellite Imitator (Signal Generator)*

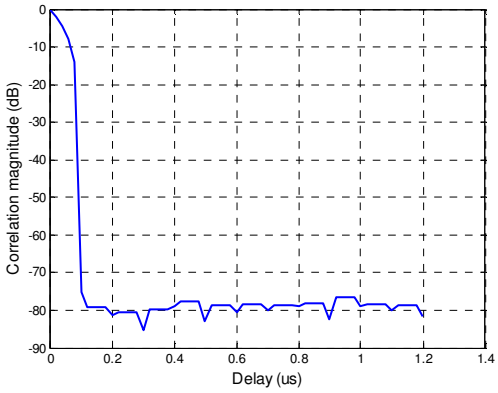

(a) ACF of L-channel signal

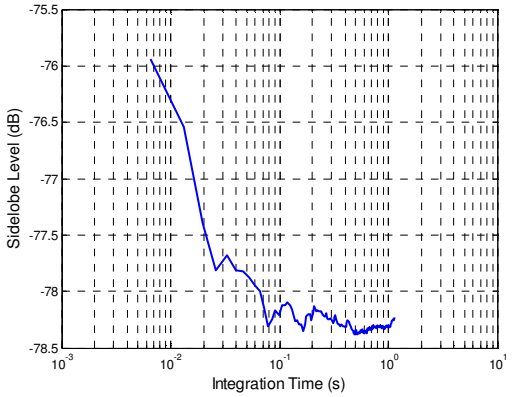

(b) sidelobe level of (a)

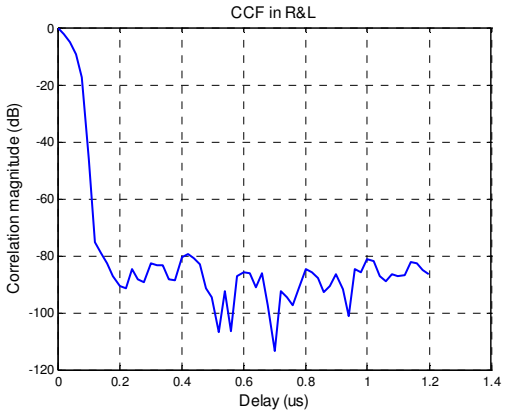

(c) CCF between L-channel and R-channel signals

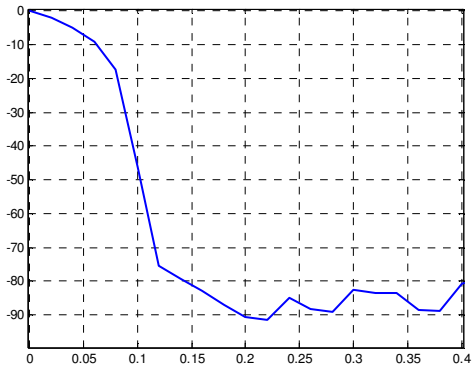

(d) zoom of (c)

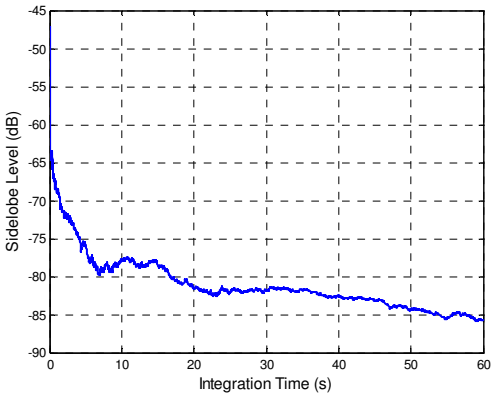

(e) sidelobe level of (c)

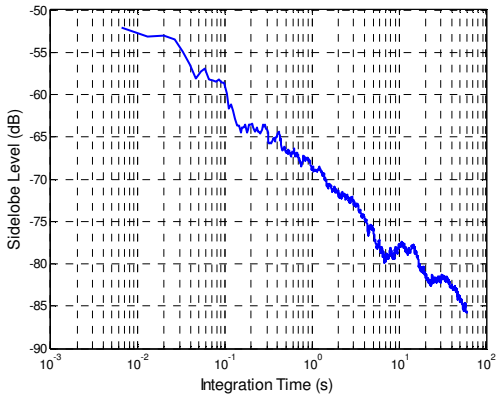

(f) log scale of (e)

Figure G.8: *Results for correlation between radar and low-gain channels*

Figure G.8 above shows the correlation results. Figure G.8 (a) shows the mainlobe of the auto-correlation peak of stored signal in channel L; and Figure G.8 (b) shows its sidelobe level. Figures G.8(c) and G.8(d) plot the cross-correlation of the stored

signals from the L and R channels. It can be clearly seen that the width of mainlobe is 0.1 us which corresponds to a 10 MHz bandwidth. Figures G.8(e) and G.8(f) display the sidelobe of CCF.

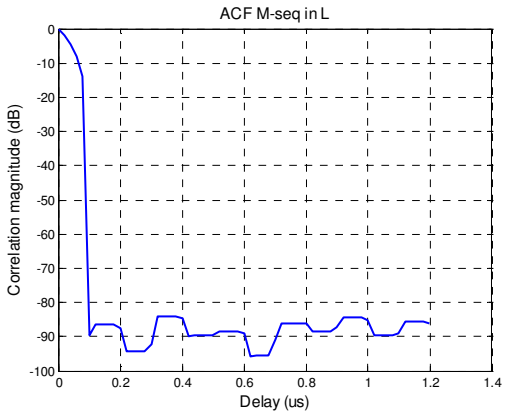

(a) ACF of L-channel signal

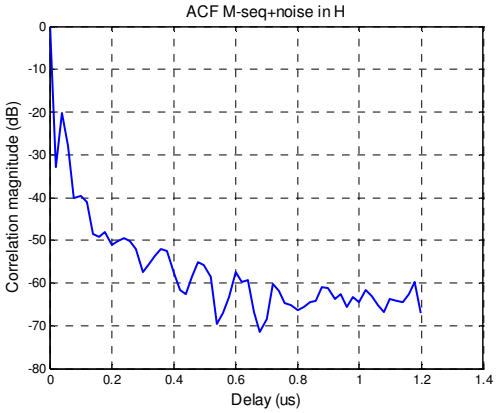

(b) ACF of H-channel signal

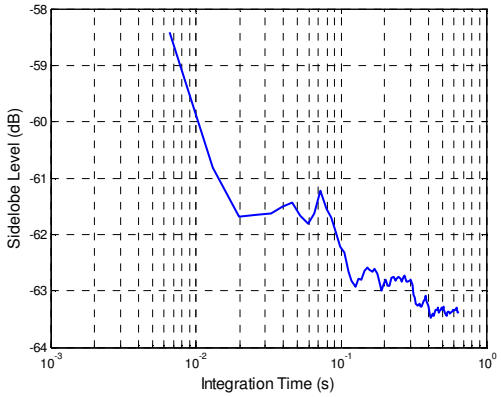

(c) log scale sidelobe level of (b)

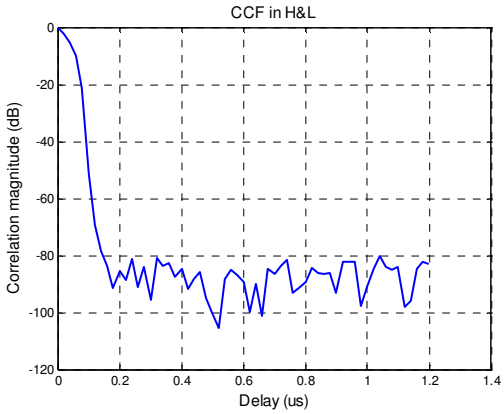

(d) CCF between L- and H-channels

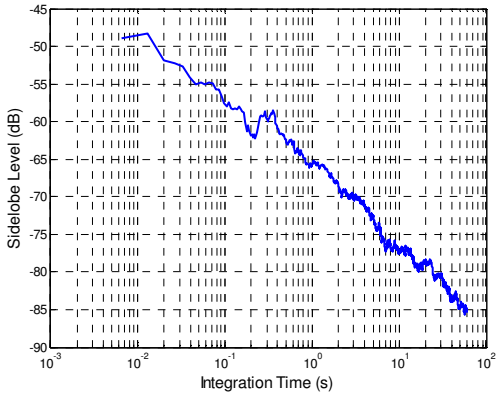

(e) log scale sidelobe level of (d)

Figure G.9: *Results for correlation between heterodyne and low-gain channels*

Figures G9 above show the similar results to Figure G.8, the only difference is channel L and H used this time. Figure G.9 (a) shows the mainlobe of auto-correlation peak of stored signal in channel L; and Figure G.9 (b) and G.9(c) show auto-correlation peak of stored signal in channel H and its sidelobe level. Figures G.9(d) and G.9(e) plot the cross-correlation of the stored signals from L and R channels and the sidelobe of cross correlation function.

1. *Galileo Open Service Signal In Space Interface Control Document*. 2006, European Space Agency / Galileo Joint Undertaking.

Appendix H Publications List

- Cherniakov, M., Antoniou, M., Saini, R., Zuo, R., & Edwards, J. (2006). *Space-Surface BSAR - Analytical and Experimental study*. Paper presented at the EuSAR conference, Dresden, Germany.
- Cherniakov, M., Saini, R., Antoniou, M., Zuo, R., & Edwards, J. (2006). *Modified Range-Doppler algorithm for Space-Surface BSAR imaging*. Paper presented at the Radar 2006, China.
- Cherniakov, M., Saini, R., Antoniou, M., Zuo, R., & Edwards, J. (2006). *Signal Processing in space-surface bistatic synthetic aperture radar*. Paper presented at the International Conference on Synthetic Aperture Sonar and Synthetic Aperture Radar, Lerici, Italy.
- Cherniakov, M., Saini, R., Antoniou, M., Zuo, R., & Edwards, J. (2006). *SS-BSAR with Transmitter of Opportunity - Practical Aspect*. Paper presented at the EMRS DTC Conference, Edinburgh, UK.
- Zuo, R., Saini, R., & Cherniakov, M. (2007). *Non-cooperative Transmitter Selections for Space-Surface Bistatic SAR*. Paper presented at the EMRC DTC 2007 conference, Edinburgh, UK.
- Saini, R., Zuo, R., & Cherniakov, M. (2007). *Signal synchronisation in SS-BSAR based on GLONASS satellite emission*. Paper presented at the Radar 2007, International conference, Edinburgh, UK.
- Cherniakov, M., Saini, R., Zuo, R., & Antoniou, M. (2007). Space-Surface Bistatic Synthetic Aperture Radar with GNSS transmitter of opportunity-Experimental Results, . *IET Proceedings Radar, Sonar and Navigation, 1*(6), 447 - 458.
- Antoniou, M., Saini, R., Cherniakov, M., & Zuo, R. (2007). *Image Formation Algorithm for Space-Surface BSAR*. Paper presented at the EuRAD 2007 conference, Munich, Germany.
- Zuo, R., Saini, R., Antoniou, M., & Cherniakov, M. (2008). *Development of a Passive BSAR with GNSS Transmitters of Opportunity*. Paper presented at the EMRC DTC 2008 conference, Edinburgh, UK.

- Saini, R., Zuo, R., & Cherniakov, M. (2008). *Development of space-surface Bistatic synthetic aperture radar with GNSS transmitter of opportunity*. Paper presented at the IEEE Radar Conference 2008, Rome, Italy.
- Cherniakov, M., Saini, R., Antoniou, M., Zuo, R., & Plakidis, E. (2008). Experiences Gained during the Development of a Passive BSAR with GNSS Transmitters of Opportunity. *International Jounal of Navigation and Observation, 2008*. doi: 10.1155/2008/807958
- Zuo, R., Antoniou, M., Plakidis, E., & Cherniakov, M. (2009). *Passive bistatic imaging using Galileo transmitters*. Paper presented at the EMRC DTC 2009 conference, Edinburgh, UK.
- Saini, R., Zuo, R. (communication author), & Cherniakov, M. (2009). Problem of Signal Synchronisation in SS-BSAR based on Global Navigation Satellite Emissions - Experimental Results. *IET Proceedings Radar, Sonar and Navigation, 4*(1), 110 - 125.